Merocyanine Dyes as Donor Materials in Vacuum-Deposited Organic Solar Cells: Insights into Structure-Property-Performance Relationships

Dissertation zur Erlangung des
Naturwissenschaftlichen Doktorgrades
der Julius-Maximilians-Universität Würzburg

vorgelegt von
Antti Ojala
aus Porvoo / Finnland

Ludwigshafen am Rhein 2011

Eingereicht am
bei der Fakultät für Chemie und Pharmazie

1. Gutachter: Prof. Dr. Frank Würthner
2. Gutachter: Prof. Dr. Jens Pflaum
der Dissertation

1. Prüfer: Prof. Dr. Frank Würthner
2. Prüfer: Prof. Dr Jens Pflaum
3. Prüfer: Prof. Dr. Bernd Engels
des Öffentlichen Promotionskolloquiums

Tag des Öffentlichen Promotionskolloquiums:

Doktorurkunde ausgehändigt am:

to Niina

List of Abbreviations

A	acceptor
AFM	atomic force microscopy
BCP	bathocuproine
BHJ	bulk heterojunction
Bphen	4,7-diphenyl-1,10-phenanthroline
Btu	British thermal units
CSD	Cambridge structural database
cBHJ	controlled bulk heterojunction
c-Si	crystalline-Si
CT	charge transfer
CV	cyclic voltammetric
D	donor
DCM	dichloromethane
DCV5T	a,a'-*bis*(2,2-dicyanovinyl)-quinquethiophene
DFT	density functional theory
DSC	differential scanning calorimetry
EA	electron affinity
EBL	electron blocking layer
EOA	electro-optical absorption
EQE	external quantum efficiency
FWHM	full-weight-half-maximum
GooF	goodness-of-fit
HHJ	hybrid heterojunction
HOMO	highest occupied molecular orbital
IDOP	indoline dioxopyridine
IP	ionization potential
IQE	internal quantum efficiency
IRSE	infrared spectroscopic ellipsometry
ITO	indium tin oxide
LUMO	lowest unoccupied molecular orbital
MC	merocyanine

MM	molecular mechanics
Mp	melting point
MPc	metal phthalocyanine
NIR	near infrared
NLO	non-linear optics
NPD	*N*,*N*-bisnaphthalen-1-yl-*N*,*N*-bisphenyl-benzidine
OECD	organization for economic growth and development
OLED	organic light emitting diode
OPV	organic photovoltaics
OPVD	organic physical vapour deposition
PCBM	[6,6]-phenyl-C_{61}-butyric acid methyl ester
PCE	power conversion efficiency
Pedot:PSS	poly(3,4-ethylenedioxythiophene):poly(styrenesulfonate)
PHJ	planar heterojunction
PI	packing index
PL	photoluminescence
PTCBI	3,4,9,10-perylene tetracarboxylic acid bis-benzimidazole
PTCDA	3,4,9,10-perylene tetracarboxylic acid dianhydride
PTCDI	3,4,9,10-perylene tetracarboxylic acid diimide
P3HT	poly(3-hexylthiophene)
QM	quantum mechanics
SCLC	space-charge-limited-current
TCO	transparent conducting oxide
UPS	ultraviolet photoemission spectroscopy
UV/Vis	ultraviolet / visible
VAC	vacuum
XRPD	X-ray powder diffraction

Table of Contents

Chapter 1 Motivation and Aim of Thesis 1

Chapter 2 Vacuum-Processed Organic Solar Cells 7

2.1 General Discussion 8

2.1.1 Fundamentals of Photovoltaic Devices 8

2.1.2 Equivalent Circuit Model 9

2.1.3 Donor/Acceptor Heterojunction 10

2.1.4 Photocurrent Generation 13

2.2 Thermally Vacuum-Deposited Organic Solar Cells 18

2.2.1 Materials 18

2.2.2 Device Architectures 21

2.2.3 Tandem Cells 25

2.2.4 Other Device Structures 28

2.2.5 Device Lifetime 29

2.2.6 Conclusions and Outlook 30

2.3 References 31

Chapter 3 Experimental Set-Ups for the Fabrication and Characterization of Solar Cells 37

3.1 Substrate 38

3.2 Device Fabrication 38

3.3 Device Characterization 39

3.3.1 Current-Voltage Characteristics 39

3.3.2 Incident Photons to Current Measurements 40

Chapter 4 Crystal Packing of Merocyanine Dyes: Effect of Molecular and Local Dipole Moments 43

4.1 Introduction 44

4.2 Results and Discussion 46

4.2.1 Space Groups and Dipole Moments 46

4.2.2 CSD Search 51

4.2.3 Packing Motifs of Merocyanines Based on the Fischer's Base 53

4.2.4 Intermolecular Dipole-Dipole Interaction as a Supramolecular Synthon 74

4.3 Conclusions 77

4.4 Experimental Section 78
4.5 References 79
Chapter 5 Parallel Bulk Heterojunction Solar Cell by Electrostatically Driven Phase Separation 83
5.1 Introduction 84
5.2 Results and Discussion 85
5.3 Conclusions 94
5.4 Experimental Section 94
5.6 References 97
Chapter 6 Merocyanine/C_{60} Planar Heterojunction Solar Cells: Effect of Dye Orientation on Exciton Dissociation and Solar Cell Performance 99
6.1 Introduction 100
6.2 Results and Discussion 102
6.2.1 Energy Level Diagram 102
6.2.2 Device Characteristics 102
6.2.3 Dye and Film Properties 105
6.2.4 Analytical Electric Field Dependent CT-State Dissociation Model 107
6.2.5 Molecular Orientations as Deduced from IRSE 111
6.2.6 Computations of the CT-state Energies at the ID583/C_{60} Interface 113
6.2.7 Bulk Heterojunction Cells 116
6.3 Conclusions 117
6.4 Experimental Section 118
6.5 References 122
Chapter 7 Planar, Bulk and Hybrid Merocyanine/C_{60} Heterojunction Devices: A Case Study on Thin Film Morphology and Photovoltaic Performance 127
7.1 Introduction 128
7.2 Results and Discussion 130
7.2.1 Characterization of Thin Films 130
7.2.2 Solar Cells 136
7.3 Conclusions 144
7.4 Experimental Section 145
7.5 References 148
Chapter 8 Summary 151

Chapter 9 Zusammenfassung (Summary in German) **157**

Appendix **163**

List of Publications and Patents **201**

Acknowledgements **203**

Chapter 1

Motivation and Aim of Thesis

The world's energy consumption in 2007 was 49.3 quadrillion Btu (1 quadrillion Btu = 2.9×10^{11} kWh) and it is estimated to increase by 49% to 73.5 quadrillion Btu in 2035 (Figure 1).[1] The growth of global energy demand will be largest in non-OECD countries where it will increase according to estimations by 85% from 2007 to 2035 whilst in OECD countries the increase of energy consumption will be 14%.[1] In the non-OECD countries the growth of energy consumption is facilitated by the economical growth which is expected to be 4.4% per year on average.

Today the most important source of energy is the liquid fuels (e.g. petroleum) by 35% share of all consumed energy, followed by coal and natural gas with 25% and 21% shares, respectively.[1] Renewable energy sources covers 18% of all global consumed energy, counting biomass, large hydro power, and new renewables (bio fuel, wind, solar, etc.).[2] Biomass accounts for 13% and large hydro power for 3.2% whereas solar photovoltaics (PV) sources represent very marginal share (< 0.01%) of the global energy consumption. However, PV is the fastest growing of all renewable technologies, with a 60% annual average growth rate.[2]

The global electricity consumption is growing significantly faster than the total need for energy, mainly because of the huge economical growth in non-OECD countries and especially in China (Figure 1).[1] Coal provides the largest share of world's electricity generation with a 42% share and it is expected to be largerly unchanged through 2035. The large share of coal in electricity generation is worrying, not only because of the vast CO_2 emissions (single most important), but also due to the particulate matter and heavy metal emissions which are released in air when coal is burned. It is estimated that only in USA particulate emissions from coal power plants cut short the lives of 30 000 people.[3]

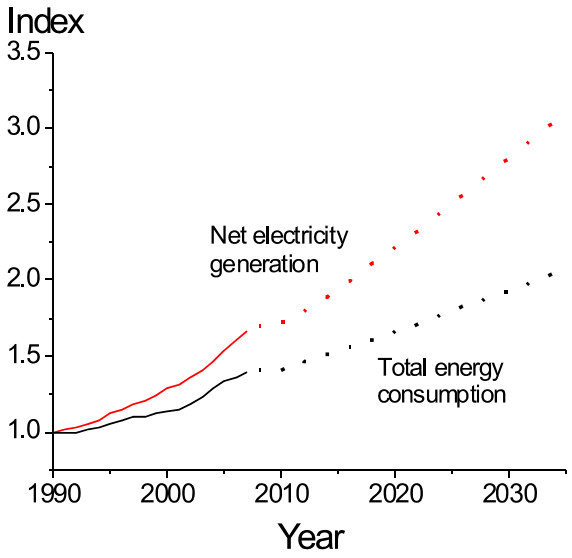

Figure 1. Growth in world electric power generation and total energy consumption, 1990-2035.[1]

The renewable share of world electricity generation was 18% in 2007 and it is estimated to grow to 23% in 2035. PV technologies account at the moment only for ~ 0.3% of the total electricity generation whilst it is estimated to reach 0.5% in 2035.[1] Although the growth rate among all renewable electricity sources is largest for PV technologies, its importance for the global energy production seems to stay marginal. However, the potential of PV technologies is enormous. It is estimated that the existing fossil and nuclear resources can be entirely replaced by harvesting less than 0.02% of the available solar energy (120,000 TW).[1]

A major reason limiting the growth of traditional Si-based PV is the price, which is still today in mid Europe, USA, and Japan ~ 30 cent (US) / kwh. For example, the equivalent price produced in a coal power plant is only ~ 10 cent / kwh.[4] The production costs of crystalline-Si (c-Si) cells are too high to significantly influence the global energy production markets, and unfortunately, the manufacturing costs are expected to remain high in the near future. Hence, new generation PV techniques are needed, such as organic photovoltaics (OPV), to satisfy the global energy hunger.[5,6] The growth of interest on OPV has been tremendous in past years, and for example, the number of journal publications related to OPV has increased almost exponentially between 1980-2007.[5] The main benefits of thin film OPV techniques in comparison with the traditional c-Si solar cells are their potentially low cost, ease of processing, and compatibility with flexible substrates (Figure 2).

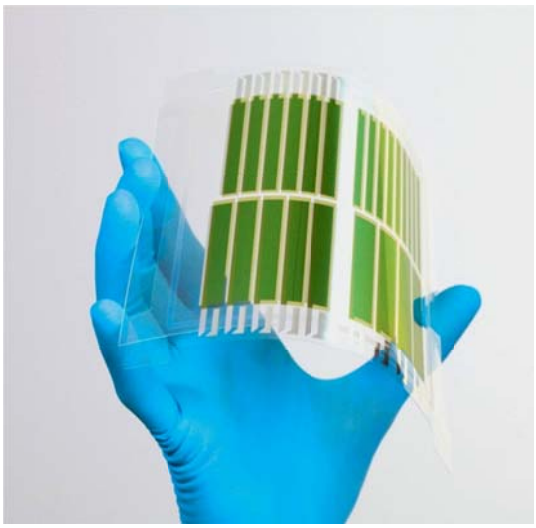

Figure 2. Organic photovoltaic devices on a flexible substrate.[7]

Currently the champion efficiency of solid state organic solar cells is 8.3% based on a p/n (p-conductor/n-conductor) heterojunction.[8] However, a lot of work is still needed in order to exceed 10% module efficiency, which is generally considered as the minimum power conversion efficiency for the wide commercialization of the concept.[9] To meet the efficiency targets, not only new chromophores with improved solar harvest properties are required, but also deeper understanding of the working mechanisms as well as the thin film structure-device-performance relationships has to be gained.

Although merocyanine dyes have been used already for decades in photorefractive and non-linear optical applications, [10] only very recently they have been introduced as new colorants in organic photovoltaic devices based on a heterojunction.[11] Significant advantages of merocyanines, compared to many other chromophore classes, are their relatively simple synthesis and high absorption strengths that enable efficient collection of photons with a thin active layer structure.[11] However, owing to the fact that merocyanines have been investigated only few years as donor materials in OPV, many of their properties are still inadequately understood. One of these is the relation between the solid-state structure and the solar cell performances, on which this thesis will try to shed more light.

The thesis is structured as follows:

Chapter 2 gives a brief introduction to fundamentals of organic photovoltaics with particular focus on vacuum-processed devices. Different materials and device architectures as well as the current state of the technologies are discussed.

Chapter 3 describes the experimental methods that were used to fabricate and characterize the vacuum-deposited organic solar cells at BASF innovations Lab in Ludwigshafen

In **Chapter 4**, the influence of molecular dipole moment on the crystal packing of highly dipolar merocyanine compounds is analyzed. The focus is on the crystal packing of merocyanine dyes with a Fischer base electron donor unit.

Chapter 5 describes how the performance of vacuum-deposited merocyanine(s):C_{60} bulk heterojunction (BHJ) solar cells can be improved by mixing two donors with complementary absorption regions.

Chapter 6 shows how the efficiency of merocyanine (ID583)/C_{60} planar heterojunction (PHJ) solar cells can be improved by controlling the dye molecules' orientation at the ID583/C_{60} heterojunction.

Chapter 7 demonstrates the effect of a transition metal oxide underlayer on the morphology of vacuum-deposited merocyanine (HB364) thin films. The film morphology is studied by crystallographic, microscopic, and spectroscopic methods. In addition, solar cells are fabricated using HB364 as the donor material and various transition metal oxides as the anode buffer layer.

Chapter 8 gives a summary of the thesis in English.

Chapter 9 gives a summary of the thesis in German.

References

[1] EIA, *International energy outlook 2010*, **2010**; Source: www.eia.gov/oiaf/ieo/index.html (read on 03.06.2011).

[2] REN21, *Renewables 2010 Global Status Report,* **2010**; Source: www.ren21.net/Portals/97/documents/GSR/REN21_GSR_2010_full_revised%20Sept2010.pdf (read on 03.06.2011).

[3] NRDC, *Coal in a Changing Climate*, **2007**; Source: www.nrdc.org (read on 03.06.2011).

[4] NREL, *Opportunities and Challenges for Development of a Mature Concentrating Photovoltaic Power Industry*, **2009**; Source: www.osti.gov/bridge (read on 03.06.2011).

[5] B. P. Rand, J. Genoe, P. Heremans, J. Poortmans, *Prog. Photovolt: Res. Appl*. **2007**, *15*, 659.

[6] For introduction to organic solar cells, see: (a) *MRS Bulletin* **2005**, *30*, the whole issue; (b) K. Walzer, B. Maennig, M. Pfeiffer, K. Leo, *Chem. Rev.* **2007**, *107*, 1233; (c) C. Brabec, U. Scherf, V. Dyakon, *Organic Photovoltaics: Materials, Device Physics and Manufacturing Technologies*, Wiley-VCH Verlag GmbH & Co. KGaA Weinheim, Germany, **2008**; (d) H. Hoppe, N. S. Sariciftci, *J. Mater. Res.* **2004**, *19*, 1924.

[7] Source: www.heliatek.com/index.php?page=16 (read on 03.06.2011)

[8] M. A. Green, K. Emery, Y. Hishikawa, W. Warta, *Prog. Photovolt: Res. Appl*. **2011**, *19*, 84.

[9] M. C. Scharber, D. Mühlbacher, M. Koppe, P. Denk, C. Waldauf, A. J. Heeger, C. J. Brabec, *Adv. Mater.* **2006**, *18*, 789.

[10] (a) F. Würthner, S. Yao, J. Schilling, R. Wortmann, M. Redi-Abshiro, E. Mecher, F. Gallego-Gomez, K. Meerholz, *J. Am. Chem. Soc*. **2001**, *123*, 2810; (b) T. Kaino, S. Tomaru, *Adv. Mater*. **1993**, *5*, 172; (c) O. Ostroverkhova, W. E. Moerner, *Chem. Rev*. **2004**, 3267; (d) F. Würthner, R. Wortmann, K. Meerholz, *ChemPhysChem.* **2002**, *3*, 17.

[11] (a) N. M. Kronenberg, M. Deppisch, F. Würthner, H. W. A. Lademann, K. Deing, K. Meerholz, *Chem. Commun.* **2008**, 6489; (b) H. Bürckstümmer, N. M. Kronenberg, M. Gsänger, M. Stolte, K. Meerholz, F. Würthner, *J. Mater. Chem.* **2010**, *20*, 240; (c) N. M. Kronenberg, V. Steinmann, H. Bürckstümmer, J. Hwang, D. Hertel, F. Würthner, K. Meerholz, *Adv. Mater.* **2010**, *22*, 4193; (d) F. Würthner, K. Meerholz, *Chem. Eur. J*. **2010**, *16*, 9366.

Chapter 2

Vacuum-Processed Organic Solar Cells

Abstract: In this chapter, first the fundamentals of organic photovoltaics are described. After that, an overview on vacuum-processed small molecule solar cells is given. The main focus of the latter part is on commonly used material classes and different device architectures. Finally, the issue of the cell lifetime is briefly discussed.

2.1 General Discussion

2.1.1 Fundamentals of Photovoltaic Devices

Photovoltaic (PV) cells convert energy of light into electrical energy.[1] The effect was described by French physicist Edmond Becquerel in 1839 but realization of the first silicon PV devices had to wait until 1954. [1] During the first energy crisis in 1970's the first organic solar cells based on a single dye layer were investigated, however, with rather modest light-to-electricity conversion efficiency. In 1986, the first organic photovoltaic cells (OPV) with a reasonable efficiency (1%) were fabricated.[2] The devices were based on a layered p/n-heterojunction structure of copper phthalocyanine (CuPc) donor and 3,4,9,10-perylene-tetracarboxylic bisbenzimidazole (PTCBI) acceptor materials, sandwiched between tin-doped indium oxide (ITO) and Ag electrodes (Figure 1a).

The PV device's performance can be analyzed by measuring current over an external voltage range under illumination as well as in dark conditions. A typical result of such a measurement (i.e. current-voltage (*J-V*) characteristics) is depicted in Figure 1b. The main parameters that can be extracted from the *J-V* curves under illumination are the short circuit current *(*J_{SC}), the open circuit voltage, (V_{OC}) and the fill factor (FF). The power conversion efficiency (PCE) of a PV cell is the maximum power that the cell can generate (P_{max}) versus the power of the incident irradiance (P_0). Thus, PCE of a device can be described by

$$PCE = \frac{P_{max}}{P_0} = \frac{V_{OC} J_{SC} FF}{P_0}, \qquad (1)$$

where P_{max} is defined at the maximum power point (mpp) of the cell and it corresponds to the area of the filled gray rectangle in Figure 1b.

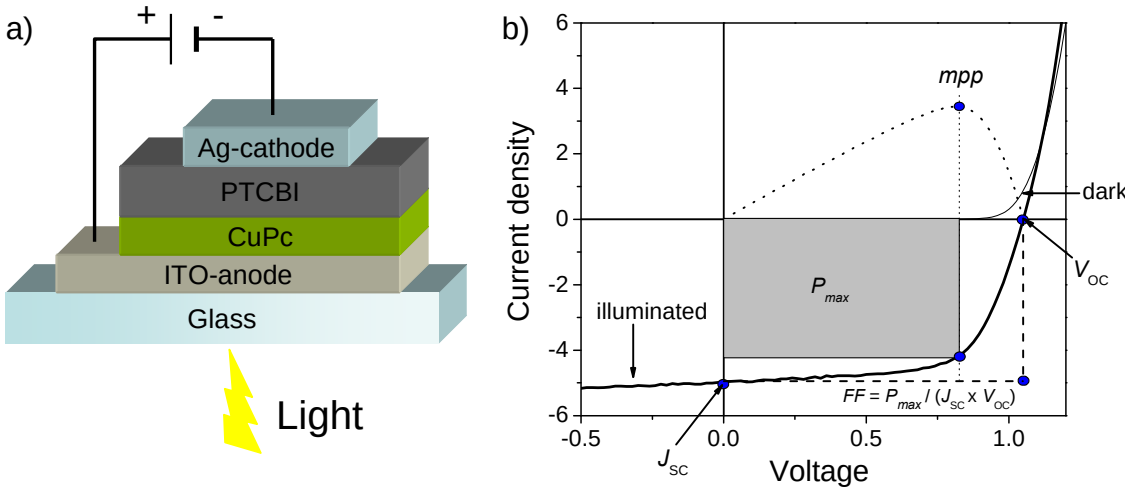

Figure 1. a) Schematic presentation of the first organic photovoltaic cell based on a donor/acceptor heterojunction.[2] b) Typical current-voltage (*J*-*V*) characteristics of a PV cell in dark conditions and under illumination. The maximum power point (mpp) is obtained from the maximum of the $V \times -J(V)$ plot (dotted line).

2.1.2 Equivalent Circuit Model

Single diode equivalent circuit model shown in Figure 2 can be used to explain the physical processes behind the experimental *J*-*V* characteristics of a PV device.[3] Because of the inevitable resistive losses of OPV cells, non-ideal device model is employed to simulate the *J*-*V* curves. This is usually done by the generalized Shockley equation:[3]

$$J = \frac{R_p}{R_s + R_p}\left[J_s\left\{\exp\frac{q(V - JR_s)}{nk_BT} - 1\right\} + \frac{V}{R_p} - J_{ph}(V)\right], \qquad (2)$$

where R_s and R_p are the series and parallel resistance, respectively, n is the ideality factor, q is the electron charge, k_B is the Boltzmann's constant, T is the temperature, J_s is the reverse saturation current density and J_{ph} is the current density under illumination.

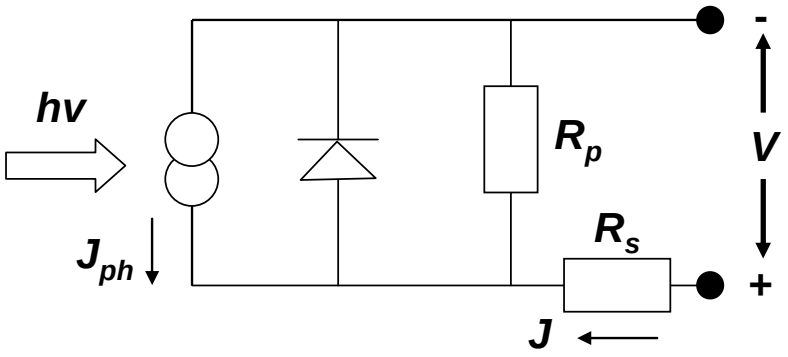

Figure 2. A single diode equivalent circuit model. The parallel and series resistance are R_p and R_s, respectively. J_{ph} denotes the photocurrent density.[3]

2.1.3 Donor/Acceptor Heterojunction

The first organic solar cells comprised of a single absorbing layer that was deposited between metallic electrodes. However, the concept was highly inefficient and the devices showed power conversion efficiencies of only about 0.01%.[4] In 1986 Tang revolutionized the OPV research field by introducing the first devices based on a heterojunction of electron donating (D) and accepting (A) components (Figure 1a).[2] The D/A heterojunction concept lifted the performance of organic solar cells to 0.95% and it instantly became a standard structure of OPV cells.

In inorganic solar cells an exciton, created upon absorption of a photon, immediately dissociates into free hole and electron charge carriers which then can be directly collected at the opposing electrodes. This process is fundamentally different in organic solar cells where absorption of a photon results in excitation of an electron from the highest occupied molecular orbital (HOMO) level to the lowest unoccupied molecular orbital (LUMO) level of a molecule (Figure 3a).[5] The formed excited state is called exciton. At the excited state, the charge carriers feel strong Coulombic attraction that is estimated – although heavily debated – to be on the order of 0.5 – 1.5 eV in organic materials.[6] Irrespective of the true value, however, this binding energy is several times larger than the available thermal energy at room temperature (k_BT = 0.025 eV) and, therefore, the created excitons cannot be efficiently dissociated by the built-in electric field of the device. The main reasons for the high binding energy and for the poor separation of the charges in organic materials are: i) negligible screening of the charges due to low dielectric constants (~ 2-4) with respect to inorganic materials (> 10) and ii) weak electronic interactions between the neighboring molecules resulting in narrow bandwidths as well as localization of the charges on the molecules.[7]

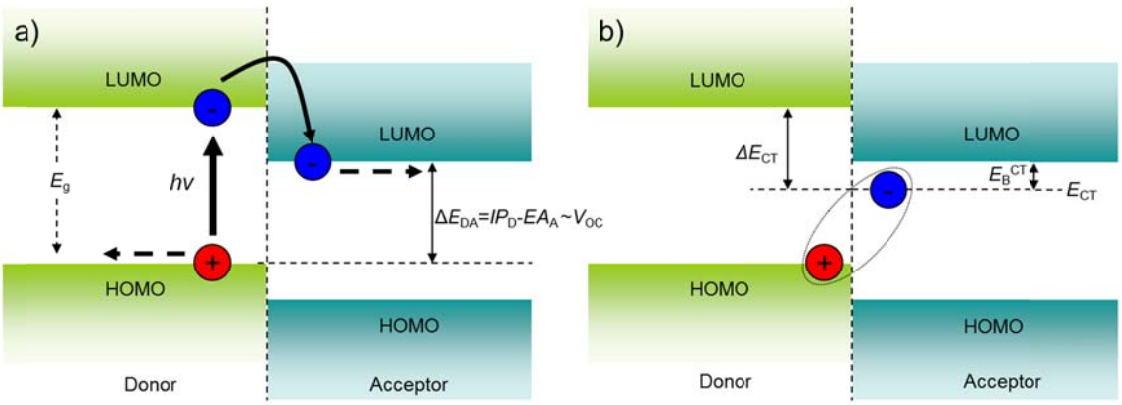

Figure 3. a) Schematic illustration of HOMO and LUMO energy level alignments of donor and acceptor materials. The formed exciton upon absorption of light (*hv*) is dissociated at the D/A interface to free charge carriers. b) Schematic illustration of the formation of the Coulombically bound electron-hole pair (i.e. CT-state). The E_B^{CT} is the binding energy of the relaxed CT-state (E_{CT}) whereas ΔE_{CT} is the energy between the optical LUMO (donor) and the E_{CT}.[7c]

For an efficient dissociation of an exciton in organic solar cells, it has to first diffuse to the D/A heterojunction that is characterized by a favorable energy level alignment (Figure 3).[2] At the D/A interface the exciton splits into free hole and electron carriers in such a way that the latter charge locates on the LUMO of the acceptor and the former charge sits on the HOMO level of the donor. After dissociation, the formed charge carriers are transported via the HOMO and LUMO level manifolds, respectively, and can eventually be collected at the opposing electrodes (Figure 3a). Note that in organic solar cells also the acceptor material may harvest solar light and create excitons which can then dissociate into free charges at the same heterojunction after the exciton transfer within the acceptor material.

Definition of the energy levels has caused some confusion in the past, and to ease the discussions, we will define some terms in following. Typically, the HOMO level refers to the ionization potential (IP) of the material i.e. the energy that is needed to remove an electron completely (to the vacuum level) from the ground state of a molecule. Accurate determination of the LUMO level has proven to be even more difficult due to degradation of the materials during measurements but also due to mixing of different terms like electron affinity (EA), conducting band, and optical LUMO. A practical way to define the LUMO level of a donor material is to subtract the optical band gap (E_g) from the *IP* ($E_{LUMO}^D = IP - E_g$). The LUMO level obtained in this way is called optical LUMO. This method is highly useful because it directly shows whether the electron transfer from the donor to the acceptor will be exothermic, which is the minimum

requirement for exciton quenching at the heterointerface. Note, that EA (not the optical LUMO) obtained from a cyclic voltammetric (CV) or an inverse photoelectron spectroscopic (IPES) measurement should be used as the LUMO level for the acceptor material.

Several studies have demonstrated that V_{OC} of organic solar cells is dependent on the band gap (ΔE_{DA}) between the IP of the donor (IP_D) and the LUMO of the acceptor (EA_A) (Figure 3a).[8] For example, Scharber *et al.* showed a linear correlation between the IPs and the open circuit voltages of multiple polymer-fullerene cells using [6,6]-phenyl-C_{61}-butyric acid methyl ester (PCBM) as the acceptor.[8a] Based on their findings, the authors proposed the following relation for the V_{OC}:

$$V_{OC} = (1/e)\left(\left|IP_D\right| - \left|EA_A\right|\right) - 0.3\ \mathrm{V} \qquad (3)$$

where e is the elementary charge and the value 0.3 V is an empirical correction factor which takes account of the influence of the dark current as well as the field dependency of the photocurrent generation.

In a more detailed picture, the excitons are not directly dissociated to free charge carrier at the heterointerface; instead, the dissociation process occurs via an intermediate charge transfer (CT) state (Figure 3b). This mechanism has experimentally been observed for several different polymer:fullerene systems[9] and very recently Clark *et al.* have reviewed[5] the topic in detail. Formation of the CT-state can be described by a photoinduced charge transfer reaction D* + A → (D^+/A^-) where the electron is transferred from the excited donor molecule (D*) to the acceptor. The process has to be exothermic in order to occur efficiently i.e. the excited state of the donor (optical LUMO) has to be higher in energy than the CT-state (E_{CT}). In the CT-state, the formed charges still feel a strong electrostatic attraction by an energy which is spectroscopically estimated to be well in excess of 0.1 eV.[7c,10] Thus, the magnitude of the charge-transfer-state binding energy (E_B^{CT}) is clearly sizable compared to the available thermal energy at room temperature (~ 0.025 eV) and should represent an energetic barrier to the exciton dissociation. Anyhow, organic solar cells have been observed to exhibit near-unit quantum yields, suggesting that the CT-states can be efficiently dissociated despite the large E_B^{CT}.[11] To explain this discrepancy, a hot process of charge separation has been proposed where the excess energy from the exciton dissociation contributes to

dissociation of the CT-state.[10] Durrant and co-workers demonstrated with several oligothiophene:fullerene blends that the population of free charge carriers increases as $\Delta E_{CT} = E_{LUMO}^{D} - E_{B}^{CT}$ gets larger.[12] In the same study, they also observed that a mere exciton quenching at the D/A interface does not imply an efficient free charge carrier generation. Hence, they concluded that a sufficient energy level offset ΔE_{CT} is needed for efficient charge dissociation. To summarize, the heterojunction in an organic solar cell has to provide sufficient ΔE_{CT} to overcome the E_{B}^{CT} while the band gap (ΔE_{DA}) between the HOMO of the donor and the LUMO of the acceptor has to be maximized to ensure optimal V_{OC}.

2.1.4 Photocurrent Generation

Formation of photoinduced current in organic solar cells involves several processes such as (1) exciton generation, (2) exciton diffusion, (3) charge separation, (4) charge transport, and (5) charge collection (Figure 4).[13] The different processes determine the external quantum efficiency (η_{EQE}) of a cell which can be described by

$$\eta_{EQE} = \eta_{A}\eta_{ED}\eta_{CD}\eta_{CT}\eta_{CC}\,, \tag{4}$$

where η_A is the absorption efficiency of solar radiation within the active region of the solar cell; η_{ED} is the exciton diffusion efficiency to the heterojunction, η_{CD} is the dissociation efficiency of the excitons to free charges; η_{CT} is the charge transport efficiency; and η_{CC} is the charge collection efficiency. In following the different steps and potential lost mechanism are briefly discussed.

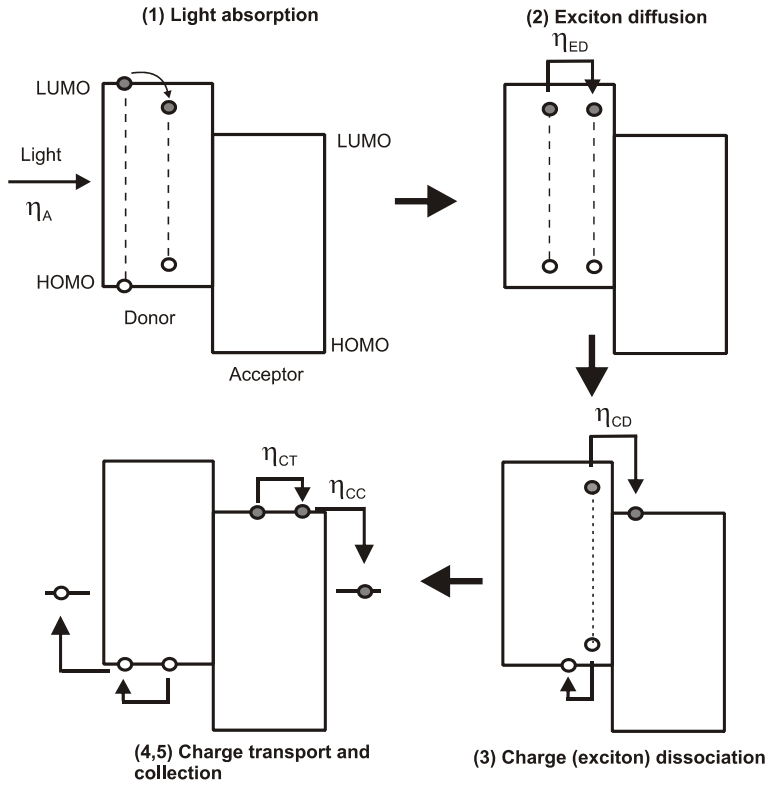

Figure 4. Schematic presentation of the photovoltaic processes in organic solar cells. The main steps are: (1) absorption of light and relaxation of the formed exciton (η_A); (2) exciton diffusion (η_{ED}); (3) charge (exciton) dissociation (η_{CD}); (4) charge transport (η_{CT}) and (5) charge collection (η_{CC}).[13]

Absorption

Photon absorption from the ground state (S_0) to the excited state occurs when the energy of the incident light corresponds to an allowed optical transition. For this situation and films of sufficient thickness the efficiency is close to unity.[3] Immediately, after the excitation, the formed excited state undergoes a relaxation to the lowest excited singlet energy level (S_1) which is observed as a bathochromic shift (Stokes shift) in the photoluminescence spectrum. This process reduces the excitonic energy and lowers the maximum V_{OC} of the device.[3]

Standardized spectral photon flux for air mass 1.5 global solar radiance (AM 1.5G) is depicted in Figure 5. In the same figure is also shown the accumulative solar power which is obtained by integrating the solar irradiance over the wavelength range. Although, the solar flux contains a significant amount of photons in the near infrared region (NIR), i.e. up to 1300 nm, the lower energy range appears useless for common OPV applications. Hence, the practical long wavelength absorption limit for organic solar cells is considered to be around 900 nm which covers ca. 70% of all incident solar energy.

Optically active materials in organic solar cells exhibit high absorption strengths commonly exceeding 1×10^{-5} cm^{-1}.[3] One of the strongly absorbing chromophores is CuPc which is an archetypal donor material in organic solar cell. For example, a 100 nm thick film of CuPc:C_{60} mixture harvests at 630 nm 90% of the incident photons whereas a traditional crystalline-Si cell covers only 10% with the same layer thickness.[3] Hence, the organic solar cells have the potential to reach η_a close to 100% with a substantially thinner active layer structure compared to inorganic counterparts. The possibility to obtain a very high EQE with a thin active layer is crucial for OPV devices which often suffer of high resistive losses due to low charge carrier mobilities.[14]

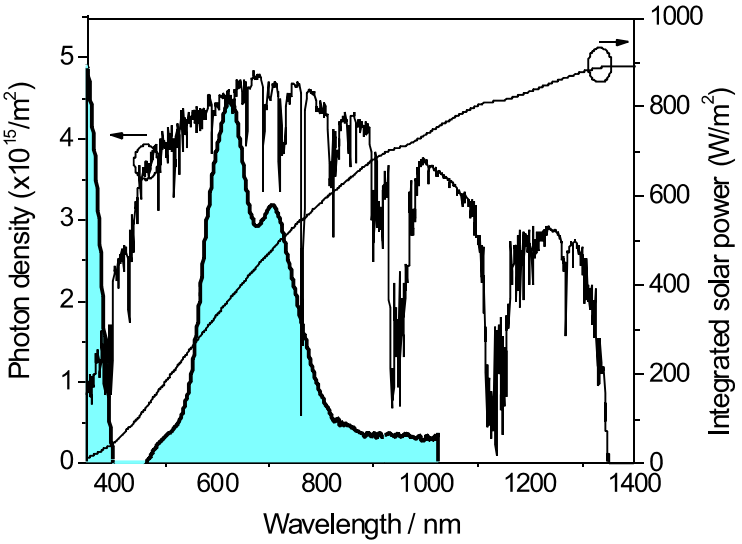

Figure 5. Solar photon flux (left), integrated solar power (right), and absorption band of a CuPc thin film (filled curve).

Exciton diffusion

As mentioned above, in organic solar cells the excitons can be efficiently dissociated to free charges only at the heterointerface. Thus, all excitons which are not formed in the vicinity of the D/A interface, must be transferred trough the manifold of the absorbing component. This process is called exciton diffusion and it may occur via a dipolar or an electron exchange mechanism.[3] In the small molecule organic solar cells the dipolar (i.e. Förster-type resonance) excitation transfer is the primary mechanism for the singlet exciton diffusion; whilst polymeric materials exhibit also the electron exchange (i.e. Dexter excitation transfer) mechanism which takes place along the π-conjugated backbone.[3]

The distance that the formed exciton can travel before recombination back to the ground state is expressed by the exciton diffusion length (L_D) and it is dependent of the material itself as well as of the homogeneity of the bulk film where the exciton has to travel.[3] For commonly used organic small molecular materials, the L_D is observed to vary between 3-20 nm[15] and typically highly ordered crystalline materials exhibit longer exciton diffusion lengths compared to amorphous surroundings.[13,16] In addition, the L_D is dependent on the crystalline dimension along which the exciton has to travel. For example, Lunt *et al.* observed that the exciton diffusion length of 3,4,9,10-perylene tetracarboxylic acid dianhydride (PTCDA) vary between 17 and 22 nm depending whether the molecules are standing or lying flat, respectively, on the substrate.[16]

The exciton diffusion length is a significant factor limiting the PCE of organic solar cells, because only the excitons, that are able to reach the D/A heterointerface, can be converted to free charges. Of particular importance is the L_D in planar heterojunction (PHJ) devices (for further discussion see section 2.2.2) where the diffusion length sets the practical limits for the thickness of the absorbing layer, and therefore, for the maximum EQE. In order to avoid the limits of a short L_D, the bulk heterojunction (BHJ) cell architecture has been developed.[13] In the BHJ concept, donor and acceptor components are co-deposited in a single active layer forming nanoscale phase separated D and A regions. The fine interface structure of BHJ cells ensures that nearly 100% of the created excitons are able to reach the heterointerface before recombining back to the ground state.[17]

Charge dissociation

As discussed above (see section 2.1.3), a sufficient energy level offset (ΔE_{CT}) between the LUMO level of the donor and the CT-state has to be provided in order to efficiently dissociate the excitons into free charges at the D/A interface. However, before the charges are fully separated, they may recombine to the ground state or return back to the excitonic species.[7] The recombination to the ground state is commonly called geminate addressing the fact that the recombined hole and electron originate from the same exciton. Several studies have addressed the geminate recombination as one of the main lost mechanism in organic solar cells.[18]

Charge transfer

The weak intermolecular interactions in organic solar cells act to localize not only the created excitons but the free charges as well.[3] Because the extended band structure is typically minimal in organic materials, transport of charges proceed via a localized hopping mechanism in accordance with the Marcus theory.[14,19] Furthermore, in organic semi-conductors the bulk film is typically amorphous, which gives for each molecule a unique environment, leading to an energetically inhomogeneous landscape. These factors give rise to carrier trapping which decreases the charge transport rates. However, the problem of the energetically inhomogeneous media can be circumvented using crystalline materials.[20]

Additionally, electrons and holes created by charge separation may recombine back to the ground state if they come within the columbic interaction distance before they are collected at the opposing electrodes.[3] To distinguish this mechanism from the geminated recombination, it is often called bimolecular or non-geminate recombination which means that the recombined charges originate from different excitonic species. Bimolecular recombination is one of the main loss mechanisms in BHJ devices where the fine intermixing of the donor and acceptor materials usually decreases the charge carrier mobilities and increases the percolation path lengths to the electrodes.[21] Additionally, the blending may induce trap sites and dead ends which serve as the recombination zones for the charges. The charge carrier mobility may be increased by inducing crystallinity which is typically done by applying thermal treatment steps (e.g. substrate heating or post-annealing) during the fabrication process.[22] Additionally, solvent vapor annealing has proved to be an efficient method to increase the crystallinity and, thus, to improve the charge transport properties of the cells.[20a]

Charge collection

Collection of photogenerated charges to external circuit in organic solar cells is accomplished by sandwiching the active layers between a transparent conducting oxide (TCO) electrode, typically tin-doped indium oxide (ITO), and a metal counter electrode (e.g. Ag). The main requirement for the efficient charge collection is a favorable energy level alignment between the electrode and the organic layer. An inappropriate energy level alignment at the organic/electrode interface has been demonstrated to result in piling up of charges as well as in anomalous *J-V* characteristics.[23] In general, formation of the interface energy states is highly complicated because several factors may

influence, such as charge transfer across the interface which gives rise to interface dipoles.[24]

2.2 Thermally Vacuum-Deposited Organic Solar Cells

Despite the fact that the first efficient solar cells were fabricated by a thermal vacuum (VAC) deposition method,[2] the main focus of the scientific community has been in solution-processed polymeric devices. This has left the development of small molecule cells behind.[25] Probable reasons for the popularity of the solution processing methods are their simplicity and lower price of experimental set-ups compared to VAC deposition techniques.[26] Currently, the state-of-the-art solution processed cells are based on polymeric donor materials of which main drawbacks are relatively difficult synthetic accessibilities as well as poorly specified molecular structures. The solution deposition technique is also more prone for impurities that may reduce the batch-to-batch reproducibility and be detrimental for the device lifetime. Furthermore, owing to the solubility issues, fabrication of stacked device architectures is very complicated by solution deposition methods.[27] The small molecular systems, instead, offer i) vast possibilities for chemical modifications, ii) well specified molecular compositions, and iii) potentially higher purities. Additionally, a significant advantage of VAC techniques is the excellent control over the device architecture, and especially, easy realization of tandem cell structures (see section 2.2.3). As a matter of fact, both vacuum- and solution-deposited solar cells, based on a heterojunction, currently held the same certified champion efficiency of 8.3%.[28]

2.2.1 Materials

Donors

Figure 6 depicts molecular structures of commonly used absorber/semiconductor materials in organic solar cells. One of the most studied chromophore class in OPV is the metal phthalocyanines (MPc) which have already been used for decades as pigments in car industry and in printing applications.[29] Generally, the MPcs are well known for their high optical strengths as well as good thermal and chemical stabilities. Several different metallophthalocyanine complexes such as Cu, Zn, H_2, Ni, Co, and Fe have

been tested in organic solar cells but only the Cu- and ZnPc derivatives are widely used.[30] The reason for the popularity of Cu- and ZnPcs is likely their superior L_D compared to other MPcs which was shown to correlate with J_{SC} in MPc/C_{60} PHJ devices.[31] Furthermore, Cu- and ZnPcs exhibit several polymorphic structures of which most relevant for OPV applications are the α- and β-forms.[30]

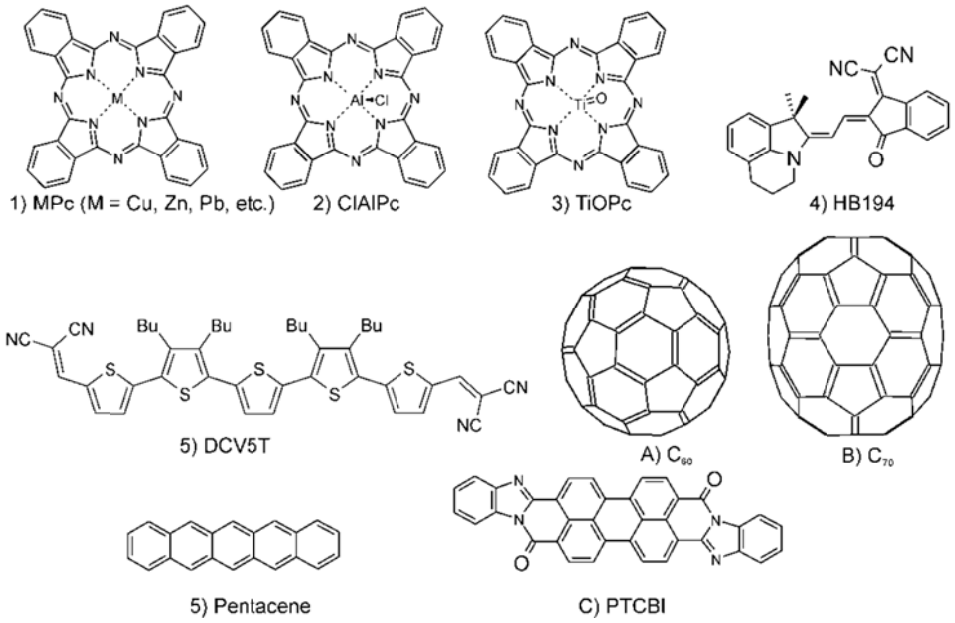

Figure 6. Examples of donor materials (1-6) and acceptor materials (A-C) employed in VAC processed OPV devices.

The crystalline nature of Cu- and ZnPc thin films (α-form) give rise to good charge transport properties in planar heterojunction devices but the suboptimal energy levels, with respect to the most commonly used electron acceptor C_{60}, substantially limit the usability of the chromophores.[30,32] Additionally, MPcs exhibit narrow absorption bands with maxima at 620 nm and onsets at 780 nm, thus excluding the near-infrared (NIR) photons (see Figure 5). This is a significant limitation because approximately 50% of all photons in solar spectrum have energies corresponding 600 nm < λ < 1000 nm.

A more optimal absorption band structure may be obtained by using non-planar MPcs such as SnPc[33] and PbPc[34] which exhibit significant absorption in the 600-900 nm range and offsets at ~ 1000 nm. However, due to the large size of Sn and Pb central metals, the phthalocyanine frame-works are contorted off the planar conformation. The bending interferes the packing of SnPc and PbPc and reduces the charge transport properties of the chromophores compared to flat phthalocyanines (e.g. CuPc).[33,34] Hence, the lower charge carrier mobilities of the twisted Pcs result in higher series

resistance limiting the FF of the solar cells whereas the red shifted absorption bands potentially increase the J_{SC}.

An alternative method to extend the absorption of phthalocyanine chromophores to the near-infrared range is to employ square-pyramidal complexes such as chloroaluminum Pc (ClAlPc)[35] or titanyl Pc (TiOPc)[36,37]. The out-of-plane Cl or O atoms are bonded to Al or Ti atoms, respectively, which strongly influences the molecular packing. Consequently, both compounds exhibit the characteristic "Phase II" polymorph which shows the Q-band maximum far in the NIR region. Additionally, ClAlPc and TiOPc feature favorable energy level alignments in respect with C_{60} which afford red-shifted absorption and higher V_{OC} compared to CuPc. For example, Armstrong and co-workers showed by ultraviolet photoelectron spectroscopic (UPS) measurements that the HOMO level of TiOPc lies 0.2 eV deeper than the HOMO level of CuPc.[36] This was consistent with TiOPc/C_{60} and CuPc/C_{60} device results which demonstrated open circuit voltages of 600 and 450 mV, respectively.[36]

Apart from Pc derivatives, also polyacenes have been used as donor materials in VAC processed organic solar cells.[38] The polyacenes such as pentacene exhibit excellent charge transport properties and hole mobilities exceeding 3 $cm^2\ V^{-1}\ s^{-1}$ have been measured for thin films.[39] However, the generally poor photon harvesting properties of the materials reduce their usability in organic solar cells. Nonetheless, despite the limited device efficiency, especially pentacene is commonly employed as a model component in experimental as well as theoretical studies.[40]

An interesting class of organic semiconductors are oligo- and polythiophenes such as a,a'-*bis*(2,2-dicyanovinyl)-quinquethiophene (DCV5T).[41] DCV5T comprises of a conjugated acceptor-donor-acceptor (A-D-A) push-pull system featuring a high absorption strength ($\varepsilon_{max} = 5.2 \times 10^{-4}$ L $mol^{-1}\ cm^{-1}$) as well as a favorable band gap (λ_{max} = 573 nm). Indeed, Schulze *et al.* have demonstrated with DCV5T/C_{60} planar heterojunction cells efficiencies > 3% and V_{OC} of 1.04 V.[41]

Merocyanines (MC) are a new donor material class for VAC processed solar cells based on a heterojunction.[42] In a very recently published study of merocyanine HB194:C_{60} BHJ devices, power conversion efficiencies exceeding 5% and V_{OC} of 1.00 V where demonstrated which are among the highest values reported for small molecule single junction cells.[42c] Several factors such as excellent absorption coefficients (typically exceeding 1×10^{-5} $M^{-1}\ cm^{-1}$) make the dyes highly attractive for organic solar cells. Furthermore, owing to the donor-acceptor push-pull structure of MCs, they often

demonstrate very high dipole moments and polarizabilities that may be favorable for the exciton dissociation at the heterojunction,[43] as recent theoretical studies have suggested for polymer:C_{60}[44] and quadrupolar-small molecule:C_{60} systems[45]. In addition, the D-A structure is synthetically easily accessible which offers great possibilities for fine tuning the physical properties.

Acceptors

Most commonly used acceptor materials in vacuum-deposited organic solar cells are perylene derivatives, such as 3,4,9,10-perylenetetracarboxylic bis-benzimidazole (PTCBI) and fullerene C_{60} and its derivatives (Figure 6).[25,30] Absorption properties of the perylene derivatives are superior compared to C_{60} which makes them highly attractive acceptor materials for organic solar cells. Suitability of perylenes for OPV was demonstrated by Kim *et al*. who fabricated planar heterojunction devices using PbPc as the donor and different perylene tetracarboxylic diimide (PTCDI) derivatives as the acceptor.[46] The manufactured devices showed broad absorption ranges 400-750 nm and PCEs up to 2.0%. Furthermore, the authors noted that packing of the acceptor layer was highly important for the photocurrent and those perylene derivatives which featured poor intermolecular distances as well as poor electron mobilities failed to perform well in solar cells. However, despite the promising PHJ cell results, the efficiency of BHJ devices based on perylene acceptors has been low so far, which has been attributed to the insufficient phase separation of the D/A components.[47] Hence, owing to C_{60}'s superior ability to form BHJ structure, it is the state-of-the-art acceptor material in organic solar cells.[47]

An attractive alternative for C_{60} and perylene compounds is C_{70} that exhibits substantially higher absorption strength at more favorable spectral region compared to C_{60}. For example, Pfuetzner *et al*. have demonstrated with ZnPc:C_{70} cells a 25% increase in J_{SC} compared to ZnPc:C_{60} devices.[48] However, the significantly higher price of C_{70} reduces its attractivity at the moment.[30]

2.2.2 Device Architectures

A major improvement to Tang's PHJ cell architecture was the introduction of the exciton blocking layer (EBL) between the electron accepting film and the Ag electrode (Figure 7a).[49] Commonly used EBL materials are bathocuproine (BCP) and 4,7-diphenyl-1,10-phenanthroline (Bphen) which both demonstrate wide band gaps, with

offsets to both the HOMO and the LUMO of the C_{60} acceptor.[30] Due to the large offsets, the excitons are reflected at the C_{60}/EBL heterointerface which significantly improves J_{SC} by preventing the exciton quenching at the metal electrode.[50] Furthermore, the EBL acts to protect the active layer from the hot metal atoms during the deposition of the cathode. The large energy offset of the EBL and the cathode should form an energetic barrier for the electrons and lead to piling up of the charges at the interface. However, this is not observed in devices and it is proposed that deposition of the metal cathode induces gap states that facilitate the charge transport through the electron blocking layer.[50,51] Consequently, the need for the efficient gap states limits the thickness of the EBL to about 10 nm.

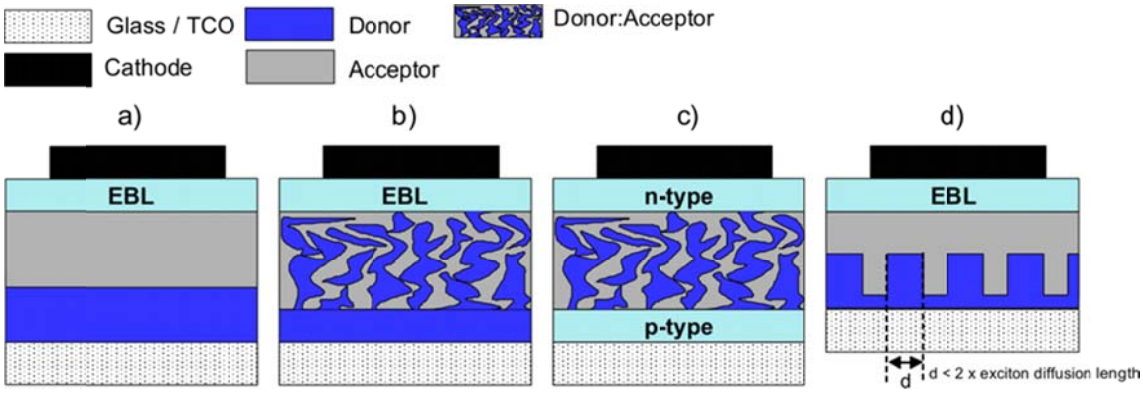

Figure 7. Schematic presentations of common device architectures used in VAC processed small-molecule solar cells. Typically, the devices are fabricated on glass substrates that are coated with a transparent conducting oxide (TCO) layer. Stack a) represents a planar heterojunction (PHJ) structure with an exciton blocking layer (EBL) between the acceptor and cathode layers.[49] Stack b) shows a hybrid heterojunction (HHJ) architecture which is a combination of the planar and bulk heterojunction structures.[51] Stack c) illustrates a full pin structure with a p-doped hole transport layer (HTL) and a n-doped elector transport layer (ETL).[52] Picture d) shows the layered structure of a controlled BHJ (cBHJ) cell with a highly ordered donor film.[53]

As mentioned above, a significant burden for the PHJ device architecture is the small optimal active layer thickness because of to the short exciton diffusion length of organic materials (typically L_D < 20 nm).[16] Hence, EQEs of the devices are generally poor resulting in low short circuit currents. The problem of the short L_D was solved by introducing a bulk heterojunction concept (BHJ) in 1991 by Hiramoto *et al.*[54] The first BHJ cells comprised of a co-deposited active film with a metal-free phthalocyanine (H_2Pc) donor and a perylene tetracarbocylic (Me-PTC) acceptor. The co-deposited components were observed to spontaneously form a finely intermixed bulk

heterojunction layer. In such a structure, the created excitons can always reach the heterointerface which affords a thicker absorbing layer and a potentially higher photocurrent in BHJ devices compared to PHJ cells. The device architecture of Hiramoto and co-workers may also be considered as a hybrid solar cell combining planar and bulk heterojunction structures.[54]

Forrest and co-workers presented in 2003, an updated version of the hybrid heterojunction (HHJ) cell architecture (Figure 7b).[51] Their devices were structured such that first a CuPc donor layer was evaporated on the ITO electrode, followed by a deposition of a CuPc:C_{60} blend film and a BCP electron blocking layer before the silver electrode. The novel HHJ cell architecture demonstrated a performance improvement of 40% compared to conventional PHJ or BHJ devices based on the CuPc donor. Very recently Yuen *et al*. used the HHJ concept to improve the performance of chloroindium Pc (ClInPc):C_{60} blend devices by implementing a ZnPc layer between the blend film and the ITO anode.[55] The PCE of the HHJ cells (1.81%) was over doubled compared to simple ZnPc/C_{60} PHJ or ClInPc:C_{60} BHJ devices. The main reason for the enhanced performance was the complementary absorption profiles of the phthalocyanine chromophores which led to a broad coverage (600-900 nm) of the solar spectrum.

The HHJ architecture may also be considered as a pin (p-conductor-intrinsic absorber-n-conductor) structure where the active bulk heterojunction layer is sandwiched between the hole and electron conducting layers. However, the first full pin structure, where the both p- and n-layers were effectively doped, was introduced in 2004 by Maenning *et al.* (Figure 7c).[52a] Efficient doping of the transport layers enables ohmic contacts to the electrodes which are essential for the charge collection from the deep (high) lying HOMO (LUMO) energy level. Moreover, in ideal case, the transport layers (p and n) have absorptions below 400 nm and conductivities above 10^{-5} S cm^{-1} which afford over 100 nm thick films with negligible optical and resistive losses.[52a] Of particular importance are the efficient p- and n-layers in tandem device architectures where highly conducting as well as transparent spacers are needed to optimize the optical properties of the cells (for discussion of the tandem device architectures see Chapter 2.2.3).[56] Furthermore, the doped layers selectively transport only specific charge carrier species and block opposite charge carries as well as excitons which makes separate electron and hole blocking layers unnecessary.

As mentioned above, a common problem with organic solar cells is the relatively low hole and electron charge carrier mobilities of organic materials.[21] The problem is

particularly severe in blend films which demonstrate typically ca. order of magnitude lower mobilities compared to pure neat films. In fact, owing to the poor charge transport properties, the optimal active layer thickness in BHJ cells is typically well below the absorption depth of the active material.[30] Therefore, despite the nearly 100% exciton dissociation efficiency of BHJ devices, the short circuit current remains low (typically < 15 mA cm^{-2}) compared to c-Si cells (ca. 25 mA cm^{-2}). To circumvent the short L_D and the poor charge transport, which are the most important factors limiting the efficiency of PHJ and BHJ cells, respectively, a controlled bulk heterojunction (cBHJ) device architecture has been developed.[53] In an idealized case, the donor film in cBHJ cells exhibits a vertical growth of needle-like crystallites whose width is < 2 × L_D and the height is ca. ½ × the absorption depth of the active material (Figure 7d). The highly ordered donor film potentially enables a good charge transport leading to high FF, whereas the needle-like structure increases the active surface area and ensures that all created excitons can reach the D/A interface. Additionally, the separate deposition of the donor and acceptor materials allows a better control over the film morphology compared to co-evaporation techniques.

Yang *et al*. demonstrated with CuPc/C_{60} cBHJ devices a PCE increase of 35% (under 100 mW/cm^2 AM 1.5 illumination) compared to conventional co-deposited BHJ cells.[53a] The main improvement was observed in FF and J_{SC} which increased by 30% and 20%, respectively, whereas V_{OC} remained constant. The devices were fabricated employing an organic-vapor-phase-deposition (OPVD) technique which enabled growth of highly ordered CuPc layers with a needle-like morphology (Figure 8a). The OPVD method employs a carrier gas to transport the active material onto the substrate, and thus, permits a better control over the film morphology compared to the conventional thermal VAC deposition method (Figure 8).

In addition to the OPVD technique, several processing methods have been used to control and/or modify the film morphology of VAC deposited solar cells. For example, to enhance the molecular order in the active layer, devices have been sublimed on a preheated substrate[57] or post-annealed after the preparation[58] or exposed to solvent vapor during the fabrication.[20a] Also templating the substrate with a thin organic layer[37] or adding a buffer film between the ITO electrode and the successive organic layer[59] have successively been used to modify the growth of the overstanding film. For example, Sullivan *et al.* demonstrated a 60% improvement in J_{SC} by modifying the preferred growth orientation of CuPc crystallites in CuPc/C_{60} PHJ devices.[37] Typically

CuPc chromophores stand up on a weakly interacting surface such as ITO but by templating the surface with a very thin PTCDA film the molecules could be forced to lie flat with respect to the substrate surface. The significantly improved of the J_{SC} was attributed to higher photon absorption of the PTCDA modified devices because of the more ideal alignment of the molecular transition vectors with respect to the incident light.

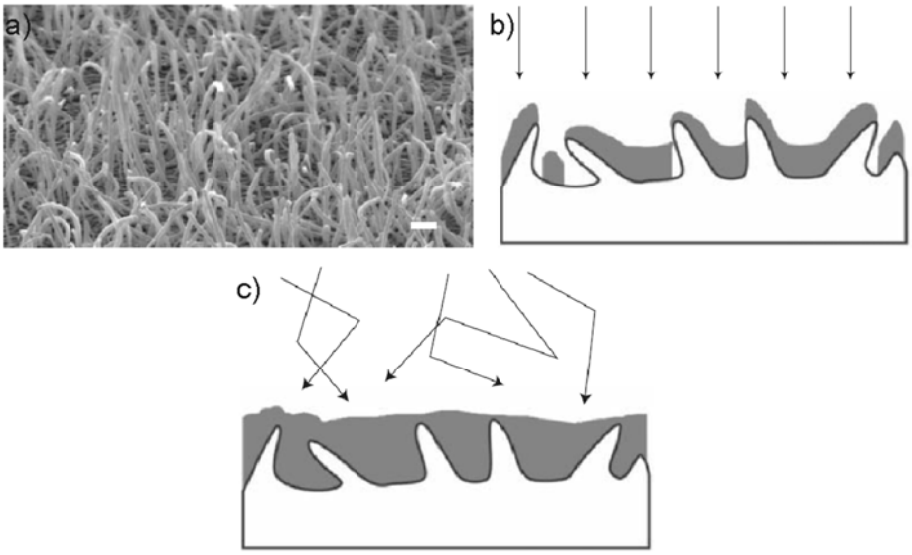

Figure 8. a) Scanning microscope image of needle-like CuPc crystallites on ITO substrate grown by OVPD technique. Schematic presentation of the intermixing of CuPc (white) and C_{60} (gray) materials prepared by b) conventional vacuum deposition and c) OVPD methods. The OVPD method gives a lateral momentum for the molecular vapor that helps on filling gaps and forming smooth films. The figures are adapted with permission from Ref. 53a.

2.2.3 Tandem Cells

As discussed above, the absorption width of organic materials is typically narrow, leaving large portions of the effective solar spectrum unexploded. Furthermore, poor charge carrier mobilities often confine the absorbing layer thickness below the absorption depth. These limitations can be overcome by stacking several singe junction cells on top of each other enabling larger coverage of the solar spectrum without increasing the active layer thickness. The most common stacked architectures are the parallel and series connected tandem cells of which operational fundamentals are shortly described in following. For a more detailed discussion of the theoretical back grounds of the tandem devices, reader is referred to Blom's and co-workers' comprehensive review article (Ref. 60).

Series connection

The device architecture as well as the energy level diagram of a series connected tandem solar cell is illustrated in Figure 9. Typically a monolithic device structure is used where the sub-cells share a common recombination zone between the stacks. The anode of the back (front) cell is electrically connected to the cathode of the front (back) cell. Due to the device setup, the total photocurrent is constant throughout the device whereas the voltages generated by the sub-cells add up. Thus, for each point of the *J-V* characteristics the following relations are valid,

$$J_{\text{Tandem}} = J_{\text{Back}} = J_{\text{Front}} \quad (5)$$

$$V_{\text{Tandem}} = V_{\text{Back}} + V_{\text{Front}}. \quad (6)$$

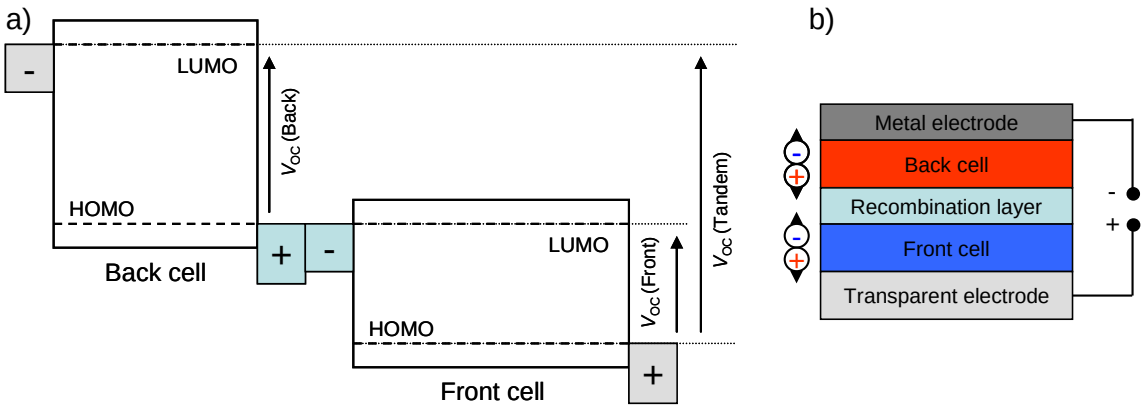

Figure 9. Series connected tandem solar cell. a) Energy level alignment at V_{OC} condition and b) Schematic presentation of a stacked device structure featuring a common recombination layer and electrical connections between the anode and the cathode of the Front and Back cells, respectively.

Parallel connection

In a parallel connected tandem device architecture, the sub-cells share a common cathode (anode) and electrically connected anode (cathode) electrodes (Figure 10). Owing to the structure of the parallel tandem cells, for each point of the *J-V* characteristics, following relations are valid,

$$V_{\text{Tandem}} = V_{\text{Back}} = V_{\text{Front}} \quad (7)$$

$$J_{\text{Tandem}} = J_{\text{Back}} + J_{\text{Front}}. \quad (8)$$

Unlike in the series connected devices, V_{OC} of the parallel connected tandem cells is confined close to the level of the sub-cell with the lowest V_{OC}. However, in the parallel connection the short circuit currents of the sub-cells add-up.

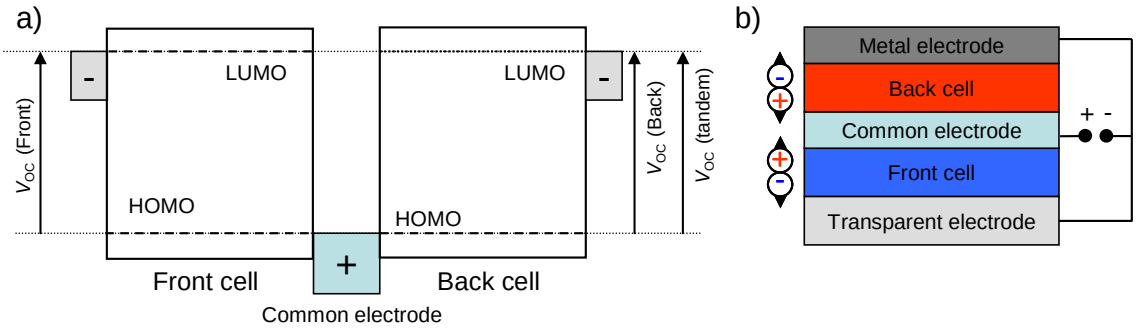

Figure 10. Parallel connected tandem solar cell. a) Energy level alignment at V_{OC} condition. b) Schematic presentation of a stacked device structure featuring a common cathode between the Front and Back cells as well as electrically connected anodes. Figure a) illustrates a hypothetical case where both sub-cells are identical, and therefore, V_{OC} of the tandem cell is exactly the same as for the single cells.

Literature examples of tandem devices

Recently, Drechsel *et al.* demonstrated an efficient series connected tandem cell architecture by stacking two ZnPc:C_{60} pin sub-cells on top of each other (Figure 11a).[56] The device showed a PCE of 3.8%, under simulated AM 1.5G illumination, which was a significant improvement compared to the respective single junction devices (2.1%). Due to the efficient series connection, the tandem cell demonstrated V_{OC} of 0.99 V which was exactly twofold compared to the optimized single junction cells (0.50 V).[56] However, the improvement of the efficiency was not twofold, due to the identical absorption range of the sub-cells which reduced the J_{SC} compared to the individual cells (Figure 11b). Therefore, a further performance increase is expected by using sub-cells that harvest photons at different parts of the solar spectrum. The broader absorption range of such devices enables a higher short circuit current compared to tandem cells featuring identical stacks. However, the use of dissimilar sub-cell systems needs a fine balancing of the current densities because the J_{SC} of the whole device is confined to the level of the sub-cell showing the lowest J_{SC} (see Eq. 5).

Kotlarski and Blom have estimated the ultimate efficiencies of single and multiple junction devices.[61] By taking account optical and electrical device models, the authors estimated the ultimate efficiency of a single junction polymer:fullerene solar cell to 11.7%. The optimal device had a band gap of 1.7 eV leading to V_{OC} of 1.00 V, J_{SC} of 15.7 mA cm^{-2}, and FF of 74.3%. Previously, Yu and co-workers presented a similar

value for the maximal efficiency of a single junction cell.[62] In the same study, Kotlarski *et al*. analyzed also series connected tandem cells and concluded that with an optimized device architecture an ultimate efficiency of 14.1% can be achieved.[61] Hereby, the optimized tandem cell structure is estimated to improve PCE of a single junction cell by approximately 20%.

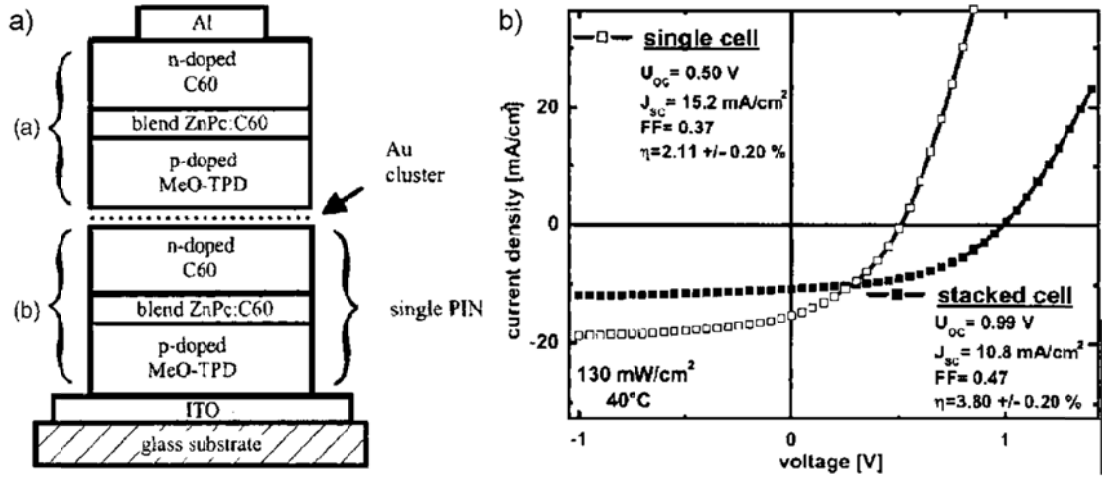

Figure 11. a) Device architecture of the stacked ZnPc:C_{60} pin solar cell connected by a ultra thin Au recombination layer. b) *J-V* characteristics of the single and stacked devices. The figures are adapted with permission from Ref. 56.

2.2.4 Other Device Structures

In the following, some novel device concepts employed in VAC processed small molecule solar cells are described.

Forrest and co-workers used a double donor PHJ device architecture with a following layered structure: ITO/CuPc/SnPc/C_{60}/BCP/Ag. The cells showed a PCE increase of 30% compared to devices with only the CuPc donor layer.[63] Implementation of the SnPc layer extended the absorption range of the double donor devices to NIR region (onset at ~ 1000 nm) and improved J_{SC} by 15% compared to optimized CuPc:C_{60} BHJ devices. However, the low hole mobility of SnPc impeded the optimal film thickness to only 5 nm.

Instead of using additional absorbing layers, the photon harvest of organic solar cells has also been improved by mixing additives in either the donor or acceptor film.[64] The idea of the concept is to use a small amount of a fluorescent dye to absorb light which would not be otherwise absorbed by the cell. However, the additive is not considered to directly donate the charges to the acceptor but it rather emits the light within the absorption range of the cell where it is reabsorbed and converted to separated charges.[64]

Alternatively, a luminescent concentrator layer – similar as in inorganic devices – has been used to collect and reemit photons which would not be otherwise absorbed by the cell.[65]

Also additives, that can directly donate the excitons by the Förster-type resonance energy transfer to the host material have been employed.[66] This method requires a careful alignment of the energy levels such that the energy transfer is possible and no charge trapping can occur. For example, Luhman and Holmes improved the performance of *N*,*N*-bisnaphthalen-1-yl-*N*,*N*-bisphenyl-benzidine NPD/C_{60} PHJ devices by incorporating *fac*-(tris-2-phenylpyridine) iridium ($Ir(ppy)_3$) phosphorescent sensitizer (5% by weight) into the NPD layer.[66] The authors proposed a complex mechanism where the singlet (S_1) excitons created in the NPD component were first able to efficiently relax on the triplet (T_1) level of the $Ir(ppy)_3$ additive from which the T_1 excitons were back transferred on the T_1 level of the NPD. Finally, the excitons diffused in the T_1 manifold of the NPD host material to the heterointerface at which they were efficiently dissociated to free charges. The authors showed that incorporation of the phosphorescent sensitizer into the NPD host layer increased the L_D from 6.5 ± 0.3 to 11.6 ± 0.6 nm which was attributed to better diffusion of the triplet excitons compared to the singlet excitons. The sensitized donor layer devices demonstrated a PCE improvement of about 80% relative to unsensitized donor layer cells.[66]

2.2.5 Device Lifetime

The issue of the lifetime has not been in the focus of the organic solar cell community so far, as most of the efforts have been placed to increase the cell efficiency. Thus, relatively few studies describing the device lifetimes have been published until now. In addition, the lack of any standardized testing protocol makes the direct comparison of different results very difficult. However, this is to be changed, as very recently a standardized testing protocol has been developed for indoor and outdoor experiments which will uniform the testing conditions and make the direct comparison more reliable in future.[67]

Several different factors may have an influence on device lifetime such as presence/absence of oxygen and humidity, ultraviolet light, temperature, as well as stability of electrodes.[30] Especially, molecular oxygen has been shown to rapidly degradate cells by oxidizing the metal electrode and/or causing irreversible photoinduced oxidation of the active materials.[68] The importance of oxygen and

humidity free environment was demonstrated with pentacene/C_{60} cells that were encapsulated with thick Al_2O_3 films.[69] The efficiency of the encapsulated devices reduced only by 6% over a period of 6100 h (~ 8.5 months) compared to a lifetime of < 10 h for unencapsulated cells. Franke *et al.* made a similar observation with encapsulated VAC processed ZnPc:C_{60} tandem cells.[70] The devices showed an efficiency reduction of only 3% in ~ 1500 h under white light illumination (halogen lamp) with intensity of 185 mW/cm^2 and temperature of 50 °C. However, a fast efficiency drop was observed only in a few hours after breakup of the encapsulation. Devices that were baked at 85 °C in dark conditions exhibited also a very fast degradation which pinpointed the challenges in the thermal stability of organic solar cells.[70]

Consequently, not only the efficiency but also the lifetime of OPV cells is a major issue before the concept can be implemented in commercial applications. As a comparison c-Si solar cells exhibit lifetimes > 25 years. Nevertheless, lifetimes exceeding 10 000 h has been demonstrated for VAC processed organic light emitting diodes (OLED) which is a highly promising result for the small molecule solar cells as well.[71] Furthermore, an accelerated degradation study at elevated temperature and light intensity indicated a lifetime > 10 000 h for a polymer solar cell with an initial PCE of 1.9%.[68a] Despite the low efficiency of the cell, the result suggested an operational lifetime over 5 years which is considered as the minimal requirement for the commercial utilization.

2.2.6 Conclusions and Outlook

The future of VAC processed organic solar cells looks promising, though, several major hurdles such as inadequate efficiency and lifetime are still to overcome. Although, polymeric cells have gathered most of the interest of the scientific community in the last years, thermally VAC deposited devices have demonstrated their potential as well. This is well reflected by the fact, that both concepts currently held the same certified record efficiency of 8.3%. The fabrication costs of polymeric devices are potentially extremely low due to cheap deposition techniques (e.g. printing) which are a significant advance compared to VAC deposition methods. However, as shown by multiple examples, the VAC processing techniques enable a very fine control over the device architecture as well as over the morphology of the active layers. Especially, the relatively easy realization of tandem cell structures is a major advantage for the VAC deposition

techniques. In addition, the excellent synthetic malleability of small molecules offers great possibilities for fine tuning the physical properties.

2.3 References

[1] S. E. Shaheen, D. S. Ginley, G. E. Jabbour, *MRS Bulletin* **2005**, *30*, 10.

[2] C. W. Tang, *Appl. Phys. Lett.* **1986**, *48*, 183.

[3] C. W. Schlenker, M. E. Thompson, *Chem. Commun.* **2011**, *47*, 3702.

[4] G. A. Chamberlain, *Sol. Cells* **1983**, *8*, 47.

[5] T. M. Clarke, J. R. Durrant, *Chem. Rev.* **2010**, *110*, 6736.

[6] I. G. Hill, A. Kahn, Z. G. Soos, R. A. Pascal, *Chem. Phys. Lett.* **2000**, *327*, 181.

[7] (a) B. A. Gregg, *J. Phys. Chem. B* **2003**, *107*, 80401; (b) B. A. Gregg, M. C. Hanna, *J. Appl. Phys.* **2003**, *93*, 3605; (c) M. Muntwiler, Q. Yang, W. A. Tisdale, X. Y. Zhu, *Phys. Rev. Lett.* **2008**, *101*, 196403.

[8] (a) M. C. Scharber, D. Mühlbacher, M. Koppe, P. Denk, C. Waldauf, A. J. Heeger, C. J. Brabec, *Adv. Mater.* **2006**, *18*, 789; (b) B. P. Rand, D. P. Burk, S. R. Forrest, *Phys. Rev. B* **2007**, *75*, 115327; (c) C. J. Brabec, A. C. Cravino, D. Meissner, N. S. Sariciftci, T. Fromherz, M. T. Rispens, L. Sanchez, J. C. Hummelen, *Adv. Funct. Mater*. **2001**, *11*, 374; (d) C. Uhrich, D. Wynands, S. Olthof, M. K. Riede, K. Leo, S. Sonntag, B. Maenning, M. Pfeiffer, *J. Appl. Phys*. **2008**, *104*, 043107.

[9] (a) D. Veldman, S. C. J. Meskers, R. A. J. Janssen, *Adv. Funct. Mater*. **2009**, *19*, 1; (b) J. Lee, K. Vandewal, S. R. Yost, M.E. Bahlke, L. Goris, M. A. Baldo, J. V. Manca, T. V. Voorhis, *J. Am. Chem. Soc.* **2010**, *132*, 11878; (c) R. A. Marsh, J. M. Hodgkiss, R. H. Friend, *Adv. Mater.* **2010**, *22*, 3672; (d) P. Peumans, S. R. Forrest, *Chem. Phys. Lett.* **2004**, *398*, 27.

[10] X. Y. Zhu, Q. Yang, M. Muntwiler, *Acc. Chem. Res.* **2009**, *42*, 1779.

[11] S. H. Park, A. Roy, S. Beaupre, S. Cho, N. Coates, J. S. Moon, D. Moses, M. Leclerc, K. Lee, A. Heeger, *J. Nat. Photonics* **2009**, *3*, 297.

[12] H. Ohkita, S. Cook, Y. Astuti, W. Duffy, S. Tierney, W. Zhang, M. Heeney, I. McCulloch, J. Nelson, D. D. C. Bradley, J. R. Durrant, *J. Am. Chem. Soc.* **2008**, *130*, 3030.

[13] S. R. Forrest, *MRS Bulletin* **2005**, *30*, 28.

[14] V. Coropceanu, J. Cornil, D. A. da Silva Filho, Y. Olivier, R. Silbey, J.-L. Bredas, *Chem. Rev.* **2007**, *107*, 926.

[15] R. R. Lunt, N. C. Giebink, A. A. Belak, J. B. Benziger, S. R. Forrest, *J. Appl. Phys.* **2009**, *105*, 053711.

[16] R. R. Lunt, J. B. Benziger, S. R. Forrest, *Adv. Mater.* **2010**, *22*, 1233.

[17] S. H. Park, A. Roy, S. Beaupre, S. Cho, N. Coates, J. S. Moon, D. Moses, M. Leclerc, K. Lee, A. J. Heeger, *Nature* **2009**, *3*, 297.

[18] (a) R. A. Marsh, J. M. Hodgkiss, R. H. Friend, *Adv. Mater.* **2010**, *22*, 3672; (b) D. Veldman, O. Ipek, S. C. J. Meskers, J. Sweelssen, M. M Koetse, S. C. Veenstra, J. M. Kroon, S. S. van Bavel, J. Loos, R. A. J. Janssen. *J. Am. Chem. Soc*. **2008**, *130*, 7721; (c) V. D. Mihailetchi, L. J. A. Koster, J. C. Hummelen, P. W.M. Blom, *Phys. Rew. Lett.* **2004**, *93*, 216601; (d) D. Kekuda, J.-H. Huang, K.-C. Ho, C.-W. Chu, *J. Phys.Chem.* **2010,** *14*, 2764; See also Chapter 6.

[19] J. Nelson, J. J. Kwiatkowski, J. Kirkpatrick, J. M. Frost, *Acc. Chem. Res.* **2009**, *42*, 1768.

[20] (a) D. Placencia, W. Wang, R. C. Shallcross, K. W. Nebesny, M. Brumbach, N. R. Armstrong, *Adv. Fuct. Mater.* **2009,** *19*, 1; (b) G. Wei, S. Wang, K. Renshaw, M. E. Thompson, S. R. Forrest, *Nano Lett.* **2010**, *4*, 1927; (c) C. H. Cheng, J. Wang, G. T. Du, S. H. Shi, Z. J. Du, Z. Q. Fan, J. M. Bian, M. S. Wang, *Appl. Phys. Lett.* **2010**, *97*, 083305.

[21] (a) M. M. Mandoc, F. B. Kooistra, J. C. Hummelen, B. de Boer, P. W. M. Blom, *Appl. Phys. Lett.* **2007**, *91*, 263505; (b) L. J. A. Koster, V. D. Mihailetchi, P. W. M. Blom, *Appl. Phys. Lett.* **2006**, *88*, 052104.

[22] (a) T. J. Savenije, J. E. Kroeze, X. Yang, J. Loos, *Adv. Funct. Mater.* **2006**, *15*, 1260; (b) S. Pfuetzner, C. Mickel, J. Jankowski, M. Hein, J. Meiss, C. Schuenemann, C. Elschner, A. A. Levin, B. Rellinghaus, K. Leo, M. Riede, *Org. Electron.* **2011**, *12*, 435.

[23] J. C. Wang, X. C. Ren, S. Q. Shi, C. W. Leung, P. K. L. Chan, *Org. Electron.* **2011**, *12*, 880.

[24] (a) J. Hwang, A. Wan, A. Kahn, *Mater. Sci. Eng. R.* **2009,** *64*, 1; (b) H. Ishii, K. Sugiyama, E. Ito, K. Seki, *Adv. Mater.* **1999**, *11*, 605.

[25] B. P. Rand, J. Genoe, P. Heremans, J. Poortmans, *Prog. Photovolt: Res. Appl.* **2007**, *15*, 659.

[26] R. C. Kwong, M. R. Nugent, L. Michalski, T. Ngo, K. Rajan, Y. J. Tung, M. S. Weaver, T. X. Zhou, M. Hack, M. E. Thompson, S. R. Forrest, J. J. Brown, *Appl. Phys. Lett.* **2002**, *81*, 162.

[27] G. Dennler, M. C. Scharber, C. J. Brabec, *Adv. Mater.* **2009**, *21*, 1323.

[28] M. A. Green, K. Emery, Y. Hishikawa, W. Warta, *Prog. Photovolt: Res. Appl*. **2011**, *19*, 84.

[29] P. Erk, H. Hengelsberg, *The Porphyrin Handbook: Applications of Phthalocyanines*, Vol. 19, Elsevier, USA, **2003**.

[30] A. W. Hains, Z. Liang, M. A. Woodhouse, B. A. Gregg, *Chem. Rev.* **2010**, *110*, 6689.

[31] Y. Terao, H. Sasabe, C. Adachi, *Appl. Phys. Lett.* **2007**, *90*, 103515.

[32] O. V. Molodtsova, M. Knupfer, *J. Appl. Phys.* **2006**, *99*, 053704.

[33] N. Li, B. E. Lassiter, R. R. Lunt, G. Wei, S. R. Forrest, *Appl. Phys. Lett.* **2009**, *94*, 023307.

[34] J. Dai, X. Jiang, H. Wang, D. Yan, *Appl. Phys. Lett.* **2007**, *91*, 253503.

[35] R. F. Bailey-Salzman, B. P. Rand, S. R. Forrest, *Appl. Phys. Lett.* **2007**, *91*, 013508.

[36] M. Brumbach, D. Placencia, N. R. Armstrong, *J. Phys. Chem. C* **2008**, *112*, 3142.

[37] K. V. Chauhan, P. Sullivan, J. L. Yang, T. S. Jones, *J. Phys. Chem. C* **2010**, *114*, 3304.

[38] S. Yoo, B. Domercq, B. Kippelen, *SPIE* **2005,** *5938*, 124.

[39] R. Ruiz, D. Choudhary, B. Nickel, T. Toccoli, K.-C. Chang, A.C. Mayer, P. Clancy, J. M. Blakely, R. L. Headrick, S. Iannotta, G. G. Malliaras, *Chem. Mater.* **2004**, *16*, 4497.

[40] (a) A. Sharma, A. Haldi, W. J. Potscavage Jr., P. Hotchkiss, S. R. Marder, B. Kippelen, *J. Mater. Chem.* **2009**, *19*, 5298; (b) S. Verlaak, D. Beljonne, D. Cheyns, C. Rolin, M. Linares, F. Castet, J. Cornil, P. Heremans, *Adv. Funct. Mater.* **2009**, *19*, 3809.

[41] K. Schulze, C. Uhrich, R. Schüppel, K. Leo, M. Pfeiffer, E. Brier, E. Reinold, P. Bäuerle, *Adv. Mater.* **2006**, *18*, 2872.

[42] (a) N. M. Kronenberg, M. Deppisch, F. Würthner, H. W. A. Lademann, K. Deing, K. Meerholz, *Chem. Commun.* **2008**, 6489; (b) H. Bürckstümmer, N. M.

Kronenberg, M. Gsänger, M. Stolte, K. Meerholz, F. Würthner, *J. Mater. Chem.* **2010**, *20*, 240; (c) N. M. Kronenberg, V. Steinmann, H. Bürckstümmer, J. Hwang, D. Hertel, F. Würthner, K. Meerholz, *Adv. Mater.* **2010**, *22*, 4193.

[43] See Chapter 6 of this thesis.

[44] T. Clarke, A. Ballantyne, F. Jamieson, C. Brabec, J. Nelson, J. Durrant, *Chem. Commun.* **2009**, 89.

[45] I. Bruder, A. Ojala, C. Lennartz, S. Sundarraj, J. Schöneboom, R. Sens, J. Hwang, P. Erk, J. Weis, *Org. Electron*. **2010**, *94*, 310.

[46] I. Kim, H. M. Haverinen, Z. Wang, S. Madakuni, J. Li, G. E. Jabbour, *Appl. Phys. Lett.* **2009**, 95, 023305.

[47] A. K. Pandey, J.-M. Nunzi, *Appl. Phys. Lett.* **2006**, *89*, 213506.

[48] S. Pfuetzner, J. Meiss, A. Petrich, M. Riede, K. Leo, *Appl. Phys. Lett.* **2009**, *94*, 223307.

[49] P. Peumans, V. Bulovic, S. R. Forrest, *Appl. Phys. Lett.* **2000**, *76*, 2650-2.

[50] (a) P. Peumans, S. R. Forrest, *Appl. Phys. Lett.* **2001**, *91*, 253503; (b) S. Yoo, W. J. Potscavage Jr., B. Domercq, S.-H. Han, T.-D. Li, S. C. Jones, R. Szoszkiewicz, D. Levi, E. Riedo, S. R. Marder, B. Kippelen, *Solid-State Electron*. **2007**, *51*, 1367.

[51] (a) J. Xue, B. P. Rand, S. Uchida, S. R. Forrest, *J. Appl. Phys. Lett.* **2005**, *98*, 124903; (b) B. P. Rand, J. Li, J.G. Xue, R. J. Holmes, M. E. Thompson, S. R. Forrest, *Adv. Mater.* **2005**, *17*, 2714; (c) J. Xue, B. P. Rand, S. Uchida, S. R. Forrest, *Adv. Mater.* **2005**, *17*, 66.

[52] (a) B. Maenning, J. Drechsel, D. Gebeyehu, P. Simon, F. Kozlowski, A. Werner, F. Li, S. Grundmann, S. Sonntag, M. Koch, K. Leo, M. Pfeiffer, H. Hoppe, D. Meissner, N. S. Sariciftci, I. Riedel, V. Dyakonov, J. Parisi, *Appl. Phys. A* **2004**, *79*, 1; (b) K. Walzer, B. Maenning, M. Pfeiffer, K. Leo, *Chem. Rev.* **2007**, *107*, 1233.

[53] (a) F. Yang, M. Shtein, S. R. Forrest, *Nature* **2005**, *4*, 37; (b) F. Yang, K. Sun, S. R. Forrest, *Adv. Mater.* **2007**, *19*, 4166.

[54] M. Hiramoto, H. Fujiwara, M. Yokoyama, *Appl. Phys. Lett.* **1991**, *58*, 1062.

[55] A. P. Yuen, A.-M. Hor, J. S. Preston, R. Klenkler, N. M. Bamsey, R. O. Loutfy, *Appl. Phys. Lett.* **2011**, *98*, 173301.

[56] J. Drechsel, B. Maenning, F. Kozlowski, M. Pfeiffer, K. Leo, H. Hoppe, *Appl. Phys. Lett.* **2005**, *86*, 244102.

[57] Y.-S. Hsiao, W.-T. Whang, S.-C. Suen, J.-Y. Shiu, C.-P. Chen, *Nanotech*. **2008**, *19*, 415603.

[58] G. Wei, R. R. Lunt, K. Sun, S. Wang, M. E. Thompson, S. R. Forrest, *Nano Lett.* **2010**, *10*, 3555.

[59] C. H. Cheng, J. Wang, G. T. Du, S. H. Shi, Z. J. Du, Z. Q. Fan, J. M. Bian, M. S. Wang, *Appl. Phys. Lett*. **2010**, *97*, 083350.

[60] A. Hadipour, B. de Boer, P.W.M. Blom, *Org. Electron.* **2009**, *9*, 617.

[61] J. D. Kotlarski, P. W. M. Blom, *Appl. Phys. Lett.* **2011**, *98*, 053301.

[62] Y. Liang, Z. Xu, J. Xia, S. T. Tsai, Y. Wu, G. Li, C. Ray, L. Yu, *Adv. Mater.* **2010**, *22*, E135.

[63] B. P. Rand, J. Xue, F. Yang, S. R. Forrest, *Appl. Phys. Lett.* **2005**, *87*, 233508.

[64] P.-C. Kao, S. Y. Chu, H.-H. Huang, Z.-L. Tseng, Y.-C. Chen, *Thin Solid Film* **2009**, *517*, 5301.

[65] R. Koeppe, N. S. Sariciftci, A. Büchtemann, *Appl. Phys. Lett.* **2007**, *90*, 181126.

[66] W. A. Luhman, R. J. Holmes, *Appl. Phys. Lett.* **2009,** *94*, 153304.

[67] M. O. Reese *et al.*, *Sol. Energy. Mater. Sol. Cells* **2011**, *95*, 1253.

[68] (a) F.C. Krebs, H. Spanggaard, *Chem. Mater.* **2005**, *17*, 5235; (b) P. Peumans, S. R. Forrest, *App. Phys. Lett.* **2004**, *80*, 338; (c) S. Heutz, P. Sullivan, B. M Sanderson, S. M. Schultes, T. S. Jones, *Sol. EnergyMater. Sol. Cells* **2004**, *83*, 229.

[69] W. J. Potscavage, S. Yoo, B. Domercq, B. Kippelen, *Appl. Phys. Lett.* **2007**, *90*, 253511.

[70] R. Franke, B. Maennig, A. Petrich, M. Pfeiffer, *Sol. Energy Mater. Sol. Cells* **2008**, *92*, 732.

[71] R. C. Kwong, M. R. Nuget, L. Michalski, T. Ngo, K. Rajan, Y.-J. Tung, M. S. Weaver, T. X. Zhou, M. Hack, M. E. Thompson, S. R. Forrest, J. J. Brown, *Appl. Phys. Lett.* **2002**, *81*, 162.

Chapter 3

Experimental Set-Ups for the Fabrication and Characterization of Solar Cells

Abstract: This chapter describes the fabrication and characterization of the solar cells. The cells are thermally vacuum-deposited on pre-structured ITO substrates in an ultra high vacuum chamber. Current-voltage (*J-V*) characteristics of the fabricated devices are measured by an automated measurement robot in ambient air. Incident photons to current spectra are recorded by an in-house built measurement set-up.

3.1 Substrate

All devices were fabricated on pre-structured indium tin oxide (ITO) covered glass substrates (Geomatec Ltd.) with a sheet resistance of about 30 Ω/cm. One substrate comprised of 64 cells with active areas of 0.04 cm^2 (Figure 1a). The purity of the substrates was so high that no additional solvent purification steps were needed. However, prior to using the substrates, they were treated in UV/O_3 oven for minimum 15 min. The purpose of this step was to remove any remaining organic dirt from the electrodes as well as to lower the work functions of the ITO anodes.

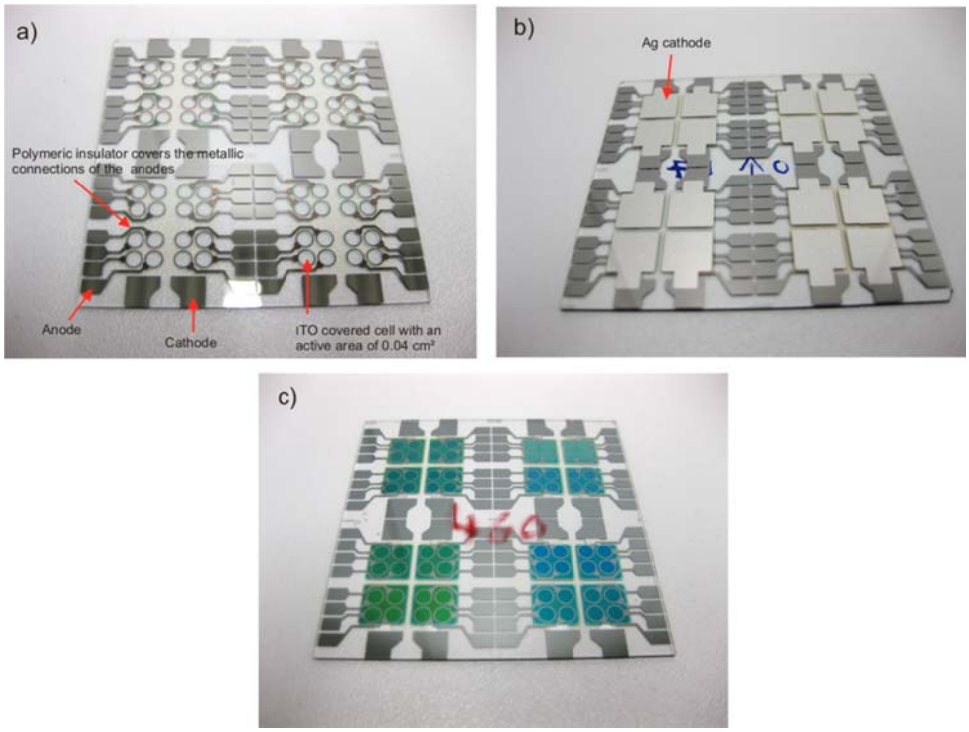

Figure 1. a) A picture of the pre-structured substrate. One substrate comprises of 64 cells with active areas of 0.04 cm². b) A picture of complete solar cells viewed from the cathodes' side. The devices were divided by shadow masks into groups of four cells that shared a common Ag cathode. c) A picture of a substrate with completed devices viewed through the glass substrate.

3.2 Device Fabrication

Solar cells were fabricated in a thermal vacuum deposition chamber (Kurt J. Lesker Ltd.) operating at base pressure of 10^{-6}-10^{-7} mbar. Organic materials as well as metals were deposited from aluminum oxide crucibles heated by metal wires. At one time, 10

crucibles (8 for organic materials and 2 for metals) could be mounted in the chamber which enabled fabrication of complete devices without breaking the vacuum in between the evaporation steps. The deposition rates of the organic sources were controlled by four quartz crystal sensors (one for two sources) which allowed simultaneous deposition at most from four different organic sources.

The substrate temperature was controlled by a copper block heater that contacted the substrate holder from behind. To improve the thermal connection a small amount of gallium was implemented between the copper block heater and the substrate holder. By this method, a maximum substrate temperature of ~ 200 °C could be reached.

The large number of the cells (64) on a single substrate enabled simultaneous fabrication of several identical devices (typically 8) improving the measurement statistics. Shadow masks were used to focus the deposition on the selected area of the substrate (Figure 1). Additionally, during the fabrication, different layer thicknesses could be realized onto a single substrate by moving a wedge tool gradually over the substrate.

3.3 Device Characterization

3.3.1 Current-Voltage Characteristics

Current-voltage (*J-V*) characteristics of the devices were recorded in ambient air using an in-house built automated measurement robot which enabled fast and accurate measurement of every cell on the substrate (Figure 2). A standard measurement of the complete substrate (64 cells) took only about 45 min. The fast measurement was important because the substrates were not typically encapsulated. Furthermore, owing to the short measurement time, the cell degradation was estimated to be negligible.

The solar illumination was simulated using a Xe lamp with an AM 1.5 filter and the light intensity of 100 W/cm^2 was fixed with a calibrated Si-photodiode. The current densities were recorded with a Keithley 2425 source measurement unit. In order to ensure reproducible measurement conditions, for every cell, first the automated measurement system searched the maximum current density spot by moving the substrate in xy-directions under the AM 1.5 simulated light after which the *J-V* characteristics was recorded.

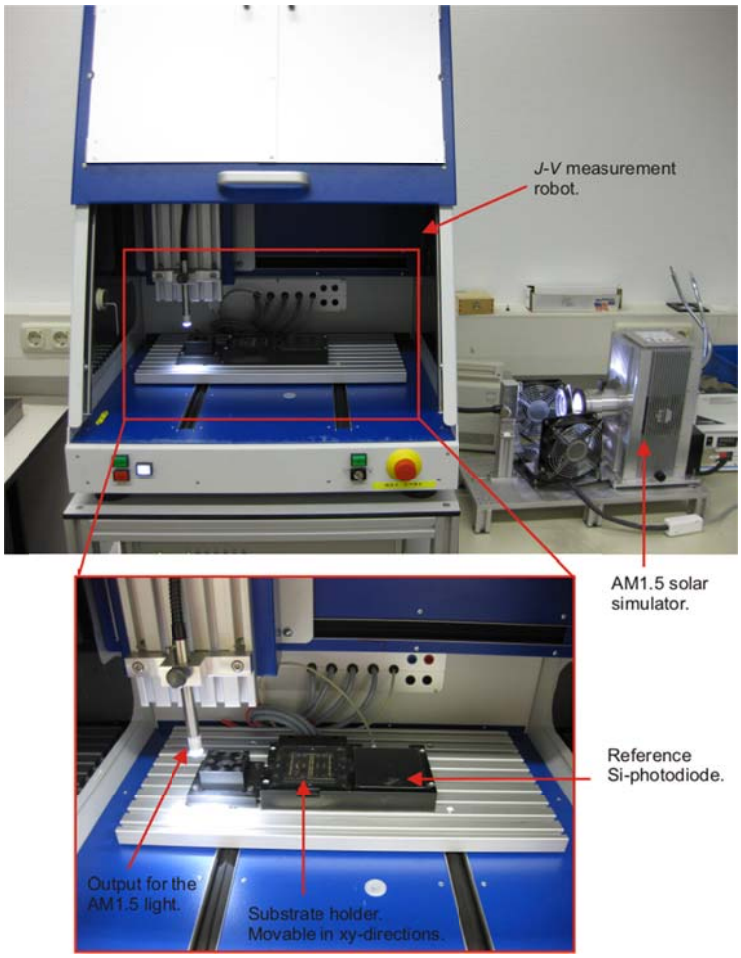

Figure 2. The automated current-voltage (*J-V*) measurement set-up.

3.3.2 Incident Photons to Current Measurements

Incident photons to current spectra (IPCE) were recorded with an in-house built measurement set-up (Figure 3). The measurements were carried out by illuminating (Xe lamp) the cells with a monochromated (ACTON SpectraPro 2150i) light. Simultaneously, a white background bias light (LED), of which intensity was fixed to give 10 mA cm^{-2} in a reference Si-photodiode, was applied to improve the measurement accuracy. The light intensities were calibrated with a Si-photodiode and the cells' response to the monochromated light was monitored with a PC connected in-house built current-voltage amplifier. The measurements were performed in ambient air.

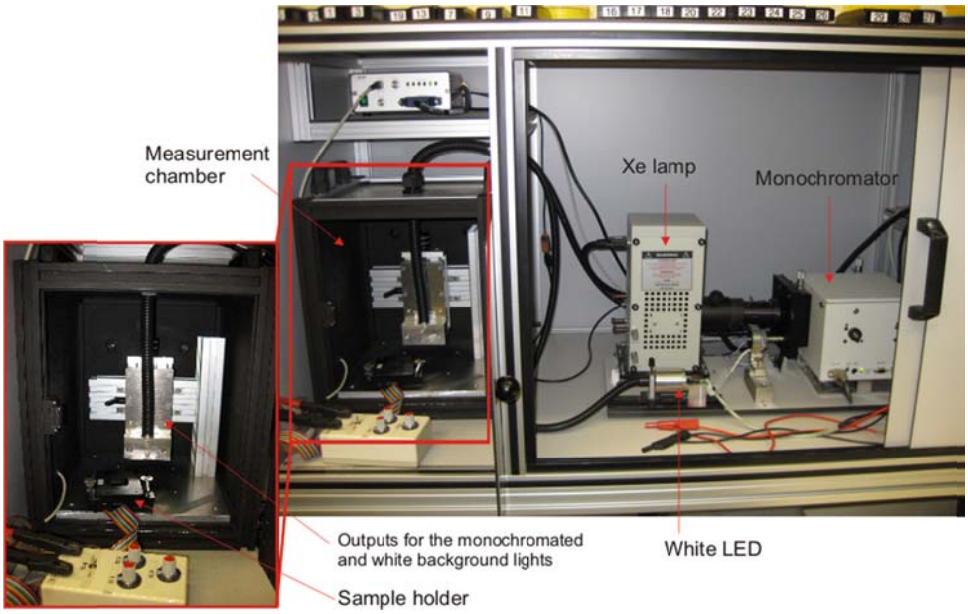

Figure 3. IPCE measurement set-up.

Chapter 4

Crystal Packing of Merocyanine Dyes: Effect of Molecular and Local Dipole Moments

Abstract: In this study, the influence of molecular dipole moment on crystal packing of merocyanine (MC) dyes is investigated in detail. Crystal structures of 45 merocyanines of which 40 are previously unpublished are analyzed. A significant overrepresentation of centrosymmetric structures is found compared to the global population of the centric and acentric space groups. As a comparison, the distribution of 170 highly dipolar compounds, retrieved from Cambridge Structural Database (CSD), to different space groups is analyzed and almost an identical result with respect to the MC structures is observed. These findings unambiguously demonstrate that a high permanent ground state dipole moment (> 8 D) significantly increases compound's probability to attain one of the centrosymmetric space groups. Furthermore, the effect of a molecular dipole moment on the formation of the closest packed structural motifs, in the crystal structures of MC dyes based on a Fischer base donor group, are investigated. Surprisingly, the influence of the molecular dipole moment is found to be minor. This is attributed to the bulky Fischer's base that impedes the molecules to stack in the face-to-face arrangement. Instead, other packing effects such as local electrostatics are, in many cases, observed to influence on the closest packed molecular assemblies.[a]

[a] The electro-optical measurements were carried out at University of Würzburg by Dr. Matthias Stolte. Part of the analyzed merocyanine crystal structures were solved at University of Würzburg by Marcel Gsänger. The crystallized merocyanine dyes were provided by Dr. Helmut Reichelt (BASF Ludwigshafen) and Hannah Bürckstümmer (University of Würzburg).

4.1 Introduction

The effect of permanent dipole moment on the crystal packing of small molecules is inadequately understood phenomenon, although, it is widely accepted that a high dipole moment increases compound's probability to attain one of the centrosymmetric space groups.[1] Especially non-linear optical (NLO) applications have often failed due to centrosymmetric packing of dipolar molecules. This has led to development of molecules with a vanishing dipole moment as well as octopolar compounds in order to promote non-centrosymmetric packing arrangements.[2]

To solve the puzzle, whether or not dipolar compounds favor centrosymmetric packing, Whitesell *et al*. did 1991 a statistical analysis of distribution of molecular dipole moments (derived from AM1 calculations) in three different space groups P1, P-1, and P21 for randomly selected structures retrieved from Cambridge Structural Database (CSD).[3] Surprisingly, the authors observed that the distribution of the molecular dipole moments was very similar in all these space groups (average dipole moments within the space groups were 3.04-3.36 D) and the highly dipolar compounds did not seem to favor the centrosymmetric P-1 space group. In the same study, Whitesell *et al.* analyzed the relative orientations of the neighboring dipole vectors – related by a two fold screw axis symmetry – in the crystal structures featuring the P21 space group. Surprisingly, the angles between the adjacent dipole vectors did not correlate with the magnitude of the molecular dipole moments which allowed the authors to concluded that "*the high preference for organic molecules to crystallize in one of the centrosymmetric space groups cannot be attributed to molecular dipole-dipole interactions*".[3]

Desiraju and co-workers repeated 2005 the statistical study of the distribution of molecular dipoles among the space groups P1, P-1, and P21 retrieved from CSD.[4] Their results essentially reproduced the findings of Whitesell *et al.*, and thus, seemed to confirm the counter intuitive observation that dipolar molecules do not prefer centrosymmetric packing motifs.[3] In the same study, Desiraju and co-workers calculated dipole moments by AM1 method for 200 randomly selected compounds taken from Aldrich catalog of chemicals. The authors observed that the distribution of the calculated dipole moments is very similar to those for the various space groups. Hence, they concluded that the synthetical procedures tend to produce molecules with

dipole moments ranging from 1-4 D and any bias for centrosymmetry would be suppressed by the vast majority of weakly dipolar compounds. In order to avoid this effect, Desiraju and co-workers analyzed 51 crystal structures of 4,4'-disubstituted diphenyl ethers of which dipole moments ranged from 0.3 to 8.0 D (AM1 computed). Interestingly, no preference for centrosymmetry was observed for compounds with a small molecular dipole moment. However, among the investigated group of diphenyl ethers, only centrosymmetric structures were obtained for molecular dipole moments above 4 D. This result allowed the authors to conclude: "*there is a strong tendency towards centrosymmetry for conjugated or aromatic molecules with large dipole moments*".[4]

Merocyanine (MC) push-pull dyes have been explored as functional materials for NLO[2,5] as well as for photorefractive[6] applications and recently also for organic bulk and planar heterojunction solar cells[7]. Earlier studies have demonstrated a strong tendency for MCs to antiparallel aggregations with dimerization constants up to $K_{dim} > 10^6$ M^{-1} in non-polar solvents.[8] This phenomenon has been attributed to the electrostatic dipole-dipole interactions arising from their very high ground-state dipole moments μ_g (up to 17 D, measured by electrooptical absorption (EOA) spectroscopy). Furthermore, the thermodynamic driving force of highly dipolar MCs to dimeric aggregates has recently been successively used for controlled growth of supramolecular assemblies.[9]

In this study, we explore the effect of molecular dipole-dipole interactions on the solid state packing of MC dyes. In particular, we will focus on the question: *to what extend the preference of MC chromophores to form antiparallel dimer aggregates in solution relate to the solid state packing, thus providing a supramolecular synthon in crystal engineering*? To answer this question, we first correlate the calculated dipole moments and space groups of 40 MCs. After this, the analysis is broadened to a selected group of dipolar compounds retrieved from CSD. The aim of the first part is to find out whether a high permanent dipole moment increases the probability of a dipolar compound to crystallize in one of the centrosymmetric space groups. In the second part of this study, we look in detail into the crystal structures of merocyanine dyes based on a sterically bulky Fischer base donor subunit. The aim of the second part is to evaluate the effect of a permanent dipole moment on the formation of the closest packed structural motifs. The molecules bearing the bulky Fischer base donor were chosen because they have not featured antiparallel aggregates in solutions – despite of very

high molecular dipole moments (up to 13 D). Furthermore, understanding the solid state packing of these dyes is of particular importance because of their very recent applications in high performance organic solar cells based on a heterojunction.[7]

4.2 Results and Discussion

4.2.1 Space Groups and Dipole Moments

Altogether 45 merocyanine crystal structures, of which 40 are previously unpublished and only four are solvates, have been investigated. Molecular structures of the MCs are depicted in Figure 1 and the corresponding space groups as well as experimental and calculated dipole moments are listed in Table 1. Notably, 18 crystal structures were solved in this work and 22 crystallographic data files were provided by Prof. Frank Würthner and his co-workers (University of Würzburg).[10] The experimental molecular dipoles are taken from existing literature or were measured separately for this study by Dr. Matthias Stolte (University of Würzburg) by EOA spectroscopy.[11] The same experimental dipole moment is taken for the chromophores that differ only by the non-conjugated R-substituents whereas an individual dipole moment is calculated[12] for every compound. For the calculations, the chromophores were taken in those geometries as found in the crystal structures without any structural optimization. If the structure contains more than one molecule in the asymmetric unit, then the average dipole moment of its individual components is given.

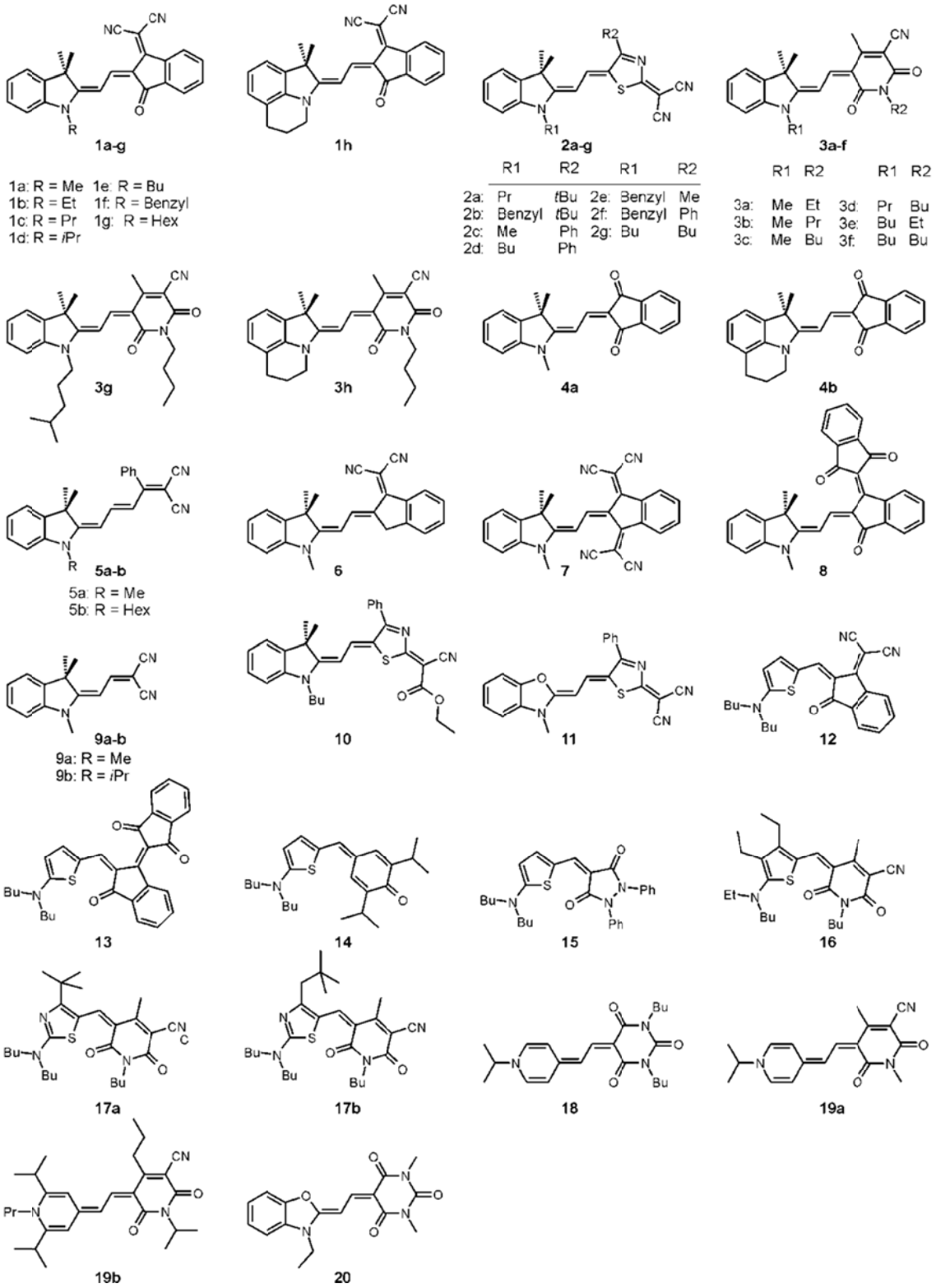

Figure 1. Molecular structures of the investigated merocyanine dyes.

Table 1. Space groups as well as experimental and calculated dipole moments of merocyanine dyes shown in Figure 1

Dye	Space group	Dipole [D]		Ref.[a]	Ref.[b]	Dye	Space group	Dipole [D]		Ref.[a]	Ref.[b]
		Exp.	Calc.					Exp.	Calc.		
1a	P21/c	6.1	6.5	11	this work	4a	P21/c	4.0	4.4	11	this work
1b	Pca21	6.1	6.9	11	this work	4b	P21/c	4.0	4.9	11	10
1c	P-1	6.1	6.7	11	this work	5a	P21/c	9.8	9.4	11	this work
1d	Pbca	6.1	6.8	11	this work	5b	P21/c	9.8	9.3	11	this work
1e	P21/c	6.1	6.4	11	10	6	P21/c	5.7	7.4	11	this work
1f	P21/c	6.1	6.6	11	this work	7	P21/c	4.9	7.3	11	this work
1g[c]	P-1	6.1	7.8	11	this work	8	P21/c	4.1	6.0	11	this work
1h	P21/n	6.1	7.1	11	7a	9a	Pnma	12.7	7.9	14	13
2a	P21/c	12.5	14.9	11	this work	9b	P212121	12.7	8.2	14	10
2b[d]	P21/c	12.5	14.8	11	this work	10[d]	P-1	11.6	13.6	11	10
2c[e]	P-1	12.5	15.6	11	this work	11	P21/c	16.2	18.0	15	10
2d	P-1	12.5	15.6	11	10	12	P-1	8.6	8.8	11	10
2e	P21/c	12.5	14.4	11	this work	13	P-1	6.1	6.9	11	10
2f	P21/n	12.5	15.2	11	this work	14	P21/n	7.9	7.8	11	10
2g	P-1	12.5	15.3	11	this work	15	Ia/2	6.8	8.4	16	10
3a	P21/c	12.8	13.1	8a	10	16	P21	14.1	14.1	17	8a
3b	P21/c	12.8	13.0	8a	10	17a	P21/a	9.6	10.2	18	this work
3c	P21/c	12.8	13.0	8a	10	17b	P21/c	9.6	11.7	18	10
3d	P-1	12.8	12.8	8a	10	18	P21/c	11.2	15.1	8a	10
3e	P-1	12.8	12.8	8a	10	19a[f]	P-1	17	21.5	18	10
3f	P-1	12.8	13.0	8a	10	19b	P-1	17	21.3	18	8a
3g	P-1	12.8	12.8	8a	10	20	P21/c	-	9.8	19	19
3h	P21/c	12.8	13.8	8a	10						

[a] Reference for the experimental dipole moment obtained by electro-optical absorption spectroscopy; [b] Reference for the crystal structure; [c] Low data quality (twin); [d] Chlorobenzene solvate; [e] EtOH solvate; [f] Hydrate, low data quality (disorder).

Figure 2a shows the correlation between experimental and calculated dipole moments of the MCs. The results demonstrate that the calculated values satisfactorily reproduce (the means square root error of the linear regression $R^2 = 0.83$) both the magnitude and the relative order of the experimental dipoles. In general, the computed values are 0.8 D higher than the experimental dipoles and only one chromophore (**9a, 9b**) clearly steps out by having a significantly higher experimental (μ_{exp} = 12.7 D measured for **9b**)[14] than the calculated (μ_{calc} = 7.9 D (**9a**) and μ_{calc} = 8.2 D (**9b**)) dipole moment. Note, that dyes **5a** and **5b** with an extended chain but otherwise identical donor and acceptor subunits as in chromophores **9a** and **9b** exhibit a significantly smaller experimental dipole moment (μ_{exp} = 9.8 D measured for **5a**). Furthermore, the calculated dipole moment of **5a** (μ_{calc} = 9.4 D) is higher than for compound **9b** which suggests an overestimation in the experimental dipole moment of the latter dye. The experimental dipole moments of all MCs range from moderate (dyes **4a** and **4b**, μ_{exp} = 4 D) to extremely high (dyes **19a** and **19b**, μ_{exp} = 17 D), respectively. The median dipole moment of these dyes is 10.6 D and thus it clearly exceeds the average dipole moment of the previous statistical studies of Desiraju *et al*.[4] and Whitesell *et al*.[3]

Figure 2b depicts the distribution of the space groups of 41 solvate free MCs with respect to the calculated molecular dipole moments. Interestingly, the centrosymmetric P21/c (57%) and P-1 (28%) space groups alone account 85% of all structures which significantly exceeds the global population (58%) of the space groups.[20] Additionally, only three other centrosymmetric space groups I2/a, Pbca, and Pnma with one structure in each are observed. Hereby, the preference for centrosymmetry is distinctly pronounced among the dyes (the ratio is 14:1) and only three non-centrosymmetric structures which all have different space groups P21 (**16**), P212121 (**9a**), and Pca21 (**1b**) are found. Note, however, that the dipole moment of dye **16** (μ_{calc} = 14.1 D) is notably higher that the median (9.4 D) of all compounds.

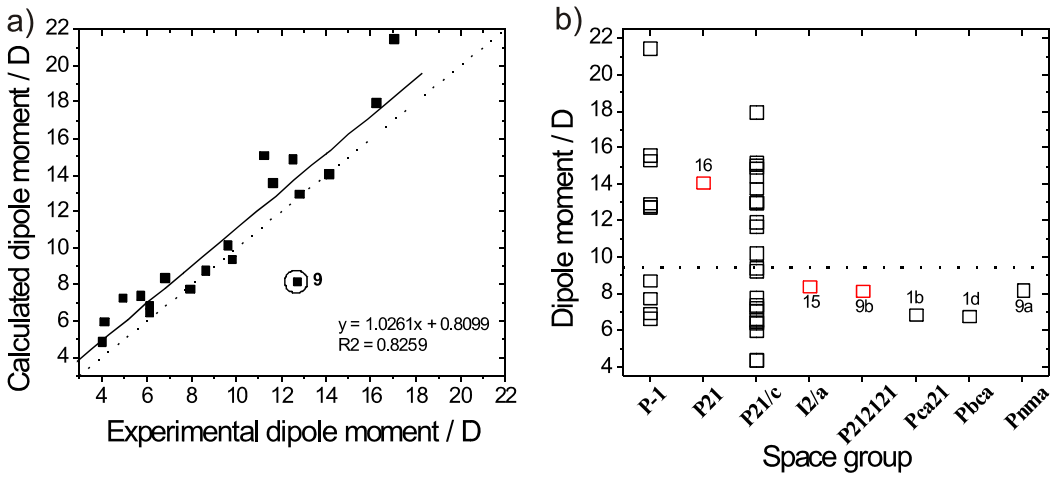

Figure 2. a) Experimental and AM1 computed molecular dipole moments of merocyanine dyes. The solid line shows the linear fit and the dotted line has a slope of unity. b) Distribution of the space groups with respect to the calculated molecular dipole moments. Non-centrosymmetric structures are denoted in red. Dotted line in (b) presents the median dipole moment (9.4 D) of the colorants.

The acentric crystal structure of highly dipolar (μ_{calc} = 14 D) chromophore **16** is interesting and needs to be discussed in more detail.[8a] The dye crystallizes in P21 space group with two molecules in the asymmetric unit. The closest intermolecular interaction observed in the crystal structure is an antiparallel dimeric motif, in which the π-planes of the neighboring dyes are stacked face-to-face to each other at van der Waals distance of about 3.6 Å (Figure 3). The calculated residual dipole moment of the dimer is 1.1 D which is only 8% of the molecular dipole moment. Hence, despite the polar space group, the packing motif essentially resembles a centrosymmetric P21/c structure in which the **π**-stacked molecules are only marginally twisted out of the inversion symmetry, presumably directed by sterical demands of the aliphatic side chains.

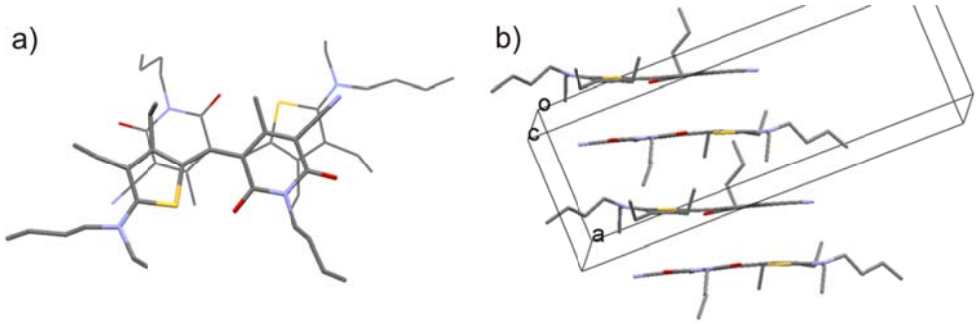

Figure 3. a) Antiparallel dimer and b) π-stack in the crystal structure of dye **16**.[8a] The calculated (AM1 method) residual dipole moment of the dimer is 1.1 D which is only 8% of the molecular dipole moment (μ_{calc} = 14 D). Hydrogen atoms have been omitted for clarity.

4.2.2 CSD Search

The findings for MCs suggest that a high molecular dipole moment increases the probability of a dipolar compound to crystallize in one of the centrosymmetric space groups. In particular, the centric space groups P-1 and P21/c are significantly overrepresented. To check whether the result holds for π-conjugated dipolar compounds in general, a CSD study was conducted.[21] In order to limit the number of hits only compounds containing amino donors and carbonyl or cyano acceptors were accepted (Scheme 1). In addition, all compounds containing over 40 non H-atoms or atoms heavier than S were left out. Moreover, to ensure comparability of the results, structures containing strong hydrogen bonds were excluded by rejecting all compounds with OH and NH groups. Molecules with internal centrosymmetry have been observed to crystallize almost exclusively in centric space groups[20] whereas enantiopure compounds can only form non-centrosymmetric structures. Therefore to draw out any influence of the centrosymmetry or the chirality only structures with one molecule per asymmetric unit were accepted and structures containing chiral carbon atoms were manually removed. Finally, the R-factor limit was set to 0.075 to ensure good data quality and not any ionic, solvate, or powder structures were accepted. These preconditions yielded 170 structures whose dipole moments were computed by the AM1 method[12] (for the CSD reference codes see Table A1 in the Appendix).

Scheme 1. Molecular subunit condition for the CSD search[21]

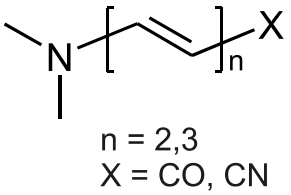

The distribution of space groups among the conjugated push-pull compounds, retrieved from CSD, is strikingly similar to our merocyanine dyes (Figure 4). The two most common space groups P-1 (29%) and P21/c (55%) cover 84% of all crystal structures which is nearly identical to what is found for our merocyanines. Surprisingly, only two other centrosymmetric space groups Pbca and C2/c with 10 and 4 structures, respectively, are observed among the 170 crystal structures. In addition, only 13 crystal structures with acentric space groups are found. The most common non-

centrosymmetric space groups are P212121 and P21 with 6 and 3 structures, respectively, while the rest Cc, Ia, Pna21, and Aba2 each have only 1 structure. The ratio between the centrosymmetric and non-centrosymmetric structures is 12:1 that is very similar to our MC structures.

The median dipole moment (6.2 D) of all structures, retrieved from CSD, is notably high. Nonetheless, the difference in the median dipole moments between the centrosymmetric (6.4 D) and non-centrosymmetric (5.8 D) space groups is surprisingly small. This can be explained by the fact that most of the compounds are accumulated at a relatively narrow dipole range: 75% of all centric and acentric structures are given by compounds whose dipole moments are below 8.6 and 7.8 D, respectively. Note, however, that only one non-centrosymmetric space group is observed when $\mu_{calc} > 10$ D while 23 of those compounds show centrosymmetric packing.

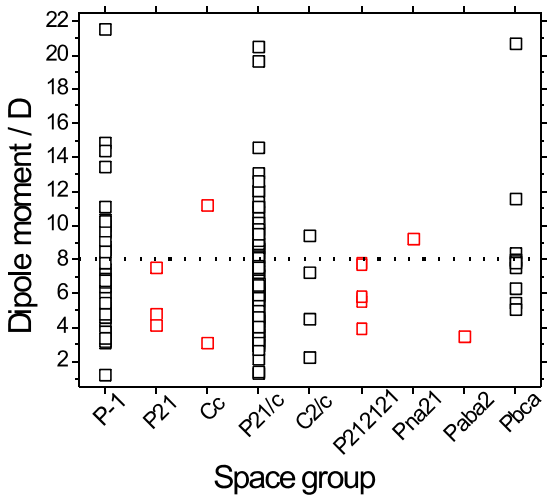

Figure 4. Distribution of calculated dipole moments of π-conjugated dipolar compounds retrieved from CSD with respect to their space groups. Non-centrosymmetric structures are denoted in red. Dotted line has a value of 8 D.

The apparent bias to centrosymmetric space groups is a clear proof that dipolar compounds tend to pack in centric structures. However, the average dipole moment of the compounds, retrieved from CSD, featuring non-centrosymmetric space groups, is notably high (5.8 D). For example, Desiraju and co-workers did not observe in their study with 4,4'-disubstituted diphenyl ethers non-centrosymmetric packing motifs above 4 D.[4] In turn, in our study, the probability of finding an acentric structure below 4 D is the same as for the whole set of compounds (12:1). However, the probability of

having a non-centrosymmetric space group significantly decreases (24:1) when the molecular dipole moment exceeds 8 D.

As the example with chromophore **16** demonstrates, even an extremely high dipole moment (μ_{calc} = 14 D) is not a guarantee of a centrosymmetric packing motif.[17] In fact, a closer look into the crystal structure of dye **16** revealed that the closest packed structural motif is an antiparallel dimer that is almost but not exactly centrosymmetric (Figure 3a). The antiparallel alignment significantly decreases the net dipole moment of the crystal, making the packing into the polar space group (P21) energetically less unfavorable. Likewise, other acentric structures of highly dipolar compounds are expected to feature packing motifs where the arrangement of the neighboring molecules significantly diminishes the net dipole moment of the crystal. Hence, an exact dipole moment limit can not be given, although, the probability of having a non-centrosymmetric space group significantly decreases when the molecular dipole moment increases (> 8 D).

4.2.3 Packing Motifs of Merocyanines Based on the Fischer's Base

In following, the crystal packing of merocyanine dyes with an indoline (Fischer's base) electron donating group are discussed. The chromophores can be divided in three different groups based on the substituted indane (**1a**-**h**, **4a**, **4b**, **6**, **7**), thiazole (**2a**-**g**, **10**), or dioxopyridine (**3a**-**h**) acceptor rings (Figure 1). In addition, the crystal structures of compounds with an indoline donor and a malonitrile acceptor connected by a tetramethine (**5a** and **5b**) or a dimethine (**9b**) bridge are presented.

Efficiency of the charge transfer from the donor (D) to the acceptor (A) along the conjugation path can be estimated by analyzing the π-conjucated C-C bond lengths D-C1 and C1-C2 or C1(/C2)-A of the dimethine and methine bridges, respectively, as well as the torsions angles between the mean planes of the donor and acceptor groups (Scheme 2). A planar molecular π-system and a significant convergence of the bond lengths are clear indications of an efficient charge transfer from the donor to the acceptor and contribution of the zwitterionic resonance form.[6d] As a comparison, for the Brooker's merocyanine, the shortening of the central bond (C1-C2) to 1.35 Å, was estimated to correspond 82% zwitterionic form.[22]

Scheme 2. Neutral and zwitterionic resonance structures of dimethine and methine bridged donor-acceptor (D-A) push-pull merocyanines

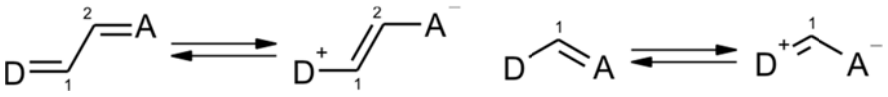

According to the point dipole approximation, the electrostatic interaction energy of antiparallelly aligned dipoles (Figure 5a) can be estimated by [23]

$$\Delta E_{\mathrm{dim}} = -\frac{\mu_g^2(1-3\cos^2\alpha)\sin^3\alpha}{4\pi\varepsilon_0 r^3}, \qquad (1)$$

where μ_g is the ground state dipole moment and α is the angle between the line parallel to the transition dipole vector and the line connecting the center of masses[24] of the stacked molecules (i.e. slipping angle); ε_0 is the relative permittivity of vacuum and r is the distance between the molecular π-planes (dipole vectors). Hence, based on the Eq. 1, it is evident that the ΔE_{dim} increases when $\alpha \rightarrow \pi/2$. Hereby, crystal structures of dipolar compounds are expected to demonstrate face-to-face stacked antiparallel dimeric motifs with α close to 90°, if the molecular dipole-dipole attraction has a significant influence on the crystal packing.

In the following discussion, the main focus is on the strongest interactions of the neighboring molecules in the crystal structures of merocyanines based on the Fischer base donor. In order to identify the strongest interactions within the crystal structures, intermolecular potential energies V between the closely packed molecules are calculated.[25] The method takes account the van der Waals interaction, which is typically the main packing force in organic crystals, but ignores any electrostatic attraction or repulsion. Hence, the energies are not accurate and should mainly be considered as relative.

The dimers featuring the highest intermolecular energies are categorized into two different groups depending on whether the neighboring dipole vectors are oriented antiparallel (AP) or parallel (PA) (Figure 5). The longitudinal offset between the stacked molecules is expressed by the slipping angle α and the rotational displacement of the dimeric motif is expressed by θ angle (Figure 5c).

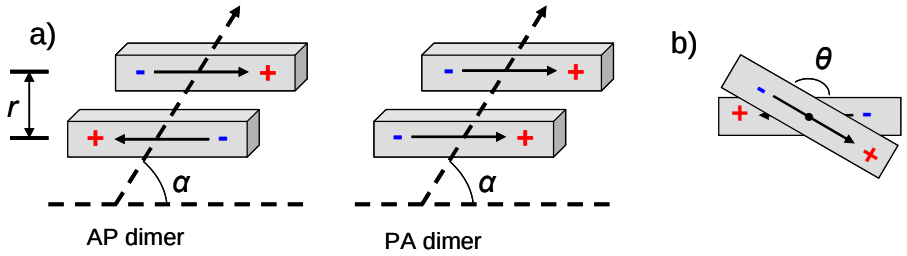

Figure 5. Schematic presentation of face-to-face stacked a) antiparallel (AP) and b) parallel (PA) dimers of permanently dipolar compounds. c) Dimer showing a rotational displacement θ viewed from top.

Indoline-indane (D-A) chromophores

For this series of dyes we were able to solve 12 crystal structures (Table 2). Eight crystal structures of chromophores **1a-h**, with spatially hindered indoline (Fischer's base) donors and well accessible 2-(3-oxo-indan-1-ylidene)-malonitrile acceptors, are only distinguished by the peripheral alkyl substituents at the indoline donor fragment (Figure 1). The structures are solvate free and have good data quality, except dye **1g** which crystallized as a twin. The R-substituents of the donor rings were systematically altered from small methyl (**1a**) to bulky benzyl (**1f**) and hexyl (**1g**) units, whereas the electron accepting groups were kept intact.

Despite the bulky R-substituents nearly coplanar π-conjugated systems (the twisting angles are from 3-14° between the mean planes of the indoline and indane rings) and significantly converged bond lengths within the conjugation paths are observed. The average bond lengths for D-C1, C1-C2, and C2-A are 1.39, 1.38, and 1.39 Å, respectively (Table 2). The almost vanished bond length alternation with a shortening of the central bond is a clear evidence of an efficient charge transfer and a significant contribution of the zwitterionic resonance structure among the compounds. Due to the orientation of the electron accepting carbonyl and malonitrile substituents at the 1- and 3-positions of the indane ring, respectively, the permanent dipole moment of the chromophores is, however, only moderate (μ_{exp} = 6.1 D) for this series of dyes. Nonetheless, the polar substituents induce high local dipoles that can interact with adjacent molecules. The dimeric motifs with the highest intermolecular interaction energies as well as the π-stacking interactions (*vertical*) and the packing motifs perpendicular to the π-stacks (*horizontal*) in the crystal structures of the indoline-indane dyes are shown in Table 2.

Table 2. Bond lengths and torsion angles as well as packing motifs found in the crystal structures of indoline-indane chromophores.

Dye	Bond length [Å]			Angle[a]	Dimer[b]	α[c]	r[d]	V[e]	Vertical	Horizontal
	D-C1	C1-C2	C1/C2-A	[°]		[°]	[Å]			
1a	1.389	1.383	1.395	7.6	AP	46	3.433	-16.5	-	Mosaic 1/ Chain 1
1b	1.387	1.385	1.402	10	-[f]	-[f]	3.423	-20.9	Column 2	Chain 1
1c	1.391	1.384	1.398	6.1	PA	22	3.420	-12.3	Brickwall 1	Chain 1
1d	1.390	1.381	1.396	7.9	-[f]	-[f]	3.396	-21.2	Column 3	-
1e	1.390	1.391	1.395	6.1	AP	85	3.368	-24.2	Column 1	Chain 1
1f	1.390	1.391	1.395	6.0	AP	90	3.398	-24.6	Column 1	Chain 1
1g	-[g]	-[g]	-[g]	-[g]	AP	-[g]	-[g]	-[g]	Column 1	Chain 1
1h	1.389	1.383	1.395	7.6	-[f]	-[f]	3.519	-20.5	Column 2	-
4a	1.383	1.399	1.377	13	AP	54	3.380	-14.3	-	Tape
4b	1.386	1.393	1.381	7.5	PA	41	3.420	-14.0	Column 4	Tape
6	1.371	1.402	1.368	7.2	AP	34	3.625	-12.4	Brickwall 1	Chain 1
7	1.404	1.375	1.420	23	AP	33	3.256	-21.2	-	-

[a] Torsion angle between the mean planes of the A and D units; [b] Type of the dimeric motif showing the strongest intermolecular interaction; [c] Slipping angle of the dimer; [d] Shortest atom-to-plane distance in the dimer; [e] Intermolecular potential energy (kcal/mol) of the dimer;[25] [f] The dimer shows a large rotational displacement; [g] Inadequate data quality.

Figure 6 depicts the dimeric arrangements showing the strongest intermolecular interactions[25] in the crystal structures of dyes **1e**[10] and **1f**. Despite the different R-substituents, the structures demonstrate isostructural AP dimers with face-to-face stacked molecules (the slipping angles are 85° (**1e**) and 90° (**1f**)). The face-to-face motifs are possible due to the orientation of the R-alkyl substituents which are pointing away from the π-π-contact planes leaving the opposing side of the conjugated π-systems open for close interactions (the closest intermolecular atom-to-plane distance for both AP dimers is circa 3.4 Å). However, the bulky 3,3'-dimethyl-methylene unit in the donor rings forces the AP motifs in transversal displacements. Furthermore, the dimers are stabilized by two crystallographically identical C-H···O hydrogen bonds between the carbonyl oxygen and one of the dimethyl-methylene hydrogen of the adjacent dye molecules. Due to the sterical demand of the R-substituents, the subsequent molecules to the face-to-face stacked AP dimer are forced in a slipped arrangement where the closest π-π-interaction (3.5 Å) is observed between the sterically less congested acceptor rings. Hereby, both crystal structures (dyes **1e** and **1f**) feature columnar stacks (Column 1) where the perpendicular and the slipped arrangements are repeated alternately as shown in Figure 6e for dye **1f**.

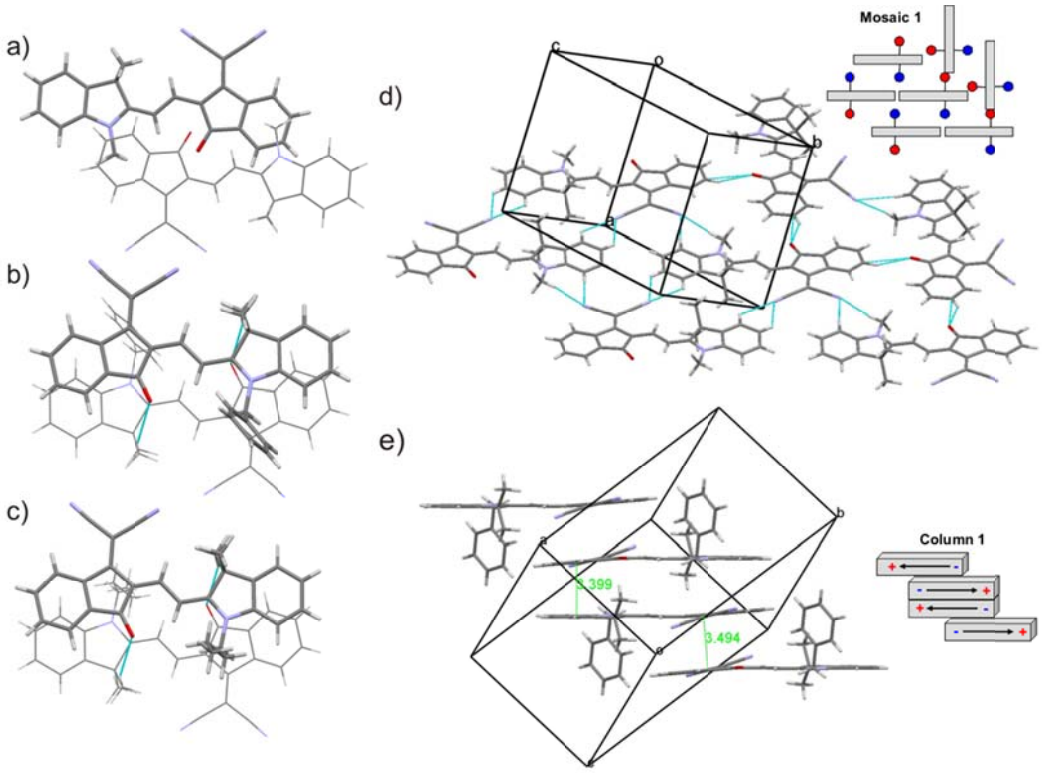

Figure 6. Dimeric motifs showing the strongest intermolecular interactions in the crystal structures of a) **1a**, b) **1e**,[10] and c) **1f**. d) Planar two-dimensional motif (Mosaic 1) in the crystal structure of chromophore **1a**. e) Stacking of **1f** molecules in a columnar one-dimensional motif (Column 1). The Column 1 –motif is also observed in the crystal structure of dye **1e**. Weak hydrogen bonds are denoted by blue dotted lines.

The small R-methyl substituent in compound **1a** allows the closest neighboring dyes to stack in a similar AP motif as seen for chromophores **1e** and **1f** (Figure 6a). However, unlike the latter dyes, the dimeric aggregate of the former chromophore does not show short C-H···O interactions. Instead, the motif in the crystal structure of **1a** demonstrates an electrostatically favorable close interaction between the antiparallelly oriented carbonyl groups (d(C···O) = 3.5 Å) of the neighboring molecules. However, in addition to the AP dimer, no evidence of further π-stacking into columnar stacks is observed in the structure of compound **1a**. In contrast, **1a** chromophores form a planar mosaic-like network (Mosaic 1) that exhibit multiple short contacts between the strong hydrogen bond acceptors (C=O and CN) and sp^2-activated C-H hydrogen atoms (Figure 6d). The arrangement is possible because of the low sterical demand of the R-methyl substituent which allows the adjacent dyes to approach in a short van der Waals distance. Moreover, the mosaic structure features a C-H···N bonded D-A···D-A···D-A submotif (Chain 1) which is also found in several other crystal structures of indoline-indane dyes (**1a-c**, **1e-g**, and **6**) (for an example of the chain motif see Figure 8c).

Surprisingly, R-ethyl substituted chromophore **1b** crystallizes in an acentric space group Pca21 showing a notably different packing structure compared to methyl substituted **1a**. The dimeric motif with the strongest intermolecular interaction in the crystal structure of chromophore **1b** demonstrates large rotational (θ = 92°) as well as longitudinal displacements. Furthermore, the dimers π-stack with equidistant connections (3.4 Å) to one-dimensional columnar motifs (Column 2) via the cofacial acceptor rings (Figure 7a).

Similar dimeric motifs as for dye **1b** are also observed in the centrosymmetric crystal structures of chromophores **1d** and **1h**[7a] (Figures 7b and 7c). However, with an exception that, in the dimeric motif of **1b** both malonitrile substituents are pointing toward the donor rings of the neighboring molecules whereas in the dimeric aggregates of chromophores **1d** and **1h** one of the molecules is rotated circa 180° about its long molecular axis and the malonitrile substituent is pointing away from the donor ring of the adjacent molecule. This has interesting consequences on the residual dipole moments of the dimers. In the crystal structure of **1b**, the directionalities of the adjacent molecular dipole vectors lower the residual dipole moment (μ_{res} = 1.5 D (AM1)) of the dimer compared to the molecular dipole moment (μ_{calc} = 6.8 D). In turn, in the crystal structures of dyes **1d** and **1h**, the residual dipole moments of the dimers are 9.1 and 8.9 D, respectively, which are significantly larger than the molecular dipole moments (μ_{calc} (**1d**) = 6.8 D, μ_{calc} (**1h**) = 7.1 D).

Chromophores **1h** π-stack in a similar columnar motif (Column 2) as observed for **1b** whereas **1d** dyes feature a totally different packing motif. Molecules **1d** stack in columns showing short π-π-contacts between the neighboring donor and acceptor groups as well as between the adjacent acceptor rings (Column 3).

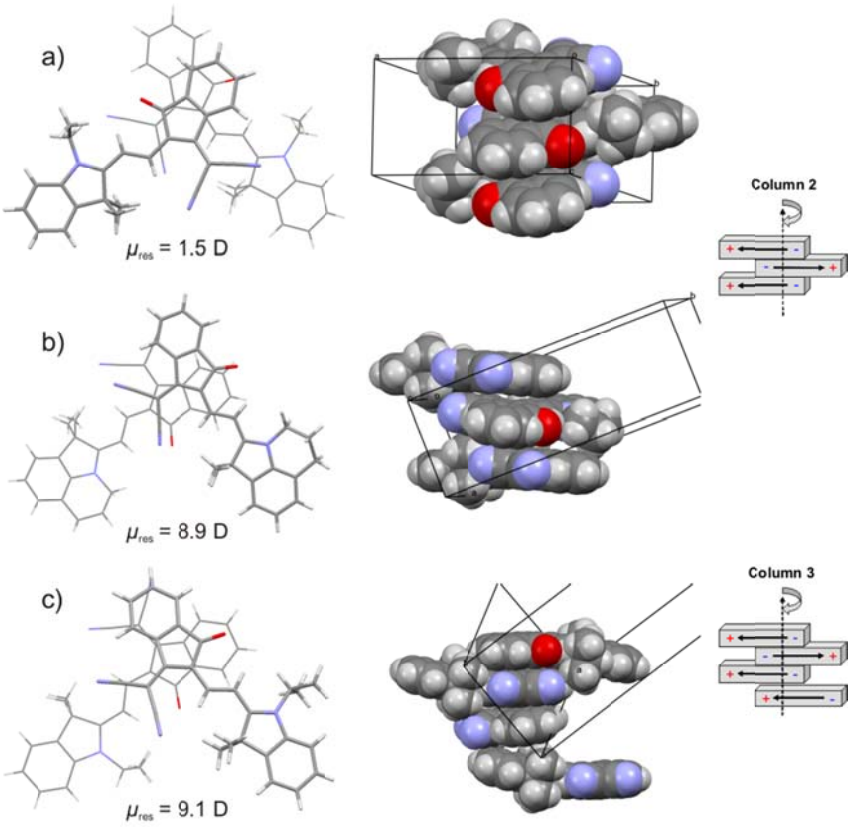

Figure 7. The strongest intermolecularly interacting dimers and π-stacking in the crystal structures of dyes a) **1b** , b) **1h**,[7a] and c) **1d**. Residual dipole moments (μ_{res}) of the dimeric motifs are also shown.

Figure 8a depicts the dimeric motif showing the strongest intermolecular interaction in the crystal structure of R-propyl substituted chromophore **1c**. The dimer is a strongly slipped AP aggregate (α = 22°) with cofacially stacked acceptor groups (atom-to-plane distance is 3.42 Å). Despite of the pronounced longitudinal displacement, the AP dimer resembles the packing motifs found in the crystal structures of chromophores **1d-f**. Furthermore, a second similarly strong interaction with a close π-π-contact (atom-to-plane distance is 3.4 Å) is observed between the parallelly orientated molecules with cofacially interacting donor and acceptor units. The second close contact is possible because the propyl chain at the donor unit points away from the molecular π-surface making one side of the chromophore sterically more accessible. However, due to the orientation of the propyl chain, the adjacent molecule on the opposing side of the π-system is forced in a substantially longer van der Waals distance (4.8 Å). Nevertheless, these slipped arrangements afford a two-dimensional brickwall (Brickwall 1) structure shown in Figure 8b. Additionally, perpendicular to the brickwall plane, the molecules are assembled in a chain motif (Chain 1) that is supported by weak C-H···N interactions

between the adjacent acceptor and donor groups. As mentioned above, also several other indoline-indane chromophores (**1a-c**, **1e-g**, and **6**) feature the Chain 1 –motif in their crystal structures.

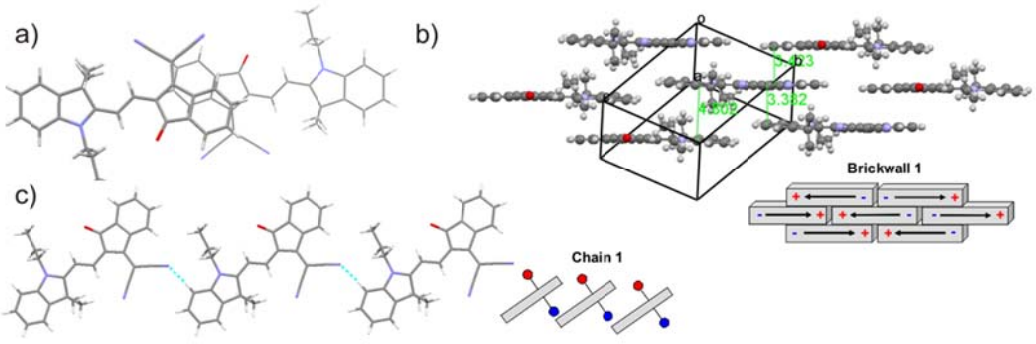

Figure 8. a) Slipped dimer showing the strongest intermolecular interaction and b) brickwall (Brickwall 1) and c) chain (Chain 1) motifs in the crystal structure of dye **1c**. Intermolecular interactions shorter than van der Waals radii are denoted by dotted blue lines.

This comparative study of eight crystal structures for dyes **1a-h** demonstrates heterogeneous dimeric packing motifs. Nevertheless, certain connecting and governing factors may be observed. For example, the bulky 3,3-dimethylmethylene group in the donor rings clearly dominates the molecules' assembly into the dimeric motifs by forcing the neighboring dyes in notable transversal and/or longitudinal displacements (Figure 6). AP aggregates with slipping angles close to 90° are observed in the crystal structures of dyes **1a** and **1e-g** whereas chromophores **1b-f** and **1h** feature smaller α angles and direct π-π-contacts between the acceptor rings. Obviously, a slipping angle close to 90°, and thus, maximized interaction of the adjacent dipole vectors is not particularly favored among the structures. This suggests that the molecular dipole-dipole interactions have only a minor effect on the crystal packing of the chromophores. The results are consistent with the statistical studies discussed in section 4.2.2 which demonstrated that the centrosymmetric space groups are not particularly pronounced among compounds with $\mu_{calc} < 8$ D.

However, the influence of the molecular dipole moments is probably detectable in the crystal packing of dyes **1b**, **1d**, and **1h** (Figure 7). As discussed above, dye **1b** crystallizes in a non-centrosymmetric space group whereas chromophores **1d** and **1h** feature centrosymmetric structures. In the crystal structure of colorant **1b**, the dipole vectors of the neighboring molecules are arranged in such a way that the net dipole

moments is significantly reduced; instead, the alignment of the adjacent dipole vectors in the crystal structures of dyes **1d** and **1h** enhances the dipole moments. Note, that the higher dipole moments are not equally important in the latter structures due to the centric space groups which ensure zero net dipole moments (Figure 7). Instead, the low residual dipole moment is energetically favorable for the polar crystal structure of **1b** (see also the discussion for chromophore **16** in section 4.2.1).

Within the indoline-indane series four more crystal structures of methyl (**4a**) and cyclic propyl (**4b**)[10] substituted indoline-1,3-indandione (D-A) dyes have been obtained. Molecular structures of **4a** and **4b** are highly similar to chromophores **1a-h** as only the malonitrile unit in the acceptor group is substituted by a carbonyl unit (Figure 1). However, the molecular dipole moments of **4a** and **4b** are significantly smaller (μ_{exp} = 4.0 D) owing to the reduced electron acceptor strength and the shorter conjugation path of a carbonyl group compared to a malonitrile unit. The average central bond length (C1-C2) of colorants **4a** and **4b** (1.40 Å) is longer than the average bond distances D-C1 and C2-A (1.38 Å) which implies a smaller contribution of the zwitterionic resonance structure and a more dominant neutral form.

The strongest intermolecular interaction in the crystal structure of **4a** is an antiparallel cofacially stacked dimer with the shortest van der Waals connection (d(C···O) = 3.38 Å) between the carbonyl groups of the neighboring dyes (Figure 9a). In addition to the AP dimer, however, no other significant π-π-interactions are observed. In contrast, **4b** molecules pack in *parallel* aggregates via cofacially π-stacked donor and acceptor rings of the adjacent dyes (Figure 9b). The PA dimers stack further in a columnar motif (Column 4) showing equidistant contacts (atom-to-plane distance is 3.80 Å) to the neighboring molecules (Figure 9c). Furthermore, also chromophore **4b** demonstrates the electrostatically favorable motif with a short van der Waals interaction (d(C···O) = 3.30 Å) between the antiparallelly stacked carbonyl groups of the adjacent molecules.

Perpendicular to the π-stacking direction both structures (dyes **4a** and **4b**) feature a one-dimensional tape motif with a 2-fold screw axis symmetry. An example of the tape structure for chromophore **4a** is shown in Figure 9d. The densely packed motif is possible because of the symmetrically substituted indane rings and the small sterical demand of the R-substituents. For example, chromophores **1a-h** cannot pack in the tape motif owing to the different sizes and hydrogen bond directionalities of the malonitrile and carbonyl substituents in the indane ring. The tape assemblies are enforced by

multiple weak C-H···O hydrogen bonds which are likely the main intermolecular interactions in the crystal structures of dyes **4a** and **4b**.

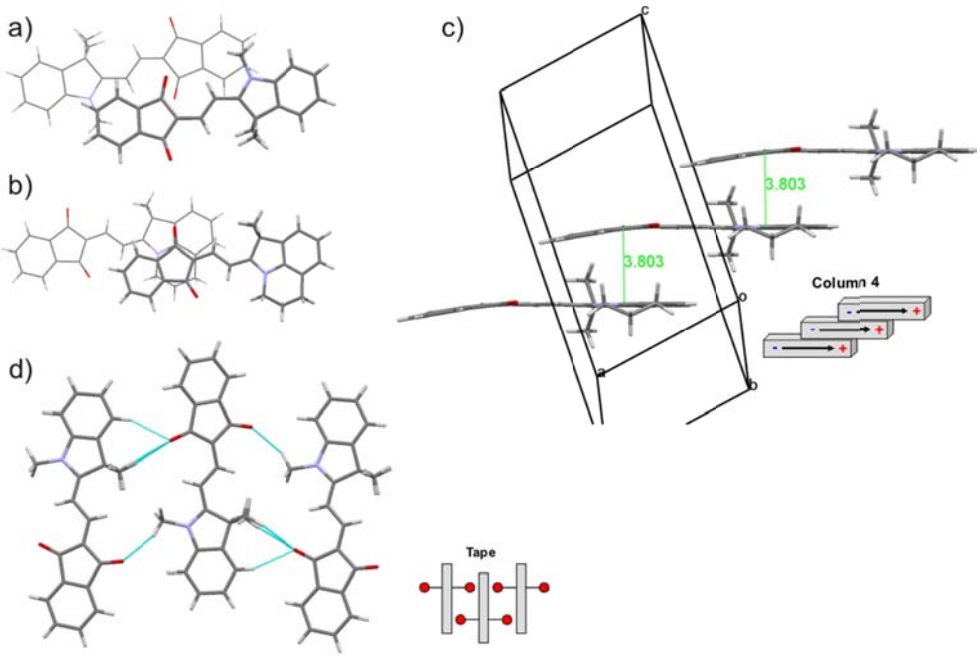

Figure 9. Dimeric motifs showing the strongest intermolecular interactions in the crystal structures of dyes a) **4a** and b) **4b**[10]. c) Columnar stack (Column 4) growing parallel to *a*-axis and d) infinite tape motif in the crystal structure of chromophore **4b** and **4a**, respectively. Intermolecular distances shorter than van der Waals radii are denoted by dotted blue lines.

In chromophore **6**, the carbonyl group at the 3-position of the indane ring is replaced by a sp^3-carbon but otherwise the molecular structure is identical to compound **1a**. The strongest intermolecular interaction in the crystal structure of dye **6** is an antiparallel slipped dimer with α = 33°. The motif features the shortest van der Waals contact (atom-to-plane distance is 3.6 Å) between the indane acceptors of the neighboring molecules (Figure 10a). The chromophores pack further in a similar Brickwall 1 -motif as observed in the crystal structure of dye **1c** (Figure 10b). Parallel to the molecular plane, the structure (dye **6**) features the common Chain 1 -arrangement which is enforced by weak C-H···N interactions between the donor and acceptor groups of the neighboring dyes (Figure 10c).

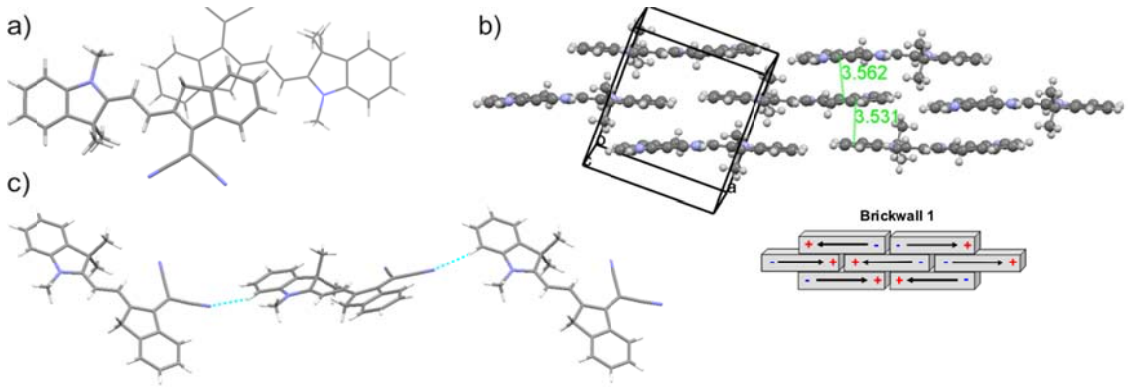

Figure 10. a) Slipped dimeric motif with π-π-contacts between the adjacent acceptor groups as well as b) chain (Chain 1) and c) π-stack (Brickwall 1) motifs in the crystal structure of chromophore **6**. Intermolecular distances shorter than van der Waals radii are denoted by dotted blue lines.

Chromophore **7** diverges of dye **6** by having two malonitrile substituents at the 1- and 3-positions of the indane ring, respectively. The central bond (C1-C2) length of the dimethine bridge is 1.375 Å which is the shortest among the investigated merocyanine dyes with the Fischer base donor subunit (Table 2). However, despite the significant charge transfer, the μ_{exp} is only 4.9 D which is attributed to the opposing orientation of the electron withdrawing malonitrile substituents. Furthermore, owing to the malonitrile substituents this chromophore is the most distorted among this series of dyes. Thus, the acceptor subunit is twisted by 23° with respect to the plane of the indoline donor unit.

The contorted but sterically accessible acceptor ring of chromophore **7** allows the π-systems of the neighboring compounds to stack closely together in an antiparallel motif with the shortest van der Waals distance of 3.26 Å. Notably, this dimer shows the highest intermolecular interaction energy (-21.2 kcal/mol) of the indoline-indane dye series (Figure 11a).[25] A second strong interaction is observed between the antiparallelly stacked malonitrile groups of the adjacent molecules. The electrostatically favorable motif demonstrates several very short π-π-contacts (the shortest d(N···O) = 3.19 Å) between the dipolar malonitrile units of the neighboring molecules (Figure 11b). However, beyond these dimers no strong π-π-interactions or horizontal contacts are observed in the crystal structure of chromophore **7**.

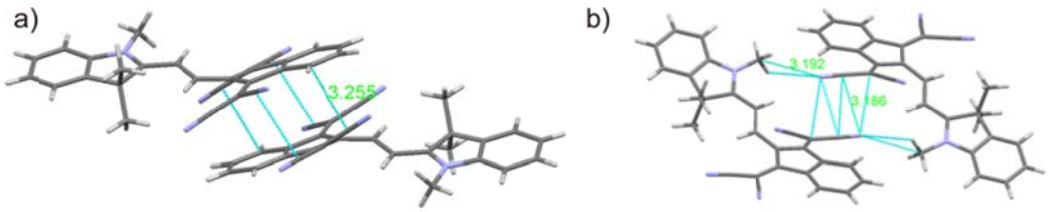

Figure 11. a) Dimer motif with close π-π-contacts between acceptor subunits and b) antiparallel assembly of the neighboring malonitrile groups in the crystal structure of chromophore **7**. Intermolecular interactions shorter than van der Waals radii are denoted by blue lines.

Indoline-thiazomalonitrile/malonitrile (D-A) chromophores

Also for this class of chromophores a significant number (11) of single crystals could be analyzed. Among this series, dyes **2a-g** with indoline donors and thiazomalonitrile acceptors are a structurally uniform group of highly dipolar compounds (μ_{exp} = 12.5 D measured for **2b**)[10]. The dyes show a strong tendency to crystallize in a needle-like morphology which makes the growth of suitable crystals for a single crystal analysis particularly difficult. However, seven crystal structures of which two are solvates have been solved (Table 1). The chromophores, as found in the crystal structures, are almost planar and the typical twisting angle of the mean planes of the indoline and thiazole rings are below 10°. This is together with the significant shortening of the C1-C2 central bonds (average length is 1.38 Å, identical for the former series of **1a-h**) of the dimethine bridges, a clear evidence of effective π-conjugations and charge transfers from the donors to the acceptors (Table 3).

Crystal structures of dye series **2a-g** demonstrate almost identical antiparallel dimer motifs with cofacially stacked thiazole rings of the neighboring molecules and slip angles α ranging from 33 to 45° (Table 3). An example of the dimer motif (**2a**) is depicted in Figure 12a. A typical distance between the S-atom and the mean plane of the adjacent thiazole heteroatom ring is 3.5 Å. In addition, the dimers feature relatively short intermolecular S···S contacts ranging from 3.6 to 4.0 Å. Furthermore, all structures, except **2f**, show a highly similar one-dimensional columnar packing motif (Column 5) in which the thiazole rings of the adjacent dyes are cofacially π-π-stacked on top of each other (Figure 12b). In the crystal structures of chromophores **2a**, **2b**, and **2e**, the columns have two-fold screw axis symmetry, and hence, show equidistant contacts to the neighboring molecules. In turn, dyes **2c**, **2d**,[10] and **2g** exhibit centrosymmetric dimers and the columnar stacks comprise of two kinds of dimeric motifs with slight variations on the π-π-distances as well as on the longitudinal

displacements. Note, however, that the dimers that are related by the screw axis symmetry (dyes **2a**, **2b**, and **2e**) exhibit only marginal rotational displacements ($178 < \theta < 180°$) and are distinctly similar to the centrosymmetric dimers.

Perpendicular to the π-stacking direction, the crystal structures of **2a-e** and **2g** feature isostructural two-dimensional sheet (Sheet 1) motifs of which an example is shown in Figure 12c. The sheet structures are supported by multiple weak C-H···N intermolecular hydrogen bonds.

Only exception in the series is chromophore **2f** with its bulky benzyl and phenyl substituents does not exhibit the columnar stacking motif in its crystal structure. Instead, the centrosymmetric aggregates are packed nearly orthogonal to the adjacent dimers showing close π-π-interactions between the R1-substituted benzyl ring and the π-plane of the molecule locating in the adjacent dimer (Figure 12d).

Table 3. Bond lengths and torsion angles as well as packing motifs found in the crystal structures of indoline-thiazomalonitrile/ malonitrile (D-A) chromophores

Dye	Bond length [Å]			Angle[a]	Dimer[b]	α[c]	r[d]	V[e]	Vertical	Horizontal
	D-C1	C1-C2	C1/C2-A	[°]		[°]	[Å]			
2a	1.399	1.382	1.398	3.8	AP	35	3.471	-25.1	Column 5	Sheet 1
2b	1.394	1.386	1.399	12	AP	34	3.516	-25.7	Column 5	Sheet 1
2c	1.402	1.381	1.402	4.4	AP	36	3.508	-23.4	Column 5	Sheet 1
2d	1.396	1.373	1.398	17	AP	45	3.514	-29.1	Column 5	Sheet 1
2e	1.393	1.377	1.395	5.5	AP	33	3.483	-22.0	Column 5	Sheet 1
2f	1.398	1.378	1.397	5.5	AP	43	3.666	-27.7	-	-
2g	1.396	1.373	1.393	8.4	AP	37	3.546	-22.3	Column 5	Sheet 1
5a	1.382	1.394	1.377	11	AP	70	3.485	-19.8	-	Chain 2
5b	1.375	1.394	1.380	6.6	AP	30	3.605	-18.9	-	Sheet 1
9b	1.372	-	1.387	0	PA	26	3.626	-8.41	Column 4	-
10	1.419	1.405	1.416	4.0	AP	70	3.548	-31.6	Column 1	Chain 2

[a] Torsion angle between the mean planes of the A and D units; [b] Type of the dimeric motif showing the strongest intermolecular interaction; [c] Slipping angle of the dimer; [d] Shortest atom-to-plane distance in the dimer; [e] Intermolecular potential energy (kcal/mol) of the dimer.[25]

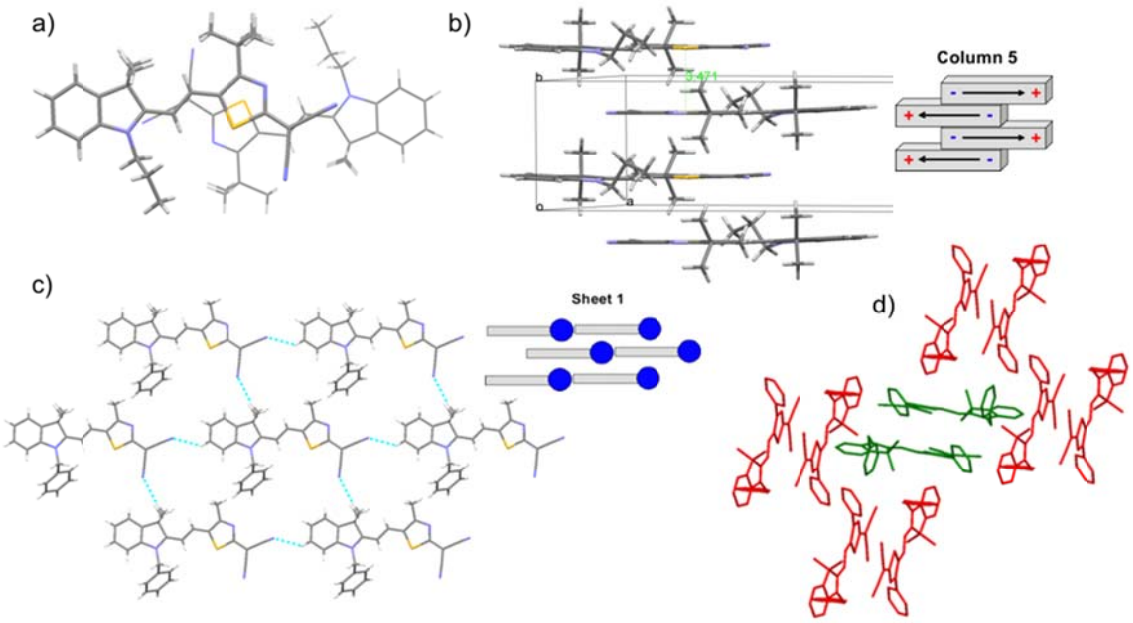

Figure 12. a) Antiparallel dimer and b) columnar π-stack (Column 5) with equidistant π-π-contacts to neighboring molecules in the crystal structure of dye **2a**. c) Sheet (Sheet 1) motif in the crystal structure of chromophore **2b**. d) Packing of the isolated dimers in the crystal structure of compound **2f**. The hydrogen atoms in figure (d) are omitted for the sake of clarity. Intermolecular distances shorter than van der Waals radii are denoted by dotted blue lines.

The molecular structure of dye **10** resembles closely chromophores **2a-g** (Figure 1). However, because of to the bulkier acceptor group adjacent molecules feature a more cofacially stacked dimeric motif with a large slipping angle α (70°) (Figure 13a). Owing to the close packing of the nearly face-to-face stacked π-systems (the closest atom-to-atom distance between the π-systems is 3.5 Å) as well as to the bulky R1- and R2-substituents, the π-planes of the neighboring molecules to the dimer are forced to a van der Waals distance of 4.7 Å (Figure 13b). Perpendicular to the π-stacking direction, the crystal structure demonstrates a chain motif (Chain 2) which is supported by weak C-H···N and C-H···π interactions (Figure 13c).

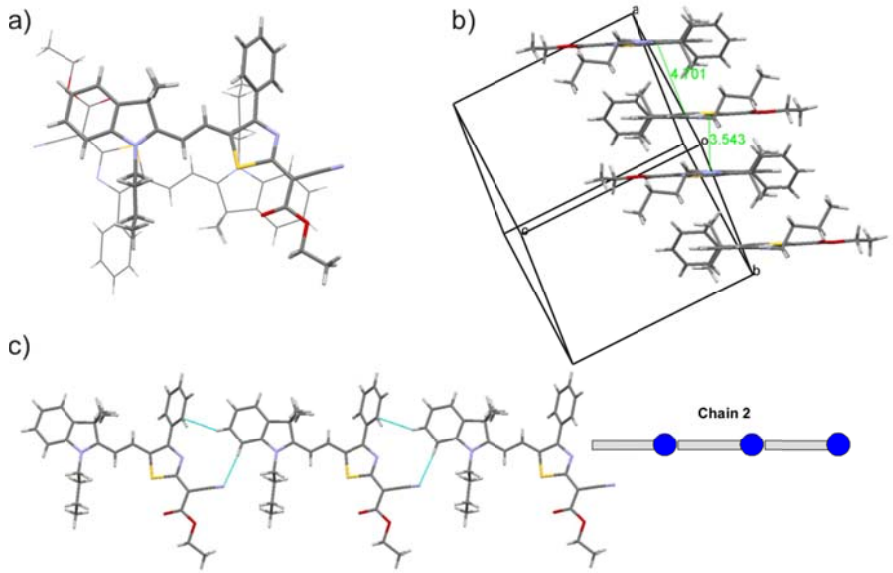

Figure 13. a) Cofacial dimer, b) columnar stack (Column 1) and c) chain assembly (Chain 2) in the crystal structure of chromophore **10**.[10]

Chromophores **5a** and **5b** comprise of a Fischer base donor unit and a malonitrile acceptor group connected by a tetramethine bridge (see Figure 1). The crystal structures of both dyes feature antiparallel dimeric aggregates (Figure 14a and 14b) with longitudinal displacements of α = 70° (**5a**) and α = 30° (**5b**). Furthermore, due to the rather small and sterically hindered π-systems, neither of the crystal structures show close π-stacking beyond the dimeric motifs (see also discussion for chromophore **10**).

Perpendicular to the dimeric π-stack of compound **5a**, the adjacent molecules are assembled in a twisted chain motif (Chain 2) showing weak C-H···N interactions between the neighboring cyano and R-methyl groups (Figure 14 c). In turn, **5b** molecules pack in a similar sheet (Sheet 1) structure as observed for dyes **2a-d**, **2f**, and **2g** (Figure 14d).

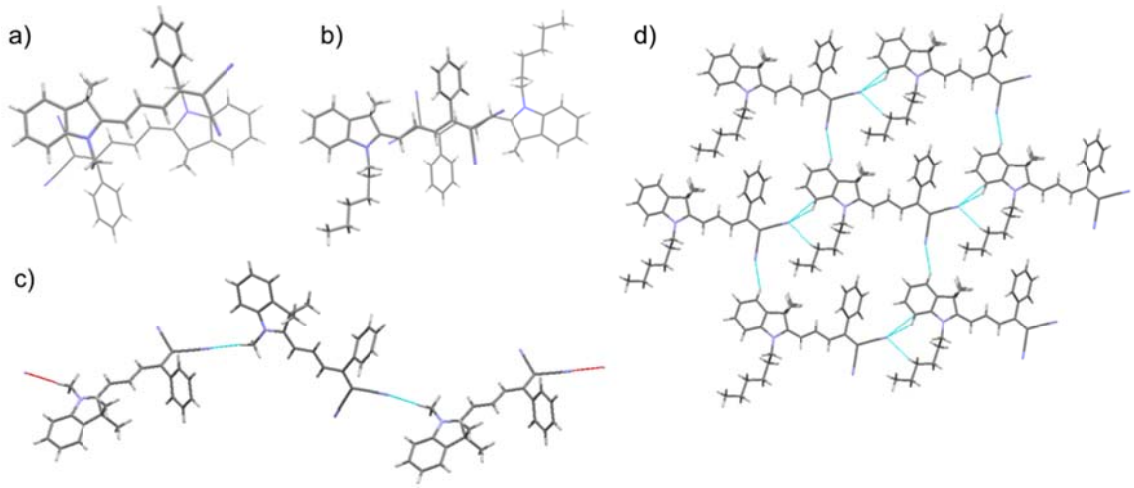

Figure 14. Antiparallel dimers in the crystal structures of dyes a) **5a** and b) **5b**. Packing of compounds **5a** and **5b** in c) chain (Chain 1) and d) sheet (Sheet 1) motifs, respectively.

Dye **9b** is an indoline-malonitrile molecule whose conjugated π-system is two carbon atoms shorter but otherwise identical to chromophores **5a** and **5b**. Nonetheless, **9b** molecules crystallize in a non-centrosymmetric P212121 space group exhibiting the strongest intermolecular interactions between the *parallelly* aligned molecules with cofacially stacked donor and acceptor subunits (Figure 15a).[13] Beyond the dimer, the parallelly assembled molecules π-stack into columnar motifs (Column 4) showing equidistant contacts (3.5 Å) to the neighboring chromophores (Figure 15b). The stacks, growing along the two-fold screw axes, closely resemble the molecular assembly of **4b** shown in Figure 9c. Considering the high permanent dipole moment of the molecule (μ_{calc} (**9b**) = 8.2 D), the parallel stacking motif and the non-centrosymmetric space group is somewhat surprising. This can be explained, however, by the antiparallel orientation of the adjacent columnar stacks that substantially reduces the net dipole moment of the crystal (Figure 15c).

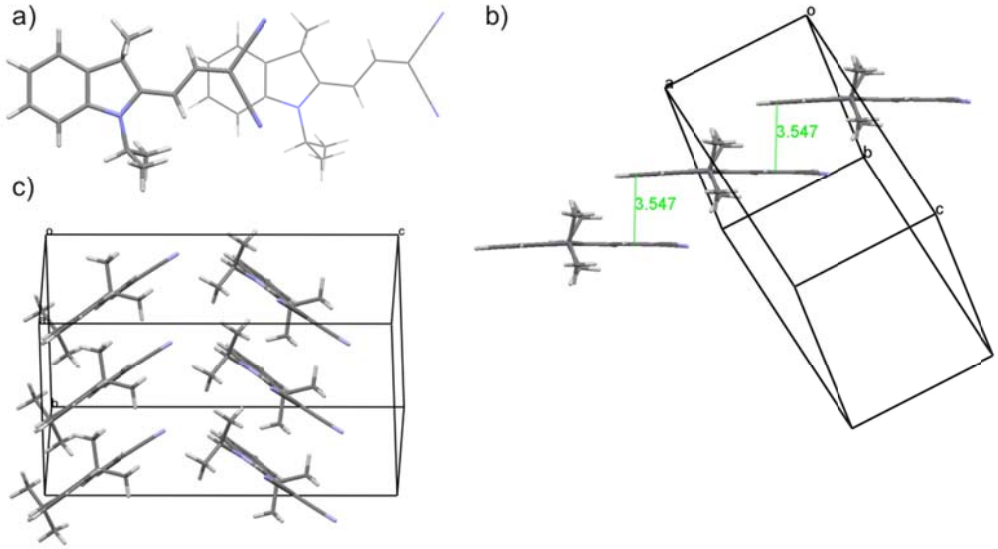

Figure 15. a) Slipped PA dimer motif, b) columnar stack (Column 4) viewed from the side and two antiparallelly growing π-stacks in the crystal structure of chromophore **9b**.[13]

In conclusion, quite similar packing motifs are found in the crystal structures of MCs based on the indoline donor and the thiazomalonitrile/malonitrile acceptor. In particular, the slipped AP dimers as well as the chain and sheet motifs are well represented. A likely cause for the highly similar dimeric motifs is the bulky R2-alkyl substituent at the 3-position of the thiazole rings (dyes **2a**-**g**) or the phenyl group in dye **5b** which afford the π-systems of the adjacent molecules to approach in a close van der Waals distance only from one direction. Furthermore, owing to the shape of the molecules and, in particular, because of the directionality of the dipolar malonitrile groups, the molecules favor similar chain and sheet assemblies where the electronegative cyano group can interact with the electropositive hydrogen atoms of the neighboring indoline ring. The formed D-A···D-A arrangement optimizes the local electrostatic interactions of the adjacent molecules.

Indoline-dioxopyridine (D-A) chromophores

Eight new crystal structures of indoline-dioxopyridine (IDOP) dyes (**3a**-**h**), of which steric hindrance has been systematically varied by different R1- and R2-substituents, have been investigated.[10] Shortening of the C1-C2 central bonds (in average 1.38 Å) in the dimethine bridges of the highly dipolar dyes (μ_{exp} ≈ 13 D), imply a significant contribution of the zwitterionic resonance structure (Table 4). Correspondingly, earlier

solution studies have demonstrated approximately 50% contribution of the zwitterionic resonance structure for IDOP dyes. [17,26]

Table 4. Bond lengths and torsion angles as well as packing motifs found in the crystal structures of IDOP dyes.

Dye	Bond length [Å]			Angle[a]	Dimer[b]	α[c]	r[d]	V[e]	Vertical	Horizontal
	D-C1	C1-C2	C1/C2-A	[°]		[°]	[Å]			
3a	1.400	1.378	1.406	17	AP	45	3.432	-16.7	Brickwall 2	Sheet 2
3b	1.404	1.383	1.410	20	AP	47	3.565	-19.5	Column 1	Mosaic 2
3c	1.406	1.386	1.410	21	AP	50	3.453	-16.5	Column 1	Mosaic 2
3d	1.404	1.386	1.410	20	AP	41	3.501	-19.7	Column 1	Sheet 2
3e	1.402	1.382	1.413	5.9	AP	42	3.342	-19.0	Brickwall 2	Sheet 2
3f	1.401	1.385	1.410	22	AP	91	5.200	-23.8	Column 1	Sheet 2
3g	1.403	1.381	1.414	17	PA	39	3.720	-18.1	Brickwall 3	Sheet 2
3h	1.402	1.381	1.409	24	AP	47	3.494	-21.0	Column 1	Mosaic 2

[a] Torsion angle between the mean planes of the A and D units; [b] Type of the dimeric aggregate showing the strongest intermolecular interaction; [c] Slipping angle of the dimer; [d] Shortest atom-to-plane distance in the dimer; [e] Intermolecular potential energy (kcal/mol) of the dimer.[25]

Figure 16a depicts the dimer with the strongest intermolecular interaction in the crystal structure of chromophore **3a**. Owing to the sterically hindered donor and acceptor rings, the neighboring dyes are forced in a substantial longitudinal displacement (α = 45°). The shortest interaction (3.43 Å) in the formed antiparallel cofacial stack is between the carbonyl oxygen and the π-plane of the neighboring dioxopyridine ring (Table 4). This interaction is supported by the strong electron withdrawing groups of the dioxopyridine which reduce the electronegativity of the aromatic ring. Furthermore, the formed dimeric motif is acentric, and thus, posses a small residual dipole moment. The crystal structures of chromophores **3b-f** and **3h** exhibit similar AP dimer motifs as dye **3a** with cofacially stacked acceptor groups (an example of the motif is shown in Figure 16b). However, unlike in the latter structure, the dimers in the former structures are centrosymmetric.

Brickwall motif (Brickwall 2) is observed in the crystal structures of dyes **3a** and **3e**. Within the brickwall structure the neighboring molecules are packed in columnar π-stacks via the cofacial dioxopyridine rings of the neighboring molecules. The columnar stacks show nearly equidistant π-π-contacts (3.4 Å) to the adjacent molecules and they closely resemble the structural features (Column 5 -motif) of dyes **2a-e** and **2g** shown in Figure 16c. For both dyes **3a** and **3e**, the R2-group in the dioxopyridine ring is an ethyl chain which is the sterically smallest R2-substituent among the investigated IDOP dyes. Hence, the divergent columnar packing motif of dyes **3a** and **3e** compared to the other

investigated IDOP dyes may be explained by the sterically less crowded acceptor ring that leaves both sides of the π-plane open for close π-π-interactions.

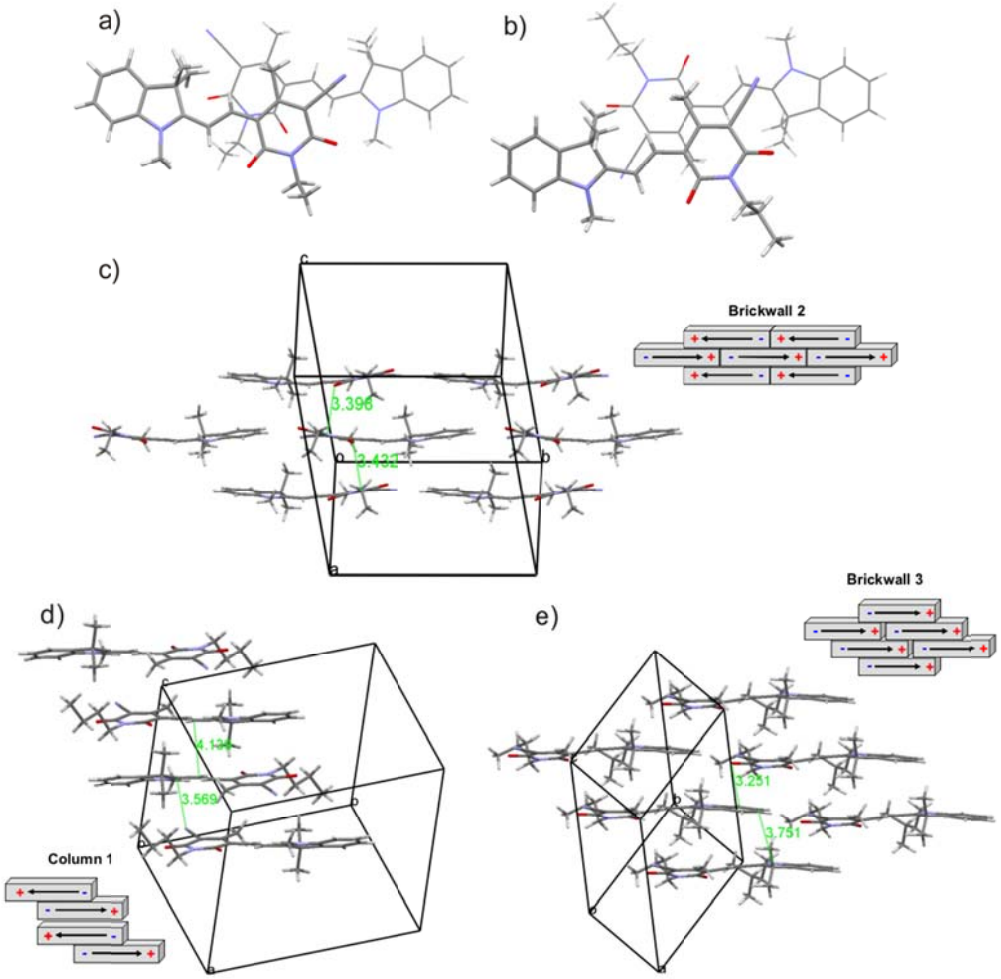

Figure 16. a) Non-centrosymmetric and centrosymmetric slipped dimers of dyes **3a** and **3b**, respectively. Stacking motifs in the single crystal structures of c) **3a**, d) **3b**, and e) **3g**.[10]

Figure 16d depicts the π-stacking of colorant **3b** into a columnar motif (Column 1). Within the columnar structure two different types of antiparallelly oriented cofacial dimers with a small and a large offset are observed. The dimer with the smaller offset shows a substantially longer van der Waals distance (circa 5 Å) between the neighboring π-systems owing to the bulky substituents. Instead, for the adjacent dyes in the more slipped dimer an approach in a short van der Waals distance is feasible (3.5 Å). The example in Figure 16d is only given for **3b** but also the crystal structures of chromophores **3c-f** and **3h** show similar Column 1 –type stacks with only minor variations in the axial displacements between the neighboring molecules.

The crystal structure of **3g** demonstrates a notably different π-stacking arrangement compared to any other compound of the investigated IDOP dyes (Figure 16 e).[10] For this dye, the strongest intermolecular interaction is observed between *parallelly* stacked molecules (PA dimer) with α = 46°. Due to the high sterical demand of the molecule, the π-systems of the cofacial molecules are forced to a substantially long van der Waals distance (the shortest atom-to-atom distance is 3.75 Å). The PA dimers are, further, stacked in Brickwall 3 –motif where the shortest (3.25 Å) π-π-contact is observed between the acceptor and donor rings of the parallelly aligned dyes locating in the adjacent stacks.

Perpendicular to the π-stacking direction, the IDOP dyes exhibit two different types of packing motifs depending on the sterical demand of the R1- and R2-alkyl substituents (Figure 17). When the sizes of the R-substituents are alike, as for **3a** and **3d**-**f**, the alkyl chains locating in the adjacent dyes are interlocked. In these structures, the molecules form antiparallelly aligned chains that are further assembled into a tightly packed two-dimensional sheet motif showing multiple weak C-H···X (X = O or N) hydrogen bonds (Figure 17a). The packing motif of **3g** resembles closely the previously discussed dyes. However, owing to the branched R-substituents, the interlocking of the alkyl groups of the neighboring dyes is not possible (Figure 17b). This result in a void space between the adjacent chains which is then filled by the R-alkyl substituents of the adjacent molecules stacked on top and below.

The packing motif of chromophores **3b**, **3c**, and **3h** perpendicular to the columnar π-stacks diverge of the other IDOP dyes. In these crystal structures, the dye molecules are assembled in an isostructural mosaic-like motif (Mosaic 2) where the long molecular axes are pointing orthogonal to the neighboring dyes (Figure 17c). The formed mosaic structures exhibit multiple weak C-H···X (X = O or N) interactions between the adjacent chromophores which satisfy the strong electron donating groups C=O and CN of the dioxopyridine rings. The main cause for the Mosaic 2 –motif is likely the different sizes of the R1- and R2-substituents that impede the interlocking of the neighboring alkyl chains.

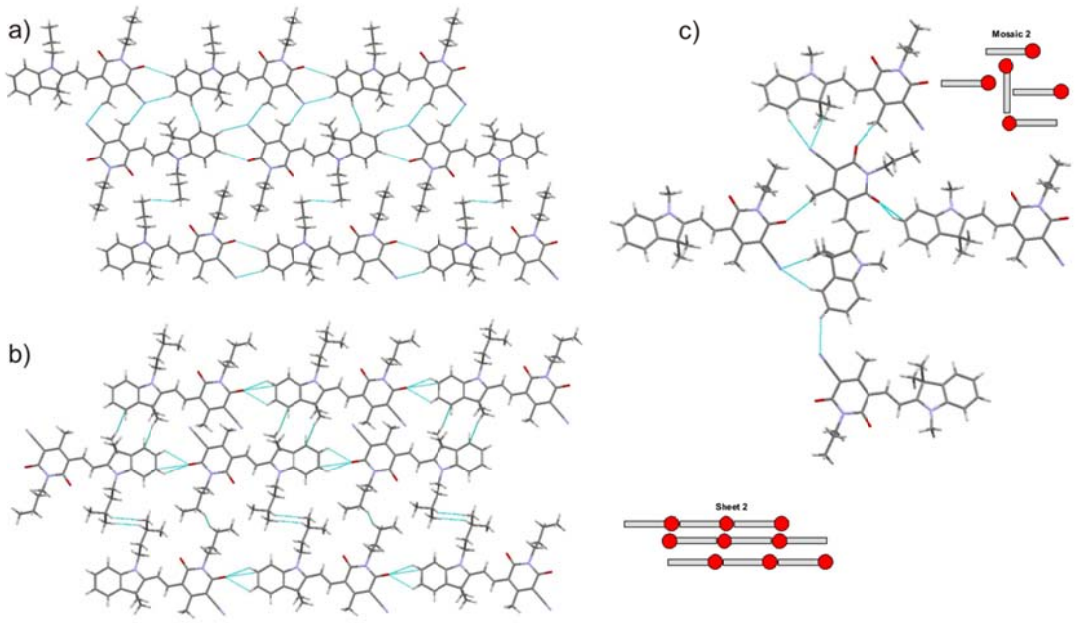

Figure 17. a) Sheet motifs of dyes a) **3f** and b) **3g**.[10] c) Mosaic motif of chromophore **3b**.[10] Interactions shorter than van der Waals radii are denoted by blue lines.

To conclude, two stacking motifs namely Column 1 and Column 5 are the most pronounced among the crystal structures of MC dyes based on the Fischer base donor. The Column 1 –motif is more common among the indoline-indane and IDOP dyes whereas the indoline-thiazomalonitrile chromophores favor the Column 5 –motif. As shown in Figure 16, the Column 1 –stack can be understood to comprise of alternating cofacial and slipped dimeric interactions of antiparallelly oriented molecular dipole vectors. In turn, the Column 5 –stacks feature only the slipped arrangements of the neighboring molecules and direct contacts between acceptor rings. The fact that the IDOP dyes favor the Column 1 –motif can be explained by the sterically hindered molecular structures that leave only one side of the acceptor groups' π-planes open for π-π-stacking. Only exceptions are dyes **3a** and **3e** of which small R2-substituents in the acceptor rings enable Column 5 –type packing (within the Brickwall 2 –structure) showing nearly equidistant π-π-connections between the stacked molecules. Likewise, the indoline-thiazomalonitrile chromophores with sterically hindered donor groups and more accessible acceptor rings feature the Column 5 –motif in their crystal structures. These observations suggest that the crystal packing of the molecules based on the Fischer base donor subunit prefer dense π-π-stacking and minimized intermolecular distances over more optimized alignments of the neighboring molecular dipole vectors. The findings are also consistent with earlier findings which did not show tendency to

electrostatically driven aggregation in non-polar solvent media for sterically bulky MC dyes.[8,9]

The space groups P-1 and P21/c are clearly the most common among the investigated crystal structures of indoline-indane, IDOP, and indoline-thiazomalonitrile dyes. However, the observed packing motifs of the chromophores do not seem to favor any particular space group. For example, as discussed above, the indoline-thiazomalonitrile dyes feature the Column 5 –type stack in their crystal structures. In the case of colorants **2a**, **2b**, and **2e**, the neighboring molecules show 2-fold screw axis symmetry whereas the adjacent chromophores in the columnar stacks of dyes **2c**, **2d**,[10] and **2g** are related by inversion symmetry.

4.2.4 Intermolecular Dipole-Dipole Interaction as a Supramolecular Synthon

The statistical study of MC crystal structures as well as the CSD search strongly hints that a high molecular dipole moment increases a compound's probability to attain one of the centrosymmetric space groups. For example, only three compounds (**1b**, **9b**, and **16**) of the 40 solvate free merocyanine chromophores show non-centrosymmetric space groups. This is significantly less than could be expected from the global distribution of molecules between the centric and the acentric space groups (9:2).[20]

As shown above, merocyanines with Fischer base donor cannot form cofacial π-π-stacks because of the bulky 3,3'-dimethylmethylene substituent. Instead, in many cases, the abundant dimeric motifs exhibit slipped stacking arrangements. This is especially pronounced among the indoline-thiazomalonitrile dyes which all demonstrate an isostructural AP dimer with a large longitudinal offset. However, the question remains, what is the influence of the dipole-dipole interaction on the formation of this motif? The magnitude of the electrostatic interaction energy of the neighboring dipole vectors can be estimated by employing Eq. 1 that yields ΔE_{dim} = -3.0 kcal/mol for the closest packed dimer in the crystal structure of **2a** (α = 35°, r = 3.58 Å). This energy corresponds approximately to a weak hydrogen bond (typically 1-3 kcal/mol)[27] but compared to the calculated[25] intermolecular potential energy (-25.1 kcal/mol) it is rather small. However, the situation completely changes if the π-systems of the adjacent molecules are able to π-stack perfectly face-to-face to each other. For example, in a hypothetical case, where the adjacent molecules (dye **2a**) feature α = 90° and r = 3.58 Å, the ΔE_{dim} increases to -49 kcal/mol. Note, that the electrostatic potential clearly exceeds the bonding energy (-7.4 kcal/mol)[28] of the supramolecular synthon: O=C-O-H···O=C-O-

H hydrogen bond. An archetype example of the cofacial dimeric motif is observed in the crystal structure of chromophore **20**.[19] The chromophore comprises of a sterically open barbituric acid acceptor and benzoxazole donor group which enables the adjacent molecules to stack with a short van der Waals distance (α = 94° and r = 3.38 Å) (Figure 18). The dimer shows ΔE_{dim} of -33 kcal/mol (μ_{calc} = 9.8 D) which is approximately of the same size as the intermolecular potential energy (V = -27.4 kcal/mol) of the dimer obtained from the force field calculations.[25] Hence, the dipole-dipole interaction is expected to be a significant driving force for the perpendicular stacking motif in the crystal structure of dye **20**.[19] This assumption is supported by the earlier findings of Würthner and co-workers which have shown that sterically unconstrained MCs tend to form antiparallel face-to-face stacks in non-polar solvents.[8,9] The authors demonstrated that the electrostatic dipole-dipole attraction, in particular, is the main driving force for the antiparallel aggregations.

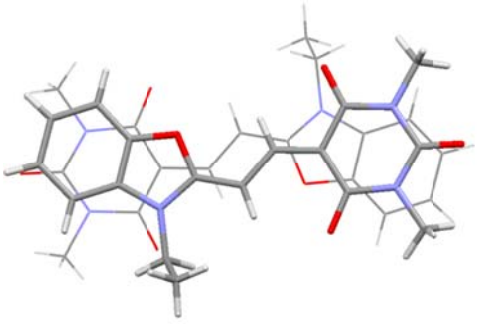

Figure 18. Face-to-face stacked antiparallel aggregate in the crystal structure of dye **20**.[19]

As discussed above, several crystal structures of highly dipolar (μ_{exp} = 12.8 D) IDOP dyes (**3b-d**, **3f**, and **3h**) feature antiparallel face-to-face π-stacked motifs with slipping angles close to 90° despite the bulky Fischer base donor subunit. For example, **3f** molecules pack in the Column 1 –arrangement (Figure 16d) showing two different kind of antiparallel stacking motifs: one where the neighboring dipoles are stacked cofacially (α = 91°) but are rather separated (r = 5.2 Å) and a second one where the distance between the adjacent molecular dipoles is short (r = 4.0 Å) but the offset is considerable (α = 42°). The estimated ΔE_{dim} of the cofacial dimer is -17 kcal/mol whereas the slipped stacking motif gives only -5.0 kcal/mol. Hence, despite the increased distance between the π-planes of the adjacent molecules in the cofacial sandwich, the dipole-dipole

interaction is substantially stronger compared to the slipped neighbor. This is attributed to the angular terms $\cos^2\alpha$ and $\sin^3\alpha$ in Eq. 1 that rapidly reduce ΔE_{dim} as α decreases. Note, that the dipole-dipole interaction energy of the sandwich is also comparable to the interaction energy of the dimer (V = -23 kcal/mol), calculated by the force field method.[25]

Small molecules feature often different polymorphs of which one phase optimizes specific intermolecular interactions whereas a second phase maximizes the packing density.[29] In such cases, it is often found that a specific intermolecular interaction (e.g. a strong hydrogen bond(s)) competes with other attractive and repulsive forces that drive the molecules into the densest possible packing structure. Likewise, the dipole-dipole attraction can be considered as a specific intermolecular interaction that is competing with other attractive and repulsive packing forces in a crystallization process. Hence, it is possible that structures showing antiparallel cofacial π-stacks could exhibit more loose packing with respect to structures featuring less ideal alignments of the dipoles.

This possibility was investigated among the IDOP dyes. Table 5 depicts the ΔE_{dim} of the strongest dipole-dipole interactions in the crystal structures of IDOP dyes as well as the packing indices (PI)[30] of the corresponding crystal structures. Dye **3a** demonstrates both the highest PI and the lowest ΔE_{dim}, but otherwise the packing densities and the dipole-dipole energies do not seem to correlate, as shown in Figure 19. Although, the PIs are not dependent on the molecular dipole-dipole interaction energies in the crystal structures of the investigated IDOP dyes, the influence of the molecular dipole-dipole interactions on the alignment of the neighboring chromophores cannot be definitely ruled out. As a matter of fact, a clear majority of the IDOP dyes exhibit cofacial π-stacks in their crystal structures of which interaction energies were estimated to be comparable to V. Furthermore, the cause that no correlation is observed may be attributed to other intermolecular interactions (e.g. hydrogen bonds) as well as to the different sterical demands of the alkyl substituents that may obscure the effect of the dipole-dipole attraction. However, it is clear that the dipole-dipole attraction is easily diminished by other packing effects.

Table 5. Calculated packing indices[30] (PI) and the highest molecular dipole-dipole interaction energies of the IDOP dyes

Dye	PI	ΔE_{dim} (kcal/mol)	Dye	PI	ΔE_{dim} (kcal/mol)
3a	71.1	4.1	3e	69.3	4.3
3b	68.8	15	3f	69.6	17
3c	69.0	17	3g[a]	67.9	-
3d	70.1	19	3h	69.0	12

[a] Parallel dipole stacking.

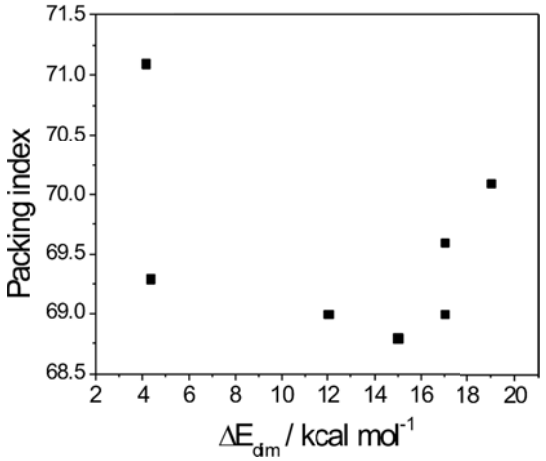

Figure 19. Dependence of the packing indices on the strongest molecular dipole-dipole interaction energies found in the crystal structures of IDOP dyes.

4.3 Conclusions

Only three non-centrosymmetric space groups were found among the 41 solvate free merocyanine crystal structures. In addition, the statistical study of highly dipolar push-pull compounds, retrieved from Cambridge crystal database (CSD), gave almost an identical result with a high overrepresentation of the centric structures. Hence, we can conclude, that a high molecular dipole moment increases the chance of having a centrosymmetric crystal structure.

Our findings are consistent with previous studies in solution which did not show electrostatically driven aggregations for MCs based on the Fischer base donor in the accessible concentration range. Hereby, we can conclude that the electrostatic attraction arising from the permanent dipole moment is not directing a distinct packing motif in the investigated crystal structures of sterically demanding MCs. However, the effect of a

permanent dipole moment on the entire crystal structure is evident as demonstrated by the statistical studies.

In turn, the local dipoles have a clear effect on the crystal packing of the investigated MC dyes. For example, no close π-π-stacking interactions between the carbonyl or cyano groups are observed whereas several crystal structures (e.g. dyes **1a**, **4a**, **4b**, and **7**) show close interactions between the antiparallelly π-stacked carbonyl or cyano substituents. In addition, a number of crystals exhibit infinite molecular chains that are supported by multiple weak hydrogen bonds. Formation of these assemblies may be attributed to following factors: (1) optimization of weak intermolecular interactions and (2) avoidance of like-like interactions of the dipolar units. The first point is well visible in the crystal structures of chromophores **4a** and **4b** which both exhibit planar tape motifs that optimize the C-H···O interactions. In turn, dye series **1a-h**, with very similar molecular structures to chromophores **4a** and **4b**, do not demonstrate the tape motifs in their crystal structures; instead most of the dyes feature the Chain 1 –motif (see Figure 8c). The cause for the different packing motifs is attributed to the different sizes and bonding directionalities of the strong hydrogen bond acceptors (CN and C=O) of dyes **1a-h** compared to dyes **4a** and **4b**. Furthermore, good examples of maximization of the intermolecular interactions are the chain and mosaic assemblies of colorants **3a-h**.

4.4 Experimental Section

Single crystal analysis

Suitable crystals for a single crystal analysis were typically grown by slow evaporation of DCM/EtOH (or hexane, heptane) solution of the dye at room temperature or at 4 °C. The single crystal structures solved in this work were commonly measured at 103 K employing a Bruker AXS CCD detector and a graphite-monochromated Cu K_α (λ = 1.51478 Å) radiation. The structures were solved by a direct method and refined on F^2 using the full matrix least square method in a SHELXTL-program-package.[31] All non-hydrogen atoms were anisotropically refined and hydrogen atoms were placed on idealized positions. Crystallographic parameters for the crystal structures solved in this work are shown in the Appendix.

4.5 References

[1] R. Glaser, *Acc. Chem. Res.* **2007**, *40*, 9.

[2] (a) M. S. Wong, C. Bosshard, P. Günter, *Adv. Mater*. **1997**, *9*, 837; (b) W. Lin, Z. Wang, L. Ma, *J. Am. Chem. Soc.* **1999**, *121*, 11249; (c) T. Verbiest, K. Clays, C. Samyn, J. Wolff, D. Reinhoudt, A. Persoons, *J. Am. Chem. Soc.* **1994**, *116*, 9320.

[3] J. K. Whitesell, R. E. Davis, L. L. Sanuders, R. J. Wilson, J. P. Feagis, *J. Am. Chem. Soc.* **1991**, *113*, 3267.

[4] A. Dey, G. R. Desiraju, *Chem. Commun*. **2005**, 2486.

[5] (a) M. Blanchard-Desce, *C. R. Phys.* **2002**, *3*, 439; (b) S. R. Marder, J. W. Perry, *Adv. Mater.* **1993**, *5*, 804.

[6] (a) F. Würthner, S. Yao, J. Schilling, R. Wortmann, M. Redi-Abshiro, E. Mecher, F. Gallego-Gomez, K. Meerholz, *J. Am. Chem. Soc.* **2001**, *123*, 2810; (b) T. Kaino, S. Tomaru, *Adv. Mater.* **1993**, *5*, 172; (c) O. Ostroverkhova, W. E. Moerner, *Chem. Rev.* **2004**, 3267; (d) F. Würthner, R. Wortmann, K. Meerholz, *ChemPhysChem* **2002**, *3*, 17.

[7] (a) H. Bürckstümmer, N. M. Kronenberg, M. Gsänger, M. Stolte, K. Meerholz, F. Würthner, *J. Mater. Chem.* **2010**, *20*, 240; (b) N. M. Kronenberg, V. Steinmann, H. Bürckstümmer, J. Hwang, D. Hertel, F. Würthner, K. Meerholz, *Adv. Mater.* **2010**, *22*, 4193; (c) H. Bürckstümmer, E. V. Tulyakova, M. Deppisch, M. R. Lenze, N. M. Krononberg, M. Gsänger, M. Stolte, K. Meerholz, F. Würthner, *Angew. Chem.* **2011**, DOI: 10.1002/anie.201105133; For planar heterojunction devices see Chapter 6.

[8] (a) F. Würthner, S. Yao, T. Debaerdemaeker, R. Wortmann, *J. Am. Chem. Soc.* **2002**, *124*, 9431; (b) A. Lohr, M. Grüne, F. Würthner, *Chem. Eur. J.* **2009**, *15*, 3691; (c) U. Rösch, S. Yao, R. Wortmann, F. Würthner, *Angew. Chem. Int. Ed.* **2006**, *45*, 7026.

[9] (a) F. Würthner, S. Yao, U. Beginn, *Angew. Chem. Int. Ed.* **2003**, *42*, 3247; (b) F. Würthner, T. E. Kaiser, C. R. Saha-Möller, *Angew. Chem. Int. Ed.* **2011**, *50*, 3376.

[10] Prof. Frank Würthner, Marcel Gsänger and Hannah Bürckstümmer, Uni. Würzburg, Würzburg, Germany. Personal communication, **2010**.

[11] Prof. Frank Würthner and Dr. Matthias Stolte, Uni. Würzburg, Würzburg, Germany. Personal communication, **2010**.

[12] Molecular dipole moments were calculated by AM1 method using MOPAC in Cerius^2-program-package (v. 4.2). The molecular geometries were taken as found from the crystal structures.

[13] A. V. Kulinich, A. A. Ishchenko, S. V. Shishkina, I. S. Konovalova, O. V. Shishkin, *J. Struct. Chem.* **2007**, *48*, 971; CSD reference code: KIYTOC.

[14] W. Leng, F. Würthner, A. M. Kelley, *J. Phys. Chem. A.* **2005**, *109*, 1570

[15] S. Beckmann, K.-H. Etzbach, P. Krämer, K. Lukaszuk, R. Matschiner, A. J. Schmidt, P. Schuhmacher, R. Send, G. Seybold, R. Wortmann, F. Würthner, *Adv. Mater.* **1999**, *11*, 536.

[16] F. Würthner, C. Thalacker, R. Matschiner, K. Lukaszuk, R. Wortmann, *Chem. Commun.* **1998**, 1739.

[17] F. Würthner, R. Wortmann, R. Matschiner, K. Lukaszuk, K. Meerholz, Y. Denardin, R. Bittner, C. Bräuchle, R. Sens, *Angew. Chem. Int. Ed. Engl.* **1997**, *36*, 2765.

[18] F. Würthner, S. Yao, R. Wortmann, *Polym. Mater. Sci. Eng.* **2000**, *83*, 183.

[19] L. Lu, R. J. Lachicotte, T. L. Penner, J. Perlstein, D. G. Whitten, *J. Am. Chem. Soc.* **1999**, *121*, 8146; CSD reference code: DOMZIO.

[20] C. P. Brock, J. D. Dunitz, *Chem. Mater.* **1994**, *6*, 1118.

[21] Structures were retrieved from Cambridge crystal database (v. 5.32) using ConQuest-program (v. 1.13).

[22] D. J. A. Ridder, D. Heijdenrijk, H. Schenk, R. A. Dommisse, G. L. Lemiere, J. A. Lepoivre, F. A. Alderweireldt, *Acta Cryst. C* **1990**, *46*, 2197.

[23] Y. Lia, B. E. Eichinger, K. A. Firestone, M. Haller, J. Luo, W. Kaminsky, J. B. Benedict, P. J. Reid, A. K.-Y. Jen, L. R. Dalton, B. H. Robinson, *J. Am. Chem. Soc.* **2005**, *127*, 2758.

[24] Center of mass of MC dyes was calculated in Mercury 2.4 by including only the π-conjugated atoms.

[25] Intermolecular potential energies were calculated in Mercury 2.4 by using universal force field: $V = A \times \exp(-BR_{ij}) - CR_{ij}^{-6}$; (a) A. Gavezzotti, *Acc. Chem. Res.* **1994**, *27*, 309; (b) A. Gavezzotti, G. Filippini, *J. Phys. Chem.* **1994**, *98*, 4831.

[26] W. Leng, F. Würthner, A. M. Kelley, *J. Phys. Chem. A* **2005**, *109*, 1570.

[27] G. R. Desiraju, T. Steiner, *The Weak Hydrogen Bond*, Oxford University Press, Oxford UK, **1999**.

[28] T. Neuheuser, B. A. Hess, C. Reutel, E. Webber, *J. Phys. Chem.* **1994**, *98*, 6459.

[29] (a) E. Nauha, A. Ojala, M. Nissinen, H. Saxell, *CrystEngComm* **2011**, *13*, 4956. (b) A. J. C. Cabeza, G. M. Day, W. D. S. Motherwell, W. Jones, *Cryst. Growth Des.* **2007**, *7*, 100.

[30] Kitaigorodskii-type packing indices were calculated in Platon-program-package (v. 1.14) by using VOID. The hydrogen atom positions were idealized in Mercury 2.4 before calculating the packing indices.

[31] SHELXTL-program-package, v. 6.14, Bruker-AXS; G. M. Sheldrick, *Acta Cryst.* **2008**, *A64*, 112.

Chapter 5

Parallel Bulk Heterojunction Solar Cell by Electrostatically Driven Phase Separation

Abstract: In this study, a double-donor concept is used to improve the performance of thermally evaporated merocyanine(s)/C_{60} bulk heterojunction (BHJ) solar cells. It is shown that the co-evaporation of two merocyanine dyes with absorption bands at ~ 500 nm (SW dye) and ~ 650 nm (LW dye), respectively, together with C_{60} fullerene results in an improvement of open-circuit voltage (V_{OC}), short-circuit current (J_{SC}) as well as total power conversion efficiency (PCE) compared to the best single-donor cell. The enhancement of J_{SC} is attributed to a higher photon harvesting efficiency of the mixed-donor devices due to a better spectral coverage. The V_{OC} of the double-donor devices is observed to be linearly dependent on the mixing ratio of the dyes. This is explained by the formation of three distinct subphases (SW, LW, and C_{60}) where the dyes are able to work independently, similarly to conventional parallel connected tandem solar cells. Electro-optical absorption (EOA) spectroscopy shows that the dipole moments of the applied dyes are very different which is assumed to provide the driving force for the phase separation between the two donor dyes by electrostatic interactions.[a]

[a] The electro-optical measurements were performed at University of Würzburg by Dr. Mathias Stolte. The synthetical work was carried out at University of Würzburg by Hannah Bürckstümmer. This chapter has previously been published in *Adv. Mater.* **2011**, DOI: 10.1002/adma.201103167.

5.1 Introduction

Organic photovoltaics (OPV) is a rapidly expanding research area that promises to become a cost efficient method for the production of renewable energy. Despite the significant progress in recent years, further work is still required to reach the 10% power conversion efficiency (PCE) which is generally considered as minimum requirement to compete with silicon and other inorganic thin film technologies.[1] Among the main limitations of performance of organic solar cells are narrow absorption band widths and low charge carrier mobilities of π-conjugated organic materials.[2] Both limitations appear to be particularly critical for organic semiconductor materials based on low-molecular-weight colorants that are utilized for the dual role of light harvesting and hole transport in bulk or bilayer heterojunction solar cells. Thus, it is well-known that the highest absorption strength can be achieved by cyanine-type chromophores, although they also exhibit the most narrow absorption widths.[3] A possible approach to broaden the optical absorption region of the devices without increasing the active layer thickness is to blend multiple donor components with different absorption regimes, together with an acceptor component, in a bulk-heterojunction (BHJ) film. Recently, this simple method has been successfully applied to improve the photon harvesting of solution-processed solar cells by adding small dye molecules in the poly(3-hexylthiophene) (P3HT)/fullerene matrix[4] or by blending several small donor molecules with fullerene derivatives.[5] In the reported cases the overall performance was limited and the improvement in performances was attributed to an increase in short-circuit current (J_{SC}) due to a broader absorption range.

Merocyanine dyes have recently been introduced as a new class of p-type semiconductor molecules in small-molecule-based organic BHJ solar cells, showing remarkable efficiencies in both solution- and vapor-processed cells.[6,7] Independently, Jen and coworkers have demonstrated similarly efficient merocyanine-based polymeric BHJ cells.[8] Interesting perspectives may arise from these initial studies because merocyanines constitute a huge class of synthetically easily accessible and intensively absorbing colorants (with molar absorption coefficients ε often exceeding 1×10^5 M^{-1} cm^{-1}) that offer multiple possibilities for the adjustment of the absorption properties and energy levels.

Herein, we report for the first time a parallel-BHJ cell that forms in situ driven by dipolar intermolecular forces when mixing two merocyanine dyes as double-donor with a C_{60} acceptor. The applied dyes have complementary absorption, which enables the harvesting of photons over a wider spectral range at a given active layer thickness. By optimizing the ratio of the two donor components and the thickness of the active layer, the power conversion efficiency (PCE) of the blend donor cells was considerably higher than either of the reference devices based on the individual dyes only. This synergetic effect is attributed to more efficient photon harvesting efficiency of the mixed donor cells compared to either of the single donor devices.

5.2 Results and Discussion

To study the effect of a mixed donor system, thermally evaporated small-molecule solar cells in single and multiple donor combinations with a C_{60} acceptor have been investigated. The short-wavelength dye (SW) absorbs at λ_{max} = 492 nm, while the long-wavelength dye (LW) features λ_{max} = 624 nm (both in dichloromethane). We define the ratio of the two dyes as

$$\mathbf{X} = \%\text{wt LW} / (\%\text{wt SW} + \%\text{wt LW}). \quad (1)$$

Thus, $\mathbf{X} = 0$ for SW-only, $\mathbf{X} = 1$ for LW-only, and $0 < \mathbf{X} < 1$ in mixed devices.

The device architecture and molecular structures are depicted in Figure 1. The identical layered device architecture was employed in all devices, starting with indium tin oxide (ITO)-coated glass substrate, on which a 4 nm MoO_3 layer was evaporated. The function of the MoO_3 layer is to improve the hole extraction from the organic layer and to shield the successive organic layer from the ITO.[9] Following the MoO_3 film, the active layer consisting of C_{60} as acceptor and either of the dyes or a mixture of these dyes in different weight ratios as donors, were co-evaporated. An additional C_{60} layer (25 nm) was deposited on top of the active layer to provide efficient electron transport and optimize the optical properties of the cells.[10] A 4,7-diphenyl-1,10-phenanthroline (Bphen) hole blocking layer (5 nm) and the silver cathode were evaporated after the C_{60} layer. The active layer thickness was generally fixed to 39 nm as it was observed to give the best results in both single and multiple donor devices. The only exception was the

SW-only device which gave the best results at active layer thickness of 26 nm. In all devices, the donor(s)/C_{60} ratio was fixed to 40:60 (weight ratio) as it was found to give the best results in the single donor cells and was not separately optimized for the blend dye devices. Figure 1b shows the positions of the energy levels of the used materials.

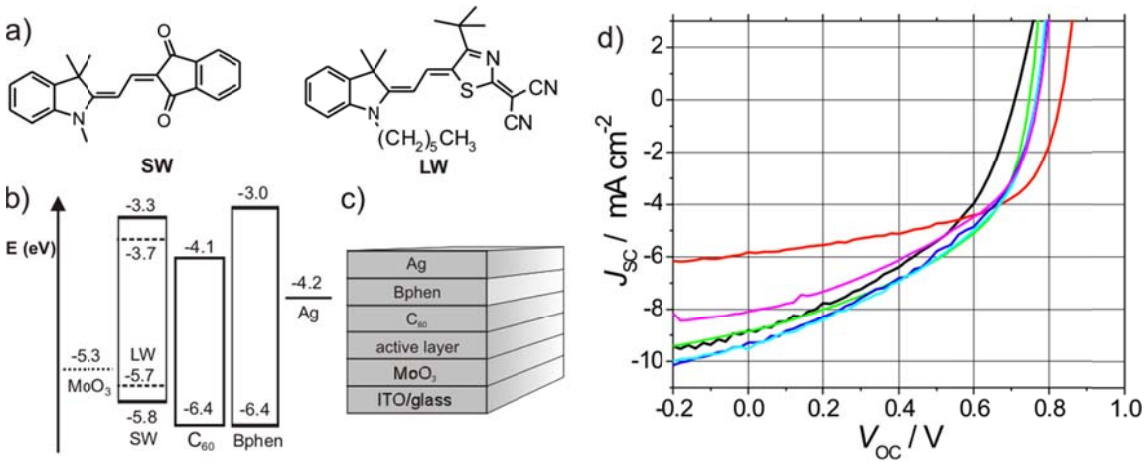

Figure 1. a) Molecular structures of the SW and LW dyes, (b) energy levels and (c) layer structure of the devices. The HOMO energy levels of LW and SW dyes were determined by cyclic voltammetry and the LUMO levels were estimated from the optical band gaps (E_g). The energy levels of C_{60}, Bphen and MoO_3 were taken from literature.[9] d) *J-V* characteristics of the **X** = 0 (red) and **X** = 1 (black) devices as well as of the cells with different SW/LW dye ratios **X** = 0.25 (purple), **X** = 0.5 (blue), **X** = 0.66 (light blue), and **X** = 0.8 (green).

Figure 1d depicts *J-V* characteristics of the single and mix donor devices whilst the dependence of the key cell parameters on the SW/LW dye ratio in the active layer are shown in Figure 2. It is generally accepted that the open-circuit voltage (V_{OC}) is proportional to the difference of the HOMO level of the donor and the LUMO energy level of the acceptor, respectively.[1] The experimental V_{OC} for SW-only and LW-only devices were 830 mV and 710 mV (ΔV_{OC} = 0.12 V), respectively, which correlates very well with the difference in the HOMO energy levels of these donors (ΔE_{HOMO} = 0.11 eV). The V_{OC} values of the blended-donor cells are found to depend linearly on the dye ratio (Figure 2a).

The short-circuit current (J_{SC}) of the SW dye-only devices (5.8 mA cm^{-2}) was significantly lower than the J_{SC} of the LW-only cells (8.8 mA cm^{-2}). Because of improved photon harvesting the short circuit current of the mix-donor devices was higher than the weighted average of the individual cells in all cases. For mixing ratios of **X** = 0.5 and 0.66 J_{SC} reached ca. 9.5 mA cm^{-2}. To verify the J_{SC} values, they were

derived independently by multiplying the EQE (External Quantum Efficiency) spectra (Figure 3a) with the AM 1.5 solar spectrum and integrating the result over the full wavelength range. The calculated J_{SC} values are in excellent agreement with the current-voltage (*J-V*) measurements (see Figure 2b, stars).

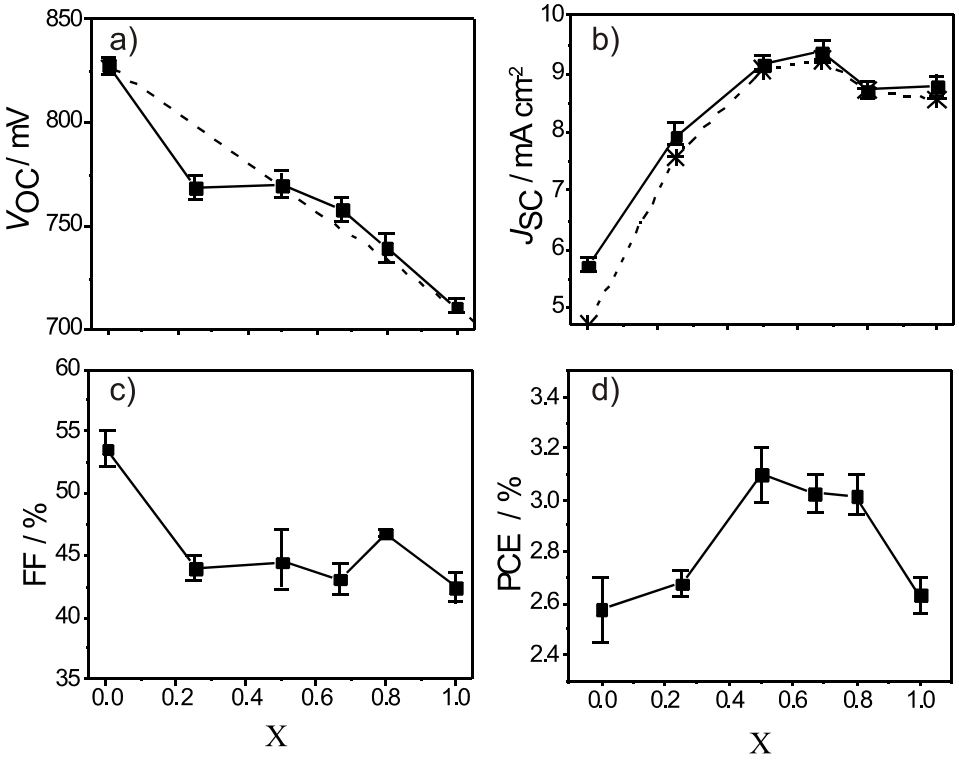

Figure 2. Dependence of V_{OC}, J_{SC}, FF, and PCE on the LW dye content. The dashed line in a) is a linear fit to the data. In figure b) is also shown the J_{SC} values calculated from the EQEs (stars). The C_{60} content was 60 %wt in all cases. The active-layer thickness was 39 nm in all cases.

The fill factor (FF) of the SW-only devices was 55 %, which was the highest of all tested solar cells whereas the LW-dye-only devices gave the lowest (42%) value. In all other cases, values between 43 and 47% were obtained. Overall, the blend devices with **X** = 0.66 show the highest PCE of 3.2%, which is a significant improvement over the single-donor cells (2.6 and 2.7%, respectively; see Fig. 2). In the highest PCE devices, although V_{OC} and FF of blended devices were always lower or in between the values obtained from single cells, the increase in J_{SC} was enough to overcompensate the loss from V_{OC} and FF.

In order to understand the reason for higher J_{SC}, in-depth investigations on the EQE of the devices were performed. The EQE spectra of the SW and LW dye-only cells exhibit maxima at 495 (59%) and 655 (64%) nm, respectively, whilst blend devices

with different weight ratios of the dyes show features with two maxima (Figure 3a). Additionally, the EQE of the LW component (at 655 nm) is always larger than the value expected from the weighted average at all mixing ratios. For example, the device **X** = 0.66 gave EQE of 59%, which is > 90% of the value of the LW-only device, although, the LW dye content was only 66%.

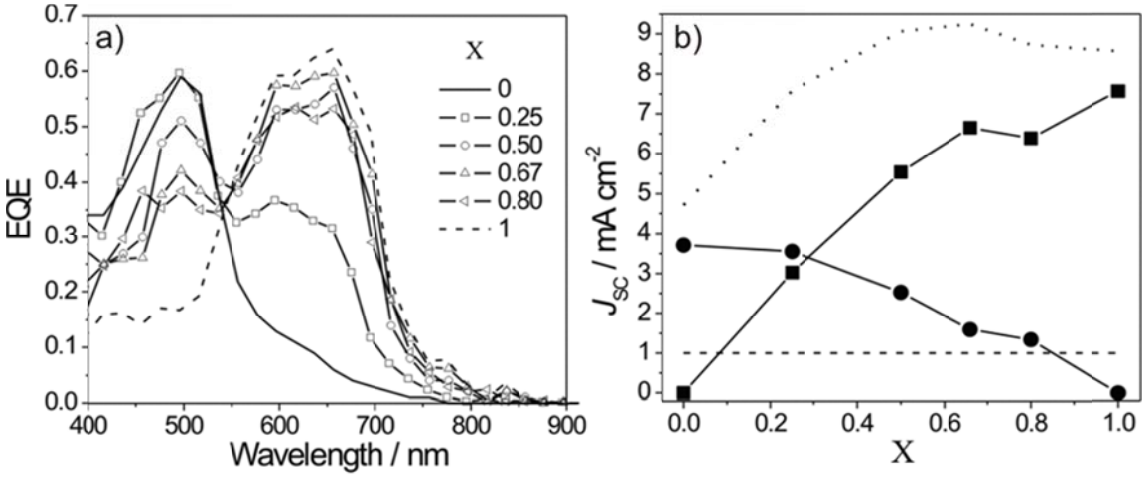

Figure 3. a) EQE spectra of the single (solid and dotted line) and blend donor solar cells (symbols and lines) with different LW dye content. b) Estimated contribution of the SW (circles) and LW (squares) components to J_{SC}. The dashed line shows the estimated contribution of C_{60} and the total calculated J_{SC} is illustrated by the dotted line. The active-layer thickness was 39 nm in all cases.

In addition, the contribution of the individual components to total J_{SC} was estimated from the EQE spectra (Figure 3b). The short-circuit current of the LW donor ($J_{SC,LW}$) is approximated by comparing the EQE of the LW-only (**X** = 1) devices with the EQEs of the mixed-donor cells **X** = y (y = 0.25, 0.5, 0.66, or 0.8) at spectral region (680 nm) where the contribution of the SW component is assumed to be minor. Thus, the $J_{SC,LW}$ at different mixing ratios **X** = y is given by

$$J_{SC,LW}(\mathbf{X} = y) = [J_{SC,calc}(\mathbf{X} = 1) - J_{SC,C60}] \times [EQE_{680}(\mathbf{X} = y) / EQE_{680}(\mathbf{X} = 1)]. \quad (2)$$

Here, $J_{SC,calc}$ is the short-circuit current calculated from the EQE spectrum of the **X** = 1 cell and $J_{SC,C60}$ is the contribution of the C_{60} component which is approximated to be constant (1 mA cm^{-2}) in all devices. The contribution of the SW dye ($J_{SC,SW}$) is calculated by

$$J_{SC,SW}(\mathbf{X} = y) = [J_{SC,calc}(\mathbf{X} = y) - J_{SC,C60}] - J_{SC,LW}(\mathbf{X} = y). \quad (3)$$

The plot in Fig. 3b shows, that the short-circuit current of the SW and LW components saturates when the $\mathbf{X} \rightarrow 0$ or $\mathbf{X} \rightarrow 1$, respectively.

In order to understand the high EQE of the LW component, absorption spectra of the cells **X** = 0, 0.66, and 1 with the active layer thickness of 39 nm were recorded and the corresponding Internal Quantum Efficiencies (IQE) were calculated by dividing the EQE spectra with the corresponding absorption spectra (Figure 4b). In the absorption region of the LW component ($\lambda \sim 660$ nm), the IQE spectra of the cells **X** = 1 and **X** = 0.66 are similar (~ 80%) whereas the latter device shows clearly lower (~ 50%) efficiency compared to the **X** = 0 cell at the photon harvesting region of the SW dye ($\lambda \sim$ 500 nm).

The different IQEs of the cells **X** = 0 and 0.66 are expected considering the fill factors which were 55% and 43%, respectively. However, the similar IQEs of the LW components (devices **X** = 1 and **X** = 0.66) show that the main reason for the higher J_{SC} is not due to improved electric properties of the blend devices compared to single donor cells, but rather the increased photon absorption of the blend devices as can be seen from the corresponding absorption spectra (Figure 4b). At 660 nm, the **X** = 1 device harvest only 10% more of the incident light compared to the **X** = 0.66 cell, although the increase of the dye content is 34%. This is due to the saturation of the absorption already at the active layer thickness of 39 nm (compare also Figure 3b). The saturation is mainly attributed to the high absorption coefficient α of the LW:C_{60} (40:60 %wt) active layer [$\alpha_{LW:C60}$ (655 nm) = 0.75×10^5 cm^{-1}] as well as to the reflective losses in the cells (Figure 4a). Similarly, owing to the very high absorption coefficient of the SW:C_{60} (40:60 %wt) layer ($\alpha_{SW:C60}$ (505 nm) = 1.0×10^5 cm^{-1}), also the SW component of the **X** = 0.66 cell is closer to the SW dye-only device than would be expected from the simple mixing ratio. Therefore, the small losses in the total absorbance at the absorption maxima of the mix donor devices are overcompensated by the broader absorption bands, leading to higher J_{SC} of the mix donor devices compared to the single donor BHJ cells.

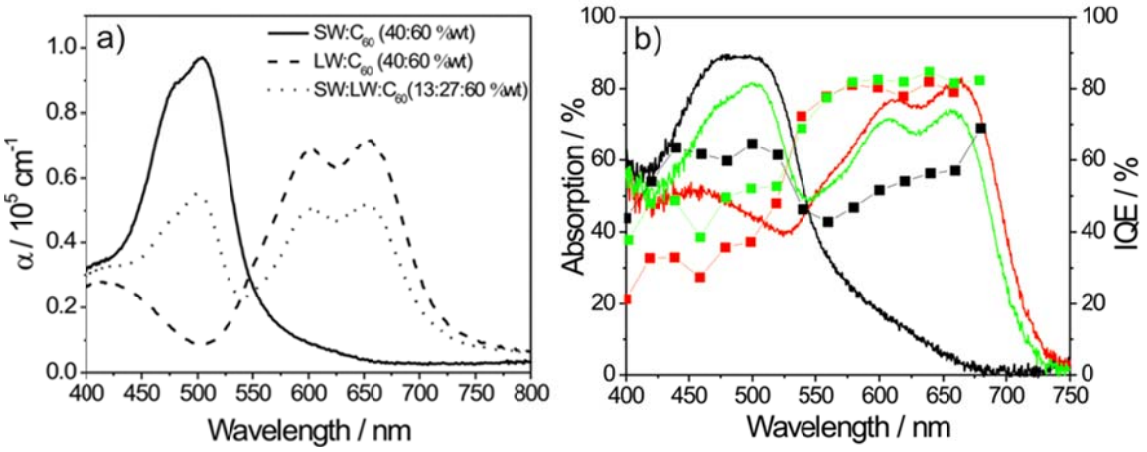

Figure 4. a) Absorption spectral of dye(s):C_{60} neat films. b) Absorption (solid lines, left axis) and IQE (lines and symbols, right axis) of the cells with the mixing ratios of **X** = 0 (black), 0.66 (green), and 1 (red). The active-layer thickness was 39 nm in all cases.

It is commonly assumed that in C_{60}/dye BHJ blends the C_{60} subphase separates due to the unusual globular shape of this molecule,[11] whilst the donor sub-phase consists of an intimate mixture of the two dyes that are both of similar shape, i.e. bearing a flat π-system. Previous examples of multiple-donor BHJ cells[4,5] fall into this category and the devices can be considered "normal" BHJ cells. In an intimate mixture of two donors, the hole transport should mainly take place on the transport manifold with the higher HOMO level. Hence, it is expected that V_{OC} is close to the V_{OC} of the single-dye device using the donor featuring the higher lying HOMO (here LW). This clearly contradicts our experimental findings of a linear dependence.

Alternatively, we propose that there could be two donor subphases (SW-rich and LW-rich) and a common acceptor subphase (C_{60}-rich); this case would lead to two formally "parallel" cells with common contacts, although they are intermingled due to the common C_{60} phase. According to Kirchhoff's law the open circuit voltage of parallel connected solar cells is defined when the net current of the subcells in the external circuit is zero. It is shown, that the net current is dependent on individual subcells' contribution to the photocurrent as well as steepness of the *J-V* characteristics of the subcells. Thus, a dependence of V_{OC} on the mixing ratio is expected, as seen experimentally. We will refer to this as Parallel-BHJ (P-BHJ) concept from now on.

Although three-phase systems are well-known for tri-block copolymers,[12] such a possibility has never been taken into account for mixtures of small molecules. It is intriguing, however, that such a situation could indeed apply for merocyanine dyes SW and LW which are expected to have considerably different dipole moments. It has

recently been shown experimentally[13] and theoretically[14] that highly dipolar merocyanines pack as centrosymmetric dimers with antiparallel dipole orientation for which the largest contribution to the cohesive energy arises from electrostatic interactions whilst for less dipolar π-systems attraction by dispersion forces prevails. The antiparallel stacking of the dyes is supported by the thin film absorption spectra of both SW and LW donor dyes depicted in Figure 5a. The figure shows the solution (in dichloromethane (DCM)) and thin film (30 nm) absorption spectra of the SW and LW dyes, respectively. The solution spectrum of the SW dye shows a narrow absorption band with a maximum at 492 nm whilst the corresponding thin film absorption spectrum features a broader aggregate band with two maxima at 479 nm and 514 nm, respectively. Likewise, specific aggregate bands arise for the thin film of the LW dye. Here the absorption spectrum in DCM solution shows a maximum at 624 nm with two vibronic progressions at higher energies.[13] Compared to the solution spectrum the intensity of the longest wavelength peak decreases and a new maximum appears at a shorter wavelength (λ_{max} = 593 nm) in the thin film. In previous studies, appearance of a hypsochromically shifted peak has been attributed to antiparallel arrangement (H-aggregate) of the chromophores.[13] Importantly, for a co-deposited film of the dyes (SW:LW 40:60 %wt) the specific spectral features of the individual aggregate bands of both dyes are clearly visible (Figure 5b). Because these aggregate bands originate from excitonic coupling of the transition dipole moments they are unambiguous signatures of the formation of homo aggregates. For hetero aggregates excitonic coupling would be negligible owing to the different excitation energies of the involved optical transitions. Hence, we can conclude that the mixed film is composed of homo-aggregated dye manifolds, i.e. two separated dye phases, as expected from the large differences in the dipole-dipole interaction energies between the homo and hetero dimers.

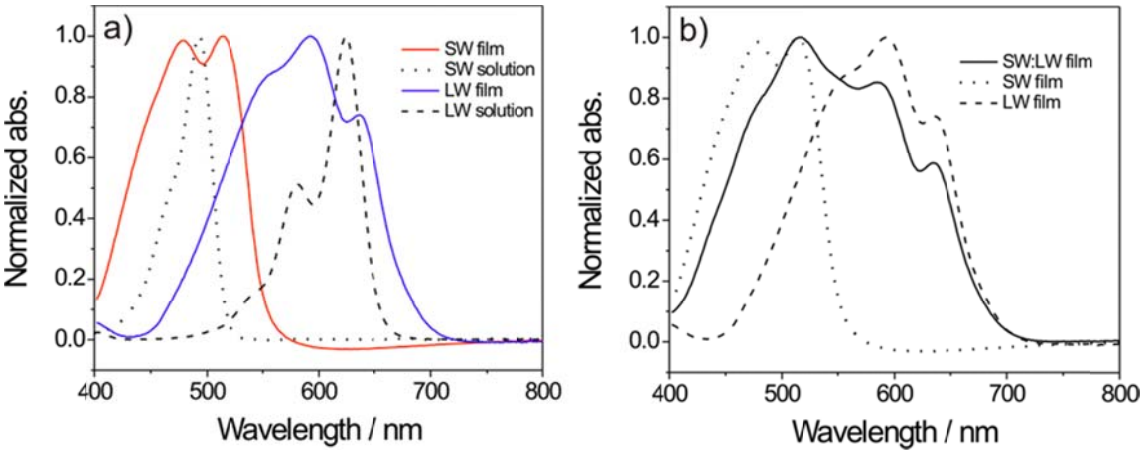

Figure 5. a) Solution and thin film absorption spectra of the pure SW-dyes and LW-dyes, respectively. b) Thin film absorption spectra of the SW-dye, LW-dye, as well as mixture of the dyes. The spectra were recorded with an Ocean Optics HR2000+ spectrometer in a transmission mode and using a Xe lamp as the light source.

The HOMO energy level offset of the donors (ΔE_{HOMO}) is 0.11 eV which is significantly larger than the available thermal energy at room temperature (0.025 eV). Therefore, in an intimate mixture of the dyes, the HOMOs of the LW donors are hole trap sites. In such a case, the charge trapping is expected to severely hamper the hole mobility as well as the performance of mixed-donor devices compared to the single-donor cells.[15] However, our mix dye devices do not show indication of severe charge trapping, and as a matter of fact, the **X** = 0.5 and **X** = 0.66 cells feature the highest PCE of the cells. To asses the effect of the dye mixing on the charge transport properties of the devices, three hole-only devices with the active layer components of **X** = 0, **X** = 0.5, and **X** = 1 were fabricated and their hole mobilities were measured employing space-charge-limited-current (SCLC) method.[16] As expected from the solar cell results, mixing the dyes does not have negative impact on the hole transport properties of the cells. On the contrary, the **X** = 0.5 cells show a slightly higher hole mobility ($\mu_0 = 1.6 \times 10^{-7}$ cm^2 / V s) compared to the X = 0 and X = 1 devices which gave $\mu_0 = 1.3 \times 10^{-7}$ cm^2 / V s and $\mu_0 = 1.2 \times 10^{-7}$ cm^2 / V s, respectively (Figure 6). Thus, the results support our assumption of SW-rich and LW-rich subphases in the mix donor devices which ensure efficient collection of the holes at the anode.

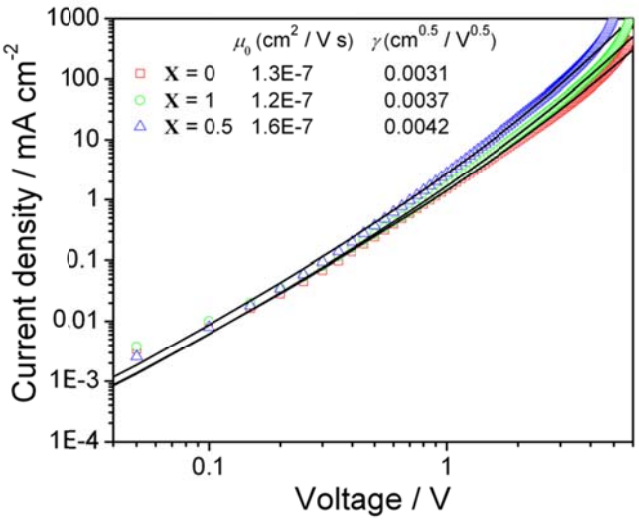

Figure 6. *J-V* characteristics of **X** = 0, 0.5, and 1 hole-only devices. Zero-field hole mobilities (μ_0) and field activation parameters (γ) of the devices were obtained by fitting the *J-V* curves to the SCLC model (back lines).

To rationalize the presence of a three-phase system from a thermodynamic point of view, we have determined the dipole moments μ_g and the zwitterionic character c^2 (i.e. the prefactor for the mixing of the wavefunctions of the neutral and zwitterionic resonance forms[3b]) of the two merocyanines applied in this study. Our results indeed confirm our assumption. Thus, the LW dye is by far more dipolar (μ_g = 13.0 D) than the SW dye (μ_g = 4.0 D) and also slightly more zwitterionic. Because the Coulomb attraction between two neighboring dipolar dyes A and B scales at a presumably constant van der Waals contact distance of 3.5 Å (π-π-contact) with the product of their dipole moment $\boldsymbol{\mu}_g(A) \cdot \boldsymbol{\mu}_g(B)$, there should be a clear preference for the formation of homo aggregates (LW-LW, leaving SW-SW behind) compared to hetero aggregates (LW-SW) which might ultimately lead to the formation of two distinct dye phases (Figure 7). In the simplest approximation where dyes assemble in an antiparallel arrangement with a distance of 3.5 Å without any lateral, transversal or rotational displacement (as shown for some related merocyanine dyes[13,17]) the homo dimerization of dye LW gives a roughly ten times higher stabilization energy than in case of merocyanine SW (Homo-SW: -22 kJ mol^{-1}; Homo-LW: -236 kJ mol^{-1}). The hetero dimer (-72 kJ mol^{-1}) yields about a third of the interaction energy of the homo dimer of merocyanine LW and has additionally a non-negligible dipole moment which could affect the further packing of dyes in the solid state. This together with our circumstantial evidence of the voltage dependence, thin film absorption of SW/LW mixtures, and hole mobility data suggests the presence of three subphases in our devices.

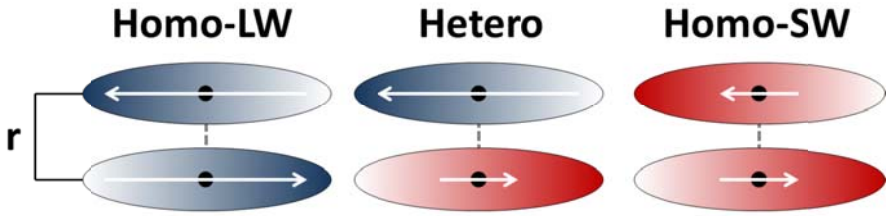

μ_g(Homo-dimer) ≈ 0 D	μ_g(Hetero-dimer) > 0 D	μ_g(Homo-dimer) ≈ 0 D
−236 kJ mol^{-1}	−72 kJ mol^{-1}	−22 kJ mol^{-1}

Figure 7. Structure model for the calculation of the dipole-dipole interaction energies of two dyes at distance **r** and an estimation of the dipole moments (μ_g) of the homo/hetero-dimers. Dipole moments are depicted as white arrows.

5.3 Conclusions

In conclusion, a simple multiple-donor concept has been introduced to improve the total power conversion efficiency of vacuum-processed small-molecule-based-BHJ solar cells. The dependence of V_{OC} of the blend donor cells on the ratio of the two donors, thin film absorption spectra of SW/LW mixtures and hole mobilities hint on formation of three distinct phases, where both donors are able to work independently. The phase separation was rationalized by the electrostatic interaction energies which are found to be very different between the two donor dyes applied in this work. The improvement of the PCE is mainly attributed to increased J_{SC} and V_{OC} of the blend donor devices compared to the single donor cells. Improvement in J_{SC} conflicts with the simple P-BHJ device model, where the J_{SC} is expected to scale with the relative dye content. However, due to the high absorption strength of the dyes, the absorption efficiency of the single-donor cells showed clear saturation at optimal active layer thickness. Thus, blending the dyes enabled broader spectral coverage, but still comparable absorption efficiencies at the maxima as in single donor cells.

5.4 Experimental Section

Device fabrication

Solar cells were thermally evaporated in a high vacuum chamber (Lesker Ltd.) at base pressure of 10^{-6} mbar on pre-structured ITO-covered glass substrates with an active cell area of 4 mm². Prior to device fabrication the substrates where exposed to UV/O_3

treatment for a minimum of 15 min. Identical cell architecture was used for all devices by starting with deposition of a 4 nm MoO_3 layer at a rate of 0.2 Å s^{-1}. After the MoO3 film, the active layer of merocyanine dye(s) and C_{60} was co-evaporated. The evaporation rate of C_{60} was fixed to 1.0 Å s^{-1} in all cells whereas the dye ratio was controlled by varying the rate from 0.20 to 1.0 Å s^{-1}. The final C60 layer (25 nm) was deposited at rate of 1.0 Å s^{-1}. The cathode was fabricated by evaporating first a 4 nm buffer layer of Bphen at a rate of 0.8 Å s^{-1} and then 100 nm thick silver electrode at rate of 4 Å s^{-1}. The current-density-voltage (*J-V*) characteristics of the devices were measured under standard AM 1.5 illumination (100 mW $cm^{-2)}$ in ambient air and controlled by a Keithley 2425 source measurement unit. The mismatch factor was calculated to be very close to unity. Electro-optical absorption (EAO) measurements are described in Ref. 18.

Synthesis of the LW and SW dyes

LW dye (2-{4-tert-Butyl-5-[2-(3,3-dimethyl-1-hexyl-1,3-dihydro-indol-2-ylidene)-ethylidene] -5H-thiazol-2-ylidene}-malononitrile was synthesized by heating a 10 mL Ac_2O solution of 1-n-hexyl-3,3-dimethyl-1,3-dihydro-indol-2-ylidene)-acetaldehyde (1.63 g, 6.0 mmol) and the 2-(4-tert-butyl-5H-thiazol-2-ylidene)-malononitrile (1.23 g, 6.0 mmol) to 90 °C for 60 min. After cooling to room temperature the precipitate was collected, washed with isopropanol, and recrystallized from CH_2Cl_2/n-hexane. **Yield:** 2.06 g (4.5 mmol, 75%), dark blue solid. **Mp** 285–286 °C. **^{1}H NMR** ($CDCl_3$, 400 MHz): δ 8.23 (d, ^{3}J = 13.3 Hz, 1H), 7.35 (m, 2H), 7.21 (m, 1H), 7.01 (d, ^{3}J = 8.0 Hz, 1H), 5.54 (d, ^{3}J = 13.3 Hz, 1H), 3.89 (t, ^{3}J = 7.5 Hz, 2H), 1.80 (m, 2H), 1.68 (s, 6H), 1.54 (s, 9H), 1.45 (m, 2H), 1.36 (m, 4H), 0.92 (t, ^{3}J = 7.1 Hz, 3H). **UV–vis** (CH_2Cl_2): λ_{max} (ε) = 581 (67500), 624 (132500 M^{-1} cm^{-1}). **HRMS** (ESI): calcd for $C_{28}H_{35}N_4S$ $[M+H]^+$: 459.2577, found: 459.2587. **Elemental analysis** (%) **calcd.** for $C_{28}H_{34}N_4S$: C, 73.32; H, 7.47; N, 12.22; S, 6.99. Found: C 73.29; H, 7.52; N, 12.21; S, 6.99.

SW dye (2-[2-(1,3,3-Trimethyl-1,3-dihydro-indol-2-ylidene)-ethylidene]-indan-1,3-dione was synthesized by heating a 1.5 mL Ac_2O solution of 1,3,3-trimethyl-1,3-dihydro-indol-2-ylidene)-acetaldehyde (1.00 g, 5.0 mmol) and the 1,3-indandione (0.73 g, 5.0 mmol) to 90 °C for 60 min. After cooling to room temperature the precipitate was collected, washed with iso-propanol and n-hexane, and recrystallized from acetic anhydride. **Yield**: 1.19 g (3.6 mmol, 72%), red solid. **Mp** 216–218 °C. **^{1}H NMR** (DMSO-d_6, 400 MHz): δ 7.97 (d, ^{3}J = 14.2 Hz, 1H), 7.71 (m, 4H), 7.57 (d,

^{3}J = 7.2 Hz, 1H), 7.39 (m, 2H), 7.30 (d, ^{3}J = 14.2 Hz, 1H), 7.22 (m, 1H), 3.56 (s, 3H), 1.66 (s, 6H). **UV–vis** (CH_2Cl_2): λ_{max} (ε) = 492 (91600 M^{-1} cm^{-1}). **HRMS** (ESI): calcd for $C_{22}H_{20}NO_2$ $[M+H]^+$: 330.1489, found: 330.1477. **Elemental analysis** (%) calcd. for $C_{22}H_{19}NO_2$: C, 80.22; H, 5.81; N, 4.25. Found: C, 80.31; H, 5.76; N, 4.33.

Cyclic voltammetric (CV) measurements

CV was performed on a standard commercial electrochemical analyzer (EC epsilon; BAS Instrument, UK) in a three electrode single-compartment cell under argon. Dichloromethane (HPLC grade) was obtained from J. T. Baker (Mumbai, India) and dried over calcium hydride and degassed prior to use. The supporting electrolyte tetrabutylammonium hexafluorophosphate (TBAHFP) was synthesized according to literature,[19] recrystallized from ethanol/water and dried in high vacuum. The measurements were carried out under exclusion of air and moisture at a concentration of 10^{-4} M with ferrocene as internal standard for the calibration of the potential. Working electrode: Pt disc; reference electrode: Ag/AgCl; auxiliary electrode: Pt wire. From the values of the reversible half wave potentials $E_{1/2}$ (ox) the HOMO levels were calculated according to $E_{HOMO} = -5.15$ eV $-$ e $\times$ $E_{1/2}$ (ox).

UV/Vis absorption measurements

Integrating sphere and reflectance mode were used to measure the UV/vis absorption spectra (OceanOptics HR2000+) of the devices. The neat film spectra were recorded in transmittance mode. A Xe lamp was employed as the light source.

External quantum efficiency

EQE measurements were carried out by illuminating (Xe lamp) the cells with a monochromated (ACTON SpectraPro 2150i) light. Simultaneously, a white background bias light (LEDs) was employed to improve the measurement accuracy. The light intensities were calibrated with a Si-photodiode. The cells' response to the monochromated light was monitored with a PC connected in-house built current-voltage amplifier.

Hole carrier mobility

Employed hole-only devices featured following cell architecture: ITO/MoO_3 (5 nm)/X (50 nm)/MoO_3 (5 nm)/Ag (100 nm) where X is SW:C_{60} (40:60 %wt), LW:C_{60} (40:60 %wt), or SW:LW:C_{60} (20:20:60 %wt). Zero-field hole mobilities (μ_0) of the hole-only devices were extracted from the current-voltage characteristics using field dependent space-charge-limited-current model (SCLC).[16] The approximated relative permittivity (ε_r) of the organic layers was 4.

5.6 References

[1] (a) M. C. Scharber, D. Mühlbacher, M. Koppe, P. Denk, C. Waldauf, A. J. Heeger, C. J. Brabec, *Adv*. *Mater*. **2006**, *18*, 789; (b) M. A. Green, K. Emery, Y. Hishikawa, W. Warta, *Prog*. *Photovolt*: *Res*. *Appl*. **2010**, *18*, 144; c) Y. Liang, Z. Xu, J. Xia, S.-T. Tsai, Y. Wu, G. Li, C. Ray, L. Yu, *Adv*. *Mater*. **2010**, *22*, 135.

[2] (a) K. M. Coakley, M. D. McGehee, *Chem*. *Mater*. **2004**, *16*, 4533; (b) P. W. M. Blom, V. D. Mihailetchi, L. J. A. Koster, D. E. Markov, *Adv*. *Mater*. **2007**, *19*, 1551. (c) F. C. Grozema, L. D. A. Siebbeles, *Internat. Rev. Phys. Chem.* **2008**, *27*, 87.

[3] (a) S. R. Marder, B. Kippelen B, A. K. Y. Jen, N. F. Peyghambarian, *Nature* **1997**, *388*, 845; (b) F. Würthner, R. Wortmann, K. Meerholz, *ChemPhysChem* **2002**, *3*, 17.

[4] (a) S. Honda, H. Ohkita, H. Benten, S. Ito, *Chem. Commun*. **2010**, *35*, 6596; b) Y. A. M. Ismail, T. S. T. Jimbo, *Sol*. *Energy Mater*. *Sol*. *Cells* **2010**, *93*, 1582.

[5] (a) A. Varotto, C.-Y. Nam, I. Radivojevic, J. P. C. Tomé, J. A. S. Cavaleiro, C. T. Black, C. M. Drain, *J. Am. Chem. Soc.* **2010**, *132*, 2552; (b) T. Rousseau, A. Cravino, T. Bura, G. Ulrich, R. Ziessel, J. Roncali, *J*. *Mater*. *Chem*. **2009**, *19*, 2298.

[6] (a) N. M. Kronenberg, M. Deppisch, F. Würthner, H. W. A. Lademann, K. Deing, K. Meerholz, *Chem*. *Commun*. **2008**, 6489; (b) H. Bürckstümmer, N. M. Kronenberg, M. Gsänger, M. Stolte, K. Meerholz, F. Würthner, *J. Mater. Chem*. **2010**, *20*, 240; (c) N. M. Kronenberg, V. Steinmann, H. Bürckstümmer, J. Hwang, D. Hertel, F. Würthner, K. Meerholz, *Adv*. *Mater*. **2010**, *22*, 4193.

[7] For early work on single junction solar cells based on merocyanine dyes, see: D. L. Morel, A. K. Gosh, T. Feng, E. L. Stogryn, P. E. Purwin, R. F. Shaw, C. Fishman, *Appl. Phys. Lett.* **1978**, *32*, 495.

[8] F. Huang, K. S. Chen, H. L. Yip, S. K. Hau, O. Acton, Y. Zhang, J. D. Luo, A. K. Y. Jen, *J. Am. Chem. Soc.* **2009**, *131*, 13886.

[9] (a) M. Kröger, S. Hamwi, J. Meyer, T. Riedl, W. Kowalsky, A. Kahn, *Appl. Phys. Lett.* **2009**, *95*, 123301; (b) Irfan, H. Ding, Y. Gao, D Y. Kim, J. Subbiah, F. So, *Appl. Phys. Lett.* **2010**, *96*, 073304.

[10] B. Maenning, J. Drechsel, D. Gebeyehu, P. Simon, F. Kozlowski, A. Werner, F. Li, S. Grundmann, S. Sonntag, M. Koch, K. Leo, M. Pfeiffer, H. Hoppe, D. Meissner, N. S. Sariciftci, I. Riedel, V. Dyakonov, J. Parisi, *Appl. Phys. A* **2004**, *79*, 1.

[11] J. L. Delgado, P.-A. Bouit, S. Filippone, M. A. Herranz, N. Martín, *Chem. Commun.* **2010**, *46*, 4853.

[12] (a) Y. Miyaki, H. Nagamatsu, M. Iwata, K. Ohkoshi, K. Se, T. Fujimoto, *Macromolecules* **1984**, *17*, 2231; (b) F. Bates, G. Fredrickson, *Physics Today* **1999**, *52*, 32; (c) For the application of block copolymers in organic photovoltaics, see: M. Sommer, S. Huettner, M. Thelakkat, *J. Mater. Chem.* **2010**, *20*, 10788.

[13] F. Würthner, S. Yao, T. Debaerdemaeker, R. Wortmann, *J. Am. Chem. Soc.* **2002**, *124*, 9431.

[14] S. Grimme, T. Schwabe, C. Mück-Lichtenfeld, *Org. Biomol. Chem.* **2007**, *5*, 741.

[15] A. Opitz, J. Wagner, W. Brütting, A. Hinderhofer, F. Schreiber, *Phys. Status Solidi A* **2009**, 1.

[16] P. N. Murgatroyd, *J. Phys. D* **1970**, *3*, 151.

[17] F. Würthner, K. Meerholz, *Chem. Eur. J.* **2010**, *16*, 9366.

[18] A. Ojala, H. Bürckstümmer, M. Stolte, R. Sens, H. Reichelt, P. Erk, J. Hwang, D. Hertel, K. Meerholz, F. Würthner, manuscript in preparation.

[19] C. Reidlinger, R. Dworczak, W. Fabian, H. Junek, *Dyes and Pigments* **1994**, *24*, 185.

Chapter 6

Merocyanine/C_{60} Planar Heterojunction Solar Cells: Effect of Dye Orientation on Exciton Dissociation and Solar Cell Performance

Abstract: In this study we investigate the charge dissociation at the donor/acceptor heterointerface of thermally evaporated planar heterojunction (PHJ) merocyanine/C_{60} organic solar cells. Deposition of the donor material on a heated substrate as well as post-annealing of the complete devices at temperatures above the glass transition temperature of the donor material results in a twofold increase of the fill factor (FF). An analytical model employing an electric field dependent exciton dissociation mechanism reveals that geminate recombination is limiting the performance of as-deposited cells. FT-IR ellipsometry shows that, at temperatures above the glass transition temperature of the donor material, the orientation of the dye molecules in the donor films undergoes changes upon annealing. Based on this finding, the influence of the dye molecules' orientations on the charge transfer (CT) state energies is calculated by quantum mechanical/molecular mechanics (QM/MM) methods. The results of these detailed studies provide new insight into the exciton dissociation process in organic photovoltaic devices, and thus valuable guidelines for designing new donor materials.[a]

[a] Andreas Petersen at BOSCH Stuttgart performed the *J-V* curve simulations. The IRSE measurements were carried out at University of Heidelberg by Dr. Robert Lovrincic, Carl Pölking, and Jens Trollman. The exciton dissociation energy calculations were done at BASF Ludwigshafen by Andreas Fuchs. This chapter has previously been published in *Adv. Funct. Mater.* **2011**, DOI: 10.1002/adfm.201101697.

6.1 Introduction

Progress in the field of organic photovoltaics (OPV) has been rapid in recent years and cell efficiencies approaching 8%[1] have been reported. However, to further increase the efficiency beyond 10%, which is generally considered as the watershed for a wider commercialization of the concept, a deeper understanding of the correlation between molecular level processes and the cell performance is needed.[2] One of the key processes in OPV cells and also the major difference compared to inorganic techniques concerns the formation of free charge carriers. In organic solar cells the absorption of a photon leads to the formation of a strongly bound electron-hole pair, known as an exciton. Because the built-in electric field of the device is insufficient to dissociate the excitons, they have to travel to a heterointerface between donor (D) and acceptor (A) components where the local energy level offset supports the dissociation. According to studies with polymer/fullerene blends, the dissociation of an exciton into free electron/hole pair takes place via an intermediate charge transfer (CT) state (D+/A-) in which the electron and hole are located on the lowest unoccupied molecular orbital (LUMO) of an acceptor molecule and on the highest occupied molecular orbital (HOMO) of the adjacent donor molecule, respectively.[3] At this point, the closely bound electron-hole pair is assumed to experience a strong Coulomb binding and can either dissociate into free charges or geminately recombine back to the ground state.[4] Several studies have identified geminate recombination as one of the main loss mechanism in OPV.[3c,5] It is widely accepted that a sufficient energy offset $\Delta E_{LUMO} = E_{LUMO}^{D} - E_{LUMO}^{A}$ between the LUMO levels of donor and acceptor materials is needed to provide the driving force for the CT-state dissociation.[3a,3b,6] On the other hand, the open circuit voltage V_{OC} of the organic planar and bulk heterojunction solar cells has been shown to be ultimately limited by the HOMO/LUMO energy level offset at the interface of donor and acceptor molecules.[7] Therefore, ΔE_{LUMO} has to be optimized in order to maximize V_{OC} and at the same time provide a sufficient driving force for the CT-state dissociation.

In polymer/fullerene[8] bulk heterojunction (BHJ) devices and planar heterojunction (PHJ) phthalocyanine (Pc)/dicyanovinyl-terthiophene (DCV)[9] and Pc/fullerene[7d] cells, an efficient CT-state dissociation has been observed for an energy offset of ~ 0.4 eV. However, very recently Gong *et al*.[10] demonstrated modest OPV performance with a

poly(3-hexylthiophene)(P3HT)/12-(3,6,-dimethoxy-fluoren-9-ylidene)-12H-dibenzo [b,h] fluorine blend which shows a LUMO level offset of only 0.12 eV.

The current-voltage (*J-V*) characteristics of PHJ solar cells often deviate from an ideal diode behavior which results in low fill factor (FF). This behavior has been attributed mainly to the following reasons: i) imbalanced charge carrier mobilities and a high series resistance,[11] ii) low effective electric field at the heterointerface,[12] and iii) accumulation of charges at the electrodes due to interface trapping.[13] The low FF can be significantly improved by inducing crystallization[12] or doping of the semiconductors[14] and thus improve the transport properties of the devices. Molecular orientation at the heterointerface may also play a significant role in the exciton dissociation process as recently discussed in theoretical studies with pentacene/C_{60}[15] and P3HT/C_{60}[16] interfaces.[17] Additionally, depending on the alignment of the molecules' dipole moment at the heterointerface with respect to the applied field, the charge dissociation might be either supported or hindered.[3e,18]

Interestingly, with highly dipolar merocyanine dyes excellent results have recently been obtained in both solution and vacuum deposited bulk heterojunction (BHJ) solar cells.[19] This was achieved, despite the relatively narrow band gap (~ 2.1 eV), owing to exceptionally high V_{OC} (1.0 V) and J_{SC} values (up to almost 12 mA cm^{-2}), whereas low FF of < 40% for solution-processed and < 50% for vacuum-processed devices pinpoint the drawback that needs to be further analyzed.[19b]

In this study, we investigate PHJ and BHJ merocyanine/C_{60} solar cells deposited by thermal evaporation. Current-voltage (*J-V*) characteristics of as-deposited devices show a strong dependence on the applied voltage. The application of thermal treatment steps during the fabrication process significantly diminishes this voltage dependence. We show that the origin of the low FF of the as-deposited cells is the initially low exciton dissociation efficiency at the D/A heterointerface. It dramatically improves during post-annealing above the glass transition temperature of the merocyanine dye. An ellipsometric analysis reveals that the preferred orientation of the donor molecules undergoes a change upon annealing. Based on this result, two heterointerface models are simulated and their charge transfer (CT) exciton energies are calculated. These results support the experimental observation that the orientation of the dye molecules at the heterointerface has a significant influence on the exciton dissociation efficiency.

6.2 Results and Discussion

6.2.1 Energy Level Diagram

The molecular structures of the employed donor and acceptor materials and the energy level diagram of the PHJ cells are depicted in Figure 1. The HOMO level of ID583 was obtained from a cyclic voltammetric (CV) measurement and the LUMO position was estimated by adding the optical band gap [λ_{max} (as-deposited thin film) = 605 nm] to the HOMO energy. The HOMO and LUMO values of ID583 are -5.81 and -3.76 eV, respectively. A commonly used HOMO value for C_{60} (obtained by ultraviolet photoelectron spectroscopic (UPS) analysis) is -6.4 eV[7c,20] whilst different values for the LUMO level have been proposed.[20a, 21] In this study, a value of -4.1 eV[20b] (obtained by an inverse photoemission spectroscopic method) is assumed as the LUMO level of C_{60}. The energy levels for MoO_3, Bphen, and Ag are taken from literature.[22]

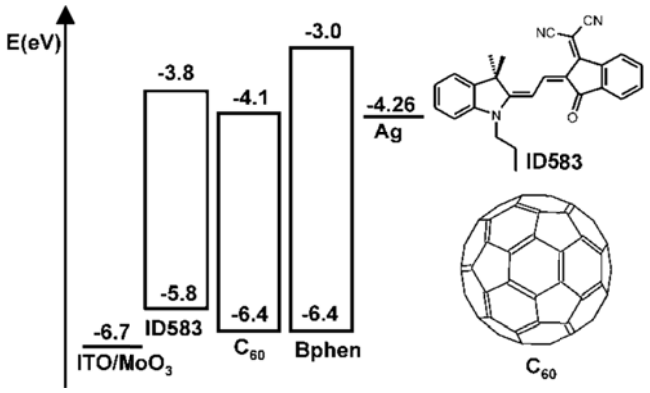

Figure 1. Energy level diagram and molecular structures of the donor (ID583) and acceptor (C_{60}) materials.

6.2.2 Device Characteristics

The device architecture of planar heterojunction (PHJ) cells comprises: ITO/MoO_3 (5 nm)/ID583 (7-28 nm)/C_{60} (35 nm)/Bphen (5 nm)/Ag (100 nm) where the ID583 layer thickness was varied in steps of 7 nm from 7-28 nm. Figure 2a depicts the current-voltage (*J-V*) characteristics of the illuminated PHJ cells with four different donor layer thicknesses. Table 1 summarizes their key device parameters. At negative applied voltage ($V < 0$ V), all cells with different thickness of the donor layer show a very similar and well saturated photocurrent indicating an efficient extraction of free charge carriers. The high leakage current of the 7 nm donor film device at the high reverse voltage region ($V < -0.4$ V) is attributed to the low parallel resistance of the cell. When

biased in forward direction ($V > 0$ V), the cells with the 14, 21, and 28 nm donor layers show a kink after which the photocurrent starts to decline linearly, until just before the open circuit voltage (V_{OC}) condition a second kink appears due to the exponential increase of the diode current. The formation of the kinks adversely affects the performance of the devices featuring a donor layer thickness of 14, 21, and 28 nm. Their FFs have been measured to be 52, 39, and 28%, respectively. The kinks are not observed; however, in the *J-V* curve of the thinnest cells (7 nm donor layer) which yields the highest fill factor (FF) of 69%. Notably, the exceptionally high V_{OC} (1.04-1.07 V) and the short circuit current (J_{SC}) are not affected by the kinks. The best J_{SC} (5.4 mA cm^{-2}) is observed for the cells with a donor layer thicknesses of 21 nm. However, due to the rapidly decreasing FF upon increasing the layer thickness, the cells with the thinnest (7 nm) donor layers give the highest power conversion efficiency (PCE) of 3.2%.

Table 1. Key device characteristics of the PHJ and BHJ devices

Fabrication temp. [°C]	**Cell type**	**Donor layer thickness [nm]**	**J_{SC} [mA cm^{-2}]**	**FF [%]**	**V_{OC} [V]**	**PCE [%]**
25	PHJ	7	4.5	69	1.04	3.2
25	PHJ	14	5.0	52	1.06	2.8
25	PHJ	21	5.4	39	1.07	2.3
25	PHJ	28	5.0	28	1.07	1.5
80[a]	PHJ	21	4.5	70	1.04	3.3
60[b]	PHJ	21	5.2	70	1.06	3.9
25	BHJ	28[c]	7.5	55	1.00	4.1

[a] Post-annealed; [b] Heated substrate; [c] ID583:C_{60} (40:60 weight ratio) layer.

Figure 2b shows *J-V* characteristics of the PHJ cells deposited on a preheated (60 °C) substrate. Interestingly, these devices do not exhibit similar kinks as the cells prepared at 25 °C. Therefore, the FF of the cells with the 14, 21, and 28 nm donor layers is significantly improved to 72, 70, and 64%, respectively. The enhancement of the FF is especially high for the thickest cells that showed a 2.2-fold increase compared to corresponding as-deposited devices. Preheating of the substrate does not influence the V_{OC} (1.04 V) but J_{SC} is slightly reduced, which is attributed to the lower absorption strength of the ID583 films evaporated on a preheated substrate (Figure 3). However, due to the significantly improved FF, the optimal donor layer thickness is increased

from 7 to 21 nm, which yielded a PCE of 3.9%, which is among the highest values achieved to date for vacuum-deposited PHJ devices.[12b,23]

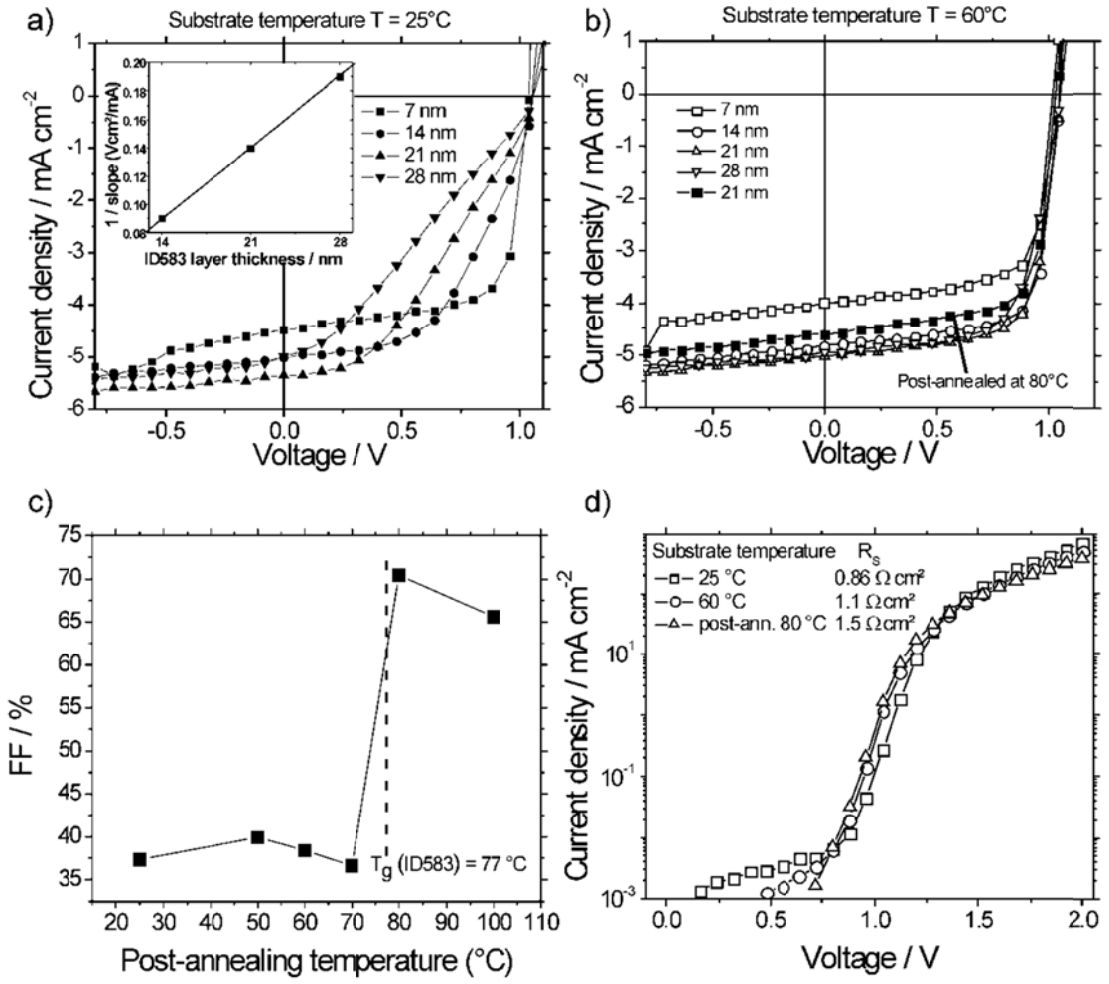

Figure 2. Current-voltage (*J-V*) characteristics of the PHJ cells prepared at substrate temperatures of a) 25 °C and b) 60 °C with four different ID583 layer thicknesses. c) Dependence of the FF of PHJ devices with a 21 nm thick donor layer on the post-annealing temperature. The glass-transition temperature (T_g) of ID583 is illustrated by the dashed line. The solid lines are to guide the eye. d) Forward dark *J-V* characteristics of the PHJ cells (21 nm donor film) after different heat treatments. Series resistance (R_S) is estimated by the slope (dV/dJ) at voltage range close to V = 2 V. Inset: inverse of the slopes (linear incline between the kinks) for the cells with 14, 21, and 28 nm thick donor layers. The solid black line represents a linear fit.

Additionally, completely manufactured PHJ cells with a 21 nm thick donor layer were tempered on a hot plate at 50, 60, 70, 80, and 100 °C for 5 min. Interestingly, post-annealing of the cells at temperatures of 50, 60 and 70 °C has a negligible or even slightly negative influence on cell performance while annealing the cells at 80 °C almost doubles the FF from 37 to 70% (Figure 2c). The reason for the significantly

improved FF is the disappearance of the kinks in the *J-V* characteristics (Figure. 2b). The V_{OC} of the post-annealed (80 °C) devices is 1.04 V but due to a reduced J_{SC} (4.5 mA cm^{-2}), PCE (3.3%) remained below the value obtained on a preheated substrate. Post-annealing of ID583 neat films at 80 °C reduces the absorption strength and shifts the maximum to slightly smaller wavelength (λ_{max} = 595 nm) compared to the as-deposited film (λ_{max} = 605 nm) (Figure 3). The decreased J_{SC} of the post-annealed devices is mainly attributed to the reduced absorption strength. However, possible changes in the thermally instable Bphen layer (T_g = 62 °C)[24] or the exciton diffusion length of the ID583 layer cannot be excluded. Increasing the temperature to 100 °C does not further improve the device performance; instead a small decline was observed in all cell parameters compared to post-annealing at 80 °C (the results are not shown).

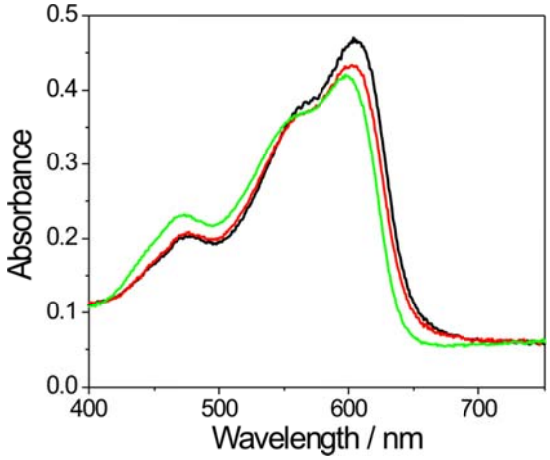

Figure 3. Absorbance spectra of ID583 neat films evaporated on a preheated substrate at 25 °C (black) and 60 °C (red) or post-annealed at 80 °C for 5 min (green).

6.2.3 Dye and Film Properties

In order to understand the behavior of the PHJ devices, especially the sudden improvement of the FFs after post-annealing at 80 °C, we applied different analytical methods. First, the thermal properties of a ID583 powder sample were analyzed by differential scanning calorimetric (DSC) method (Figure 4). Heating of an amorphous sample of ID583 (prepared by fast cooling from the melt) reveals an endothermic step in the base line at 77 °C which is attributed to the glass transition temperature (T_g) of the material. Additionally, an exothermic crystallization peak and endothermic melting characteristics have been observed at 141 and 221 °C, respectively. Hence the T_g is observed at the same temperature region where the post-annealing significantly improves the FF of the PHJ devices (see Fig. 2c).

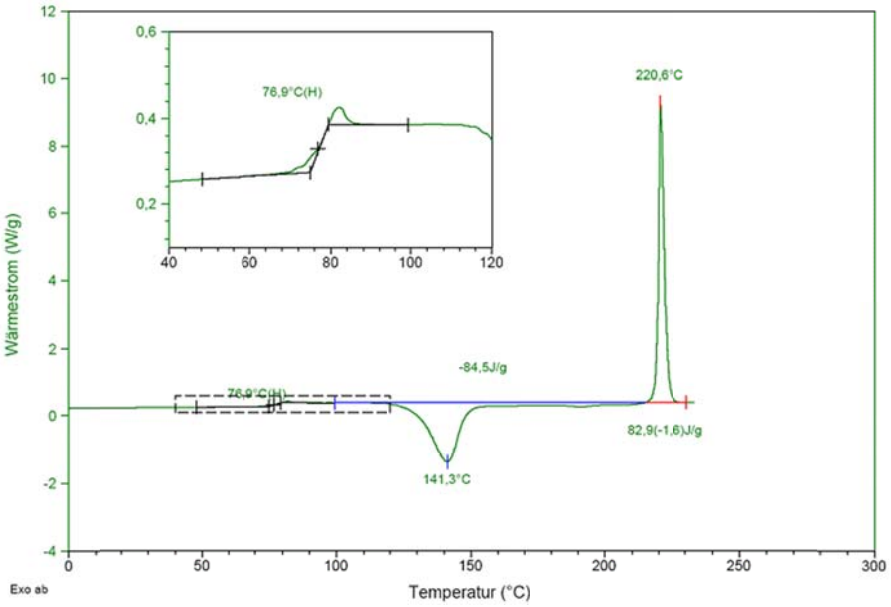

Figure 4. Differential scanning calorimetry profile of ID583. The green curve shows the result of the second heating cycle. Inset: Endothermic incline at 77 °C is attributed to the glass transition point.

Changes of the film morphology were investigated by atomic force microscopy (AFM). Two samples with 21 nm ID583 neat films were evaporated on ITO/MoO_3 (5 nm) covered glass slides at substrate temperatures of 25 and 60 °C. The ID583 films deposited at 25 °C show a root-mean-square (RMS) roughness of 0.84 nm whereas the films deposited at 60 °C have a significantly lower roughness of 0.62 nm (Figure 5). Additionally, X-ray powder diffraction (XRPD) patterns were recorded for ID583 neat films prepared at 25 and 60 °C or post-annealed at 80 °C. No coherent reflections arising from the ID583 layers have been observed (the XRPD graphs are not shown). This, together with the AFM results (decreasing roughness at elevated deposition temperatures), suggests that the films are X-ray amorphous.

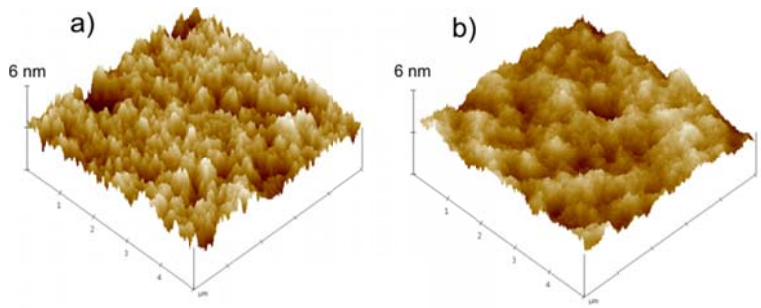

Figure 5. AFM pictures of ID583 neat films deposited at substrate temperatures of a) 25 °C and b) 60 °C.

In a recent study on small molecule PHJ solar cells anomalous *J-V* characteristics were attributed to imbalanced charge carrier mobilities between the donor and acceptor layers.[11] This possibility in our devices was explored by measuring the hole mobilities of the ID583 hole-only devices prepared under different thermal conditions and by applying a space-charge-limited-current (SCLC) model.[25] The hole mobility of the devices fabricated at 25 °C is 6×10^{-6} cm^2 / V s, whereas the deposition at 60 °C or post-annealing at 80 °C yields only 2×10^{-6} and 6×10^{-7} cm^2 / V s, respectively (Figure 6). The previously reported electron mobility of C_{60} is approximately 10^{-2} cm^2 / V s.[26] Obviously, the decrease in hole mobilities with increased deposition temperature or with thermal annealing cannot explain the cause of the improved FFs in our PHJ devices. Consistently with the experimental hole mobilities, also the series resistance (R_S) of the PHJ cells with a 21 nm thick ID583 layer gets worse after the thermal treatments (Figure 2d). Devices prepared at 25 °C show the lowest R_S of 0.86 Ω cm² whilst the highest R_S of 1.5 Ω cm² is observed for the post-annealed (80 °C) devices. Depositing the cells at 60 °C results in an intermediate value (R_S = 1.1 Ω cm²). Note, that FFs of the devices prepared at 25 and 60 °C or post-annealed at 80 °C were 39, 70, and 70%, respectively.

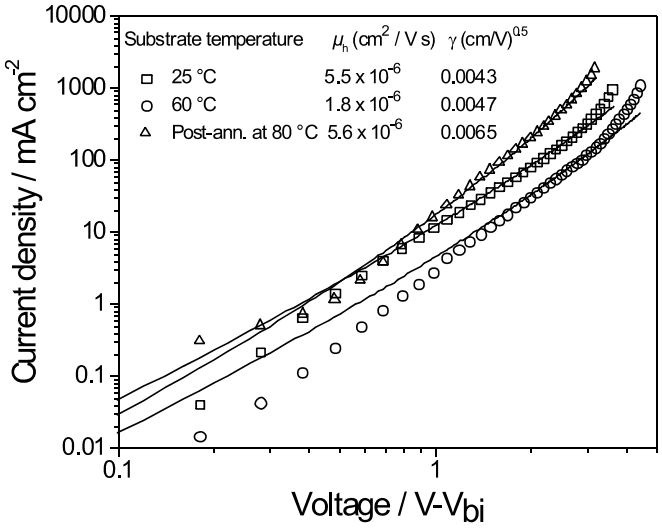

Figure 6. *J-V* characteristics (symbols) of devices prepared at different thermal conditions in logarithmic scales and fits of the SCLC model (lines). Fitted hole mobilities μ_h and field activation parameters γ are shown.

6.2.4 Analytical Electric Field Dependent CT-State Dissociation Model

As discussed above and depicted in Figure 2a, the onset of the kinks in the *J-V* characteristics of the as-deposited PHJ cells gradually shifts to lower applied voltages

with increasing donor layer thickness. By calculating the inverse of the slopes between the kinks and plotting them against the corresponding donor layer thicknesses, a linear correlation is observed (see inset in Figure 2a). This correlation is directly reflected in the FF of the devices which also linearly declines as the device thickness increases. These findings strongly suggest that the photocurrent at voltages around the maximum power point (mpp) depends on the effective electric field that can be approximated by

$$F_{el} = \frac{(V - V_{bi})}{d}, \quad (1)$$

where $d = d_{\text{donor}} + d_{\text{acceptor}}$ is the total cell thickness. The applied and the built-in voltage are labeled V and V_{bi}, respectively. In previous studies, the strong field dependence has been attributed to a high series resistance[11] or to a low exciton dissociation efficiency at the D/A heterointerface[12].

Because it was found that the hole mobility and thus the charge transport properties of the donor material did not improve and even slightly decline during thermal treatment, the R_S cannot be the cause of the low FF and high field dependency of the as-deposited (substrate temperature T = 25 °C) PHJ cells. Furthermore, the field dependency cannot be attributed to non-geminate recombination because we have a planar heterojunction structure. In order to analyze the charge dissociation efficiency at the heterointerface, a field dependent CT-state dissociation model has been used to describe the illuminated *J-V* characteristics of the as-deposited devices. Within the frame of this model the current is given by

$$J(V) = J_{dark,exp}(V) - J_{photo}(V), \quad (2)$$

where $J_{\text{dark,exp}}(V)$ is the measured current of the not illuminated cell and the voltage dependent photocurrent is given by

$$J_{photo}(V) = p(V) J_{photo,sat}. \quad (3)$$

Here $J_{photo,sat}$ is the saturation value of the photocurrent and $p(V)$ denotes the voltage dependent CT-state dissociation probability which can be calculated from the CT-state dissociation rate $k_{diss}(V)$ and its recombination rate k_f

$$p(V) = \frac{k_{diss}(V)}{k_{diss}(V) + k_f} = \frac{1}{1 + \frac{k_f}{k_{diss}(V)}}. \quad (4)$$

This expression assumes a finite lifetime of the CT-state $\tau = k_f^{-1}$ with respect to recombination and was introduced by Braun[27]. The CT-state dissociation rate is expressed as[28]

$$k_{diss}(V) = k_{diss,0} \frac{\left[1 - \exp\left(\frac{-qF_{el}r_s}{k_B T}\right)\right] k_B T}{qF_{el}r_s}, \quad (5)$$

where $k_{diss,0}$ is the dissociation rate at zero field, k_B and T are the Boltzmann constant and the temperature, respectively, and r_s is the distance over which the electric field is acting on the CT-state. This distance is the difference between the initial electron/hole pair separation in the CT-state and the distance at which the two charge carriers can be considered free. We use r_s as a fitting parameter. A more detailed discussion of the model will be published elsewhere.[28]

Using the loss ratio k_f/k_{diss} and the separation distance r_s as free parameters, the exciton dissociation model is fitted to the *J-V* characteristics of the illuminated as-deposited PHJ cells. Figure 7 shows the excellent agreement of the model and the experimental data. The parameters used in the simulation are given in Table 2. The well saturated current densities at the applied voltage region of $V < 0$, imply an efficient CT-state dissociation in all devices. However, when the direction of the applied electric field is reversed ($V > 0$), the CT-state separation probability $p(V)$ decreases notably. For cells with a nominal donor layer thickness of 14 nm and at $V = 0.5$ V, the model predicts a separation probability of $p = 89\%$ while the cells with a 21 nm donor layer only reach about 76%, at the same value of the applied voltage V. Furthermore, when the nominal donor layer thickness increases to 28 nm, the predicted probability for the

CT-state dissociation at V = 0.5 V is only 62%. Because the internal field decreases with increasing cell thickness, the concurrent decrease of the field-assisted separation probability is a strong indication of the photocurrent being controlled by a geminate recombination process. Thus, the formation of kinks around the mpp of the as-deposited solar cells may be attributed to the high recombination rates of the geminately bound electron-hole pairs (CT-states).

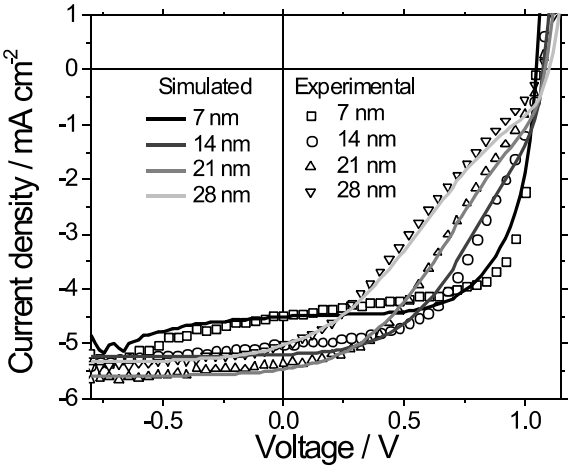

Figure 7. Experimental (symbols) and simulated (solid lines) *J-V* characteristics of PHJ cells with different donor layer thicknesses. The simulated curves are calculated according to Eq. 3 using the parameters shown in Table 2.

Table 2. Model parameters used to simulate the *J-V* characteristics of PHJ cells (see Figure 7)

Parameter	Symbol	Value	Origin
Loss ratio	k_f/k_{diss}	31	Fit
Separation distance	r_s	8.7 nm	Fit
Built-in voltage	V_{bi}	1.54 V	Experiment[a]
Acceptor thickness	$d_{acceptor}$	31.5 nm	Experiment[b]
Donor thickness	d_{donor}	7.7 to 30.8 nm	Experiment[c]
Saturation photocurrent	$J_{ph,sat}$	4.5 to 5.6 mA cm^{-2}	Experiment[d]
Temperature	T	298 K	Experiment[e]

[a] Calculated from the energy difference between the cathode work function and the HOMO level of ID583 (assumes Fermi level pinning at the anode). For the cells with a donor thickness of 7 nm, the electrical field at the donor/acceptor interface has been increased by 15%. The increase is attributed to a band bending close to the anode;[29] [b] 90% of the nominal value (the experimental uncertainty of the layer thicknesses is 10%); [c] 110% of the nominal value (the experimental uncertainty of the layer thicknesses is 10%); [d] Experimental current assumed at V = -0.5 V for donor thicknesses d_{donor} > 7 nm. For d_{donor} = 7 nm the value V = 0 V is taken in order to avoid influences of the low parallel resistance; [e] Temperature of the substrate.

6.2.5 Molecular Orientations as Deduced from IRSE

The XRPD measurements indicate that the amorphous ID583 neat films did not crystallize upon evaporation at elevated substrate temperatures or at post-annealing above the T_g of the dye. However, it is well known that organic films may possess different degrees of order, although the size of the ordered regions is too small to give coherent reflections in XRPD (X-ray amorphous). Therefore, we have performed IRSE analysis for two types of samples: thin films of ID583 (28 nm) evaporated on $Si/SiO_2/MoO_3$ with and without post annealing at 80 °C for 5 min. In all cases the thicknesses of the MoO_3 and the natural Si oxide have been found to be around 3 nm. Figure 8a shows the ellipsometric parameters obtained from both sample types at an angle of incidence of $\theta = 60°$ and the corresponding modeled spectra. Already the raw data reveal clear indications for a change of molecular orientation upon annealing. Thus, the peak at 2209 cm-1 ($\nu_{C\text{-}N}$) is a dip-down in Ψ for the annealed film and a dip-up for the as-deposited film, corresponding to out-of-plane and in-plane vibrations, respectively.[30] For a precise determination of the structural change in the film upon annealing, the accordance between the modeled dielectric function and the DFT (BP86/SV(P) level of theory) predicted absorption intensities was optimized by rotating a basis molecule set (and thereby the dipole moments) relative to the substrate. For each orientation a figure of merit (rating) was computed, and the orientation with best rating is then regarded as the preferred orientation of the molecules (for details of the method see Ref. 31). The optimization process was performed on three pronounced peaks at 1555 ($\delta_{C\text{-}H}$), 1678 ($\nu_{C\text{-}O}$), and 2209 cm^{-1} ($\nu_{C\text{-}N}$). Figure 8b shows the experimentally derived imaginary parts ε_2 of the dielectric functions for the two direction components of each sample in comparison to DFT intensity predictions for the optimized orientations of the molecule. As can be seen in Figure 9, the result indicates that in the as-deposited film the molecules are preferably standing with their long axis perpendicular to the substrate surface, and undergo a tilt of 45° upon annealing at 80 °C. This change is certainly driven by a higher packing density for the tilted orientation. As no peaks were observed in X-ray diffraction measurements for both annealed and non-annealed films, it can be concluded that the films are X-ray amorphous but the molecules tend to align their long molecular axes along certain directions, namely along the surface normal in as-deposited films and along 45° relative to the surface normal after annealing.

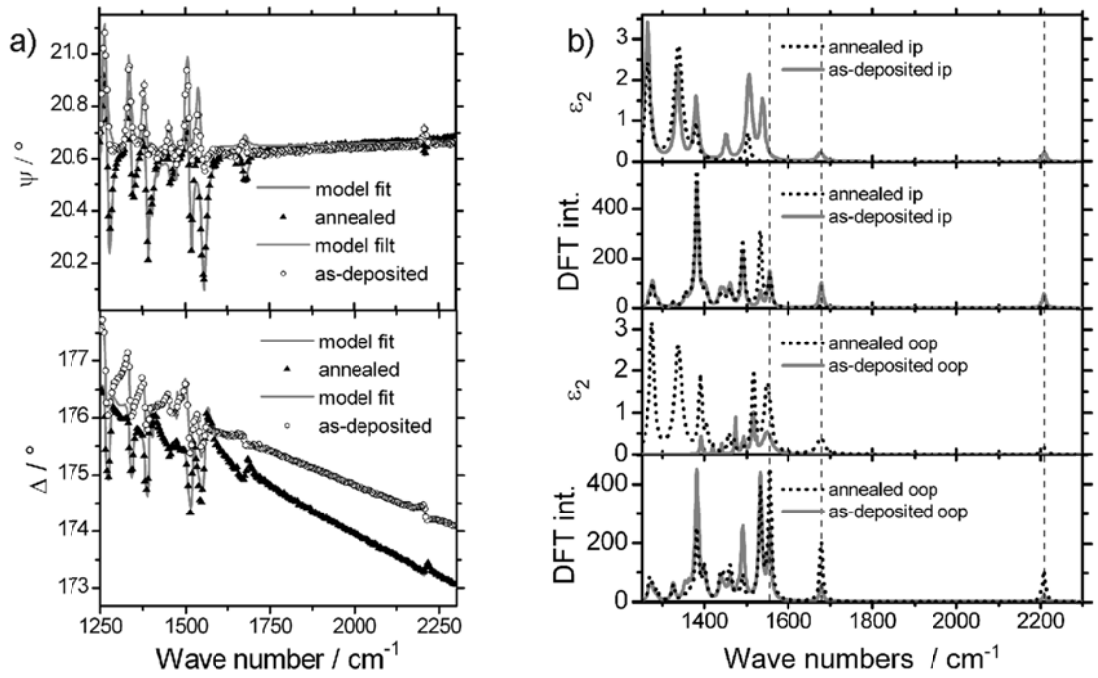

Figure 8. a) Measured ellipsometric parameters (symbols) Ψ and Δ for an as-deposited and annealed film on $MoO_3/SiO_2/Si$ substrates, and the corresponding modeled spectra (continuous lines). The ID583 films (thicknesses around 30 nm) were modeled as optically uniaxial. b) In-plane (ip) and out-of-plane (oop) contributions of ε_2 and the absorption peaks calculated by DFT. Fitting of DFT (BP86/SV(P) level of theory) based intensities to the experimental results was performed by using the three peaks marked with broken lines.

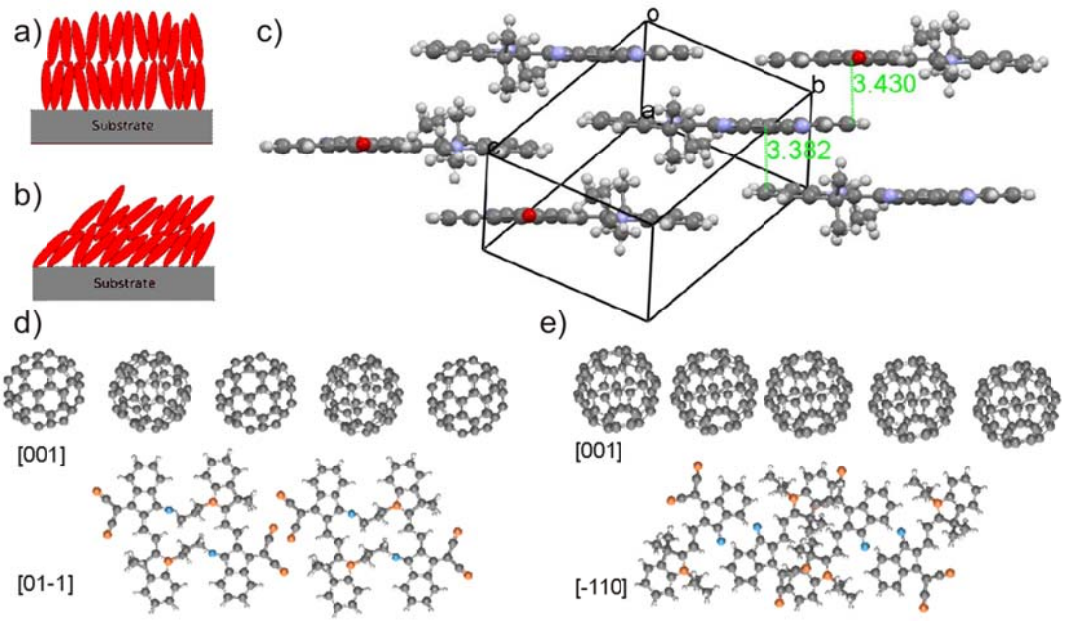

Figure 9. Schematics of the dye molecules' orientations a) before and b) after annealing at 80 °C deduced from the ellipsometric analysis. c) Brickwall packing motif in the single crystal structure of ID583. The shortest atom-to-π-plane distances are also shown. Schematics of the interfaces d) ID583[01-1]:C_{60}[001] and e) ID583[-110]:C_{60}[001].

6.2.6 Computations of the CT-state Energies at the ID583/C_{60} Interface

The kinks disappear and the fill factors significantly improve when substrate heating is applied or the devices are post-annealed at 80 °C which is just above the T_g (77 °C) of the dye. The fact that the post-annealing below the T_g has negligible influence on the device performance strongly suggests that the reorientation of the dyes, as shown by the IRSE spectroscopic analysis, is the key for the improved device performance. In a recent theoretical[15] study with pentacene/C_{60} PHJ cells, it was observed that changes on the relative orientation of the quadrupolar donor molecule at the D/A interface have a significant influence on the charge dissociation energetics. Exposing the negatively charged π-plane of the pentacene to the C_{60} interface was found to give an additional driving force for the exciton dissociation. Unlike pentacene, ID583 contains a donor-acceptor π-conjugated molecular scaffold with a permanent ground state dipole moment (7.1 D along the long and 5.5 D along the short axis of the molecule on BP86/TZVP level of theory).[32] Upon optical excitation of such push-pull chromophores the electron density is even further displaced toward the acceptor part of the dye leading to even larger dipole moments in the excited state.[33] Therefore, the relative orientation of molecules close to or at the D/A interface can have a significant impact on stabilization of the electron/hole pair and its dissociation at the interface.[15]

To assess the influence of the dyes' orientation on the stabilization of the electron/hole pair in the ID583/C_{60} cells, two model-interfaces were built using the crystal structures of C_{60} and ID583. In order to create meaningful interface structures, the preferred orientations from the IRSE study were compared with the single crystal structure of ID583 (Figure 9c). It is obvious that the perpendicular orientation of the long molecular axis of ID583 in the as-deposited films and the tilted (45°) arrangement after annealing match very well with the lattice planes [01-1] and [-110], respectively. Therefore, the interface models ([01-1]:[001] and [-110]:[001]) were constructed by positioning the C_{60} plane [001] over the dye layers. The distances between the layers were optimized using the Dreiding-force field[34] (Figure 9). All other degrees of freedom (intramolecular relaxation, translation and rotation of the molecules) were kept fixed. Note, that the space group of the crystal structure of ID583 is centrosymmetric P-1 having two molecules with antiparallel orientation of the long molecular axis in the unit cell. We expect the antiparallel orientation of ID583 also to be found at the interface of the planar heterojunction. Therefore, two different types of interfaces with clearly distinct contacts between the merocyanine and fullerene components must be

considered: One where the acceptor part (indane) of the ID583 dye molecule is exposed to the C_{60} surface (in the following called A configurations) and one where the dyes' donor part (indoline) is exposed (in the following called D configurations). A detailed description of the simulations can be found in Ref. 31.

The energy of the charge transfer exciton for the different bimolecular (ID583/C_{60}) interface configurations is shown in Table 3. Figure 10 demonstrates the energy level diagram of the ID583/C_{60} interface with energy levels of the different electron/hole-pairs at the perpendicular and tilted interfaces. The energy levels of the electron/hole-pairs are given relative to the HOMO energy of ID583. As expected, the energy of the CT-state critically depends on the interface geometry as well as on the orientation of ID583 towards the C_{60} surface. It is interesting to note that, irrespective of the interface geometry, the CT-state is lower in energy when the (partially negatively charged) indane acceptor group of the dye is exposed to the C_{60} surface (configurations 1A and 2A). Due to the antiparallel orientation, the neighboring ID583 molecules of the bimolecular complexes 1A and 2A (which define the local polarization field) are oriented such that the indoline group is exposed to the C_{60} surface. Therefore, the CT-state is stabilized by the positive partial charge of the indoline group of the neighboring ID583 molecules. Furthermore, due to the fact that the CT-state is generated by an electron transfer from the S_1-state of ID583 to the LUMO of C_{60}, the electron density distribution of the ID583 S_1-state crucially influences the energy of the CT-state. Therefore, when the vectors of the transition dipole moment of the $S_0 \rightarrow S_1$ transition in ID583 and the transition dipole moment of the S_1(ID583) $\rightarrow$ CT excitation are oriented parallel, the electron density distribution is closer to the interface and the CT-state is already preformed in the S_1-state of ID583. Hence, the CT-state at the interface can be formed more easily due to the kinetic reasons.

Table 3. Energy of the CT-state for different bimolecular ID583/C_{60} interface configurations

Interface	Exposed side of the dye	E(CT) [eV]	$\Delta G_{S1\rightarrow CT}$ [eV][a]	Configuration
[-110]:[001]	Acceptor	1.54	-0.51	2A
[-110]:[001]	Donor	1.95	-0.10	2D
[01-1]:[001]	Acceptor	1.35	-0.70	1A
[01-1]:[001]	Donor	1.61	-0.45	1D

[a] The driving force between the measured optical gap (S_1) of ID583 (2.05 eV) and the calculated energy of the CT-state.

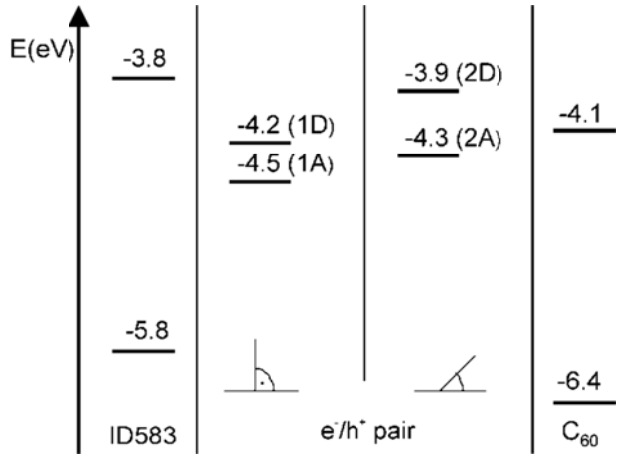

Figure 10. Energy level diagram of the ID583/C_{60} interface with energy levels of the different electron/hole-pairs at the perpendicular (second column) and tilted (third column) interfaces. D configurations refer to orientations where the dyes' donor subunit is in contact to C_{60}; A configurations refer to orientations where the dyes' acceptor subunit is in contact to C_{60}. The energy levels of the electron/hole-pairs are obtained by adding the energy of the charge transfer state *E*(CT) (see Table 3) to the HOMO of ID583.

As can be seen in Table 3, the driving force for the formation of the CT-state, which is defined as the energy difference between the optical gap and the energy of the CT-state ($\Delta G_{S1\rightarrow CT} = E_{CT} - E_{opt}$), is negative for all interface configurations and relative orientations. Therefore, in principle the generation of a CT-state is possible for all four molecular orientations.

It is known from Marcus theory that the rate of charge transfer depends on the driving force.[35] The highest rates are realized when $\Delta G_{S1\rightarrow CT}$ is equal to the negative reorganization energy λ of the system. The estimated λ is 0.3-0.5 eV so that the highest charge transfer rates occur at configurations 2A and 1D.[36] Note that 2A corresponds to the low energy CT-state at the tilted interface whereas 1D is the high energy CT–state at the perpendicular interface (see Figure 9). Therefore, the electron/hole pair is expected to stay on the bimolecular complex 2A in the tilted case whereas the hole hops to the bimolecular complex 1A in the perpendicular case. The energy difference of 0.26 eV between the bimolecular complexes 1D and 1A prevents the hole from hopping back to the other ID583 so that 1A acts as a trap state at the perpendicular interface. The rate of an electron leaving the interface can be approximated from the energy distance between the CT-state and the transport level (LUMO) of C_{60} ($\Delta E_{CT\text{-}LUMO}^{A}$). Using the Marcus formula and assuming a reorganization energy λ of 0.4 eV and a transfer integral of 0.050 eV, the rate for the electron hopping from the C_{60} molecule in configuration 2A to

the bulk C_{60} is 400 times higher (3×10^{10} Hz vs. 8×10^{7} Hz) than the respective rate for the configuration 1A, which is due to the high $\Delta E_{\text{CT-LUMO}}^{\text{A}}$ of 0.4 eV. Note that it can be assumed that the LUMO level of the C_{60} molecules close to the interface is different from the respective bulk level so that the electron does not need to perform the λ energetic jump of 0.4 eV in one step but could reach the bulk LUMO level in several smaller steps.[15] Because this effect is expected to be similar for both interfaces, the dissociation rate of the CT-state at the tilted interface remains higher than the respective rate at the perpendicular interface. This shows that the high energetic stabilization of the CT-state 1A (which is the global minimum of all calculated interface excitons) makes its dissociation at the perpendicular interface very unlikely. Due to the absence of an energetic trap and the lower stabilization of the exciton at the tilted interface, it is expected to show a higher exciton dissociation rate compared to the perpendicular orientation, as indicated by the CT-state dissociation simulations.

Summarizing the theoretical discussion, we have demonstrated that the CT-state is stabilized when the neighboring molecules are oriented such that the positive end of ID583 is exposed to the interface. Furthermore, the exciton dissociation rate is higher when the energy difference between the interface and bulk energy level is smaller. The calculated changes of the CT-state energies, caused by the change of the molecular orientation, also agree with our CT-state dissociation model. It predicts that the driving force for the CT-state dissociation has to be increased by at least 0.1 eV in order to account for the observed device behavior.[28] Our results are also in accordance with previous findings on merocyanine dye sensitized solar cells (DSC) which suggest that the electron injection efficiency improves if the electron accepting part of the push-pull chromophores, e.g. cyano groups, are closely located at the titanium dioxide (TiO_2) surface.[37] Likewise, in our ID583/C_{60} devices, the tilted orientation, in which the two cyano groups of the ID583 are closest to the C_{60} surface, yields the highest CT-state dissociation efficiency.

6.2.7 Bulk Heterojunction Cells

As a comparison, we also fabricated bulk heterojunction (BHJ) cells featuring following layer structure: ITO/MoO_3 (5 nm)/ID583:C_{60} (7-28 nm)/C_{60} (35 nm)/BPhen (5 nm)/Ag (100 nm). The active layer thickness (ID583:C_{60} 40:60 wt %) was varied from 7-28 nm in steps of 7 nm. Figure 11 shows that the *J-V* characteristics of these devices do not demonstrate similar kinks as has been observed for the PHJ cells. Instead,

even with the active layer thicknesses of 28 nm, the devices exhibit a high FF of 55%. Although the open circuit voltage V_{OC} = 1.00 V is lower than for the PHJ cells, the PCE (4.1%) is slightly increased due to a significantly increased J_{SC} (7.5 mA cm^{-2}).

It is intriguing that the *J-V* characteristics of the BHJ cells resemble that of the heat-treated PHJ devices. This is explained by the different heterointerface structures of PHJ and BHJ devices. It can be assumed that the interface structure of BHJ blends is random which leads to broad distribution of energetically different pathways for excitons to dissociate. Due to the energetically heterogeneous landscape a significant number of excitons are able to dissociate into free charges even at low effective electric field strength. In contrast, in the PHJ devices, the interface structure is expected to be more ordered leading to energetically homogenous surrounding which, depending of the dyes' relative orientation, either supports or hinders the exciton dissociation.

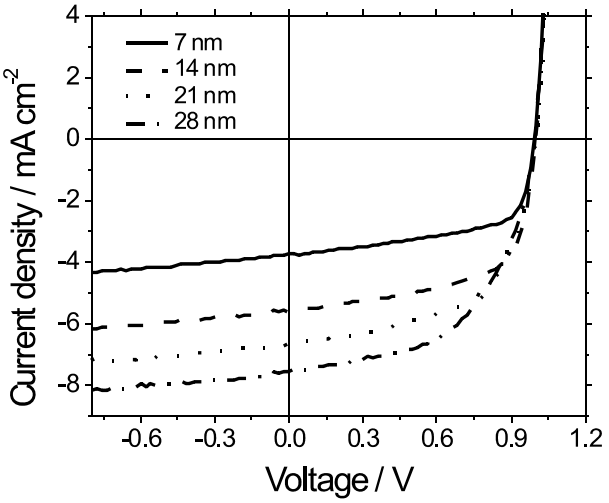

Figure 11. Illuminated *J-V* characteristics of BHJ devices with different ID583:C_{60} layer thicknesses.

6.3 Conclusions

We have shown that by evaporating the dye film on a heated substrate or by post-annealing the complete devices above the glass transition temperature (T_g) of the donor material, we can significantly improve the FF of merocyanine/C_{60} PHJ solar cells. By employing a field dependent charge transfer (CT) state dissociation model, we show that the low FF of the as-deposited cells is a result of the poor exciton dissociation efficiency at the D/A heterointerface which is significantly improved after the heat

treatments. Although, we observe no coherent reflections in the XRPD study, the utilization of an IRSE spectroscopic analysis demonstrated that the preferred orientation of the dye molecules in the donor film changes upon post-annealing at 80 °C. Based on this finding, we simulated two D/A heterointerface models and estimated their CT-state energies via QM/MM calculations. The computations suggest that the exciton dissociation rate is higher in post-annealed devices compared to as-deposited cells. Hereby, we argue that the low exciton dissociation efficiency of as-deposited devices is a result of the unfavorable molecular orientation at the heterointerface together with an insufficient driving force (LUMO(D)-LUMO(A) offset is ~0.3 eV). However, post-annealing the devices above the T_g of the donor material changes the interface structure, facilitates the CT-state dissociation, and thus leads to a two-fold increase of the FF. Furthermore, the kinks cannot be observed in the *J-V* characteristics of the BHJ devices deposited at 25 °C; instead the curves resemble heat treated PHJ cells. This is due to the random orientation of the dyes at the heterointerface in BHJ devices which is expected to result in energetically favorable pathways for a significant number of excitons to dissociate.

Our comprehensive study suggests that push-pull chromophores can be beneficial for exciton dissociation at the planar and bulk heterojunction interface if they are oriented in a proper way with respect to the acceptor manifold. This finding hints that by carefully tailoring the molecular structure and/or the film morphology, the energy level alignment at the heterojunction can be further optimized. This is important, especially because dyes with pronounced charge redistributions upon electronic excitation, e.g. in particular dipolar merocyanines (D-A),[19] but also quadrupolar squaraines and diketopyrrolopyrroles (D-A-D),[38,39] or dicyanovinyloligothiophenes (A-D-A)[40] are increasingly utilized in organic small-molecule planar and bulk heterojunction solar cells.

6.4 Experimental Section

Synthesis

Merocyanine dye ID583 (1-propyl-2-[2-(3,3-trimethyl-1,3-dihydro-indol-2-ylidene)-ethylidene]-3-dicyanovinyl-indan-1-one) was synthesized by refluxing a mixture of methylene base (8.05 g, 0.04 mol), 3-dicyanovinylindan-1-one (7.76 g, 0.04 mol) and

orthoformic ethyl ester (8.88 g, 0.06 mol) two hours in ethanol. After cooling, the crystallized product was filtered and washed with ethanol. Finally, the product was purified by recrystallizing it from dimethylformamide. **Yield:** 14.0 g (0.034 mol, 85%), green solid. **Mp.** 219–221 °C. **1H NMR** ($CDCl_3$, 360 MHz): δ = 9.05 (d, J = 13.6 Hz, 1H), 8.57 (m, 1H), 8.08 (d, J = 14.0 Hz, 1H), 7.72 (m, 1H), 7.59 (m, 2H), 7.36 (m, 2H), 7.25 (m, 1H), 7.07 (m, 1H), 4.04 (t, J = 7.2 Hz, 2H), 1.96 (m, 2H), 1.81 (s, 6H), 1.09 (t, J = 7.2 Hz, 3H). **UV–vis** (CH_2Cl_2): λ_{max} (λ) = 575 nm (66501 M^{-1} cm^{-1}). **Elemental analysis** (%) calcd. for $C_{27}H_{23}N_3O$: C, 80.0; H, 5.7; N, 10.4; O, 4.0. Found: C, 80.1; H, 5.8; N, 10.4; O, 4.1.

Cyclic voltammetry (CV)

The CV measurement of ID583 was performed on a commercial electrochemical analyzer (EC epsilon; BAS Instrument, UK) in a three electrode single-compartment cell under argon. Dichloromethane (HPLC grade; J. T. Baker) was dried over calcium hydride and degassed prior to use. The supporting electrolyte tetrabutylammonium hexafluorophosphate (TBAHFP) was synthesized according to a published method.[41] The measurements were carried out under exclusion of air and moisture at a concentration of 10^{-4} M with ferrocene (-5.15 eV) as internal standard for the calibration of the potential; working electrode: Pt disc; reference electrode: Ag/AgCl; auxiliary electrode: Pt wire.

Atomic force microscopy (AFM)

The AFM experiments (Dimension 5000 Microscope, Veeco Instruments) were performed on two different 21 nm-thick ID583 films evaporated on ITO substrates at substrate temperatures of 25 and 60 °C. The measurements were carried out in the tapping mode using silicon cantilevers with a nominal force constant of 42 N/m and a tip radius of ~7 nm from Olympus, type OMCL-AC160TS (Tokyo, Japan) at a resonance frequency of about 320 kHz. The scan rate was kept at 0.7 Hz, while the tip-sample forces were carefully minimized to avoid artifacts.

Differential scanning calorimetry (DSC)

The glass transition temperature of ID583 was measured using Q2000 (TA-instruments) differential scanning calorimeter (DSC). ID583 powder (5.4 mg) was heated/cooled at rate 20 K/min in aluminum pan under nitrogen atmosphere.

UV/Vis absorption spectra

Absorbance spectra of ID583 films were recorded using HR+2000 spectrometer (OceanOptics) in transmission mode employing a Xe lamp as the light source. The 21 nm thick films were fabricated on ITO covered glass slides at substrate temperatures of 25 and 60 °C or post-annealed at 80 °C for 5 min.

Single crystal analysis

Red block crystals of ID583 were grown by slow evaporation of a dichloromethane solution of this dye at room temperature. The diffraction data were collected at 103 K with a Bruker AXS CCD detector, using graphite-monochromated Cu K_α (λ = 1.51478 Å) radiation. The structure was solved by a direct method and refined on F^2 using the full matrix least square method in SHELXTL program package.[42] All non-hydrogen atoms were anisotropically refined and hydrogen atoms were placed on idealized positions. The unit cell of the analyzed crystal is a = 9.2930(10) Å, b = 9.6240(11) Å, c = 12.6184(13) Å, α = 104.859(5)°, β = 97.120(4)°, and γ = 90.374(5)°. The space group is P-1 with Z = 2. A total amount of 2067 reflections was collected with 1651 unique reflections in the range from 3.65 - 57.29° (2θ). The R1 and wR1 of the refinement are 0.0354 and 0.0832, respectively. The goodness of fit (GooF) for the solution is 1.065. Crystallographic data (excluding structure factors) for the structure reported in this paper have been deposited with the Cambridge Crystallographic Data Centre as supplementary publication no. CCDC-834686. Copies of the data can be obtained free of charge from www.ccdc.cam.ac.uk/conts/retrieving.html.

X-ray diffraction

X-ray powder diffraction (XRPD) scans were recorded in a Bragg – Brentano geometry using a PANalytica's X'Pert Pro MPD diffractometer employing Cu K_α radiation (λ =1.542 nm). The scanning range was 3-35° (2θ) with a step size of 0.017° and counting time of 101 s/step. ID583 neat films (30 nm) were prepared on ITO covered glass slides at substrate temperatures of 25 °C and 60 °C, or post-annealed at 80 °C for 5 min.

Charge carrier mobilities

ID583 hole-only devices were fabricated by depositing the ID583 films at substrate temperatures of 25 and 60 °C or post-annealing the complete cell at 80 °C for 5 min.

The used device architecture was ITO/MoO_3 (5nm)/ID583/MoO_3 (5nm)/Ag (100 nm) with an ID583 layer thickness of 80 nm for the devices evaporated at 25 and 60 °C. The ID583 layer thickness of the post-annealed device was 50 nm. The hole mobilities were extracted from the current-voltage characteristics of the devices using a space charge limited current model (SCLC).

Device fabrication

The same materials were used in all planar heterojunction (PHJ) and bulk heterojunction (BHJ) cells throughout this work. The commercial MoO_3 (Merck), C_{60} (CreaPhys, 2 × sublimed), 4,7-diphenyl-1,10-phenanthroline (Bphen; Fluka) and the synthesized ID583 dye were used as received. The solar cells were manufactured in a high vacuum (typically 2×10^{-6} mbar) chamber (Lesker Ltd) on prestructured indium tin oxide (ITO) substrates with an active cell area of 4 mm². Prior to transferring the ITO substrates into the chamber they were cleaned in UV/O_3 oven for 15 min. All PHJ devices were fabricated according to following steps: first a MoO_3 film (5 nm ±10%) was evaporated on the ITO substrate, followed by a 7, 14, 21, or 28 nm (±10%) thick ID583 donor layer. After the ID583 film, a C_{60} acceptor layer (35 nm ±10%) and a Bphen buffer film (5 nm ±10%) were deposited before preparation of the silver cathode (100 nm ±10%). The evaporation rate of all organic materials was 1.0 Å/s whereas the MoO_3 and Ag layers were deposited at rates of 0.8 and 4 Å/s, respectively. Compared to the PHJ cells, the following changes were made in fabrication of the BHJ devices: the ID583 layers were replaced with ID583:C_{60} (40:60 wt ratio) mixed layers with thicknesses of 7, 14, 21, and 28 nm (±10%), followed by a 25 nm (±10%) thick C_{60} layer. Some of the PHJ devices were prepared on a heated substrate or post-annealed after fabrication. When substrate heating was applied, the substrate was first heated with a copper block heater to 60 °C before evaporation of the ID583 layer after which the substrate was cooled below 30 °C until the successive layers were deposited. Post-annealing of the cells was carried out such that the complete devices were heated directly after fabrication on a hot plate at 50, 60, 70, 80, and 100 °C for 5 min in nitrogen atmosphere. The current-voltage (*J-V*) characteristics of the cells were measured under AM 1.5G simulated illumination (Xe lamp) in ambient air and controlled by a Keithley 2425 source measurement unit. The light intensity (100 mW cm^{-2}) was adjusted by a calibrated Si reference cell.

Infrared spectroscopic ellipsometry (IRSE)

Ellipsometry measures the complex reflectance ratio $\rho = r_p / r_s = \tan(\Psi)\exp(i\Delta)$, where r_p and r_s are the reflection coefficients for light polarized parallel and perpendicular to the plane of incidence and Ψ and Δ are the standard ellipsometric parameters.[43] By modeling the obtained values for Ψ and Δ, a best-fit parameterized description of the dielectric function can be achieved, including optical anisotropy.[44] IRSE measurements at different angles of incidence were performed with a Woollam IR-VASE ellipsometer. The modeling was done using the WVASE-32 software package, which appropriately considers the layered structure of the samples. The anisotropic dielectric function can then provide information on crystal orientation and structural disorder of the film.[45] For polycrystalline thin films and amorphous films with a substrate-induced preferred orientation of the molecules, an effective uniaxial anisotropy can be expected with vibrations parallel (in-plane) and perpendicular (out-of-plane) to the substrate surface,[46] even if the single molecules are orientated with an angle off the surface normal.

To obtain the orientation of the molecules with regard to the substrate, the experimentally observed vibrational modes were compared to density functional theory (DFT) calculations (SV(P)/BP86 level of theory)[47] of vibrational eigenvalues and eigenvectors for a single molecule; DFT yields peak positions of vibrational modes and the directions of dipole moments relative to the molecule for each normal mode. Further information on the calculation of vibrational frequencies can be found in the Supporting Information. We developed a software tool that optimizes the accordance between DFT based vibration spectra and the experimental anisotropic dielectric function by varying the orientation of a molecule relative to the substrate.[48] In that way, by combining DFT results, which give us the orientation of the dipole moments with respect to the molecule, and ellipsometry results, which give us the orientation of the dipole moments with respect to the substrate surface, we can reliably determine the orientation of the molecules with respect to the substrate surface.

6.5 References

[1] (a) C. J. Brabec, S. Gowrisanker, J. J. M. Halls, D. Laird, S. Jia, S. P. Williams, *Adv. Mater.* **2010**, *22*, 3839; (b) M. A. Green, K. Emery, Y. Hishikawa, W.

Warta, *Prog. Photovolt: Res. Appl.* **2010**, *18*, 144; (c) P.-L. T. Boudreault, A. Najari, M. Leclerc, *Chem. Mater.* **2011**, *23*, 456.

[2] P. K. Nayak , J. Bisquert , D. Cahen, *Adv. Mater.* **2011**, *23*, 2870.

[3] (a) D. Veldman, S. C. J. Meskers, R. A. J. Janssen, *Adv. Funct. Mater.* **2009**, *19*, 1; (b) H. Ohkita, S. Cook, Y. Astuti, W. Duffy, S. Tierney, W. Zhang, M. Heeney, I. McCulloch, J. Nelson, D. D. C. Brandley, J. R. Durrant, *J. Am. Chem. Soc.* **2008**, *130*, 3030; (c) R. A. Marsh, J. M. Hodgkiss, R. H. Friend, *Adv. Mater.* **2010**, *22*, 3672; (e) P. Peumans, S. R. Forrest, *Chem. Phys. Lett.* **2004**, *398*, 27.

[4] I. G. Hill, A. Kahn, Z. G. Soos, R. A. Paskal, *Chem. Phys. Lett*. **2000**, *327*, 181.

[5] (a) D. Veldman, O. Ipek, S. C. J. Meskers, J. Sweelssen, M. M. Koetse, S. C. Veenstra, J. M. Kroon, S. S. van Bavel, J. Loos, R. A. J. Janssen, *J. Am. Chem. Soc.* **2008**, *130*, 7721; (b) V. D. Mihailetchi, L. J. A. Koster, J. C. Hummelen, P. W. M. Blom*, Phys. Rev. Lett.* **2004**, *93*, 216601.

[6] (a) S. Kalyan, T. Kesti, M. Maiti, F. Zhang, O. Inganäs, S. Hellström, M. R. Andersson, F. Oswald, F. Langa, T. Österman, T. Pascher, A. Yartsev, V. Sundström, *J. Am. Chem. Soc.* **2010**, *132*, 12440; (b) J.-L. Bredas, D. Beljonne, V. Coropceanu, J. Cornil, *Chem. Rev.* **2004**, *104*, 4971.

[7] (a) M. C. Scharber, D. Mühlbacher, M. Koppe, P. Denk, C. Waldauf, A. J. Heeger, C. J. Brabec, *Adv. Mater.* **2006**, *18*, 789: (b) B. P. Rand, D. P. Burk, S. R. Forrest, *Phys. Rev. B* **2007**, *75*, 115327; (c) C. J. Brabec, A. C. Cravino, D. Meissner, N. S. Sariciftci, T. Fromherz, M. T. Rispens, L. Sanchez, J. C. Hummelen, *Adv. Funct. Mater.* **2001**, *11*, 374; (d) Uhrich, C. D. Wynands, S. Olthof, M. K. Riede, K. Leo, S. Sonntag, B. Maenning, M. Pfeiffer, *J. Appl. Phys.* **2008**, *104*, 043107.

[8] B. C. Thompson, J. M. J. Fréchet, *Angew. Chem. Int. Ed.* **2008**, *47*, 58.

[9] C. Uhrich, R. Schüppel, A. Petrich, M. Pfeiffer, K. Leo, E. Brier, P. Kilickiran, P. Bäuerle, *Adv. Funct. Mater.* **2007**, *17*, 2991.

[10] X. Gong, M. Tong, F. G. Brunetti, J. Seo, Y. Sun, D. Moses, F. Wudl, A. J. Heeger, *Adv. Mater.* **2011**, *23*, 2272.

[11] (a) W. Tress, A. Petrich, M. Hummert, M. Hein, K. Leo, M. Riede, *Appl. Phys. Lett.* **2011**, *98*, 063301; (b) D. Kekuda, J.-H. Huang, K.-C. Ho, C.-W. Chu, *J. Phys.Chem. C* **2010**, *14*, 2764.

[12] (a) A. Liu, S. Zhao, S.-B. Rim, J. Wu, M. Könemann, P. Erk, P. Peumans, *Adv. Mater.* **2008**, *20*, 1065; (b) J. Wagner, M. Gruber, A. Hinderhofer, A. Wilke, B. Bröker, J. Frisch, P. Amsalem, A. Vollmer, A. Opitz, N. Koch, F. Schreiber, W. Brütting, *Adv. Funct. Mater.* **2010**, *20*, 4295.

[13] J. C. Wang, X. C. Ren, S. Q. Shi, C. W. Leung, P. K. L. Chan, *Org. Electron.* **2011**, *12*, 880.

[14] M. Chikamatsu, T. Taima, Y. Yoshida, K. Saito, K. Yase, *Appl. Phys. Lett.* **2004**, *84*, 127.

[15] S. Verlaak, D. Beljonne, D. Cheyns, C. Rolin, M. Linares, F. Castet, J. Cornil, P. Heremans, *Adv. Funct. Mater.* **2009**, *19*, 3809.

[16] C. F. N. Marchiori, M. Koehler, *Synth. Met.* **2010**, *160*, 643.

[17] R. D. Pensack, K. M. Banyas, L. W. Barbour, M. Hegadorn, J. B. Asbury, Phys. *Chem. Chem. Phys.* **2009**, *11*, 2575.

[18] (a) V. I. Arkhipov, P. Heremans, H. Bässler, *Appl. Phys. Lett.* **2003**, *82*, 4605; (b) N. Koch, *ChemPhysChem* **2007**, *8*, 1438; (c) G. Heimel, I. Salzmann, S. Duhm, N. Koch, *Chem. Mater.* **2011**, *23*, 359.

[19] (a) F. Würthner, K. Meerholz, *Chem. Eur. J.* **2010**, *16*, 9366; (b) N. M. Kronenberg, V. Steinmann, H. Bürckstümmer, J. Hwang, D. Hertel, F. Würthner, K. Meerholz, *Adv. Mater.* **2010**, *22*, 4193; (c) N. Kronenberg, M. Deppisch, F. Würthner, H. W. A. Lademann, K. Deing, K. Meerholz, *Chem. Commun.* **2008**, 6489.

[20] (a) M. Brumbach, D. Placencia, N. R. Armstrong, *J. Phys. Chem. C* **2008**, *112*, 3142; (b) Y. Tanaka, K. Kanai, Y. Ouchi, K. Seki, *Chem. Phys. Lett.* **2007**, *441*, 63.

[21] (a) R. W. Lof, M. A. Vanveenendaal, B. Koopmans, H. T. Jonkman, G. A. Sawatzky, *Phys. Rev. Lett.* **1992**, *68*, 3924; (b) Z.-L. Guan, J. B. Kim, H. Wang, C. Jaye, D. A. Fischer, Y.-L. Loo, A. Kahn, *Org. Electron.* **2010**, *11*, 1779; (c) K. Kanai, K. Akaike, K. Koyasu, K. Sakai, T. Nishi, Y. Kamizuru, T. Nishi, Y. Ouchi, K. Seki, *Appl. Phys. A* **2009**, *95*, 309.

[22] (a) M. Kröger, S. Hamwi, J. Meyer, T. Riedl, W. Kowalsky, A. Kahn, *Org. Electron.* **2009**, *10*, 932; (b) M. Y. Chan, L. Lai, M. Lau, C. S. Lee, S. Lee, T. *Appl. Phys. Lett.* **2006**, *89*, 163515; (c) D.R. Lide, *Handbook of Chemistry and Physics, 75th ed*., CRC Press, Boca Raton, USA **1995**.

[23] (a) K. Schulze, C. Uhrich, R. Schüppel, K. Leo, M. Pfeiffer, E. Brier, E. Reinold, P. Bäuerle, *Adv. Mater.* **2006**, *18*, 2872; (b) H.-W. Lin, L.-Y. Lin, Y.-H. Chen, C.-W. Chen, Y.-T. Lin, S.-W. Chiu, K.-T. Wong, *Chem. Commun*. **2011**, *47*, 7872.

[24] B. W. D'Andrade, S. R. Forrest, A. B. Chwang, *Appl. Phys. Lett.* **2003**, *19*, 3858.

[25] V. D. Mihailetchi, J. Wildeman, P. W. M. Blom, *Phys. Rev. Lett.* **2005**, *94*, 1.

[26] B. P. Rand, J. Xue, S. Uchida, S. R. Forrest, *J. Appl. Phys*. **2005**, *98*, 124902.

[27] C. L. Braun, *J. Chem. Phys.* **1984**, *80*, 4157.

[28] A. Petersen, A. Ojala, T. Kirchartz, T. A. Wagner, F. Würthner, U. Rau, manuscript in preparation.

[29] M. Kemerink, J. M. Kramer, H. H. P. Gommans, R. A. J. Janssen, *Appl. Phys. Lett.* **2006**, *88*, 192108.

[30] K. Hinrichs, S. D. Silaghi, C. Cobet, N. Esser, D. R. T. Zahn, *Phys. Status Solidi B* **2005**, *242*, 2681.

[31] A. Ojala, A. Petersen, A. Fuchs, R. Lovrincic, C. Pölking, J. Trollmann, J. Hwang, C. Lennartz, H. Reichelt, W. Höffken, A. Pucci, P. Erk, T. Kirchartz, F. Würthner, *Adv. Funct. Mater*. **2011**, accepted.

[32] F. Weigend, R. Ahlrichs, *Phys. Chem. Chem. Phys*. **2007**, *7*, 3297.

[33] S. Beckmann, K.-H. Etzbach, P. Krämer, K. Lukaszuk, R. Matschiner, A. J. Schmidt, P. Schuhmacher, R. Sens, G. Seybold, R. Wortmann, F. Würthner, *Adv. Mater.* **1999**, *11*, 536

[34] S. L. Mayo, B. D. Olafson, W. A. Goddard, *J. Phys. Chem.* **1990**, *94*, 8897.

[35] (a) R. A. Marcus, *J. Chem. Phys.* **1956**, *24*, 966; (b) R. A. Marcus, *J. Chem. Phys*. **1957**, *26*, 872.

[36] Y. Yi, V. Coropceanu, J.-L. Brédas, *J. Mater. Chem.* **2011**, *21*, 1479.

[37] (a) Y. Ooyama, Y. Shimada, S. Inoue, T. Nagano, T. Fujikawa, K. Komaguchi, I. Imae, Y. Harima, *New. J. Chem.* **2011**, *35*, 111; (b) Y. Ooyama, Y. Shimada, Y. Kawaga, Y. Yamada, I. Imae, K. Komaguchi, Y. Harima, *J. Photochem. Phtobiol. A* **2009**, *203*, 177; (c) Y. Hao, X. Yang, J. Cong, H. Tian, A. Hagfeldt, L. Sun, *Chem. Commun.* **2009**, 4031.

[38] B. Walker, C. Kim, T.-Q. Nguyen, *Chem. Mater*. **2011**, *23*, 470.

[39] G. Wei, S. Wang, K. Sun, M. E. Thompson, S. R. Forrest, *Adv. Energy Mater.* **2011**, *2*, 184.

[40] R. Fitzner, E. Reinold, A. Mishra, E. Mena-Osteritz, H. Ziehlke, M. Pfeiffer, P. Bäuerle, *Adv. Funct. Mater*. **2011**, *21*, 897.

[41] A. J. Fry, *Laboratory Techniques in Electroanalytical Chemistry,* Marcel Dekker Ltd, New York, USA **1996**, p. 481.

[42] SHELXTL-program-package, Version 6.14, Bruker-AXS; G. M. Sheldrick, *Acta Cryst.* **2008**, *A64*, 112.

[43] R. M. A. Azzam, N. M. Bashara, *Ellipsometry and polarized light,* North-Holland, **1987**.

[44] M. Schubert, *Infrared Ellipsometry on semiconductor layer structures; Springer Tracts in Modern Physics*, Springer-Verlag Berlin, Heidelberg, Germany **2005**.

[45] M. Schubert, T. E. Tiwald, C. M. Herzinger, *Phys. Rev. B* **2000**, *61*, 8187.

[46] M. Schubert, C. Bundesmann, G. Jacopic, H. Maresch, H. Arwin, *Appl. Phys. Lett.* **2004**, *84*, 200.

[47] (a) J. P. Perdew, *Phys. Rev. B* **1986**, *33*, 8822; (b) A. D. Becke, *Phys. Rev. A* **1988**, *38*, 3098.

[48] R. Lovrincic, J. Trollmann, C. Pölking, A. Pucci, manuscript in preparation.

Chapter 7

Planar, Bulk and Hybrid Merocyanine/C_{60} Heterojunction Devices: A Case Study on Thin Film Morphology and Photovoltaic Performance

Abstract: The growth of a thermally deposited merocyanine (HB364) thin film can be modified through insertion of a transition metal oxide layer between an indium tin oxide (ITO) covered glass substrate and the dye film. Pure or V_2O_5 modified ITO substrates result in highly crystalline HB364 films where the dye molecules adopt an edge-on orientation. Changing the transition metal oxide layer to WO_3 or MoO_3 results in a less ordered dye film with a mixed growth of edge-on and face-on orientations. Planar HB364/C_{60} heterojunction (PHJ) solar cells are fabricated using the different transition metal oxides as the anode buffer layers. The devices with a pure ITO or a V_2O_5 modified anode demonstrate the highest power conversion efficiencies up to 2.7% that also outperform HB364:C_{60} bulk heterojunction (BHJ) devices (2.5%). Finally, HB364/ HB364:C_{60} hybrid heterojunction (HHJ) cells are fabricated showing the highest power conversion efficiency of 2.9%.[a]

[a] The atomic force microscopy scans were recorded at BASF Ludwigshafen by Katja Graf. The contact angle measurements were carried out at BASF Ludwigshafen by Dr. von Vacano. The HB364 was synthesized at University of Würzburg by Hannah Bürckstümmer. This Chapter has been previously published in *J. Mater. Chem.* **2011**, DOI:10.1039/C2JM14927C.

7.1 Introduction

Organic photovoltaics (OPV) is a merging concept for a cost efficient and an environment friendly energy source.[1] Compared to inorganic counterparts OPV has several advantages such as potentially very low production costs, vast diversity of active materials, and significantly thinner as well as lighter devices.

Two different device architectures, namely, a planar heterojunction (PHJ) and a bulk heterojunction (BHJ) are commonly used in OPV. The PHJ devices comprise of separately stacked donor (D) and acceptor (A) layers featuring a distinct heterointerface. In turn, in the BHJ cells, the donor and the acceptor are co-deposited in a common bulk film leading to fine intermixing of the components. The main advantage of the PHJ structure over the BHJ concept is the well defined p- and n-semiconducting layers which enable efficient collection of the photogenerated charges. However, because of the layered structure, the interface area between the D and A components is limited restricting the thickness of the photon absorbing layer to the exciton diffusion length of the absorber compound which is, typically, for organic small molecules 1-20 nm.[2] The exciton diffusion length is not usually considered the limiting factor in BHJ devices, due to the fine intermixing of the donor and acceptor components. However, an inadequate phase separation of D and A molecules results in dead ends as well as high resistive loses which are common problems in BHJ devices.[3]

A promising approach to improve the photon harvesting efficiency of PHJ devices is to alter the morphology of the light absorbing donor layer. Higher crystallinity is considered advantages for exciton and charge carrier transport and way also to improve the absorption coefficient if the molecules are deposited suitably with regard to the direction of the light. Furthermore, in an ideal growth situation, the donor layer may feature vertically grown rod-shaped crystallites with a width that is usually smaller than the exciton diffusion length and a height that is approximately half of the absorption length (Figure 1). Several different methods have been used to realize well ordered film structures in organic solar cells, such as vapor phase deposition,[4] substrate heating,[5] thermal annealing,[6] and solvent vapor soaking.[7] Additionally, templating the ITO surface with a thin organic layer[8] or adding a thin buffer film between the ITO electrode and the successive organic layer,[9] have proved to be efficient methods to enhance crystallinity of the overstanding donor film. Other functions of a thin buffer

layer are to alter the work function of the anode, and thus, to improve the charge collection from the deep lying highest occupied molecular orbital (HOMO) energy level of the donor material as well as to shield the successive organic layer from the highly reactive ITO surface.[10] A commonly used organic buffer material is poly(3,4-ethylenedioxythiophene):poly(styrenesulfonate) (PEDOT:PSS) copolymer but because of its acidity, the long term stability of the devices has proved to suffer from this treatment.[11] Alternative buffer materials to the PEDOT:PSS are transition metal oxides MoO_3,[10b] WO_3,[12] and V_2O_5[10b] which have shown high hole collection efficiencies as well as improved device stabilities in organic solar cells.

Merocyanine dyes have recently demonstrated remarkable progress in OPV devices.[13] The chromophores show very high absorption strengths which enable efficient solar light collection with a thin active layer structure. However, due to a still quite limited number of studies for these organic semiconductors, the relation between the thin film morphology and the solar cell performance is mostly unexplored.[14]

In this chapter, we investigate the influence of various transition metal oxide layers on the thin film morphology of a merocyanine dye (HB364) (Figure 1). We also fabricate planar heterojunction (PHJ) cells using the transition metal oxides as the anode buffer layer between the ITO electrode and the HB364 donor film. Furthermore, HB364:C_{60} BHJ and HB364/HB364:C_{60} hybrid heterojunction (HHJ) devices are prepared.

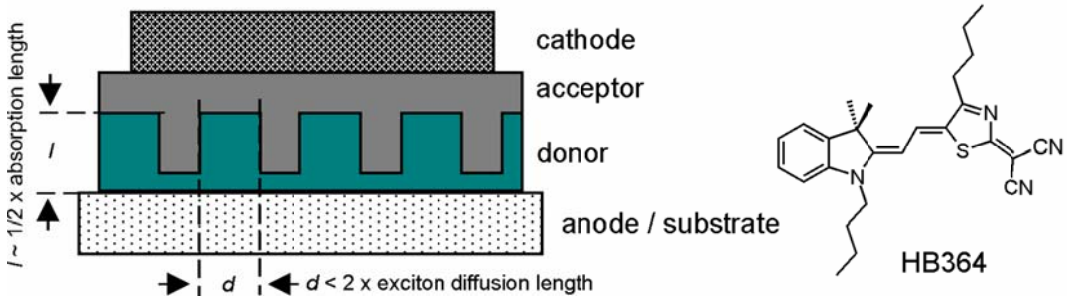

Figure 1. Idealized device architecture of PHJ cells and molecular structure of HB364.

7.2 Results and Discussion

7.2.1 Characterization of Thin Films

X-ray diffraction

The growth of HB364 neat films was investigated after insertion of a ~ 5 nm thick transition metal oxide layer between the HB364 film and the indium tin oxide (ITO) covered glass substrate. The samples were fabricated by depositing first a thin MoO_3, WO_3, or V_2O_5 layer (~ 5 nm) on an ITO substrate (cleaned in UV/O_3 oven at least 15 min), following the evaporation of a merocyanine (MC) HB364 layer with a nominal thickness of 10-40 nm. Additionally, also samples without the metal oxide layer were prepared. The results of the X-ray diffraction (XRD) scans of the 10 nm thick dye films on the different substrates are depicted in Figure 2a and analyzed in detail in Table 1. In the HB364 thin film diffraction graphs, the strong reflection at 2θ = 21.5° corresponds to the [211] diffraction plane of the crystalline ITO substrate[15] whilst the reflection at 2θ = 7.7° is attributed to the polycrystalline dye film. The 2θ = 7.7° reflection is observed with 10 nm thick dye films on the pure and V_2O_5 modified ITO substrates whereas the HB364 films on the WO_3 or MoO_3 modified ITO substrates do not show any coherent reflection arising from the dye layer.

Figure 2b depicts the XRD patterns of 20 nm thick HB364 layers on the different substrates. Deposition of the films on the pure and V_2O_5 modified ITO substrates result in strong 2θ = 7.7° reflections whose intensities are over doubled compared to the 10 nm thick films on the corresponding substrates. In the case of the pure ITO substrate, the peak width decreases as the film thickness increases indicating a more uniform particle size (see also Table 1). In turn, the width of the 2θ = 7.7° reflection on the V_2O_5 modified substrate does not substantially change when the HB364 film thickness increases from 10 to 20 nm. Furthermore, the dye film on the pure ITO substrate shows a very weak reflection at 2θ = 23.4° which is not observed in the graph of the V_2O_5 modified sample. In turn, the 20 nm thick dye films on the WO_3 and MoO_3 modified ITO substrates demonstrate two very weak diffractions at 2θ = 7.7° and at 2θ = 23.4°, respectively.

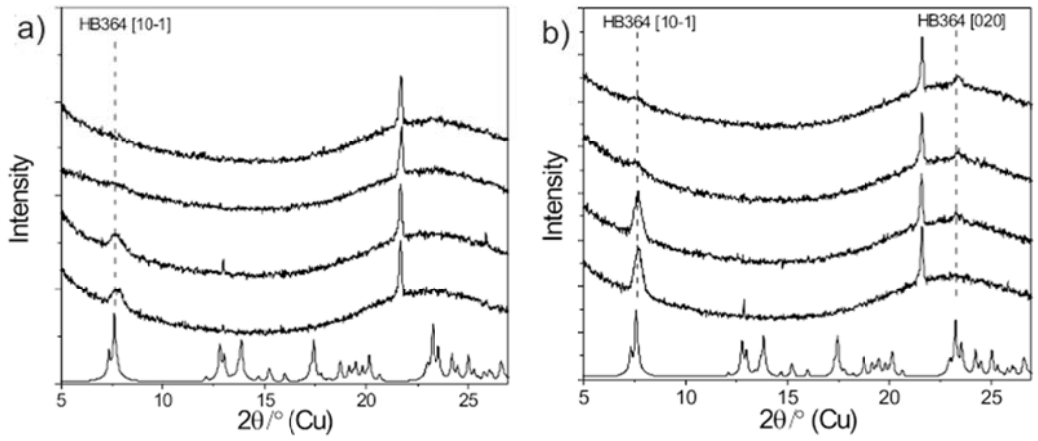

Figure 2. a) From bottom to top: a calculated X-ray diffraction (XRD) pattern of the HB364 single crystal structure as well as XRD scans of 10 nm thick HB364 neat films on ITO/-, ITO/V_2O_5, ITO/WO_3, and ITO/MoO_3 substrates. b) From bottom to top: a calculated XRD pattern of the HB364 single crystal structure as well as thin film XRD scans of 20 nm thick HB364 layers on ITO/-, ITO/V_2O_5, ITO/WO_3, and ITO/MoO_3 substrates. The strong peak at 2θ = 21.4° is attributed to the [211] reflection of the polycrystalline ITO substrate.[15]

Table 1. Results of the XRD scans of HB364 neat films on different substrates

Substrate	HB364 layer thickness (nm)	Intensity[a] of the 2θ = 7.7° peak	FWHM[b] of the 2θ = 7.7° peak	Intensity[a] of the 2θ = 23.4° peak	FWHM[b] of the 2θ = 23.4° peak
ITO/-	10	382	0.60	-	-
ITO/-	20	874	0.46	224	n/a[c]
ITO/-	40	1460	0.31	576	0.23
ITO/V_2O_5	10	363	0.48	-	-
ITO/V_2O_5	20	1010	0.45	-	-
ITO/MoO_3	10	-	-	-	-
ITO/MoO_3	20	n/a[c]	n/a[c]	240	n/a[c]
ITO/MoO_3	40	362	0.35	798	0.24
ITO/WO_3	10	-	-	-	-
ITO/WO_3	20	n/a[c]	n/a[c]	248	n/a[c]

[a] Counts; [b] Full-weight-half-maximum; [c] Too weak reflection.

Suitable crystals for a single crystal X-ray analysis were grown by slow evaporation of a dichloromethane (DCM)/heptane solution of the dye at 4 °C. The dye molecules were found to crystallize in P21/n space group with one molecule in the asymmetric unit. The unit cell features two antiparallel stacked chromophores showing a close π-π-contact (3.6 Å) between the acceptor heterocycles (Figure 3a). These dimers are further stacked in one dimensional columnar structures which grow along the 2-fold screw axis (*b*-axis). The calculated diffraction pattern of the single crystal structure is compared with the experimental neat film graphs in Figure 2. Based on the calculated peaks, the thin film reflections at 2θ = 7.7° and at 2θ = 23.4° are attributed to the [10-1] and [020] diffraction planes of the single crystal structure, respectively. The [10-1] reflection

originates from an orientation where the chromophores stand up with the long molecular axis in a tilt of ~ 60° to the substrate normal (i.e. "edge-on", Figure 3b) whilst the [020] diffraction plane corresponds to the orientation where the dyes' π-planes lie flat on the substrate (i.e. "face-on", Figure 3c). Interestingly, the 20 nm thick HB364 layers on the pure and V_2O_5 modified ITO substrates feature almost exclusively the edge-on arrangement whereas the WO_3 and MoO_3 modifications result in a mixed growth of the edge-on and face-on orientations (Figure 2b).

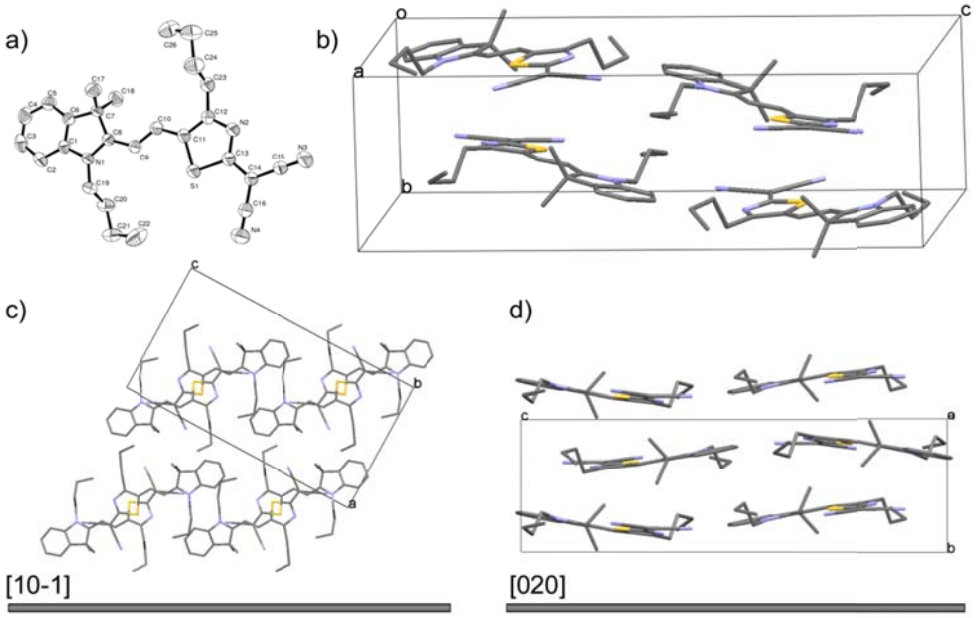

Figure 3. a) ORTEP drawing of HB364 with the 50% probability ellipsoids and atom labeling. b) Unit cell of the single crystal structure of HB364 and molecular packing with respect to the c) [10-1] and d) [020] diffraction planes (gray lines) viewed from the side.

To gain deeper understanding of the growth of HB364 neat films, also 40 nm thick dye layers were deposited on pure and MoO_3 modified ITO substrates (Figure 4). Furthermore, a sample with a 40 nm thick HB364 film on a 35 nm thick C_{60} layer was prepared. Deposition of HB364 layers on the pure or MoO_3 modified ITO substrates results in strong reflections at $2\theta = 7.7°$ and at $2\theta = 23.4°$. Compared to the 20 nm thick samples, the [020] diffraction at $2\theta = 23.4°$ is substantially strengthened in both cases. Notably, the dye film on the C_{60} modified substrate shows only the wide angle reflection whilst the low angle peak is completely absent.

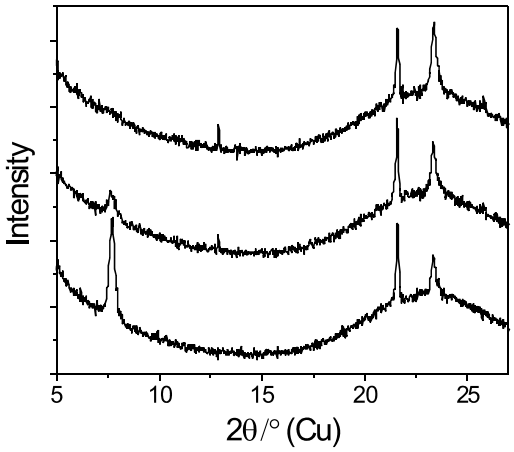

Figure 4. XRD scans of 40 nm thick HB364 films on (from bottom to top) ITO/-, ITO/MoO_3, and ITO/C_{60} substrates. The strong peak at 2θ = 21.4° is attributed to the [211] reflection of the polycrystalline ITO substrate.[15]

Surface energies

To investigate the surface properties, contact angles of water, formamide, and diiodomethane on a pure ITO substrate and after insertion of a thin (~ 5 nm) transition metal oxide layer on the ITO substrate were analyzed. Additionally, based on the obtained contact angles, surface energies E_{total} were calculated employing the method of Owens-Wendt.[16] An UV/O_3 treatment of the ITO substrate results in a highly hydrophilic surface with a water contact angle θ_{water} of 11° whereas the V_2O_5, WO_3, or MoO_3 modified (~ 5 nm film) ITO substrates demonstrate rather hydrophobic surfaces with θ_{water} of 66°, 73°, and 62°, respectively (Table 2). Correspondingly, the surface energy of the pure ITO substrate is substantially higher (71 mN/m) compared to the V_2O_5, WO_3, and MoO_3 modified substrates which demonstrate E_{total} of 51, 48, and 52 mN/m, respectively. As a comparison, surface energies of ITO substrates with and without a 10 nm thick WO_3 film of 48 and 72 mN/m, respectively, were reported previously.[12] According to Owens-Wendt analysis, the contributions of the disperse $E_{disperse}$ and the polar E_{polar} parts to the E_{total} between the transition metal oxide modified surfaces are similar (Table 2). In agreement with the molecular structure, the substrate with a 50 nm thick C_{60} layer shows a highly hydrophobic surface with only a marginal contribution of the E_{polar} part (0.5 mN/m) to the E_{total} (46 mN/m). Hence, we can conclude, that the dye molecules seem to prefer the edge-on orientation on highly hydrophilic substrates (e.g. ITO) whereas hydrophobic substrates (e.g. C_{60}) result in the face-on orientation. However, it is unclear why the molecules feature exclusively the [10-1] orientation on the V_2O_5 modified substrate whilst the MoO_3 and WO_3

modifications result in HB364 films with a low degree of crystallinity and a mixed growth of the [10-1] and [020] orientations.

Table 2. Contact angles θ for different solvents and calculated surface energies E of different substrates according to Owens-Wendt analysis[16]

Substrate	Water θ_{water} [°]	Formamide θ_{FM} [°]	Diiodomethane θ_{DM} [°]	$E_{disperse}$ [mN/m]	E_{polar} [mN/m]	E_{total} [mN/m]
ITO/-	11	2.7	28	44	26	71
ITO/MoO_3 (5 nm)	62	14	44	40	12	52
ITO/V_2O_5 (5 nm)	66	23	40	42	9.2	51
ITO/WO_3 (5 nm)	73	32	43	41	6.5	48
ITO/C_{60} (50 nm)	104	78	11	45	0.5	46

Atomic force microscopy

Atomic force microscopy (AFM) scans were recorded for nominally 10 nm thick HB364 neat films deposited on the different substrates (Figure 5). The dye film on a pure ITO substrate shows a particle size ranging from 10-40 nm and agglomerates of circa 65 nm. Deposition of HB364 on a MoO_3 modified substrate results in more homogeneous layer with a particle size of ~ 40 nm, whereas the HB364 film on a WO_3 modified substrate demonstrates a particle size of 30-65 nm. Crystallites with a size of 30-50 nm are observed in the dye film on a V_2O_5 modified substrate.

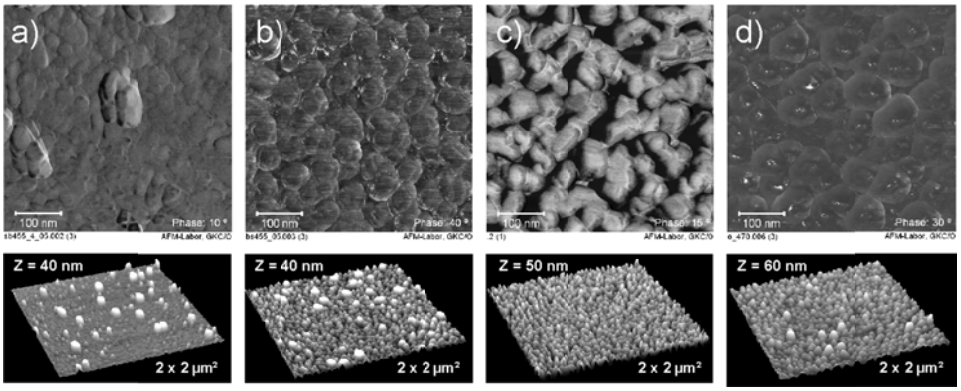

Figure 5. Atomic force microscopic phase (above) and 3D topographic (below) images of 10 nm thick HB364 films deposited on a) ITO/- , b) ITO/MoO_3, c) ITO/V_2O_5, and d) ITO/WO_3 substrates.

Absorption spectra

Figure 6a depicts the normalized absorption spectra of HB364 neat films (20 nm) on pure or MoO_3, V_2O_5, and WO_3 modified ITO substrates. Furthermore, absorption spectra of HB364 in dichloromethane and of a C_{60} neat film are shown. The solution spectrum features a strong ($\varepsilon_{max} = 1.32 \times 10^5$ M^{-1} cm^{-1}) but narrow absorption band with

a maximum at 618 nm and a smaller peak at 576 nm. In turn, deposition of the dye on the different substrates results in uniform and broad absorption bands ranging from 450-700 nm. Compared to the solution spectrum, a broadening of the band and alternations of the vibronic progressions are observed that are indicative of excitonic coupling between molecular transition dipoles in the solid state. According to the excitonic coupling theory, π-stacked molecules with strongly interacting π-orbitals are expected to show hypsochromically shifted absorption bands with respect to the monomeric spectra.[17] Correspondingly, in previous solution studies with MCs, a hypsochromic shift in the absorption spectrum has been attributed to an antiparallel face-to-face packing of chromophores (H-type aggregation).[18] Hence, the predominantly hypsochromic shift in the thin film absorption spectra ($\lambda_{max} \approx 593$ nm), with respect to the monomeric solution band of HB364 ($\lambda_{max} = 616$ nm), can be attributed to H-type coupling of the dye molecules that originates from closely packed antiparallel dimers as observed in the single crystal.

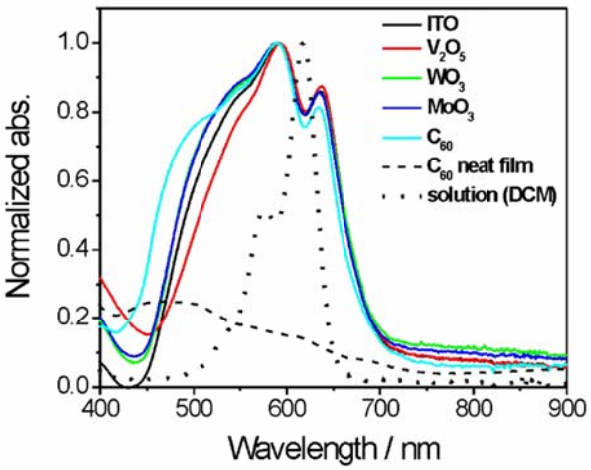

Figure 6. Absorption spectra of 20 nm thick HB364 films on different substrates. The solution spectrum of HB364 in dichloromethane (dotted line) and the neat film spectrum of C_{60} (dashed line) are also shown.

The absorption coefficient α of the dye films on a pure ITO substrate as well as on V_2O_5 and MoO_3 modified substrates is circa 2.3×10^5 cm^{-1} at $\lambda = 593$ nm whereas deposition of the dye film on a WO_3 modified substrate results in $\alpha_{593} \approx 1.7 \times 10^5$ cm^{-1}. These absorption coefficients are very high, which is attributed to the nearly perpendicular orientation of the dipole transition vectors of the molecules with respect to the incident light.

As shown above, orientation of HB364 molecules is dependent on the substrate modification. Previous studies with copper phthalocyanine (CuPC) have shown, that the molecules either stand edge-on or lie face-on on the substrate depending on the chromophore-surface interactions.[9,19] On weakly interacting surfaces (such as ITO and SiO_2) the chromophores prefer edge-on arrangement whereas strong interactions (e.g. with PTCDA or CuI) force the molecules to face-on alignment. Furthermore, orientation of the first chromophore layers on the substrate has been observed to control the growth of the whole crystalline CuPc film.[19]

Correspondingly, the observed preferred growth of HB364 films on the different substrates are attributed to dye-surface interactions. As shown above, the 10 nm thick HB364 layer on the pure ITO substrate features only the [10-1] reflection suggesting that only the edge-on orientation is present. However, when the thickness of the HB364 layer increases (> 10 nm), the relative strength of the large angle [020] reflection increases as well (Table 1). This may be rationalized by assuming that the first dye layers on the weakly interacting ITO substrate adopt the edge-on orientation which triggers the growth of the [10-1] crystallites. However, when the HB364 film thickness increases (> 10 nm) and the ITO substrate is fully covered with the dye, the successive molecules gradually adopt the face-on orientation which is, in turn, observed as enhancement of the [020] reflection. Instead, the C_{60} modified substrate shows only the [020] peak of HB364 which suggests that already the first dye layers on the C_{60} surface adopt the face-on arrangement. This may be explained by the strong dispersive interactions between the π-systems of the dye and C_{60} molecules.

7.2.2 Solar Cells

In the second part of this chapter, the effect of transition metal oxide buffer layers on the performance of HB364/C_{60} PHJ solar cells is presented. As a comparison also HB364:C_{60} bulk heterojunction (BHJ) and HB364/HB364:C_{60} hybrid heterojunction (HHJ)[20] devices were fabricated (Figure 7). As shown above, the orientation and the degree of crystallinity of the dye film can be altered by changing the underlying layer. The crystalline donor layers are expected to show several benefits over the less crystalline counterparts such as i) better charge transport properties,[21] ii) longer exciton diffusion lengths,[2b] and iii) improved photon collection efficiencies due to the larger interface areas.[6]

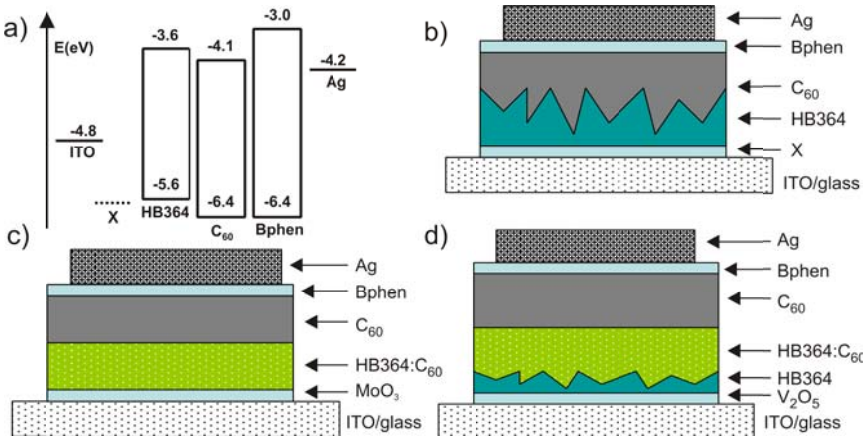

Figure 7. a) Energy level diagram of the used materials. Schematic presentation of the layered device architectures of the fabricated b) PHJ, c) BHJ, and d) HHJ cells. The anode buffer layer (X) was MoO_3,[10b] WO_3, [12] and V_2O_5.[10b]

Energy level diagram

The energy level diagram of the used materials is depicted in Figure 7a. The HOMO level (-5.6 eV) of HB364 is obtained from a cyclic voltammetric measurement and the lowest unoccupied molecular orbital (LUMO) level is estimated by subtracting the optical bad gap (E_g) from the experimental HOMO level. The E_g is taken from the absorption maximum (λ_{max} = 616 nm) in DCM yielding the LUMO level of -3.6 eV. Previously reported HOMO levels (E_{HOMO}) of MoO_3, WO_3, and V_2O_5 are -5.3, -5.1, and -4.7 eV, respectively.[10b,12] Note, that the energy level positions of MoO_3 are under discussions, and for example, Kahn and co-workers have proposed E_{HOMO} = -6.7 eV.[22] Irrespective of the exact position of the energy levels, transition metal oxides have successively been used to replace the commonly employed anode buffer layer PEDOT:PSS (E_{HOMO} = -5.2 eV) in OPV devices.[12] The energy levels of C_{60} and Bphen are taken from literature.[22,23]

PHJ devices

The influence of the transition metal oxide layer on the performance of HB364/C_{60} PHJ devices was investigated. The used device architecture was ITO/X (0 or 5 nm)/HB364 (5-20 nm)/C_{60} (35 nm)/Bphen (5 nm)/Ag (100 nm), where the thickness of the HB364 layer was changed in steps of 5 nm from 5-20 nm (Figure 7b). The buffer layer X was a ~ 5 nm thick film of MoO_3, WO_3, or V_2O_5. In addition, also devices without the metal oxide layer were fabricated. From now on, we refer to the different devices by the buffer layer and the cells without a transition metal oxide film are called ITO.

Table 3 shows the key cell parameters of the average PHJ devices and the corresponding current-voltage (*J-V*) characteristics are illustrated in Figure 8. Moreover, Figure 9 illustrates the dependence of the key device characteristics of the best PHJ cells on the donor layer thickness. The ITO, MoO_3, and WO_3 devices feature the highest power conversion efficiency (PCE) with a 5 nm thick donor layer whereas the optimal HB364 film thickness of the V_2O_5 cells is 10 nm. The V_2O_5 devices with a 10 nm thick donor layer show open circuit voltage (V_{OC}) of 740 mV, short circuit current (J_{SC}) of 5.3 mA cm^{-2} and fill factor (FF) of 68% yielding PCE of 2.7% that is the highest value among the PHJ devices. Instead, the WO_3 cells demonstrate clearly the lowest PCE of 1.8% which is mainly attributed to the low V_{OC} of 527 mV.

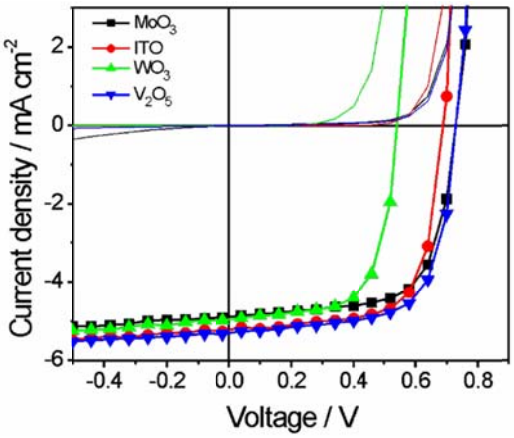

Figure 8. *J-V* characteristics of PHJ cells with different anode buffer layers. The HB364 donor layer thickness was 5 nm (MoO_3, ITO, and WO_3) and 10 nm (V_2O_5). Photocurrents under AM 1.5, 100 mW cm^{-2} conditions are indicated by lines and symbols, corresponding dark curves are shown with solid lines.

Table 3. Device characteristics of the average HB364 solar cells under AM 1.5, 100 mW cm^{-2} illumination

Device type	Anode	Active layer thickness [nm]	V_{OC} [mV]	J_{SC} [mA cm^{-2}]	FF [%]	PCE [%]
PHJ	ITO/-	5	690 ±10	5.35 ±0.1	69.0 ±0.2	2.53 ±0.05
PHJ	ITO/MoO_3 (5 nm)	5	735 ±10	4.94 ±0.04	66.7 ±0.04	2.42 ±0.03
PHJ	ITO/V_2O_5 (5 nm)	5	705 ±10	4.80 ±0.04	66.7 ±0.8	2.40 ±0.02
PHJ	ITO/V_2O_5 (5 nm)	10	740 ±10	5.30 ±0.06	68.0 ±2	2.70 ±0.1
PHJ	ITO/WO_3 (5 nm)	5	527 ±20	4.98 ±0.06	62.6 ±6	1.60 ±0.2
BHJ	ITO/MoO_3 (5 nm)	30	705 ±10	7.64 ±0.07	45.9 ±0.6	2.47 ±0.02
HHJ	ITO/V_2O_5 (5 nm)	5/20	740 ±10	7.03 ±0.05	54.4 ±0.7	2.85 ±0.02

The V_{OC} of the ITO and V_2O_5 devices stay constant or slightly increases when the active layer thickness increases. Instead, the V_{OC} of the MoO_3 and WO_3 cells gradually decreases with the increasing donor layer thickness (Figure 9). All devices show similar

J_{SC} values at donor layer thicknesses of 5 and 10 nm. The ITO cells give J_{SC} of 5.4 mA cm^{-2}, a value that is already reached at the donor layer thickness of 5 nm. Increasing the donor layer thickness beyond 10 nm results in a decrease in J_{SC} for all devices. The J_{SC} of the WO_3 cells decreases fastest beyond a donor layer thickness of 10 nm. Furthermore, all devices show a decrease of the fill factor upon increasing the layer thickness. Because this decrease is, however, least pronounced for V_2O_5 cells, these devices are the only ones whose highest PCE is reached at the active layer thickness of 10 nm. The efficiency value of 2.7% is also the best one among all our measured PHJ solar cells.

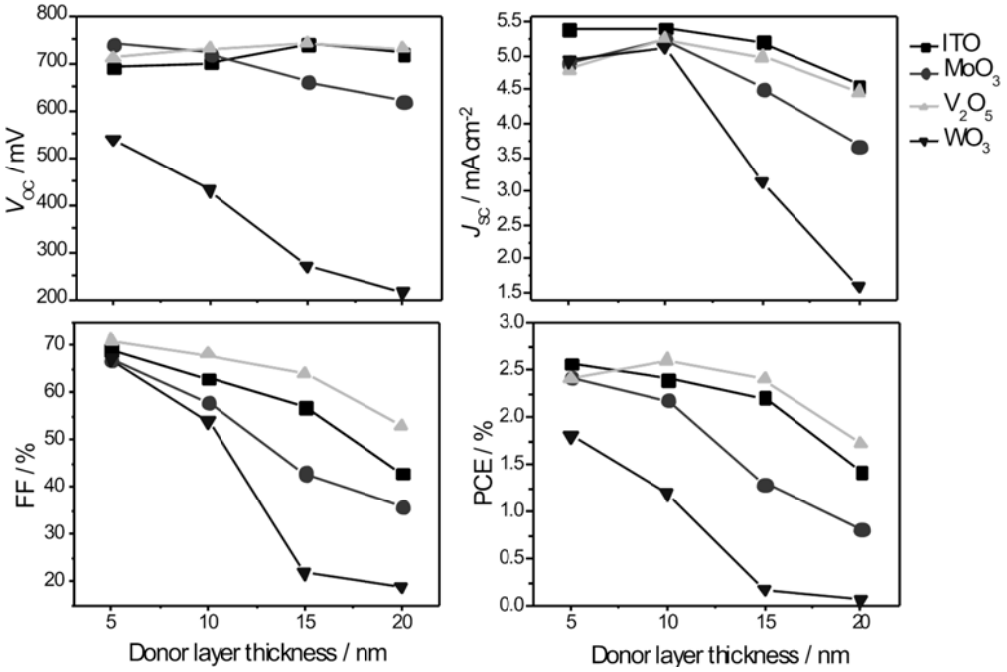

Figure 9. Dependence of the key device parameters of the best PHJ cells on the donor layer thickness. The lines are to guide the eye.

With the exception of the J_{SC} dependence we always observed the larges differences between the devices prepared on WO_3 and V_2O_5 covered substrates in Figure 9. For this reason a closer look on *J-V* characteristics of the WO_3 and V_2O_5 cells with the 10 and 20 nm thick donor layers is particularly interesting (Figure 10). The WO_3 cells, with the 10 nm thick donor layer, show "normal" *J-V* characteristics whereas the 20 nm thick cells demonstrate S-shaped curves. Instead, both the 10 and 20 nm thick V_2O_5 cells feature "normal" *J-V* curves (Figure 10a). Correspondingly, fill factor of the WO_3 cells drops from 55 to 18% when the donor layer thickness increases from 10 to 20 nm, respectively, whilst the FF of the V_2O_5 cells decreases only from 68 to 53% for the

same donor layer thicknesses. The sudden drop of the FF and formation of the S-kink in the *J-V* characteristics of the WO_3 devices are attributed to bad hole transport characteristics of the active layers. This is illustrated in Figure 10b that depicts the dark curves of the corresponding V_2O_5 and WO_3 cells at the forward current range. By looking at the dark curves, it is evident that the charge transport properties of the WO_3 cells with 20 nm thick donor layers are significantly lower compared to the V_2O_5 devices with the same donor layer thicknesses. This is also observed in the series resistance R_S (estimated from the slope (dV/dJ) close to V = 1.5 V) of the WO_3 cells which increases from 16 to 2100 Ω cm^2 when the active layer thickness rises from 10 to 20 nm, respectively. The corresponding R_S of the V_2O_5 devices are 11 and 72 Ω cm^2. The poor hole transport properties of the WO_3 cells may be explained by the HB364 neat film structure (Figure 2). The 10 nm thick dye film on the WO_3 modified substrate is amorphous whilst the 20 nm thick film features mixed growth of the [10-1] and [020] preferred orientations. In turn, both the 10 nm and 20 nm thick HB364 films on the V_2O_5 modified substrates show a single strong peak which is attributed to the [10-1] reflection. The low degree of crystallinity and the mixed growth of the preferred orientations on the WO_3 modified substrates are expected to result in a more pronounced energetic disorder. Hence, the poor hole mobility results in an imbalanced charge transport of the holes and the electrons which is observed as the S-kinks in the illuminated *J-V* characteristics.[24] Instead, the highly crystalline donor films on the V_2O_5 modified substrates result in a more balanced charge transport, and thus, a higher FF in the PHJ devices.

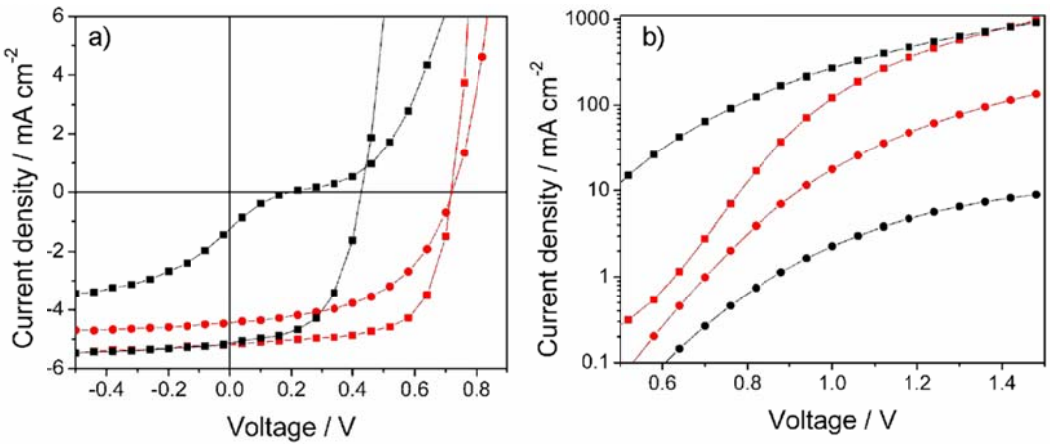

Figure 10. a) *J-V* characteristics under AM 1.5 100 mW cm^{-2} illumination of the PHJ cells with WO_3 (black) and V_2O_5 (red) anode buffer layers. The HB364 donor layer thickness is 10 (square) and 20 (circle) nm. b) Dark *J-V* characteristics of the corresponding devices.

Figure 11a depicts the absorption spectra (measured in reflectance mode) of ITO devices with nominally 5 and 10 nm thick donor layers. Due to the high absorption coefficient of the HB364 film, the absorption of the PHJ cells is extremely high as well. However, irrespective of the two times higher absorption strength (at 590 nm) of the cells with a 10 nm thick donor layer the J_{SC} is only marginally (~ 0.1 mA cm^{-2}) higher compared to the devices with a 5 nm thick donor layer.

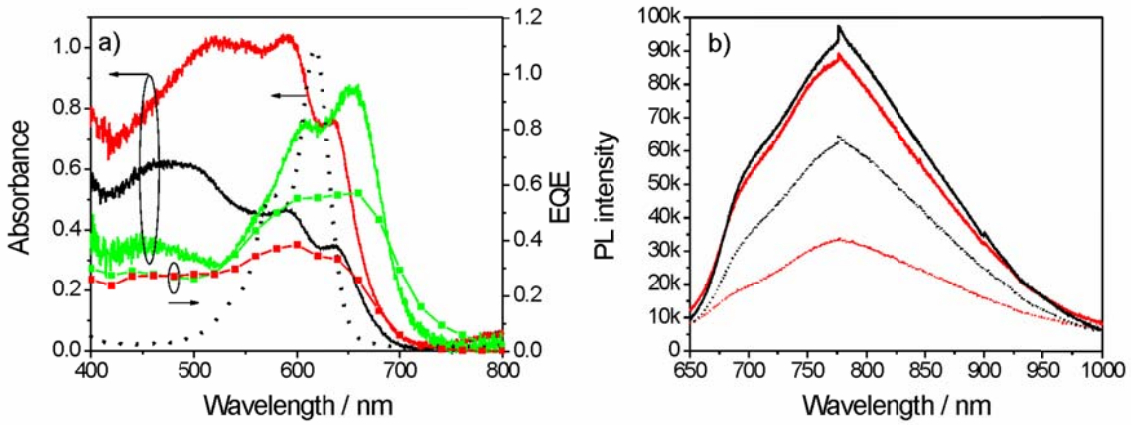

Figure 11. a) Absorption spectra of the ITO PHJ devices with nominally 5 (black) and 10 (red) nm thick donor layers and of the BHJ device with a 30 nm (green) thick HB364:C_{60} layer. The external quantum efficiencies (EQE) of the ITO PHJ (red squares) and the BHJ (green squares) cells with a 10 thick donor layer and with a 30 nm thick HB364:C_{60} layer, respectively. Absorption spectrum of HB364 in DCM is shown by the black dotted line. b) Photoluminescence (PL) spectra of 5 (black) and 10 nm (red) thick HB364 films with (dotted lines) and without (solid lines) a 5 nm thick C_{60} quenching layer on ITO substrates.

The marginal improvement in J_{SC}, when the donor layer thickness increases from 5 to 10 nm, can be explained by the structure of the donor film (Figure 5).The film shows an island like growth of crystallites of a size beyond the typical exciton diffusion length of organic small molecules (1-20 nm)[2]. Therefore, it is likely that a major part of the formed excitons upon illumination are not able to reach the D/A interface which, in turn, explains the marginal improvement in J_{SC} when the donor layer thickness increases. In order to investigate this possibility, photoluminescence (PL) spectra of 5 and 10 nm thick dye films with and without a 5 nm thick C_{60} exciton quenching layer were recorded (Figure 11b). Despite the overlap of the excitation wavelength (the 532 nm line of an Ar laser) and the C_{60} absorption band, the contribution of the C_{60} layer to the PL intensity is assumed to be negligible. The 5 and 10 nm thick dye films without the quenching layer demonstrate similar emission bands with a maximum at 775 nm.

However, deposition of the C_{60} quenching layer on top of the 5 nm thick dye film results in an emission band with 30% of the original PL intensity. In turn, the 10 nm thick HB364 film with the overstanding C_{60} layer shows a significantly higher residual emission (65% of the intensity of the sample without the quenching layer). These results clearly demonstrate that the exciton quenching is more efficient in devices with a 5 nm thick donor layer. Furthermore, both thin films with the quenching layer show significant residual PL intensities suggesting that a substantially higher J_{SC} could be achieved by a better control over the particle size of the donor layer in HB364/C_{60} PHJ devices.

BHJ devices

For comparison also bulk heterojunction (BHJ) devices were fabricated with a following cell architecture: ITO/MoO_3 (5 nm)/HB364:C_{60} (10-40 nm)/C_{60} (25 nm)/BPhen (5 nm)/Ag (100 nm), where the thickness of the active layer (HB364:C_{60} 40:60 by weight) was changed in steps of 10 nm from 10-40 nm (Figure 7c). The *J-V* characteristics of the BHJ devices are depicted in Figure 13a and Figure 15 shows the key device parameters with respect to the active layer thickness. The J_{SC} improves from 4.4 to 7.7 mA cm^{-2} when the active layer thickness increases from 10-30 nm, respectively, whilst the FF decreases from 65 to 45%. The PCE (2.5%) is maximized at the active layer thickness of 30 nm (see rest of the device parameters in Table 3).

The absorption spectrum of the BHJ devices with a 30 nm thick active layer (HB364:C_{60}) is depicted in Figure 11a. The absorption band is remarkably different from those of PHJ devices and resembles the solution spectrum with a clear maximum at 655 nm and a shoulder at 610 nm. The solution-like spectrum suggests an amorphous film structure. Hence, the donor phase does not grow into large crystalline domains as seen for the thin films because the donor and acceptor components are finely intermixed in the active layer enabling efficient exciton collection at the D/A heterointerface in the BHJ cells. Indeed, despite the lower absorption of the BHJ cells (Figure 11a), the J_{SC} of the best devices is approximately 30% higher compared to the best PHJ cells. However, the fill factor of the BHJ devices is lower and strongly dependent on the HB364:C_{60} layer thickness which is attributed to the poor charge transport properties of the amorphous active layer. Consequently, the PCE (2.5%) of the best BHJ devices remains below the best PHJ cells (2.7%).

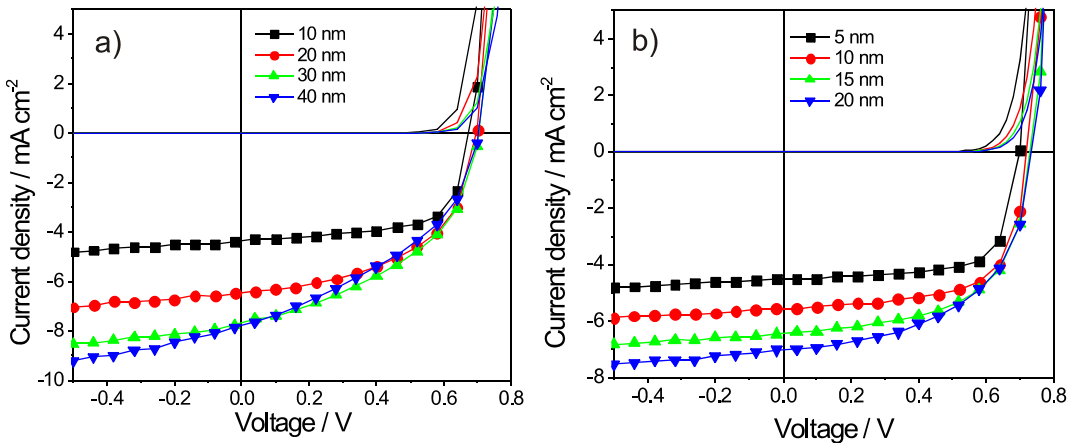

Figure 13. a) *J-V* characteristics under AM 1.5, 100 mW cm^{-2} illumination of a) BHJ and b) HHJ devices with different HB364:C_{60} layer thicknesses (lines and symbols) and the corresponding dark curves (lines).

Hybrid HJ devices

As shown above, the short circuit current density of the BHJ devices is clearly higher compared to the PHJ cells. However, the PCE stays modest because of the poor FF which is attributed to the weak charge transport properties of the amorphous active layer in the BHJ cells. In order to improve the photon harvesting efficiency of the cells but at the same time maintain good FF, hybrid heterojunction (HHJ)[20] devices were fabricated. The HHJ cells present the following device architecture: ITO/V_2O_5 (5 nm)/HB364 (5 nm)/HB364:C_{60} (5-20 nm)/C_{60} (35 nm)/Bphen (5 nm)/Ag (100 nm) (Figure 7d). The thickness of the HB364 layer was fixed to 5 nm which is a compromise between the photon collection efficiency and the charge transport property of the film.

Figure 13b demonstrates the *J-V* characteristics of the HHJ devices and Figure 14 shows the evolution of the key devices parameters with respect to the active layer thickness. Every cell parameter of the HHJ devices shows improvement compared to the BHJ cells with the same HB364:C_{60} layer thickness. The best HHJ cells with 15 and 20 nm thick HB364:C_{60} active layers demonstrate PCE of 2.9% which is clearly higher than the highest PCE (2.5%) of the BHJ cells. However, compared to the best PHJ devices (2.7%) the efficiency improvement is small. This is attributed to the rapidly declining FF of the HHJ cells, with increasing HB364:C_{60} layer thickness, which is only partially compensated by the improvement of J_{SC}.

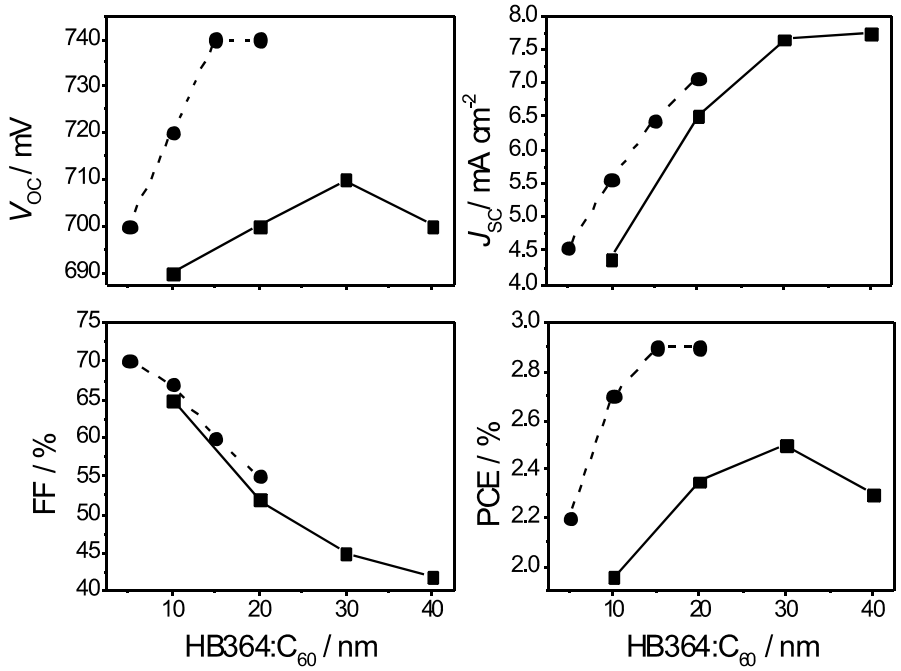

Figure 14. Dependence of the key device parameters on the active layer (HB364:C_{60}) thickness in the BHJ (squares) and HHJ (circles) cells. The lines are to guide the eye.

7.3 Conclusions

We have shown that the morphology of HB364 merocyanine thin films can be modified through insertion of a transition metal oxide layer between the ITO covered glass substrate and the dye film. We have also shown that deposition of the molecules on a pure or V_2O_5 modified ITO substrate result in highly crystalline dye films where the chromophores have adopted an edge-on orientation with respect to the substrate surface. In turn, the merocyanine films on WO_3 or MoO_3 modified ITO surfaces exhibit a lower degree of crystallinity as well as a simultaneous growth of the edge-on and face-on orientations. A highly crystalline film showing exclusively the face-on arrangement is obtained when the dye molecules are deposited on top of a C_{60} layer.

Planar heterojunction HB364/C_{60} devices were fabricated employing the transition metal oxides as the anode buffer layers. The PHJ devices with a pure ITO or V_2O_5 modified anode demonstrated the highest device performances up to 2.7% whereas the efficiency of the devices with a WO_3 buffer layer was clearly inferior. The best PHJ cells outperformed also the HB364:C_{60} bulk heterojunction (BHJ) cells whose efficiency reached 2.5%. However, despite the broader and stronger absorption of the PHJ devices, the J_{SC} remained lower compared to the BHJ cells. This was explained by

the particle size of the HB364 donor film which is larger than the exciton diffusion length of the dye. Finally the highest power conversion efficiency of 2.9% could be achieved with the HB364/HB364:C_{60} hybrid heterojunction device architecture.

7.4 Experimental Section

Synthesis

The HB364 2-{4-Butyl-5-[2-(1-butyl-3,3-dimethyl-1,3-dihydro-indol-2-ylidene) ethylidene]-5H-thiazol-2-ylidene}-malononitrile was synthesized by heating a 8 mL Ac_2O solution of (1-*n*-butyl-3,3-dimethyl-1,3-dihydro-indol-2-ylidene)-acetaldehyde (1.98 g, 8.0 mmol) and 2-(4-tert-butyl-5H-thiazol-2-ylidene)-malononitrile (1.50 g, 7.3 mmol) to 90 °C for 95 min after which *n*-hexane was added and the solution was decanted. After cooling to room temperature the precipitate was collected, washed with iso-propanol, and recrystallized from CH_2Cl_2/*n*-hexane. **Yield**: 2.24 g (5.2 mmol, 71%), dark blue solid. **1H NMR** (CD_2Cl_2, 400 MHz): δ 7.97 (d, 3J = 13.5 Hz, 1H), 7.40 (m, 2H), 7.26 (m, 1H), 7.09 (m, 1H), 5.72 (d, 3J = 13.6 Hz, 1H), 2.89 (m, 2H), 1.79 (m, 2H), 1.69 (s, 6H), 1.48 (m, 2H), 1.00 (t, 3J = 7.4 Hz, 3H). **UV/Vis** (CH_2Cl_2): λ_{max} : 618 nm (137100 M^{-1} cm^{-1}). **HRMS** (ESI): calcd. for $C_{26}H_{30}N_4S$ $[M]^+$: 430.2191, found: 430.2185. **Elemental analysis (%)** calcd**.** for $C_{26}H_{30}N_4S$: C, 72.52; H, 7.02; N, 13.01; S, 7.45. Found: C, 72.56; H, 7.02; N, 13.02; S, 7.42.

Atomic force microscopy

Atomic force microscopy (AFM) experiments (Dimension 5000 Microscope, Veeco Instruments) were performed with silicon cantilevers from Olympus type OMCL-AC160TS (Tokyo, Japan). For more details of the measurements, see section 6.4 of this thesis.

X-ray powder diffraction

X-ray powder diffraction (XRPD) graphs of the thin films were recorded by a PANalytica's X'Pert Pro MPD diffractometer employing Cu K_α radiation (λ =1.542 nm). A typical scan was from 3-35° (2θ) with a step size of 0.017° and a counting time of 100 s/step. The samples were prepared on a cleaned (15 min at an UV/O_3 oven) ITO covered glass substrates by depositing a ~ 5 nm thick transition metal oxide layer,

following a 5-40 nm thick HB364 film. The deposition rate of the HB364 layer was 0.3 Å/s.

Single crystal analysis

Deep blue block crystals were grown by a slow evaporation of dichloromethane/hexane solution of the dye at 4 °C. The data was collected at 296 K with a Bruker AXS CCD detector, using a graphite-monochromated Cu K_α (λ = 1.51478 Å) radiation. The structure was solved by direct method and refined on full-matrix-least-square method, using 3402 unique reflections and 285 parameters.[25] All non-hydrogen atoms were anisotropically refined and hydrogen atoms were placed on idealized positions. The measurement angle was from $2\theta_{min}$ = 3.65° to $2\theta_{max}$ = 57.29°. The analyzed crystal belongs to monoclinic crystal system with the cell dimensions a = 13.1462(17) Å, b = 7.6460(11) Å and c = 24.1006(32) Å and the angle β = 91.010(4)°. The space group is P21/n with Z = 4. The final R_1 is 0.0493 and the weighted R_1 is 0.1242. The goodness-of-fit (GooF) for the solution is 1.078.

UV/vis absorption spectra

Absorbance spectra of the HB364 films were recorded in transmission mode employing a HR2000+ spectrometer (OceanOptics) and a Xe lamp as the light source. The absorption measurements of the devices were performed in reflectance mode employing HR2000+ spectrometer and an integrating sphere.

Cyclic voltammetry

CV was performed on a standard commercial electrochemical analyzer (EC epsilon; BAS Instrument, UK) in a three electrode single-compartment cell under argon. Dichloromethane (HPLC grade) was obtained from J. T. Baker (Mumbai, India) and dried over calcium hydride and degassed prior to use. The supporting electrolyte tetrabutylammonium hexafluorophosphate (TBAHFP) was recrystallized from ethanol/water and dried in high vacuum. The measurements were carried out under exclusion of air and moisture at a concentration of 10^{-4} M with ferrocene as internal standard for the calibration of the potential. Working electrode: Pt disc; reference electrode: Ag/AgCl; auxiliary electrode: Pt wire. The reversible half wave potential $E_{1/2}$ of the ferrocene/ferrocenium redox couple was associated with a HOMO orbital level of -5.15 eV.

Wetting analyses

Contact angles were measured with a standard drop shape analysis instrumentation (DSA 10, Kruss Germany). Reported values are advancing contact angles: A drop of the test liquid was placed on the sample surface and continuosly fed at 2 µl/min flow rate up to 20 µL total liquid volume. Starting from a minimum of about 3 µL, contact angles were measured while the syringe needle used for dosing remained in the droplet. Drop shape images were analyzed at a rate of ~ 0.5 Hz, evaluated by a tangent method to determine the contact angle only from the parts of the image directly at the three-phase contact line. These contact angles were averaged over time: For each sample, five advancing droplets were measured at different positions and the average value is reported.

Device fabrication

Planar heterojunction (PHJ) solar cells with different transition metal oxide anode buffer layers were fabricated on prestructured indium tin oxide (ITO) covered glass substrates with a cell area of 0.04 cm^2. The devices were prepared by a thermal evaporation in a high vacuum (~ 2×10^{-6} mbar) chamber (Lesker Ltd). Prior to the fabrication of the cells, the ITO substrates were cleaned in an UV/O_3 oven for 15 min after which they were transferred into the vacuum chamber. All layers were successively deposited at substrate temperature of 25 °C without breaking the vacuum in between the fabrication steps. The HB364 neat films as well as the donor films in the PHJ and HHJ devices were deposited at the rate of 0.3 Å/s. All other organic and transition metal oxide layers were deposited at the rate of 1 Å/s. The silver cathode layers were evaporated at the rate of 4 Å/s.

Device characterization

Current-voltage (*J-V*) characteristics were recorded with a Keithley 2425 measurement unit at 25 °C in ambient air. During the *J-V* measurements, the cells were illuminated by 1.5 AM filtered light with intensity of 100 W/cm². The light intensity was set with a calibrated Si-photodiode. The cell degradation during the measurements was observed to be negligible.

7.5 References

[1] G. Dennler, M. C. Scharber, C. J. Brabec, *Adv. Mater.* **2009**, *21*, 1323.

[2] (a) R. R. Lunt, N. C. Giebink, A. A. Belak, J. B. Benzinger, S. R. Forrest, *J. Appl. Phys*. **2009**, *105*, 053771; (b) R. R. Lunt, J. B. Benziger, S. R. Forrest, *Adv. Mater*. **2010**, *22*, 1233.

[3] P. W. M. Blom, V. D. Mihailetchi, L. J. A. Koster, D. E. Markov, *Adv. Mater*. **2007**, *19*, 1551.

[4] F. Yang, M. Shtein, S. R. Forrest, *Nature* **2005**, *4*, 37.

[5] Y.-S. Hsiao, W.-T. Whang, S.-C. Suen, J.-Y. Shiu, C.-P. Chen, *Nanotech.* **2008**, *19*, 415603.

[6] G. Wei, R. R. Lunt, K. Sun, S. Wang, M. E. Thompson, S. R. Forrest, *Nano Lett.* **2010**, *10*, 3555.

[7] D. Placencia, W. Wang, R. C. Shallcross, K. W. Nebesny, M. Brumbach, N. R. Armstrong, *Adv. Funct. Mater*. **2009**, *19*, 1.

[8] K. V. Chauhan, P. Sullivan, J. L. Yang, T. S. Jones, *J. Phys. Chem. C* **2010**, *114*, 3304.

[9] C. H. Cheng, J. Wang, G. T. Du, S. H. Shi, Z. J. Du, Z. Q. Fan, J. M. Bian, M. S. Wang, *Appl. Phys. Lett.* **2010**, *97*, 083350.

[10] (a) Irfan, H. Ding, Y. Gao, D. Y. Kim, J. Subbiah, F. So, *Appl. Phys. Lett*. **2010**, *96*, 073304; (b) V. Shrotriya, G. Li, Y. Yao, C.-W. Chu, Y. Yang, *Appl. Phys. Lett.* **2006**, *88*, 073508.

[11] M. P. de Jong, L. J. van IJzendoorn, M. J. A. de Voigt, *Appl. Phys. Lett.* **2000**, *77*, 2255.

[12] S. Han, W. S. Shin, M. Seo, D. Gupta, S.-J. Moon, S. Yoo, *Org. Electron*. **2009**, *10*, 791.

[13] N. M. Kronenberg, V. Steinmann, H. Bürckstümmer, J. Hwang, D. Hertel, F. Würthner, K. Meerholz, *Adv*. *Mater*. **2010**, *22*, 4193.

[14] F. Würthner, K. Meerholz, *Chem. Eur. J*. **2010**, *16*, 9366.

[15] D. Raoufi, A. Kiasatpour, H. R. Fallah, A. S. H. Rozatian, *Appl. Surf. Sci*. **2007**, *253*, 9085.

[16] D. K. Owens, R. C. Wendt, *J. Appl. Polym. Sci*. **1969**, *13*, 1741.

[17] (a) A. Mishra, R. K. Behera, P. K. Behera, B. K. Mishra, G. B. Behera, *Chem. Rev.* **2000**, *100*, 1973; (b) Z. Sainudeen, P. C. Ray, *J. Phys. Chem. A* **2005**, *109*, 9095.

[18] (a) F. Würthner, S. Yao, T. Debaerdemaeker, R. Wortmann, *J. Am. Chem. Soc.* **2002**, *124*, 9431; (b) A. Lohr, M. Grüne, F. Würthner, *Chem. Eur. J.* **2009**, *15*, 3691; (c) U. Rösch, S. Yao, R. Wortmann, F. Würthner, *Angew. Chem. Int. Ed.* **2006**, *45*, 7026.

[19] (a) H. Peisert, T. Schwieger, J. M. Auerhammer, M. Knupfer, M. S. Golden, J. Fink, P. R. Bressler, M. Mast, *J. Appl. Phys.* **2001**, *90*, 466; (b) P. Sullivan, T. S. Jones, A. J. Ferguson, S. Heutz, *Appl.Phys.Lett.* **2007**, *91*, 233114.

[20] (a) J. Xue, B. P. Rand, S. Uchida, S. R. Forrest, *J. Appl. Phys. Lett.* **2005**, *98*, 124903; (b) B. P. Rand, J. Li, J.G. Xue, R. J. Holmes, M. E. Thompson, S. R. Forrest, *Adv. Mater.* **2005**, *17*, 2714; (c) J. Xue, B. P. Rand, S. Uchida, S .R. Forrest, *Adv. Mater.* **2005**, *17*, 66.

[21] D. Kekuda, J.-H. Huang, K.-C. Ho, C.-W. Chu, *J. Phys. Chem. C* **2010**, *114*, 2764.

[22] M. Kröger, S. Hamwi, J. Meyer, T. Riedl, W. Kowalsky, A. Kahn, *Org. Electron*. **2009**, *10*, 932.

[23] Y. Chan, L. Lai, M. Lau, C. S. Lee, S. T. Lee, *Appl. Phys. Lett*. **2006**, *89*, 163515.

[24] (a) W. Tress, A. Petrich, M. Hummert, M. Hein, K. Leo, M. Riede, *Appl. Phys. Lett.* **2011**, *98*, 063301; (b) D. Kekuda, J.-H. Huang, K.-C. Ho, C.-W. Chu, *J. Phys.Chem. C* **2010,** *14*, 2764.

[25] SHELXTL-program-package, Version 6.14, Bruker-AXS; G. M. Sheldrick, *Acta Cryst.* **2008**, *A64*, 112.

Chapter 8

Summary

In this thesis, the relationship between the solid state packing and the solar cell performance of merocyanine dyes was investigated. X-ray diffraction and several other analytical methods were used to analyze the single crystal and thin film structures of merocyanines. The effect of solid state packing on the device performance was unambiguously demonstrated.

Chapter 2 gave a brief introduction to fundamentals of organic photovoltaics as well as an overview on vacuum-deposited small molecule based solar cells. The progress on vacuum-deposited small molecule solar cells has been rapid in recent years and first commercial products are entering the markets. Vacuum deposition techniques offer relatively easy realization of different device architectures and enable the utilization of a vast number of potential active materials.

In Chapter 3 the set-ups for the fabrication and characterization of solar cells applied in this thesis were discussed.

Chapter 4 presented a comprehensive study on the single crystal packing of dipolar merocyanine dyes. The aim of the investigation was to evaluate the effect of a molecular dipole-dipole interaction on the formation of the closest packed structural motifs in the crystal structures of merocyanine chromophores. The statistical results proved that a high molecular dipole moment (> 8 D) significantly increases a molecule's probability to adopt one of the centrosymmetric space groups.

Dimers with antiparallelly oriented dipole vectors were frequently observed (Figure 1a). However, a detailed analysis of the single crystal structures of merocyanines based on the Fischer base donor and various acceptors revealed limitations despite of the high molecular dipole moments (up to 13 D) of these dyes. This was explained by the steric demand of the bulky Fischer's base that forces the adjacent dyes in a slipped arrangement. Hence, the effect of the molecular dipole-dipole interaction was estimated to be minor in these structures. In turn, other packing effects such as local dipole-dipole

interactions were observed to have a significant influence on the formation of the closest packed structural motifs (Figure 1b).

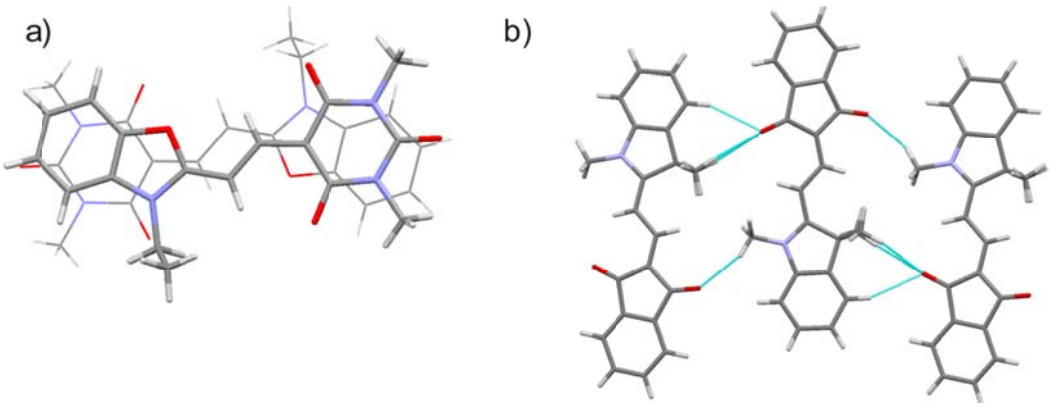

Figure 1. a) Dimer motif with antiparallelly oriented dipole vectors. b) Tape motif showing short intermolecular interactions (blue dotted lines) between the oxygen and hydrogen atoms of the neighboring molecules.

Chapter 5 elucidated a simple concept to improve the power conversion efficiency (PCE) of vacuum-deposited merocyanine:C_{60} bulk heterojunction (BHJ) solar cells. Mixing two merocyanines (LW and SW) with absorption maxima at different spectral ranges in a single active layer improved the device performance with respect to the single donor cells (Figure 2). The improvement in short circuit current (J_{SC}) was attributed to the more efficient solar photon harvest of the mix donor cells compared to the single donor devices (Figure 2b). Furthermore, open circuit voltage (V_{OC}) of the mix donor devices was observed to correlate with the mixing ratio of the donors (Figure 2c). This was rationalized by formation of a three-phases system (SW-rich, LW-rich, C_{60}-rich) where the merocyanine components are able to work independently similar to conventional parallel connected tandem solar cells.

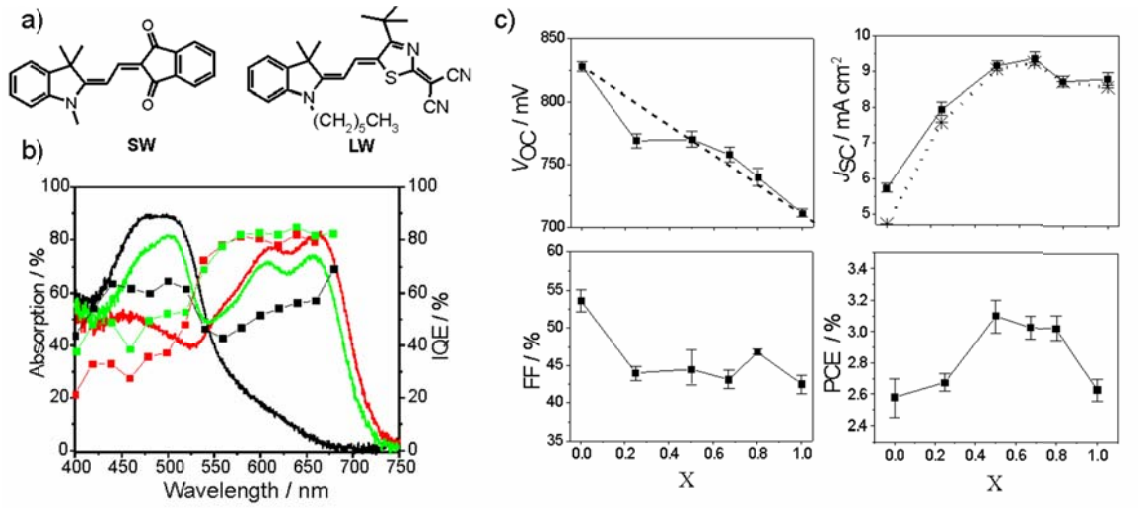

Figure 2. a) Molecular structures of SW and LW merocyanine dyes. b) Absorption (solid lines) and IQE (lines and symbols) efficiencies of cells with the donor mixing ratios of **X** = 0 (black), 0.66 (green), and 1 (red). Dependence of V_{OC}, J_{SC}, FF, and PCE on the LW dye content (**X**) in the mix donor devices.

In Chapter 6 the effect of the molecular orientation on the performance of merocyanine ID583/C_{60} planar heterojunction (PHJ) solar cells was investigated. Deposition of the dye on a heated substrate or post-annealing the complete devices above the glass transition point of ID583 was found to increase the fill factor (FF) of the cells up to 2.2-fold (Figure 3). Employing an exciton dissociation model we showed that the FF of the as-deposited devices (fabricated at room temperature) is limited by the geminate charge recombination at the ID583/C_{60} interface. Moreover, applying an infrared spectroscopic ellipsometry (IRSE) method we demonstrated that the as-deposited ID583 films exhibit a preferred orientation of the dyes with the long molecular axis perpendicular to the substrate surface (Figure 4a). However, upon annealing the films above the glass transition point of the dye (T_g = 77) the molecules undergo a tilt of 45° (Figure 4b). Based on the IRSE measurements and the solved single crystal structure of ID583, two ID583/C_{60} heterointerface models were constructed and their CT-state energies were computed by a state-of-the-art quantum mechanics/molecular mechanics (QM/MM) method (Figure 4). The computations suggested that the exciton dissociation is more efficient when the dyes are tilted with respect to the C_{60} interface. Hereby, based on the experimental as well as theoretical results, we concluded that the geminate recombination process limits the PCE of the as-deposited ID583/C_{60} devices. The low exciton dissociation efficiency of these cells was attributed to the insufficient energy level offset (~ 0.3 eV) between the LUMO levels of

the donor and acceptor materials. Our findings give new insight into the exciton dissociation process in organic solar cells as well as guidelines for the synthesis of new donor materials.

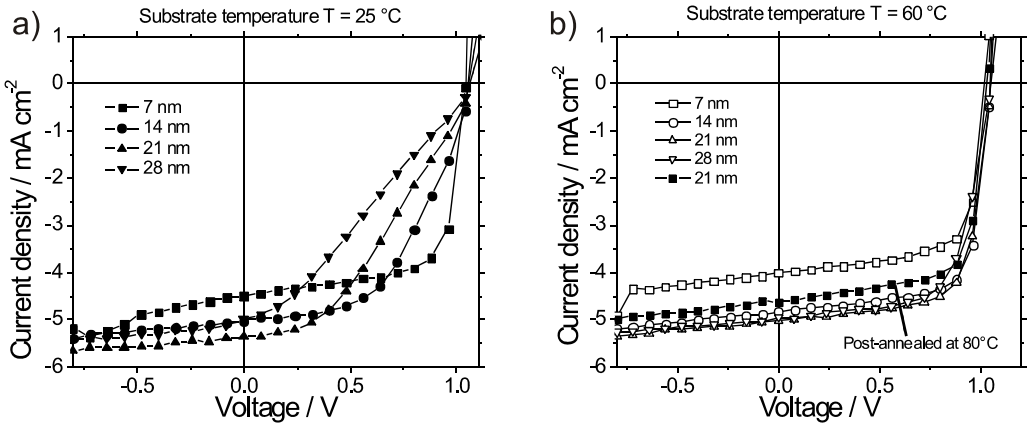

Figure 3. Current-voltage (*J-V*) characteristics of the PHJ cells prepared at substrate temperatures of a) 25 °C and b) 60 °C with four different ID583 layer thicknesses.

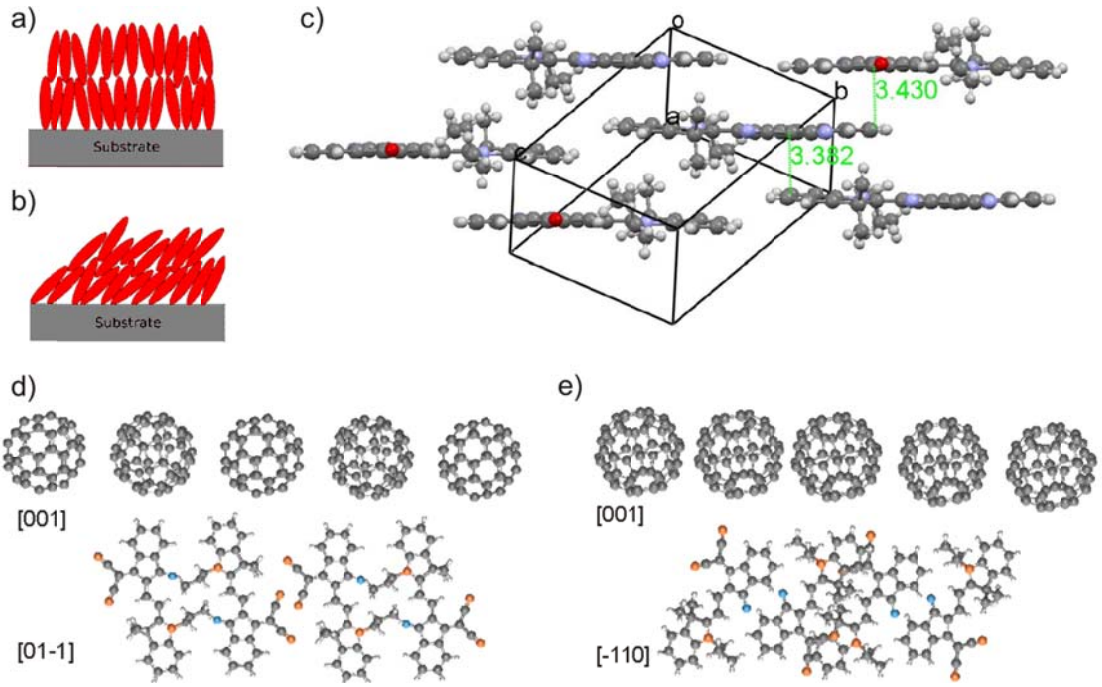

Figure 4. Schematics of the dye molecules' orientations a) before and b) after annealing at 80 °C deduced from the ellipsometric analysis. c) Brickwall packing motif in the single crystal structure of ID583. The shortest atom-to-π-plane distances are shown. Schematics of the interfaces d) ID583[01-1]:C_{60}[001] and e) ID583[-110]:C_{60}[001].

In Chapter 7 we demonstrated, how the film morphology of merocyanine HB364 can be controlled by inserting a thin transition metal oxide or C_{60} layer between the ITO substrate and the dye film. Crystalline HB364 films on the pure and V_2O_5 modified ITO

substrates demonstrated a preferred growth orientation of HB364 crystallites normal to the [10-1] diffraction plane (Figure 5c). In turn, deposition of the HB364 film on a C_{60} layer resulted in a preferred growth of the crystallites normal to the [020] diffraction plane (Figure 5d).

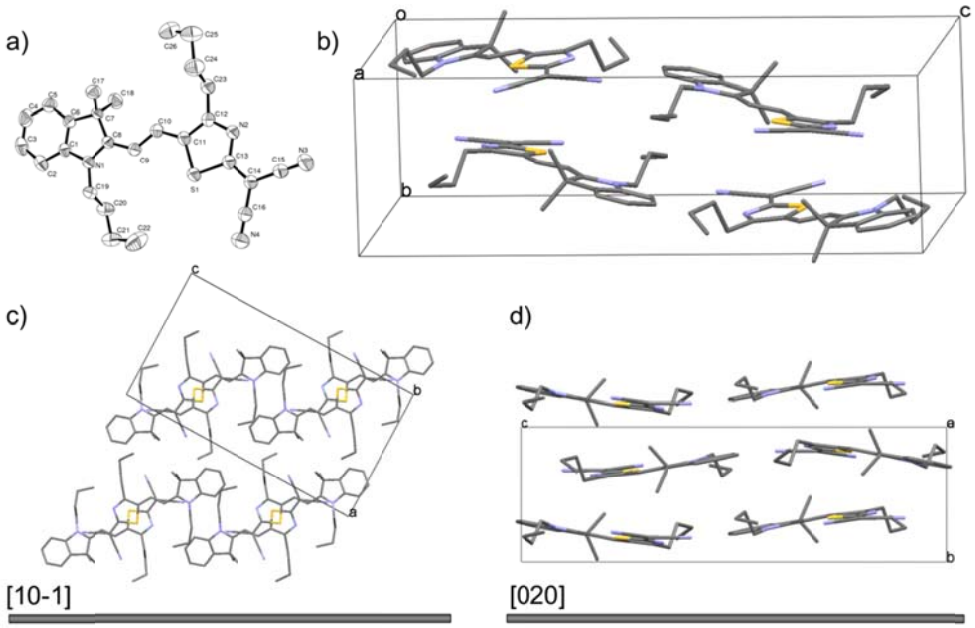

Figure 5. a) ORTEP drawing of HB364 with the 50% probability ellipsoids and atom labeling. b) Unit cell content and molecular packing with respect to the c) [10-1] and d) [020] diffraction planes (viewed from the side) of the single crystal structure of HB364.

Furthermore, HB364/C_{60} PHJ solar cells were fabricated using various transition metal oxides as the anode buffer layers. The PHJ devices having the V_2O_5 buffer layer showed the highest power conversion efficiencies which also outperformed the best HB364:C_{60} BHJ cells. Despite the very high absorption of the PHJ devices, the J_{SC} stayed < 6 mA cm^{-2} whereas the best BHJ cells gave short circuit current close to 8 mA cm^{-2}. The low J_{SC} in PHJ devices was rationalized by the large particle size (diameters up to 90 nm) of the crystalline HB364 donor films that exceeded the exciton diffusion length of the dye. Finally, hybrid heterojunction (HHJ) devices with stacked planar and bulk heterojunction layers were fabricated. The HHJ cells demonstrated the highest PCE (2.9%) of all device-types.

Chapter 9

Zusammenfassung

Im Rahmen dieser Arbeit wurden Struktur-Eigenschafts-Beziehungen zwischen der Festkörpermorphologie und der Leistung organischer Solarzellen auf der Basis von Merocyanin-Farbstoffen untersucht. Verschiedene analytische Methoden, vor allem optische Untersuchungen und Röntgenbeugung, wurden verwendet, um die Einkristall- bzw. Dünnschichtstruktur der Merocyanine aufzuklären. Zusammenhänge zwischen der Festkörperstruktur der Farbstoffe und deren Leistung in Solarzellen wurden eindeutig nachgewiesen.

In Kapitel 2 werden die Grundlagen der organischen Photovoltaik erläutert und ein Überblick über den Stand der Forschung auf dem Gebiet der durch Vakuumabscheidung von kleinen Molek*ülen hergestellten* Solarzellen gegeben. Die Technologie der *Vakuumverdampfung* kleiner Molek*üle* hat sich in den letzten Jahren rasch weiterentwickelt und steht inzwischen an der Schwelle zur Kommerzialisierung erster Produkte. Vakuumabgeschiedene Solarzellen lassen sich mit hoher Reproduzierbarkeit herstellen und weisen gute Stabilitäten auf. Aus wissenschaftlicher Sicht ist vor allem die gute Verfügbarkeit zahlreicher Donoren und die einfache und exakte Realisierung verschiedenster Bauteilarchitekturen von Interesse.

Im Kapitel 3 werden die in dieser Arbeit benutzten Architekturen für die Herstellung und Charakterisierung der Solarzellen vorgestellt und diskutiert.

Kapitel 4 präsentiert eine umfassende Studie über die Kristallpackungen der dipolaren Merocyanin-Farbstoffe. Hier wurde vor allem die Wirkung der Dipol-Dipol-Wechselwirkungen auf die gefundenen Strukturmotive in den Kristallstrukturen der Merocyanin-Farbstoffe analysiert. Die statistischen Auswertung zeigt, dass bei einem hohen molekularen Dipolmoment (> 8 D) die Wahrscheinlichkeit für die Anordnung der Moleküle in einer zentrosymmetrischen Raumgruppen erhöht wird.

Dimere mit einer antiparallelen Orientierung der Dipolmomente wurden häufig gefunden (Abbildung 1a). Eine detaillierte Untersuchung der Kristallstrukturen zahlreicher Merocyanine, in denen Fischerbase als Donor-Baustein in Kombination mit

verschiedenen Akzeptoren verwendet wird, zeigte, dass die Moleküle trotz hoher Dipolmomente (bis 13 D) im Stapel nicht antiparallel packen. Dieses Verhalten wurde dem Raumanspruch der aus der Molekülebene herausragenden Methylsubstituenten der Fischerbase zugeschrieben. Die im Kristallgitter benachbarten Farbstoff-Moleküle sind daher gegeneinander verschoben angeordnet und die Dipol-Dipol-Wechselwirkung zwischen der Molekülen etwas unterdrückt. Im diesen Strukturen haben unter anderem Wechselwirkung zwischen verschiedenen polaren Gruppen einen signifikanten Einfluss auf die Bildung der Packungsmotive (Abbildung 1b).

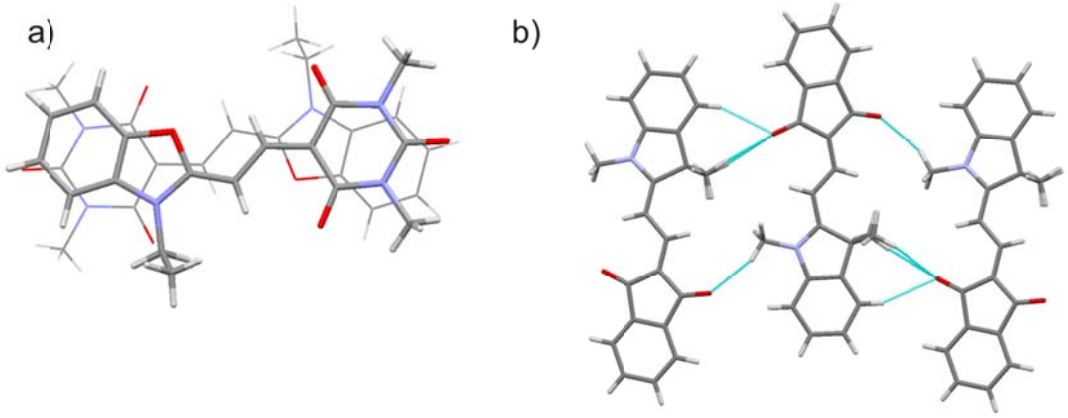

Abbildung 1. a) Dimere mit einer antiparallelen Orientierung der Dipolmomente. b) Ein bandartiges Packungsmotiv mit kurzen intermolekularen CH-O-Wechselwirkungen (blau gestrichelte Linien) der lateral benachbarten Moleküle.

Kapitel 5 erläutert ein elegantes Konzept, um den Wirkungsgrad (PCE) der im Vakuum abgeschiedenen Mischschichten aus Merocyanin und C_{60} in Volumen-Heteroübergang (engl.: bulk heterojunction, BHJ) Solarzellen zu verbessern. Das Mischen zweier Merocyanine (kurzwelliger Typ SW und langwelliger Typ LW) mit komplementären Absorptionsbanden verbessert die Leistung der Zellen im Vergleich zu Zellen der einzelnen verwendeten Donoren im untersuchten Fall um ca. 20 % (Abbildung 2). Durch die Verbreiterung der Absorption wird eine höherer Kurzschlussstrom (engl.: short circuit current, J_{SC}) gewonnen (Abbildung 2b). Die Leerlaufspannung (engl.: open circuit voltage, V_{OC}) der Zellen korreliert mit den Mischverhältnissen der Merocyanin-Donoren (Abbildung 2c). Dies wird durch die Bildung eines Drei-Phasen-Systems (SW-reich, LW-reich, C60-reich) erklärt. Die Merocyanin Komponenten sind damit in der Lage, ähnlich wie herkömmliche parallel geschaltete Tandem-Solarzellen, unabhängig zu arbeiten.

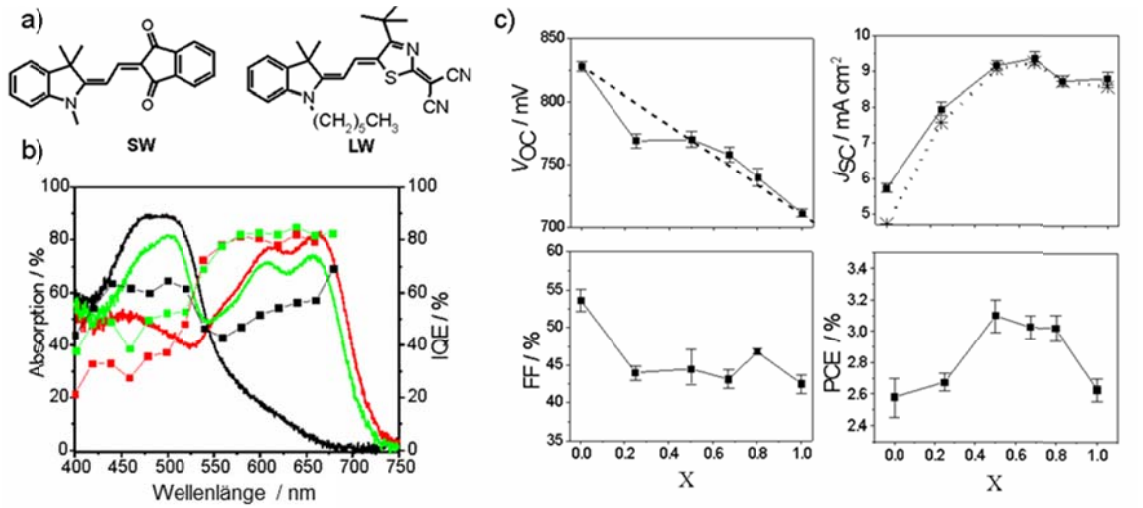

Abbildung 2. a) Molekülstrukturen von SW und LW der Merocyanin-Farbstoffe. b) Absorptionspektren im Film (30 nm, durchgezogene Linien), IQE (Linien und Symbole) Wirkungsgrade (PCE) der Zellen mit Mischungsverhältnissen der Donoren von X = 0 (schwarz), 0,66 (grün) und 1 (rot). V_{OC}, J_{SC}, FF, und PCE der Bauteile in Abhängigkeit des LW-Farbstoff-Gehalts (X).

Im Kapitel 6 wurde die Auswirkung der molekularen Orientierung auf die Leistung einer Zelle mit planarem Heteroübergang (PHJ) von Merocyanin ID583 und C_{60} untersucht. Bei der Abscheidung des Farbstoffs auf einem erhitzten Substrat oder beim Erhitzen des Bauteils nach der Abscheidung über dem Glasübergangspunkt von ID583 wurde festgestellt, dass der Füllfaktor (*FF*) der Zellen mehr als Verdoppelt wird (Abbildung 3). Simulationen mit Hilfe eines Drift-Diffusions-Modells zeigen, dass der Füllfaktor der Bauteile bei Raumtemperatur durch die geminale Ladungsträger-Rekombination an der ID583/C_{60}-Grenzschicht limitiert ist. Durch infrarot-spektroskopische Ellipsometrie (IRSE) wurde gezeigt, dass kalt abgeschiedene ID583 Filme eine bevorzugte Orientierung der Farbstoffe zeigen, bei der die lange molekulare Achse senkrecht zur Substratoberfläche steht (Abbildung 4a). Nach dem Erhitzen der Filme über den Glasübergangspunkt des Farbstoffes (T_g = 77 °C) orientieren sich die Moleküle um und stehen dann mit einer Neigung von 45° auf der Substratoberfläche (Abb. 4b). Basierend auf den IRSE Messungen wurden aus der Kristallstruktur von ID583 zwei Strukturmodelle für den Heteroübergang ID583/C_{60} entwickelt. Die Energieniveaus der Strukturmodelle und Raten für die Erzeugung der jeweiligen CT-Zustände wurden durch eine hochentwickelte Kombination aus Quantenmechanik und molekularer Mechanik (QM/MM) berechnet (Abbildung 4).

Die Ergebnisse der Berechnungen zeigen, dass die Effizienz der Exzitonendissoziation in der gekippten Orientierung höher ist. Sowohl bei den

experimentellen Beobachtungen als auch bei den theoretischen Ergebnissen stellen wurde festgestellt, dass die geminale Rekombination die Effizienz der ID583/C_{60} Bauteile begrenzt.

Die geringe Effizienz der Exzitonendissoziation dieser Zellen ist auf den unzureichenden Energie-Offset (~ 0,3 eV) zwischen dem LUMO-Zuständen von Donor- und Akzeptor zurückzuführen. Die Ergebnisse geben neue Einblicke in die Exzitonendissoziation organischer Solarzellen und lassen daraus Richtlinien für die Synthese neuer Donormaterialien ableiten.

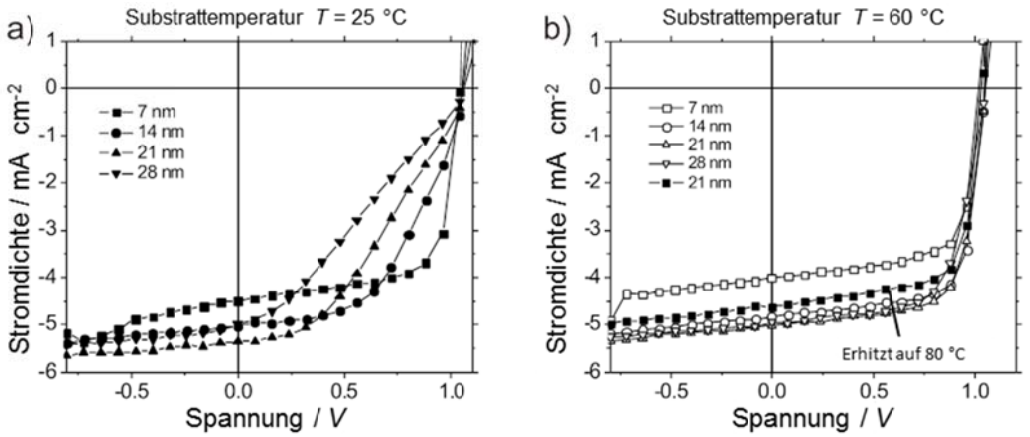

Abbildung 3. *J-V* Kennlinien von Zellen mit planarem Heteroübergang ID583/C_{60} bei verschiedenen Substrattemperaturen (*T*). Die ID583 Schichtdicke betrug in beiden Bauteilen 21 nm.

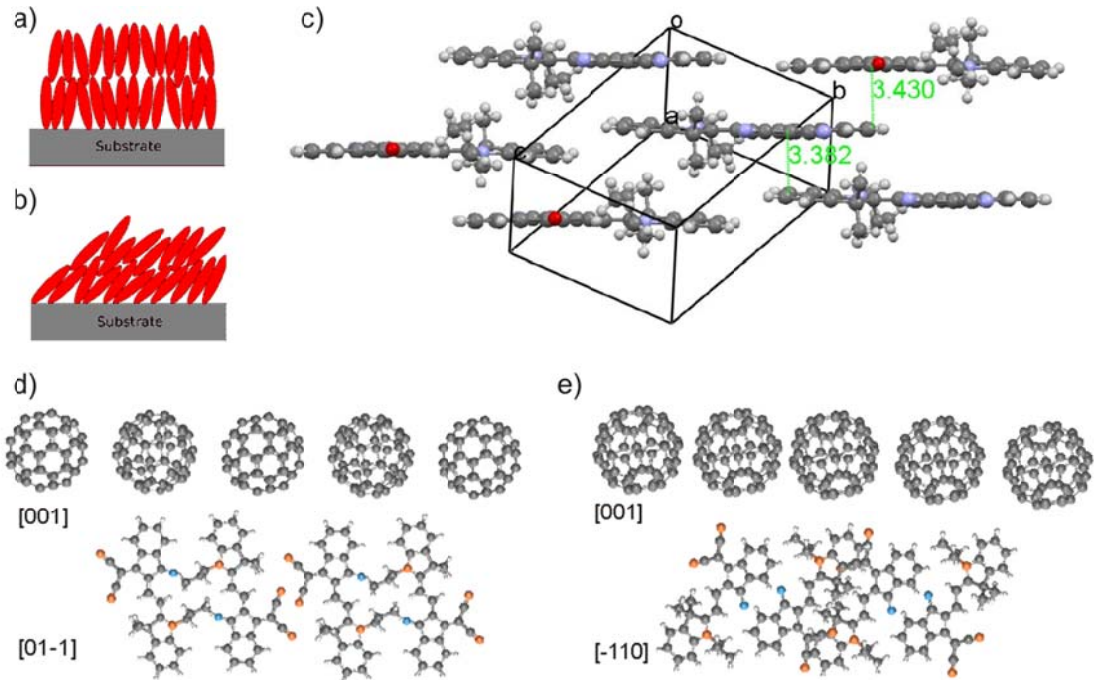

Abbildung 4. Schematische Darstellung der Orientierung der Farbstoffsmoleküle von ID583 a) vor und b) nach dem Erhitzen auf 80 °C, abgeleitet aus der ellipsometrischen Analyse. c) Backsteinmotiv aus der Einkristall-Struktur der ID583. Die kürzesten Distanzen (Abstand zwischen einem Atom und der π-Fläche) werden angezeigt. Schematische Darstellung der Grenzflächen d) ID583 [01-1]: C60 [001] und e) ID583 [-110]: C60 [001].

Im Kapitel 7 wird gezeigt, wie die Filmmorphologie des Merocyanins HB364 kontrolliert werden kann, indem dünne Übergangsmetalloxid oder C_{60}-Schichten zwischen der ITO-Schicht und der HB364 Film aufgebracht werden. Kristalline HB364 Filme auf reinem und mit V_2O_5 modifizierten ITO-Substrat wachsen bevorzugt mit einer Orientierung der HB364 Kristallite senkrecht zur [10-1]-Fläche (Abbildung 5c). Die Abscheidung der HB364-Filme auf einer C_{60}-Schicht führt zu einer bevorzugten Wachstumsorientierung der Kristallite senkrecht zur [020]-Fläche (Abbildung 5d).

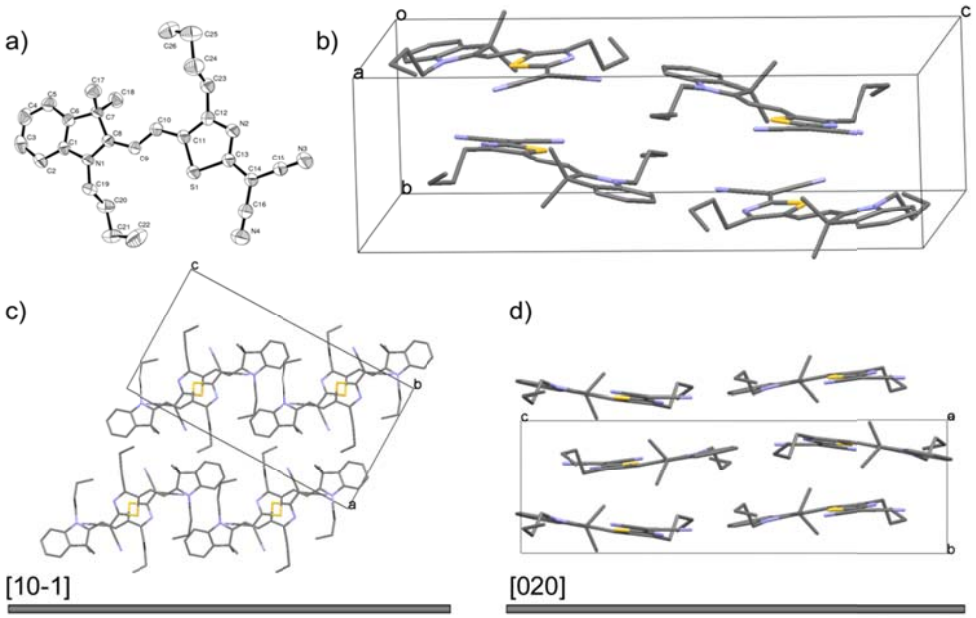

Abbildung 5. a) ORTEP-Darstellung der HB364 mit 50% Aufenthaltswahrscheinlichkeit und Kennzeichnung der einzelnen Atome. b) Der Inhalt der Elementarzelle und die Packung der Moleküle an der c) [10-1]-Fläche und d) [020]-Fläche (von der Seite betrachtet).

ID583/C_{60} PHJ Solarzellen wurden mit verschiedenen Übergangsmetalloxiden als Pufferschicht auf der Anode hergestellt. PHJ Bauteile mit V_2O_5 Pufferschicht zeigen die höchste Effizienz, die sogar über der besten Effizienz einer HB364:C_{60} BHJ-Zelle liegt. Trotz der sehr hohen Absorption der PHJ Zellen bleibt der Kurzschlussstrom J_{SC} < 6 mA cm^{-2}, während die besten BHJ-Zellen mit diesen Materialien einen Kurzschlussstrom von ca. 8 mA cm^{-2} aufweisen. Der J_{SC} der PHJ Bauteile wird durch die Exzitonen-Diffusionslänge der HB364 Donor-Filme limitiert. Ein Hybrid-Bauteil aus einer Schichtfolge von PHJ und BHJ wies die höchste mit diesem Donor gemessene PCE von 2.9% auf.

Appendix

Additional Crystallographic Information for Chapter 4

Dipolar compounds retrieved from Cambridge Crystal Database

Table A1. Reference codes, R-factors, space groups, and AM1 computed dipole moments of the dipolar compounds retrieved from CSD

Ref. code	R	Space group	Dipole moment [debye]	Ref. code	R	Space group	Dipole moment [debye]
ACUPAP	4.45	P21/n	9.0	DUJJUO	5.59	P21/c	4.6
ACUPET	5.52	P-1	11.1	IHAGUU	5.54	P21/c	9.6
AGAHAR	5.34	P21/c	20.5	MUMROC	6.27	P-1	7.5
AJAXAK	4.3	P-1	8.6	OBICIL	5.56	P21/c	6.6
AJIXEW	4.41	P21/n	6.6	OCIGOW	5.21	P21/c	2.9
AMFULV	7.5	P212121	7.8	OCIGUC	4.57	P-1	3.2
ASULIJ	4.53	P21/c	6.4	OCIHAJ	4.19	P21/c	3.0
BEPFEH	4.41	P21/n	9.1	OCIHEN	4.29	P21/c	3.3
BESMER	4.8	P1121/b	6.5	PABMIP	5.22	P-1	21.6
BETQIB	4.62	P21	4.8	PHPYHP	5.7	P-1	9.1
BUFDIP	4.3	P21/n	4.1	PIHCUE	4.5	P-1	1.2
CAXKIW	4.02	P21/c	9.8	POCYUC	4.54	P-1	4.6
CAYSUQ	4.3	P-1	4.9	PODXEL	5.8	P-1	5.1
CEJHIJ	4.42	P21/c	3.2	POVSAU	5.9	P-1	6.9
CIHZUO	4.6	Pbca	7.5	QADMIR	4.4	P21/c	4.5
CIPWIH	6.3	P21/n	3.8	QEHBAH	4.56	P-1	3.8
CUFFOY	4.6	P21/a	2.7	QICTUR	5.6	P21/c	3.8
DIZNEF	4.3	P-1	14.4	QOGZUI	4.4	P21/n	3.8
DOCKIP	4.39	P-1	6.4	QUMGOU	7	P-1	7.2
DOMZIO	5.39	P21/n	9.8	QUSKEU	4.14	P21/n	6.5
EBTVPH10	6.2	P21/c	14.6	QUSKIY	4.59	P-1	6.9
ECNTPO	5.9	P21/c	2.9	REVNOV	4.3	P-1	3.4
EDUYUX	7.5	P21/a	6.2	RINXOB	5	P21/c	7.4
EMILIV	4.65	P21/c	5.6	RIWTIA	6.29	P21/c	5.1
EMILOB	4.14	P21/c	5.6	ROFLAA	4.79	P-1	4.8
ERANEQ	5.97	P-1	6.0	RUHFAB	4.45	P21/c	4.6
ERANIU	5.23	P21/n	1.4	RUHFIJ	4.02	P-1	5.5
ETOBOE	3.83	P-1	5.2	RUHFOP	4.89	P21/c	6.6
EXAHIU	5.93	P21/c	8.1	SAMGOC	4.3	P21/c	1.3
FACWEM	2.56	P21/a	7.6	SAPNAY	4.1	P212121	4.0
FARQUL	4.22	P21/c	7.5	SAYXUL	4.9	P21/n	6.6
FIMPOG	5.9	P21/c	10.2	SETWEU	3.99	P-1	10.3
GAVMAS	5.16	Pbca	5.1	SIPBEY	4.4	C2/c	9.4
GEWBOZ	5.6	P21/n	5.0	SOHVAM01	4.7	Pbca	7.9
GIMQAV	4.71	Pbca	11.6	SOWJIX	4.6	P21/c	6.6
GODQOF	5.9	P21/n	10.2	TAXSOB	4.53	P21/c	5.8
HABTAG	7.34	P21/n	9.6	TECPEX	6.02	C2/c	2.3
HABWEN	3.68	P-1	7.8	TINXIY	4	P21/n	5.9
HEGPEO	4.2	P21/c	2.2	TLPIND	4.2	P1121/b	3.6
HEPHUG	5.96	P-1	10.4	TOHFIF	3.9	P-1	9.7
HIVRUA	7.5	P21/n	8.2	TOVMUM	4	P-1	5.9
HIVSAH	7.1	P21/a	4.3	TULYUU	4.5	Pna21	9.2
HIVSEL	6.6	Pbca	5.5	TUZFEZ	4.92	C2/c	4.5
HIYLUW	5.4	P-1	4.8	UJALOG	3.7	P-1	5.9
HOCVIE	4.3	P1121/b	5.8	UJALUM	4.9	P21/a	6.0
IFUNON	4.84	P-1	5.0	UJAMAT	3.82	P21/n	8.8
IFUNUT	5.42	P-1	3.1	UNOFEI	4.18	P21/c	6.3
IJEWID	3.89	Pbca	7.8	VAKZAI	5.2	Cc	11.2
ILIRAW	5.72	P-1	4.6	VATCIC	3.1	P-1	10.0
ITACOV	4.29	P21/n	19.7	VAXKUA	5.6	P212121	5.6
ITACUB	5.5	Pbca	20.7	VERNIP	4.4	P-1	13.5
IXAQAZ	3.9	P21/c	7.1	VIFZUG	6.24	P21/a	12.6

JAFBAT	6.5	P21/c	4.6	VIJYOC	4.7	P-1	6.4
JAMNOA	3.7	P21/a	6.8	WALCUH	5.4	P21/c	11.1
JEGVOG	5.4	Pbca	8.0	WEVMUF	3.8	P-1	14.9
JEXPOR	3.83	P21/c	4.9	WIZHIX	6.05	P21/c	10.8
JIBHEH	6.3	P21/c	6.0	WUDHIM	5.14	P-1	4.7
JOFTIH	6.13	P21/a	8.7	WUGGUA	4.8	P212121	5.9
JOFTON	5.24	P21/c	11.4	XASPIQ	6.73	P21/n	3.6
JUHFAT	4.8	P-1	9.6	XASWIY	4.15	P21/n	3.5
JUHFEX	5.5	P21/c	6.0	XATTIW	7.24	P212121	7.8
KANREX	7.28	P21	7.5	XECNUP	5	P21/a	4.4
LAFMUA	6.4	P-1	5.3	XECPAX	4.8	P-1	3.8
LAVLUP	6.2	P21/n	7.6	XECPEB	7.2	P21/a	5.9
LAVMEA	5.5	C2/c	7.3	XECPIF	5.6	P-1	3.2
LAVMIE	5.2	P21/n	8.4	XECPOL	5.18	P-1	4.6
LEMHAN	4.42	P-1	4.3	XIMSOC	7.06	P21/n	6.2
LEXNOS	3.74	P-1	4.8	XIMTOD	5.05	P21/n	7.1
MANBAE	3.9	P21/n	5.4	XOFROZ	5.36	P21/n	5.8
MEWLIJ	6.4	P21/a	6.4	YABFOW	5.09	P-1	3.7
MOPKOR	5.7	P21/c	8.7	YADYIM	3.01	P21/c	5.3
MOPKUX	5.4	P-1	8.6	YAMXIT	3.58	P21/c	12.1
MOPLAE	5.6	P21/n	8.6	YAMXUF	3.5	Pbca	8.4
MOPLEI	4.4	P-1	8.5	YEGLEB01	4.65	P21/n	7.1
MUDWIR	4.43	P21/n	10.5	YEGZEQ	7.45	Pbca	6.3
MUHYIX	6.06	P21/n	12.1	YEGZIU	6.68	P21/c	4.5
NEQNAY	6.9	P212121	5.8	YEJNUW	5.85	P21/n	4.2
NEVPEJ	4.43	Aba2	3.5	YIBYIS	4.61	P21/n	3.1
NITQOW	4.55	P-1	6.7	ZIPWIE	3	P1121/a	4.4
NOCVEH	4.7	P21/c	7.9	ZIYSUV	5.2	P21/a	4.0
NOLBIA	4.28	P21	4.2	ZULKAS	6.8	P21/c	9.0
NOPCAW	6.6	Ia	3.1	YOTPED	5.93	P21/c	13.1
NUTMOE	5.5	P-1	6.8	HOYPER	4.41	P21/c	5.6
PUGNOV	4.01	P-1	5.0	PUBJEC	4.62	P21/n	6.0
RUFPOY	4.57	P-1	8.8				

Crystallographic parameters for the solved crystal structures

Table A2. Numerical details of the solution and refinement of the solved crystal structures

Compound	**1a**	**1b**	**1c**	**1d**	**1f**	**1g**
Formula	C25H19N3O	C26H21N3O	C27H23N3O	C27H23N3O	C31H23N3O	C30H28N3O
Formula mass	377.43	391.46	405.48	405.48	453.52	446.55
Space group	P21/c	Pca21	P-1	Pbca	P21/c	P-1
a / Å	11.462(3)	13.839(3)	9.2930(10)	24.722(3)	10.2335(11)	13(2)
b / Å	13.595(3)	19.234(5)	9.6240(11)	10.9911(12)	21.690(2)	13.432(3)
c / Å	12.427(3)	7.8300(19)	12.6184(13)	31.768(3)	10.0187(11)	14.614(3)
α / Å	90.00	90.00	104.859(5)	90.00	90	88.394(3)
β / Å	99.345(12)	90.00	97.120(4)	90.00	96.670(6)	81.23(3)
γ / Å	90.00	90.00	90.374(5)	90.00	90	75.19(3)
V / Å^3	1910.75	2084.18	1081.52	8632.06	2306.7	2438.06
T / K	173(2)	173(2)	173(2)	173(2)	173(2)	173(2)
Z	4	4	2	16	4	4
D_{calc} / g cm^{-3}	1.312	1.248	1.245	1.248	1.306	1.196
Radiation, *λ* / Å	CuKα, 1.54178	CuKα, 1.54178	CuKα, 1.54178	CuKα, 1.54178	CuKα, 1.54178	CuKα, 1.54178
$2\theta_{max}$ /°	57.83	45.65	57.29	58.42	57.61	58.28
Reflections collected	7997	4846	5110	38880	18562	7250
No. of indep. ref.	2055	1649	2067	5631	2989	7250
Variables in final ref.	266	275	284	568	319	620
R_1 [I>2σ(I)]	0.0397	0.0407	0.0354	0.0539	0.0371	0.0615
R_w[I>2σ(I)]	0.0911	0.0893	0.0832	0.1193	0.0935	0.1730
GooF	1.143	0.937	1.065	1.093	1.090	0.654
Largest diff. peak and hole / e.Å^{-3}	0.199 and -0.316	0.120 and -0.103	0.148 and -0.175	0.236 and -0.202	0.208 and -0.194	0.390 and -0.389

Compound	**2a**	**2b**	**2c**	**2e**	**2f**	**2g**
Formula	C25H28N4S	(C29H28N4S)·(C6H5Cl)	(C25H20N4S)(C2H6O)	C31H24N4S	C26H30N4S	C26H22N4S
Formula mass	416.57	502.68	863.09	484.60	430.60	422.54
Space group	P21/c	P21/c	P-1	P 21/c	P21/n	P-1
a / Å	12.490(3)	12.690(3)	13.070(3)	11.8246(15)	13.0466(3)	6.946(2)
b / Å	6.9700(14)	7.0200(14)	13.900(3)	11.2626(13)	7.5537(2)	12.377(4)
c / Å	25.040(5)	31.000(6)	13.970(3)	18.988(2)	23.8222(6)	12.788(4)
α / Å	90.00	90.00	89.35(3)	90.00	90	87.993(8)
β / Å	91.15(3)	92.71(3)	63.74(3)	96.910(5)	91.0020(10)	82.469(10)
γ / Å	90.00	90.00	89.77(3)	90.00	90	80.189(12)
V / Å^3	2179.4	2758.51	2275.89	2510.3	2347.32(10)	1073.8(6)
T / K	293(2)	173(2)	173(2)	273(2)	296(2)	173(2)
Z	4	4	2	4	4	2
D_{calc} / g cm^{-3}	1.270	1.254	1.259	1.282	1.218	1.307
Radiation, *λ* / Å	Synchrotron, 0.71073	Synchrotron, 0.73000	Synchrotron, 0.71073	CuKα, 1.54178	CuKα, 1.54178	CuKα, 1.54178
$2\theta_{max}$ /°	30.51	27.14	24.79	57.92	62.37	58.22
Reflections collected	12017	10534	6907	11525	15562	5172
No. of indep. ref.	6265	5510	6907	2760	3503	2109
Variables in final ref.	278	375	576	328	285	284
R_1 [I>2σ(I)]	0.0562	0.0536	0.0641	0.0380	0.0340	0.0409
R_w[I>2σ(I)]	0.1537	0.1406	0.1722	0.0865	0.0930	0.0999
GooF	1.060	1.038	1.087	1.080	1.033	1.094
Largest diff. peak and hole / e.Å^{-3}	1.091 and -0.822	0.391 and -0.582	0.73 and -0.45	0.174 and -0.227	0.257 and -0.183	0.234 and -0.271

Table A2. Continued

Compound	**4a**	**5a**	**5b**	**6**	**7**	**8**	**17a**
Formula	C22H19NO2	C24H21N3	C29H31N3	C25H21N3	C28H19N5	C31H23NO3	C27H40O2S
Formula mass	329.38	351.44	421.57	363.45	425.48	457.50	484.69
Space group	P21/c	P21/c	P21/n	P21/c	P21/n	P21/c	P21/c
a / Å	8.7600(18)	10.128(3)	13.007(6)	10.5185(3)	10.480(2)	11.660(2)	12.205(4)
b / Å	14.110(3)	7.6749(19)	15.274(7)	11.2161(3)	14.790(3)	25.940(5)	22.572(6)
c / Å	13.830(3)	25.474(7)	13.080(6)	16.1668(5)	14.140(3)	7.3500(15)	10.365(3)
α / Å	90.00	90.00	90	90	90	90	90
β / Å	95.39(3)	97.653(12)	111.48(2)	95.8550(10)	100.78(3)	96.17(3)	111.103(13)
γ / Å	90.00	90.00	90	90	90	90	90
V / Å^3	1701.9(6)	1962.5(9)	2418.0(19)	1897.35(9)	2153.0(7)	2210.21	2663.8(13)
T / K	173(2)	173(2)	173(2)	296(2)	173(2)	173(2)	173(2)
Z	4	4	4	4	4	4	4
D_{calc} / g cm^{-3}	1.286	1.189	1.158	1.272	1.313	1.375	1.209
Radiation, λ / Å	Synchrotron, 0.71073	CuKα, 1.54178	CuKα, 1.54178	CuKα, 1.54178	Synchrotron, 0.71073	Synchrotron, 0.71073	CuKα, 1.54178
$2\theta_{max}$ /°	23.82	57.59	57.85	55.56	24.70	24.70	57.50
Reflections collected	4878	9598	19517	9817	6833	7333	8233
No. of indep. ref.	2521	2296	3169	2178	3559	3718	2888
Variables in final ref.	229	248	293	257	301	319	315
R_1 [I>2σ(I)]	0.0388	0.0357	0.0542	0.0494	0.0527	0.0362	0.0574
R_w [I>2σ(I)]	0.1031	0.0825	0.1296	0.1181	0.1426	0.0858	0.1103
GooF	1.053	1.083	0.971	1.149	1.040	1.050	0.953
Largest diff. peak and hole / e.Å^{-3}	0.248 and -0.208	0.181 and -0.175	0.217 and -0.215	0.205 and -0.271	0.293 and -0.270	0.271 and -0.213	0.254 and -0.236

Crystallographic tables for dye 1a

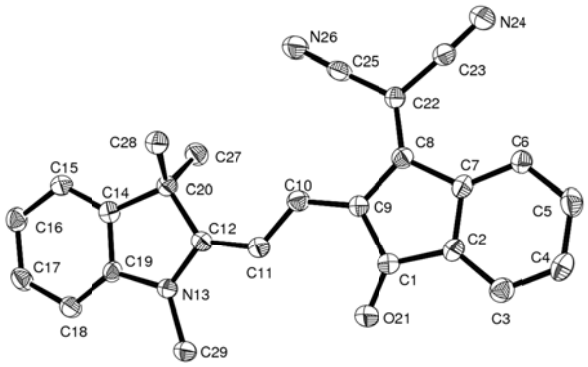

Figure A1. ORTEP drawing of **1a** with atom labelling and 50% probability ellipsoids.

Table A3. Atomic coordinates (× 10^4) and equivalent isotropic displacement parameters (Å^2 × 10^3) for **1a**

Atom	**x**	**y**	**z**	**U(eq)**
C(1)	6200(2)	10706(1)	-659(1)	25(1)
C(2)	5769(2)	11595(1)	-1286(1)	24(1)
C(3)	5108(2)	11661(1)	-2313(2)	29(1)
C(4)	4824(2)	12590(1)	-2748(2)	31(1)
C(5)	5195(2)	13422(1)	-2146(2)	32(1)
C(6)	5853(2)	13356(1)	-1111(2)	28(1)
C(7)	6152(2)	12429(1)	-674(1)	23(1)
C(8)	6865(2)	12106(1)	371(1)	23(1)
C(9)	6900(2)	11048(1)	368(1)	23(1)
C(10)	7445(2)	10421(1)	1187(1)	25(1)

C(11)	7404(2)	9405(1)	1161(1)	25(1)
C(12)	7938(2)	8791(1)	1992(1)	22(1)
N(13)	7825(1)	7804(1)	1918(1)	23(1)
C(14)	8987(2)	8034(1)	3559(1)	24(1)
C(15)	9672(2)	7752(1)	4526(2)	27(1)
C(16)	9746(2)	6755(1)	4788(2)	30(1)
C(17)	9122(2)	6068(1)	4096(2)	30(1)
C(18)	8447(2)	6337(1)	3117(1)	27(1)
C(19)	8417(2)	7329(1)	2861(1)	22(1)
C(20)	8697(2)	9048(1)	3080(1)	24(1)
O(21)	5995(1)	9856(1)	-968(1)	36(1)
C(22)	7368(2)	12743(1)	1180(1)	24(1)
C(23)	7181(2)	13783(1)	1140(1)	27(1)
N(24)	7046(1)	14624(1)	1160(1)	36(1)
C(25)	8092(2)	12437(1)	2168(2)	29(1)
N(26)	8684(2)	12220(1)	2974(2)	40(1)
C(27)	7987(2)	9629(1)	3817(1)	31(1)
C(28)	9825(2)	9603(1)	2936(1)	30(1)
C(29)	7195(2)	7287(1)	966(1)	28(1)

Table A4. Bond lengths [Å] and angles [°] for **1a**

C(1)-O(21)	1.2277(19)	C(10)-C(11)	1.383(2)	C(18)-C(19)	1.384(2)
C(1)-C(2)	1.480(2)	C(11)-C(12)	1.389(2)	C(20)-C(28)	1.532(2)
C(2)-C(3)	1.377(3)	C(12)-N(13)	1.350(2)	C(20)-C(27)	1.539(2)
C(2)-C(7)	1.396(2)	C(12)-C(20)	1.525(3)	C(22)-C(25)	1.427(3)
C(3)-C(4)	1.390(2)	N(13)-C(19)	1.411(2)	C(22)-C(23)	1.430(2)
C(3)-H(3)	0.95	N(13)-C(29)	1.461(2)	C(23)-N(24)	1.155(2)
C(4)-C(5)	1.385(3)	C(14)-C(15)	1.379(3)	C(25)-N(26)	1.153(2)
C(4)-H(4)	0.95	C(14)-C(19)	1.384(2)		
C(5)-C(6)	1.384(3)	C(14)-C(20)	1.517(2)		
C(6)-C(7)	1.393(2)	C(15)-C(16)	1.394(2)		
C(7)-C(8)	1.484(3)	C(16)-C(17)	1.387(3)		
C(8)-C(9)	1.440(2)	C(17)-C(18)	1.382(3)		
O(21)-C(1)-C(9)	128.31(16)	C(10)-C(9)-C(8)	128.15(15)	C(18)-C(17)-C(16)	121.80(16)
O(21)-C(1)-C(2)	124.98(16)	C(10)-C(9)-C(1)	123.90(15)	C(17)-C(18)-C(19)	116.73(16)
C(9)-C(1)-C(2)	106.71(14)	C(8)-C(9)-C(1)	107.90(14)	C(14)-C(19)-C(18)	122.62(16)
C(3)-C(2)-C(7)	121.94(16)	C(11)-C(10)-C(9)	125.71(16)	C(14)-C(19)-N(13)	108.54(14)
C(3)-C(2)-C(1)	128.89(16)	C(10)-C(11)-C(12)	125.01(16)	C(18)-C(19)-N(13)	128.82(16)
C(7)-C(2)-C(1)	109.16(16)	N(13)-C(12)-C(11)	121.38(15)	C(14)-C(20)-C(12)	101.32(13)
C(2)-C(3)-C(4)	118.55(17)	N(13)-C(12)-C(20)	108.86(14)	C(14)-C(20)-C(28)	111.00(14)
C(5)-C(4)-C(3)	120.00(18)	C(11)-C(12)-C(20)	129.77(14)	C(12)-C(20)-C(28)	112.35(13)
C(6)-C(5)-C(4)	121.51(16)	C(12)-N(13)-C(19)	111.73(13)	C(14)-C(20)-C(27)	109.61(13)
C(5)-C(6)-C(7)	118.89(16)	C(12)-N(13)-C(29)	124.19(14)	C(12)-C(20)-C(27)	111.40(14)
C(6)-C(7)-C(2)	119.11(17)	C(19)-N(13)-C(29)	124.05(13)	C(28)-C(20)-C(27)	110.79(14)
C(6)-C(7)-C(8)	132.46(16)	C(15)-C(14)-C(19)	119.89(16)	C(8)-C(22)-C(25)	124.04(15)
C(2)-C(7)-C(8)	108.42(14)	C(15)-C(14)-C(20)	130.66(16)	C(8)-C(22)-C(23)	123.54(16)
C(22)-C(8)-C(9)	128.34(15)	C(19)-C(14)-C(20)	109.44(16)	C(25)-C(22)-C(23)	112.38(14)
C(22)-C(8)-C(7)	123.87(15)	C(14)-C(15)-C(16)	118.55(17)	N(24)-C(23)-C(22)	176.80(18)
C(9)-C(8)-C(7)	107.78(14)	C(17)-C(16)-C(15)	120.29(17)	N(26)-C(25)-C(22)	177.89(17)

Crystallographic tables for dye 1b

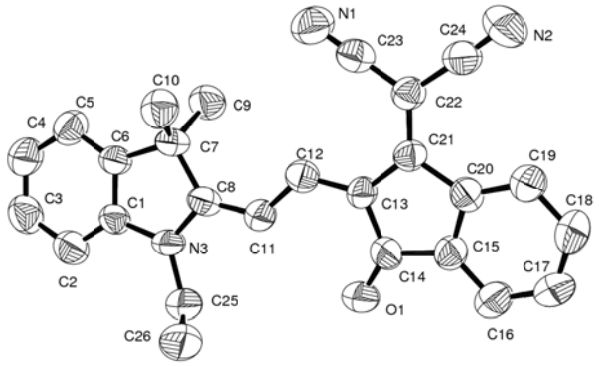

Figure A2. ORTEP drawing of **1b** with atom labelling and 50% probability ellipsoids.

Table A5. Atomic coordinates ($\times 10^4$) and equivalent isotropic displacement parameters ($Å^2 \times 10^3$) for **1b**

Atom	x	y	z	U(eq)
C(1)	6777(4)	3421(3)	118(7)	55(1)
C(8)	5283(4)	2919(2)	460(6)	57(1)
C(7)	5118(3)	3672(2)	-110(7)	55(1)
O(1)	4174(3)	1055(2)	2367(5)	81(1)
C(11)	4634(4)	2396(2)	875(6)	61(2)
N(3)	6243(3)	2819(2)	580(6)	63(1)
C(6)	6141(3)	3948(3)	-259(7)	56(1)
C(5)	6476(4)	4596(3)	-713(7)	68(2)
C(20)	1659(5)	1173(3)	1850(7)	56(2)
C(4)	7467(5)	4694(3)	-755(7)	81(2)
C(15)	2483(5)	819(3)	2406(7)	58(1)
C(9)	4556(3)	4081(2)	1271(7)	74(2)
C(12)	3636(4)	2424(2)	762(6)	57(1)
C(2)	7761(4)	3505(3)	69(8)	71(2)
C(21)	1982(4)	1854(3)	1145(6)	52(1)
C(17)	1527(5)	-132(3)	3341(8)	85(2)
C(22)	1356(4)	2343(3)	501(7)	55(1)
C(18)	716(5)	212(3)	2823(9)	92(2)
C(24)	330(4)	2257(2)	447(7)	68(2)
C(13)	3010(4)	1886(3)	1248(7)	52(1)
C(10)	4590(3)	3732(3)	-1828(6)	71(2)
N(1)	1910(3)	3533(2)	-637(7)	88(2)
N(2)	-497(3)	2215(2)	389(7)	101(2)
C(23)	1662(3)	2999(3)	-132(8)	65(2)
C(3)	8094(4)	4156(3)	-390(9)	81(2)
C(25)	6697(3)	2173(3)	1173(9)	80(2)

Table A6. Bond lengths [Å] and angles [°] for **1b**

C(1)-C(2)	1.371(5)	N(3)-C(25)	1.468(5)	C(21)-C(22)	1.374(6)
C(1)-C(6)	1.374(5)	C(6)-C(5)	1.376(6)	C(21)-C(13)	1.426(5)
C(1)-N(3)	1.421(5)	C(5)-C(4)	1.384(6)	C(17)-C(18)	1.364(6)
C(8)-N(3)	1.346(5)	C(20)-C(19)	1.384(7)	C(17)-C(16)	1.383(7)
C(8)-C(11)	1.388(6)	C(20)-C(15)	1.398(6)	C(22)-C(23)	1.420(7)

C(8)-C(7)	1.531(6)	C(20)-C(21)	1.490(7)	C(22)-C(24)	1.431(7)
C(7)-C(6)	1.517(6)	C(4)-C(3)	1.380(6)	C(18)-C(19)	1.401(7)
C(7)-C(10)	1.534(7)	C(15)-C(16)	1.388(6)	C(24)-N(2)	1.149(6)
C(7)-C(9)	1.548(6)	C(15)-C(14)	1.463(7)	C(13)-C(14)	1.470(7)
O(1)-C(14)	1.230(6)	C(12)-C(13)	1.402(6)	N(1)-C(23)	1.152(6)
C(11)-C(12)	1.386(6)	C(2)-C(3)	1.381(6)	C(25)-C(26)	1.500(8)
C(2)-C(1)-C(6)	122.9(5)	C(1)-C(6)-C(7)	108.9(4)	C(21)-C(22)-C(24)	123.8(5)
C(2)-C(1)-N(3)	128.3(5)	C(5)-C(6)-C(7)	130.6(5)	C(23)-C(22)-C(24)	112.9(5)
C(6)-C(1)-N(3)	108.8(4)	C(6)-C(5)-C(4)	117.6(5)	C(17)-C(18)-C(19)	121.9(5)
N(3)-C(8)-C(11)	121.2(4)	C(19)-C(20)-C(15)	119.3(5)	N(2)-C(24)-C(22)	177.3(6)
N(3)-C(8)-C(7)	107.7(4)	C(19)-C(20)-C(21)	133.2(6)	C(12)-C(13)-C(21)	129.3(6)
C(11)-C(8)-C(7)	131.1(4)	C(15)-C(20)-C(21)	107.5(5)	C(12)-C(13)-C(14)	123.3(5)
C(6)-C(7)-C(8)	102.3(4)	C(3)-C(4)-C(5)	121.1(5)	C(21)-C(13)-C(14)	107.4(5)
C(6)-C(7)-C(10)	110.5(4)	C(16)-C(15)-C(20)	122.0(6)	N(1)-C(23)-C(22)	179.6(6)
C(8)-C(7)-C(10)	113.5(4)	C(16)-C(15)-C(14)	128.5(6)	C(4)-C(3)-C(2)	121.5(5)
C(6)-C(7)-C(9)	110.1(4)	C(20)-C(15)-C(14)	109.5(4)	N(3)-C(25)-C(26)	114.4(5)
C(8)-C(7)-C(9)	110.6(4)	C(11)-C(12)-C(13)	124.8(5)	O(1)-C(14)-C(15)	124.3(5)
C(10)-C(7)-C(9)	109.5(4)	C(1)-C(2)-C(3)	116.5(5)	O(1)-C(14)-C(13)	128.5(5)
C(12)-C(11)-C(8)	127.0(4)	C(22)-C(21)-C(13)	128.3(5)	C(15)-C(14)-C(13)	107.2(5)
C(8)-N(3)-C(1)	112.2(4)	C(22)-C(21)-C(20)	123.3(5)	C(17)-C(16)-C(15)	117.8(6)
C(8)-N(3)-C(25)	124.5(4)	C(13)-C(21)-C(20)	108.5(5)	C(20)-C(19)-C(18)	118.1(5)
C(1)-N(3)-C(25)	123.2(4)	C(18)-C(17)-C(16)	120.7(5)		
C(1)-C(6)-C(5)	120.5(4)	C(21)-C(22)-C(23)	123.3(5)		

Crystallographic tables for dye 1c

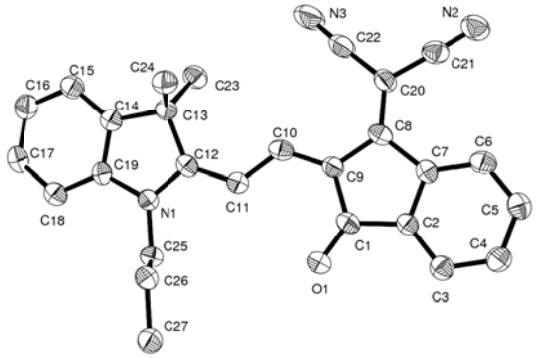

Figure A3. ORTEP drawing of **1c** with atom labelling and 50% probability ellipsoids.

Table A7. Atomic coordinates ($\times 10^4$) and equivalent isotropic displacement parameters ($Å^2 \times 10^3$) for **1c**

Atom	x	y	z	U(eq)
C(1)	3008(2)	8717(3)	1027(2)	33(1)
C(2)	2523(2)	9991(2)	652(2)	29(1)
C(3)	3050(2)	10588(3)	-116(2)	36(1)
C(4)	2421(2)	11808(3)	-325(2)	38(1)
C(5)	1268(2)	12381(3)	216(2)	39(1)
C(6)	720(2)	11772(3)	977(2)	36(1)
C(7)	1366(2)	10563(3)	1202(2)	29(1)
C(8)	1059(2)	9668(2)	1956(2)	31(1)
C(9)	2060(2)	8523(3)	1821(2)	30(1)

C(10)	2183(2)	7419(3)	2359(2)	33(1)
C(11)	3132(2)	6306(3)	2172(2)	33(1)
C(12)	3234(2)	5205(3)	2704(2)	30(1)
C(13)	2453(2)	5005(2)	3655(2)	30(1)
C(14)	3008(2)	3577(3)	3784(2)	30(1)
C(15)	2675(2)	2750(3)	4476(2)	37(1)
C(16)	3357(2)	1459(3)	4425(2)	41(1)
C(17)	4374(2)	1016(3)	3702(2)	38(1)
C(18)	4723(2)	1836(3)	3007(2)	34(1)
C(19)	4018(2)	3107(3)	3062(2)	29(1)
C(20)	-14(2)	9941(3)	2635(2)	36(1)
C(21)	-956(3)	11123(3)	2694(2)	39(1)
C(22)	-360(3)	9056(3)	3320(2)	61(1)
C(23)	787(2)	4944(3)	3421(2)	39(1)
C(24)	2986(2)	6204(2)	4703(2)	39(1)
C(25)	5194(2)	4018(2)	1646(2)	35(1)
C(26)	6537(2)	4982(2)	2120(2)	37(1)
C(27)	7609(2)	4844(3)	1283(2)	42(1)
N(1)	4148(2)	4120(2)	2441(1)	31(1)
N(2)	-1746(2)	12050(2)	2759(2)	48(1)
N(3)	-690(3)	8362(3)	3871(3)	112(1)
O(1)	4049(2)	8000(2)	716(1)	41(1)

Table A8. Bond lengths [Å] and angles [°] for **1c**

C(1)-O(1)	1.237(2)	C(9)-C(10)	1.398(3)	C(17)-C(18)	1.386(3)
C(1)-C(9)	1.459(3)	C(10)-C(11)	1.384(3)	C(18)-C(19)	1.381(3)
C(1)-C(2)	1.477(3)	C(11)-C(12)	1.390(3)	C(19)-N(1)	1.411(3)
C(2)-C(3)	1.382(3)	C(12)-N(1)	1.351(3)	C(20)-C(22)	1.421(4)
C(2)-C(7)	1.392(3)	C(12)-C(13)	1.528(3)	C(20)-C(21)	1.432(4)
C(3)-C(4)	1.386(3)	C(13)-C(14)	1.511(3)	C(21)-N(2)	1.153(3)
C(4)-C(5)	1.383(3)	C(13)-C(23)	1.538(3)	C(22)-N(3)	1.147(3)
C(5)-C(6)	1.389(3)	C(13)-C(24)	1.540(3)	C(25)-N(1)	1.468(3)
C(6)-C(7)	1.390(3)	C(14)-C(15)	1.383(3)	C(25)-C(26)	1.514(3)
C(7)-C(8)	1.488(3)	C(14)-C(19)	1.387(3)	C(26)-C(27)	1.522(3)
C(8)-C(20)	1.377(3)	C(15)-C(16)	1.388(3)		
C(8)-C(9)	1.437(3)	C(16)-C(17)	1.388(3)		
O(1)-C(1)-C(9)	128.5(2)	C(10)-C(9)-C(1)	123.9(2)	C(17)-C(16)-C(15)	120.5(2)
O(1)-C(1)-C(2)	124.5(2)	C(8)-C(9)-C(1)	108.1(2)	C(18)-C(17)-C(16)	121.2(2)
C(9)-C(1)-C(2)	107.0(2)	C(11)-C(10)-C(9)	126.0(2)	C(19)-C(18)-C(17)	117.4(2)
C(3)-C(2)-C(7)	121.9(2)	C(10)-C(11)-C(12)	125.5(2)	C(18)-C(19)-C(14)	122.5(2)
C(3)-C(2)-C(1)	129.1(2)	N(1)-C(12)-C(11)	121.9(2)	C(18)-C(19)-N(1)	129.0(2)
C(7)-C(2)-C(1)	109.0(2)	N(1)-C(12)-C(13)	108.9(2)	C(14)-C(19)-N(1)	108.5(2)
C(2)-C(3)-C(4)	118.7(2)	C(11)-C(12)-C(13)	129.1(2)	C(8)-C(20)-C(22)	124.2(2)
C(5)-C(4)-C(3)	119.7(2)	C(14)-C(13)-C(12)	101.18(18)	C(8)-C(20)-C(21)	123.6(2)
C(4)-C(5)-C(6)	121.9(2)	C(14)-C(13)-C(23)	110.95(17)	C(22)-C(20)-C(21)	112.1(2)
C(5)-C(6)-C(7)	118.5(2)	C(12)-C(13)-C(23)	114.77(17)	N(2)-C(21)-C(20)	177.6(2)
C(6)-C(7)-C(2)	119.3(2)	C(14)-C(13)-C(24)	109.91(16)	N(3)-C(22)-C(20)	177.4(3)
C(6)-C(7)-C(8)	132.2(2)	C(12)-C(13)-C(24)	109.00(17)	N(1)-C(25)-C(26)	112.61(17)
C(2)-C(7)-C(8)	108.5(2)	C(23)-C(13)-C(24)	110.62(18)	C(25)-C(26)-C(27)	111.50(18)
C(20)-C(8)-C(9)	128.8(2)	C(15)-C(14)-C(19)	119.4(2)	C(12)-N(1)-C(19)	111.56(19)
C(20)-C(8)-C(7)	123.8(2)	C(15)-C(14)-C(13)	130.9(2)	C(12)-N(1)-C(25)	125.00(19)
C(9)-C(8)-C(7)	107.39(19)	C(19)-C(14)-C(13)	109.7(2)	C(19)-N(1)-C(25)	123.4(2)

C(10)-C(9)-C(8)	128.0(2)	C(14)-C(15)-C(16)	119.0(2)

Crystallographic tables for dye 1d

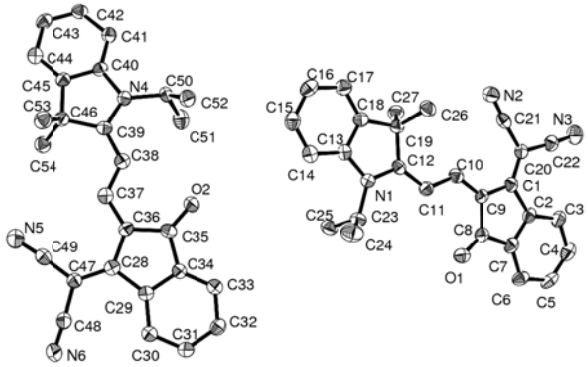

Figure A4. ORTEP drawing of **1d** with atom labelling and 50% probability ellipsoids.

Table A9. Atomic coordinates ($\times 10^4$) and equivalent isotropic displacement parameters ($Å^2 \times 10^3$) for **1d**

Atom	x	y	z	U(eq)
O(1)	166(1)	4507(2)	597(1)	36(1)
C(12)	1375(1)	3134(2)	1425(1)	28(1)
C(22)	-1302(1)	1575(3)	1716(1)	33(1)
N(1)	1860(1)	3489(2)	1269(1)	30(1)
N(3)	-1724(1)	1234(2)	1812(1)	46(1)
C(8)	-177(1)	3914(2)	788(1)	31(1)
C(9)	-109(1)	3200(2)	1177(1)	28(1)
C(1)	-631(1)	2724(2)	1293(1)	29(1)
C(2)	-1029(1)	3133(2)	970(1)	31(1)
C(14)	2846(1)	3244(2)	1481(1)	36(1)
C(27)	1289(1)	1041(2)	1752(1)	37(1)
C(10)	384(1)	2990(2)	1374(1)	30(1)
C(18)	2077(1)	2411(2)	1858(1)	30(1)
C(7)	-754(1)	3805(2)	663(1)	31(1)
C(21)	-390(1)	1569(2)	1939(1)	31(1)
C(15)	3177(1)	2720(3)	1782(1)	38(1)
C(6)	-1011(1)	4249(2)	306(1)	36(1)
N(2)	-110(1)	1213(2)	2202(1)	41(1)
C(13)	2293(1)	3077(2)	1527(1)	31(1)
C(19)	1471(1)	2363(2)	1820(1)	30(1)
C(26)	1204(1)	2932(3)	2211(1)	39(1)
C(11)	882(1)	3416(2)	1238(1)	30(1)
C(20)	-765(1)	1983(2)	1628(1)	29(1)
C(25)	2199(1)	3365(3)	540(1)	38(1)
C(3)	-1582(1)	2945(2)	925(1)	39(1)
C(17)	2414(1)	1892(3)	2153(1)	38(1)
C(23)	1941(1)	4169(2)	869(1)	36(1)
C(5)	-1561(1)	4036(3)	269(1)	40(1)
C(4)	-1841(1)	3407(3)	573(1)	42(1)
C(16)	2969(1)	2058(3)	2115(1)	42(1)
C(24)	2211(1)	5376(3)	939(1)	53(1)
O(2)	4685(1)	5064(2)	1019(1)	35(1)

N(4)	5648(1)	1959(2)	1658(1)	28(1)
C(39)	5915(1)	2699(2)	1387(1)	27(1)
C(29)	5196(1)	6576(2)	128(1)	26(1)
N(6)	6350(1)	7099(2)	-636(1)	48(1)
C(40)	5996(1)	1044(2)	1819(1)	26(1)
C(38)	5653(1)	3642(2)	1178(1)	30(1)
C(50)	5066(1)	2002(2)	1781(1)	31(1)
C(31)	4593(1)	7872(2)	-251(1)	31(1)
C(41)	5883(1)	111(2)	2097(1)	29(1)
C(35)	4966(1)	5455(2)	728(1)	27(1)
C(52)	4910(1)	3194(2)	1993(1)	38(1)
C(42)	6305(1)	-659(2)	2206(1)	31(1)
C(51)	4699(1)	1658(3)	1416(1)	42(1)
C(46)	6506(1)	2293(2)	1358(1)	27(1)
C(34)	4770(1)	6296(2)	401(1)	26(1)
C(54)	6664(1)	1873(2)	913(1)	34(1)
C(53)	6890(1)	3296(2)	1512(1)	36(1)
C(45)	6507(1)	1213(2)	1654(1)	26(1)
C(43)	6818(1)	-503(2)	2045(1)	32(1)
C(44)	6924(1)	448(2)	1768(1)	33(1)
C(37)	5854(1)	4384(2)	865(1)	29(1)
C(32)	4170(1)	7567(2)	16(1)	32(1)
C(36)	5542(1)	5214(2)	639(1)	26(1)
C(28)	5684(1)	5902(2)	268(1)	26(1)
C(49)	6633(1)	5249(3)	177(1)	43(1)
C(48)	6256(1)	6586(3)	-325(1)	34(1)
C(30)	5103(1)	7388(2)	-202(1)	29(1)
C(33)	4257(1)	6768(2)	347(1)	29(1)
N(5)	7019(1)	4702(3)	253(1)	69(1)
C(47)	6170(1)	5931(2)	55(1)	30(1)

Table A10. Bond lengths [Å] and angles [°] for **1d**

O(1)-C(8)	1.228(3)	C(7)-C(6)	1.391(3)	C(38)-C(37)	1.381(3)
C(12)-N(1)	1.355(3)	C(21)-N(2)	1.153(3)	C(50)-C(51)	1.519(3)
C(12)-C(11)	1.390(3)	C(21)-C(20)	1.429(4)	C(50)-C(52)	1.523(4)
C(12)-C(19)	1.532(3)	C(15)-C(16)	1.384(4)	C(31)-C(30)	1.378(3)
C(22)-N(3)	1.150(3)	C(6)-C(5)	1.386(4)	C(31)-C(32)	1.388(3)
C(22)-C(20)	1.428(4)	C(19)-C(26)	1.538(3)	C(41)-C(42)	1.389(3)
N(1)-C(13)	1.425(3)	C(25)-C(23)	1.509(3)	C(35)-C(36)	1.476(3)
N(1)-C(23)	1.488(3)	C(3)-C(4)	1.387(4)	C(35)-C(34)	1.474(3)
C(8)-C(9)	1.474(4)	C(17)-C(16)	1.388(4)	C(42)-C(43)	1.377(3)
C(8)-C(7)	1.484(3)	C(23)-C(24)	1.502(4)	C(46)-C(45)	1.514(3)
C(9)-C(10)	1.389(3)	C(5)-C(4)	1.374(4)	C(46)-C(53)	1.535(3)
C(9)-C(1)	1.442(3)	O(2)-C(35)	1.233(3)	C(46)-C(54)	1.540(3)
C(1)-C(20)	1.382(3)	N(4)-C(39)	1.357(3)	C(34)-C(33)	1.381(3)
C(1)-C(2)	1.490(3)	N(4)-C(40)	1.418(3)	C(45)-C(44)	1.378(3)
C(2)-C(3)	1.390(3)	N(4)-C(50)	1.492(3)	C(43)-C(44)	1.390(4)
C(2)-C(7)	1.398(3)	C(39)-C(38)	1.389(3)	C(37)-C(36)	1.394(3)
C(14)-C(15)	1.382(4)	C(39)-C(46)	1.531(3)	C(32)-C(33)	1.385(3)
C(14)-C(13)	1.386(3)	C(29)-C(30)	1.396(3)	C(36)-C(28)	1.443(3)
C(27)-C(19)	1.536(4)	C(29)-C(34)	1.398(3)	C(28)-C(47)	1.380(3)
C(10)-C(11)	1.387(3)	C(29)-C(28)	1.484(3)	C(49)-N(5)	1.153(3)
C(18)-C(17)	1.377(3)	N(6)-C(48)	1.162(3)	C(49)-C(47)	1.422(4)

C(18)-C(13)	1.386(3)	C(40)-C(41)	1.382(3)	C(48)-C(47)	1.420(4)
C(18)-C(19)	1.506(3)	C(40)-C(45)	1.381(3)		
N(1)-C(12)-C(11)	123.7(2)	C(12)-C(19)-C(26)	111.7(2)	O(2)-C(35)-C(34)	124.2(2)
N(1)-C(12)-C(19)	108.8(2)	C(18)-C(19)-C(27)	109.5(2)	C(36)-C(35)-C(34)	107.1(2)
C(11)-C(12)-C(19)	127.5(2)	C(12)-C(19)-C(27)	111.2(2)	C(43)-C(42)-C(41)	121.5(2)
N(3)-C(22)-C(20)	175.9(3)	C(26)-C(19)-C(27)	112.0(2)	C(45)-C(46)-C(39)	101.21(19)
C(12)-N(1)-C(13)	111.3(2)	C(12)-C(11)-C(10)	124.8(2)	C(45)-C(46)-C(53)	111.37(19)
C(12)-N(1)-C(23)	125.3(2)	C(1)-C(20)-C(22)	123.9(2)	C(39)-C(46)-C(53)	111.3(2)
C(13)-N(1)-C(23)	123.4(2)	C(1)-C(20)-C(21)	124.4(2)	C(45)-C(46)-C(54)	109.6(2)
O(1)-C(8)-C(9)	128.1(2)	C(22)-C(20)-C(21)	111.6(2)	C(39)-C(46)-C(54)	112.61(19)
O(1)-C(8)-C(7)	125.0(2)	C(4)-C(3)-C(2)	118.8(3)	C(53)-C(46)-C(54)	110.5(2)
C(9)-C(8)-C(7)	106.8(2)	C(18)-C(17)-C(16)	118.9(3)	C(33)-C(34)-C(29)	122.2(2)
C(10)-C(9)-C(1)	127.5(2)	N(1)-C(23)-C(24)	112.1(2)	C(33)-C(34)-C(35)	128.7(2)
C(10)-C(9)-C(8)	124.6(2)	N(1)-C(23)-C(25)	110.7(2)	C(29)-C(34)-C(35)	109.1(2)
C(1)-C(9)-C(8)	107.8(2)	C(24)-C(23)-C(25)	115.6(2)	C(44)-C(45)-C(40)	120.2(2)
C(20)-C(1)-C(9)	128.7(2)	C(4)-C(5)-C(6)	121.3(2)	C(44)-C(45)-C(46)	130.1(2)
C(20)-C(1)-C(2)	123.5(2)	C(5)-C(4)-C(3)	121.3(3)	C(40)-C(45)-C(46)	109.8(2)
C(9)-C(1)-C(2)	107.7(2)	C(15)-C(16)-C(17)	120.2(3)	C(42)-C(43)-C(44)	120.2(2)
C(3)-C(2)-C(7)	119.1(2)	C(39)-N(4)-C(40)	111.05(19)	C(45)-C(44)-C(43)	118.9(2)
C(3)-C(2)-C(1)	132.3(2)	C(39)-N(4)-C(50)	128.0(2)	C(38)-C(37)-C(36)	123.9(2)
C(7)-C(2)-C(1)	108.5(2)	C(40)-N(4)-C(50)	120.9(2)	C(33)-C(32)-C(31)	120.0(2)
C(15)-C(14)-C(13)	117.1(2)	N(4)-C(39)-C(38)	121.6(2)	C(37)-C(36)-C(28)	128.8(2)
C(11)-C(10)-C(9)	125.6(2)	N(4)-C(39)-C(46)	109.1(2)	C(37)-C(36)-C(35)	123.6(2)
C(17)-C(18)-C(13)	120.0(2)	C(38)-C(39)-C(46)	129.3(2)	C(28)-C(36)-C(35)	107.4(2)
C(17)-C(18)-C(19)	130.0(2)	C(30)-C(29)-C(34)	118.8(2)	C(47)-C(28)-C(36)	128.7(2)
C(13)-C(18)-C(19)	110.0(2)	C(30)-C(29)-C(28)	132.7(2)	C(47)-C(28)-C(29)	123.3(2)
C(6)-C(7)-C(2)	122.1(2)	C(34)-C(29)-C(28)	108.5(2)	C(36)-C(28)-C(29)	107.9(2)
C(6)-C(7)-C(8)	128.9(2)	C(41)-C(40)-C(45)	121.8(2)	N(5)-C(49)-C(47)	176.1(3)
C(2)-C(7)-C(8)	109.0(2)	C(41)-C(40)-N(4)	129.3(2)	N(6)-C(48)-C(47)	176.8(3)
N(2)-C(21)-C(20)	176.5(3)	C(45)-C(40)-N(4)	108.9(2)	C(31)-C(30)-C(29)	118.9(2)
C(16)-C(15)-C(14)	121.8(3)	C(37)-C(38)-C(39)	128.1(2)	C(34)-C(33)-C(32)	118.3(2)
C(5)-C(6)-C(7)	117.3(3)	N(4)-C(50)-C(51)	111.72(19)	C(28)-C(47)-C(48)	124.0(2)
C(18)-C(13)-C(14)	122.0(2)	N(4)-C(50)-C(52)	112.7(2)	C(28)-C(47)-C(49)	123.6(2)
C(18)-C(13)-N(1)	108.4(2)	C(51)-C(50)-C(52)	113.6(2)	C(48)-C(47)-C(49)	112.3(2)
C(14)-C(13)-N(1)	129.6(2)	C(30)-C(31)-C(32)	121.8(2)		
C(18)-C(19)-C(12)	101.51(19)	C(40)-C(41)-C(42)	117.3(2)		
C(18)-C(19)-C(26)	110.4(2)	O(2)-C(35)-C(36)	128.7(2)		

Crystallographic tables for dye 1f

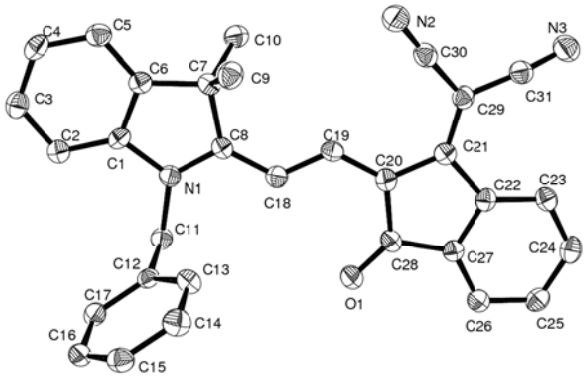

Figure A5. ORTEP drawing of **1f** with atom labelling and 50% probability ellipsoids.

Table A11. Atomic coordinates ($\times 10^4$) and equivalent isotropic displacement parameters ($Å^2 \times 10^3$) for **1f**

Atom	x	y	z	U(eq)
O(1)	2767(1)	5490(1)	6020(1)	33(1)
N(1)	5921(1)	3869(1)	7019(1)	22(1)
C(8)	4993(2)	3797(1)	6072(2)	22(1)
C(1)	6716(2)	3324(1)	7206(2)	23(1)
C(12)	5364(2)	4275(1)	9063(2)	22(1)
N(3)	-599(2)	4290(1)	557(2)	38(1)
N(2)	1615(2)	3049(1)	2921(1)	38(1)
C(15)	4096(2)	4048(1)	11239(2)	29(1)
C(21)	1201(2)	4692(1)	3419(2)	23(1)
C(28)	2109(2)	5304(1)	5087(2)	24(1)
C(27)	1095(2)	5681(1)	4376(2)	23(1)
C(17)	6051(2)	4307(1)	10219(2)	26(1)
C(31)	29(2)	4273(1)	1493(2)	28(1)
C(10)	5360(2)	3121(1)	4150(2)	32(1)
C(19)	3095(2)	4222(1)	4795(2)	24(1)
C(16)	5421(2)	4193(1)	11302(2)	28(1)
C(25)	-295(2)	6545(1)	3804(2)	29(1)
C(20)	2176(2)	4692(1)	4459(2)	24(1)
C(13)	4028(2)	4127(1)	9013(2)	29(1)
C(7)	5114(2)	3131(1)	5542(2)	24(1)
C(3)	8399(2)	2651(1)	8025(2)	30(1)
C(18)	4080(2)	4265(1)	5739(2)	24(1)
C(29)	859(2)	4202(1)	2608(2)	26(1)
C(6)	6295(2)	2881(1)	6322(2)	24(1)
C(11)	6056(2)	4402(1)	7887(2)	25(1)
C(23)	-411(2)	5591(1)	2559(2)	28(1)
C(4)	8002(2)	2202(1)	7143(2)	30(1)
C(22)	563(2)	5328(1)	3368(2)	24(1)
C(26)	678(2)	6285(1)	4608(2)	27(1)
C(9)	3879(2)	2743(1)	5816(2)	33(1)
C(24)	-818(2)	6201(1)	2794(2)	30(1)
C(2)	7756(2)	3227(1)	8079(2)	25(1)
C(5)	6947(2)	2312(1)	6283(2)	29(1)
C(30)	1299(2)	3568(1)	2796(2)	28(1)
C(14)	3397(2)	4017(1)	10093(2)	32(1)

Table A12. Bond lengths [Å] and angles [°] for **1f**

O(1)-C(28)	1.2324(19)	C(15)-C(14)	1.382(2)	C(25)-C(24)	1.384(2)
N(1)-C(8)	1.349(2)	C(21)-C(29)	1.385(2)	C(13)-C(14)	1.379(2)
N(1)-C(1)	1.418(2)	C(21)-C(20)	1.443(2)	C(7)-C(6)	1.513(2)
N(1)-C(11)	1.467(2)	C(21)-C(22)	1.498(2)	C(7)-C(9)	1.544(2)
C(8)-C(18)	1.390(2)	C(28)-C(20)	1.467(2)	C(3)-C(4)	1.386(2)
C(8)-C(7)	1.532(2)	C(28)-C(27)	1.476(2)	C(3)-C(2)	1.389(2)
C(1)-C(2)	1.381(2)	C(27)-C(26)	1.379(2)	C(29)-C(30)	1.429(3)
C(1)-C(6)	1.383(2)	C(27)-C(22)	1.396(2)	C(6)-C(5)	1.379(2)
C(12)-C(17)	1.386(2)	C(17)-C(16)	1.382(2)	C(23)-C(24)	1.388(2)
C(12)-C(13)	1.388(2)	C(31)-C(29)	1.427(3)	C(23)-C(22)	1.390(2)
C(12)-C(11)	1.507(2)	C(10)-C(7)	1.529(2)	C(4)-C(5)	1.387(2)
N(3)-C(31)	1.155(2)	C(19)-C(18)	1.380(2)		
N(2)-C(30)	1.154(2)	C(19)-C(20)	1.397(2)		

C(15)-C(16)	1.376(2)	C(25)-C(26)	1.384(2)		
C(8)-N(1)-C(1)	112.11(14)	C(26)-C(27)-C(22)	122.10(16)	C(19)-C(18)-C(8)	125.48(16)
C(8)-N(1)-C(11)	126.73(14)	C(26)-C(27)-C(28)	128.48(16)	C(21)-C(29)-C(31)	123.98(16)
C(1)-N(1)-C(11)	120.80(14)	C(22)-C(27)-C(28)	109.41(15)	C(21)-C(29)-C(30)	123.75(16)
N(1)-C(8)-C(18)	122.24(15)	C(16)-C(17)-C(12)	120.72(17)	C(31)-C(29)-C(30)	112.28(15)
N(1)-C(8)-C(7)	108.43(14)	N(3)-C(31)-C(29)	174.88(19)	C(5)-C(6)-C(1)	119.25(16)
C(18)-C(8)-C(7)	129.26(15)	C(18)-C(19)-C(20)	125.59(16)	C(5)-C(6)-C(7)	130.89(16)
C(2)-C(1)-C(6)	123.60(16)	C(15)-C(16)-C(17)	120.01(17)	C(1)-C(6)-C(7)	109.85(15)
C(2)-C(1)-N(1)	128.30(16)	C(26)-C(25)-C(24)	120.04(17)	N(1)-C(11)-C(12)	111.34(13)
C(6)-C(1)-N(1)	108.09(15)	C(19)-C(20)-C(21)	127.73(15)	C(24)-C(23)-C(22)	117.99(16)
C(17)-C(12)-C(13)	118.68(16)	C(19)-C(20)-C(28)	124.33(16)	C(3)-C(4)-C(5)	121.08(17)
C(17)-C(12)-C(11)	120.42(16)	C(21)-C(20)-C(28)	107.83(14)	C(23)-C(22)-C(27)	119.54(16)
C(13)-C(12)-C(11)	120.90(15)	C(14)-C(13)-C(12)	120.67(17)	C(23)-C(22)-C(21)	132.34(16)
C(16)-C(15)-C(14)	119.93(17)	C(6)-C(7)-C(10)	111.26(14)	C(27)-C(22)-C(21)	108.10(14)
C(29)-C(21)-C(20)	128.16(16)	C(6)-C(7)-C(8)	101.41(13)	C(27)-C(26)-C(25)	118.26(16)
C(29)-C(21)-C(22)	124.33(15)	C(10)-C(7)-C(8)	113.45(13)	C(25)-C(24)-C(23)	122.07(17)
C(20)-C(21)-C(22)	107.50(14)	C(6)-C(7)-C(9)	109.31(14)	C(1)-C(2)-C(3)	116.27(16)
O(1)-C(28)-C(20)	128.19(16)	C(10)-C(7)-C(9)	111.29(14)	C(6)-C(5)-C(4)	118.61(17)
O(1)-C(28)-C(27)	124.72(16)	C(8)-C(7)-C(9)	109.66(14)	N(2)-C(30)-C(29)	177.53(19)
C(20)-C(28)-C(27)	107.08(15)	C(4)-C(3)-C(2)	121.20(17)	C(13)-C(14)-C(15)	119.99(17)

Crystallographic tables for dye 1g

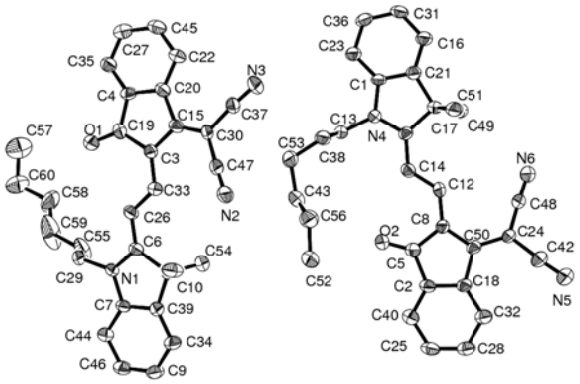

Figure A6. ORTEP drawing of **1g** with atom labelling and 50% probability ellipsoids.

Table A13. Atomic coordinates ($\times 10^4$) and equivalent isotropic displacement parameters ($Å^2 \times 10^3$) for **1g**

Atom	x	y	z	U(eq)
N(1)	11346(4)	3152(4)	969(4)	29(1)
C(2)	12066(5)	2153(5)	894(4)	29(2)
C(3)	13141(5)	1903(5)	874(5)	36(2)
C(4)	13674(6)	859(6)	766(5)	40(2)
C(5)	13145(6)	104(6)	661(5)	39(2)
C(6)	12064(6)	380(6)	678(5)	41(2)
C(7)	11512(5)	1414(5)	804(5)	32(2)
C(8)	10363(5)	1949(5)	828(5)	35(2)
C(9)	10359(5)	3095(5)	932(4)	29(2)
C(10)	9507(5)	3978(5)	1000(5)	34(2)
C(11)	8475(5)	3963(5)	968(4)	31(2)

C(12)	7616(5)	4833(5)	1028(5)	31(2)
C(13)	6534(5)	4831(5)	1050(5)	32(2)
C(14)	5885(5)	5911(5)	1297(4)	31(2)
C(15)	4804(5)	6339(5)	1476(5)	36(2)
C(16)	4428(6)	7394(6)	1664(5)	43(2)
C(17)	5121(6)	8023(6)	1680(5)	45(2)
C(18)	6203(6)	7606(6)	1518(5)	39(2)
C(19)	6562(5)	6553(5)	1346(5)	30(2)
C(20)	7665(5)	5902(5)	1169(5)	31(2)
C(21)	11663(5)	4112(5)	1064(5)	34(2)
C(22)	11640(7)	4415(7)	2063(6)	62(3)
C(27)	10016(6)	1766(6)	-99(5)	47(2)
C(28)	9721(6)	1570(6)	1655(6)	50(2)
C(29)	6136(5)	4026(5)	832(5)	32(2)
C(30)	6769(6)	3071(6)	428(5)	36(2)
N(31)	7243(5)	2288(5)	80(5)	47(2)
C(32)	5038(6)	4081(5)	947(5)	37(2)
N(33)	4174(5)	4064(5)	1040(5)	50(2)
O(34)	8448(4)	6249(3)	1132(3)	37(1)
N(35)	3240(4)	11506(4)	4126(4)	30(1)
C(36)	2233(5)	12222(5)	4248(5)	29(2)
C(37)	1997(5)	13293(5)	4257(5)	36(2)
C(38)	943(6)	13824(6)	4408(5)	40(2)
C(39)	168(5)	13282(6)	4536(5)	42(2)
C(40)	435(6)	12203(5)	4521(5)	40(2)
C(41)	1483(5)	11676(5)	4372(5)	33(2)
C(42)	2006(5)	10517(5)	4341(5)	32(2)
C(43)	3168(5)	10518(5)	4171(4)	30(2)
C(44)	4059(5)	9671(5)	4074(4)	32(2)
C(45)	4037(5)	8642(5)	4125(5)	30(2)
C(46)	4910(5)	7796(5)	4013(5)	30(2)
C(47)	4915(5)	6713(5)	3986(5)	31(2)
C(48)	6037(5)	6082(5)	3736(5)	31(2)
C(49)	6491(6)	5030(5)	3606(5)	38(2)
C(50)	7576(6)	4701(6)	3410(5)	40(2)
C(51)	8205(6)	5373(6)	3347(5)	42(2)
C(52)	7741(6)	6426(6)	3472(5)	39(2)
C(53)	6671(5)	6784(5)	3665(5)	32(2)
C(54)	6013(5)	7861(6)	3827(5)	32(2)
C(55)	4213(5)	11818(5)	3951(5)	34(2)
C(56)	4574(5)	11933(6)	2924(5)	41(2)
C(57)	5673(6)	12136(6)	2761(6)	51(2)
C(58)	6579(6)	11186(6)	2809(6)	48(2)
C(59)	6747(6)	10414(6)	2007(6)	54(2)
C(60)	7754(6)	9549(6)	1984(6)	57(2)
C(61)	1717(6)	10020(6)	5282(5)	45(2)
C(62)	1697(6)	10002(6)	3524(6)	46(2)
C(63)	4071(5)	6280(5)	4173(5)	35(2)
C(64)	3054(6)	6845(6)	4551(6)	45(2)
N(65)	2213(6)	7284(5)	4893(6)	77(3)
C(66)	4135(6)	5216(6)	4001(5)	39(2)
N(67)	4143(5)	4359(5)	3862(5)	51(2)
O(68)	6336(4)	8638(4)	3821(3)	39(1)
C(23)	11783(11)	5476(10)	2161(9)	132(6)

C(24)	11051(11)	6240(8)	2509(13)	169(8)
C(25)	11233(9)	7326(8)	2548(10)	114(5)
C(26)	10239(8)	8114(8)	2684(7)	84(3)

Table A14. Bond lengths [Å] and angles [°] for **1g**

N(1)-C(9)	1.3(2)	C(18)-C(19)	1.389(10)	C(46)-C(47)	1.454(9)
N(1)-C(2)	1.43(6)	C(19)-C(20)	1.49(18)	C(46)-C(54)	1.5(2)
N(1)-C(21)	1.47(3)	C(20)-O(34)	1.23(15)	C(47)-C(63)	1.37(15)
C(2)-C(3)	1.4(2)	C(21)-C(22)	1.521(11)	C(47)-C(48)	1.50(18)
C(2)-C(7)	1.40(8)	C(22)-C(23)	1.497(17)	C(48)-C(49)	1.393(17)
C(3)-C(4)	1.40(3)	C(29)-C(32)	1.4(2)	C(48)-C(53)	1.41(10)
C(4)-C(5)	1.39(8)	C(29)-C(30)	1.43(4)	C(49)-C(50)	1.4(2)
C(5)-C(6)	1.4(2)	C(30)-N(31)	1.16(2)	C(50)-C(51)	1.37(10)
C(6)-C(7)	1.40(3)	C(32)-N(33)	1.14(17)	C(51)-C(52)	1.395(18)
C(7)-C(8)	1.5(2)	N(35)-C(43)	1.353(9)	C(52)-C(53)	1.4(2)
C(8)-C(28)	1.52(7)	N(35)-C(36)	1.42(15)	C(53)-C(54)	1.49(4)
C(8)-C(27)	1.54(3)	N(35)-C(55)	1.44(18)	C(54)-O(68)	1.22(4)
C(8)-C(9)	1.550(9)	C(36)-C(41)	1.36(13)	C(55)-C(56)	1.520(17)
C(9)-C(10)	1.41(10)	C(36)-C(37)	1.392(9)	C(56)-C(57)	1.5(2)
C(10)-C(11)	1.4(2)	C(37)-C(38)	1.38(18)	C(57)-C(58)	1.52(11)
C(11)-C(12)	1.40(10)	C(38)-C(39)	1.39(13)	C(58)-C(59)	1.538(12)
C(12)-C(13)	1.4(2)	C(39)-C(40)	1.402(10)	C(59)-C(60)	1.52(14)
C(12)-C(20)	1.476(10)	C(40)-C(41)	1.37(18)	C(63)-C(64)	1.40(16)
C(13)-C(29)	1.38(5)	C(41)-C(42)	1.53(2)	C(63)-C(66)	1.437(11)
C(13)-C(14)	1.51(4)	C(42)-C(43)	1.5(2)	C(64)-N(65)	1.16(13)
C(14)-C(15)	1.38(19)	C(42)-C(61)	1.549(16)	C(66)-N(67)	1.171(9)
C(14)-C(19)	1.40(11)	C(42)-C(62)	1.55(3)	C(23)-C(24)	1.27(7)
C(15)-C(16)	1.397(11)	C(43)-C(44)	1.40(11)	C(24)-C(25)	1.54(2)
C(16)-C(17)	1.40(11)	C(44)-C(45)	1.390(9)	C(25)-C(26)	1.45(14)
C(17)-C(18)	1.4(2)	C(45)-C(46)	1.39(11)		
C(9)-N(1)-C(2)	111(6)	C(18)-C(19)-C(14)	123(6)	C(45)-C(46)-C(47)	128(6)
C(9)-N(1)-C(21)	125.0(17)	C(18)-C(19)-C(20)	129(2)	C(45)-C(46)-C(54)	124(6)
C(2)-N(1)-C(21)	124(7)	C(14)-C(19)-C(20)	108(8)	C(47)-C(46)-C(54)	107.7(7)
C(3)-C(2)-C(7)	122(5)	O(34)-C(20)-C(12)	129(2)	C(63)-C(47)-C(46)	128(3)
C(3)-C(2)-N(1)	128(3)	O(34)-C(20)-C(19)	123(8)	C(63)-C(47)-C(48)	123(7)
C(7)-C(2)-N(1)	109(8)	C(12)-C(20)-C(19)	108(5)	C(46)-C(47)-C(48)	109(5)
C(2)-C(3)-C(4)	117(2)	N(1)-C(21)-C(22)	113.6(6)	C(49)-C(48)-C(53)	121(7)
C(5)-C(4)-C(3)	122(7)	C(23)-C(22)-C(21)	113.2(8)	C(49)-C(48)-C(47)	133.3(12)
C(6)-C(5)-C(4)	120(5)	C(13)-C(29)-C(32)	123(3)	C(53)-C(48)-C(47)	106(8)
C(5)-C(6)-C(7)	119(2)	C(13)-C(29)-C(30)	124(7)	C(50)-C(49)-C(48)	118.0(10)
C(2)-C(7)-C(6)	119(8)	C(32)-C(29)-C(30)	112(4)	C(51)-C(50)-C(49)	122(6)
C(2)-C(7)-C(8)	109(7)	N(31)-C(30)-C(29)	176.7(8)	C(50)-C(51)-C(52)	120(7)
C(6)-C(7)-C(8)	131.8(7)	N(33)-C(32)-C(29)	176.0(10)	C(53)-C(52)-C(51)	120.4(9)
C(7)-C(8)-C(28)	109(6)	C(43)-N(35)-C(36)	112(6)	C(52)-C(53)-C(48)	119(6)
C(7)-C(8)-C(27)	109(4)	C(43)-N(35)-C(55)	125.0(17)	C(52)-C(53)-C(54)	129.5(17)
C(28)-C(8)-C(27)	113(6)	C(36)-N(35)-C(55)	123(7)	C(48)-C(53)-C(54)	111(8)
C(7)-C(8)-C(9)	102(4)	C(41)-C(36)-C(37)	124(5)	O(68)-C(54)-C(46)	127(2)
C(28)-C(8)-C(9)	112.4(7)	C(41)-C(36)-N(35)	108(8)	O(68)-C(54)-C(53)	127(7)
C(27)-C(8)-C(9)	110.4(6)	C(37)-C(36)-N(35)	129(3)	C(46)-C(54)-C(53)	106(5)
N(1)-C(9)-C(10)	122(6)	C(38)-C(37)-C(36)	118(2)	N(35)-C(55)-C(56)	112.3(13)
N(1)-C(9)-C(8)	108.8(7)	C(37)-C(38)-C(39)	120(7)	C(55)-C(56)-C(57)	110.7(14)
C(10)-C(9)-C(8)	129(6)	C(38)-C(39)-C(40)	121(5)	C(58)-C(57)-C(56)	115(7)

C(11)-C(10)-C(9)	124(6)	C(41)-C(40)-C(39)	119(2)	C(57)-C(58)-C(59)	114(2)
C(10)-C(11)-C(12)	125(6)	C(36)-C(41)-C(40)	119(7)	C(60)-C(59)-C(58)	113(2)
C(11)-C(12)-C(13)	126(6)	C(36)-C(41)-C(42)	110(7)	C(47)-C(63)-C(64)	123(7)
C(11)-C(12)-C(20)	126(6)	C(40)-C(41)-C(42)	130.7(8)	C(47)-C(63)-C(66)	124(3)
C(13)-C(12)-C(20)	108.2(7)	C(43)-C(42)-C(41)	101(4)	C(64)-C(63)-C(66)	113(4)
C(29)-C(13)-C(12)	128(3)	C(43)-C(42)-C(61)	111.2(10)	N(65)-C(64)-C(63)	177.3(9)
C(29)-C(13)-C(14)	125(7)	C(41)-C(42)-C(61)	110.6(19)	N(67)-C(66)-C(63)	177.3(9)
C(12)-C(13)-C(14)	107(5)	C(43)-C(42)-C(62)	112(3)	C(24)-C(23)-C(22)	124(6)
C(15)-C(14)-C(19)	118(7)	C(41)-C(42)-C(62)	110(3)	C(23)-C(24)-C(25)	122(6)
C(15)-C(14)-C(13)	132.2(11)	C(61)-C(42)-C(62)	112(2)	C(26)-C(25)-C(24)	111(7)
C(19)-C(14)-C(13)	109(8)	N(35)-C(43)-C(44)	123(6)		
C(14)-C(15)-C(16)	119.1(10)	N(35)-C(43)-C(42)	108.6(8)		
C(15)-C(16)-C(17)	121(6)	C(44)-C(43)-C(42)	128(6)		
C(18)-C(17)-C(16)	120(7)	C(45)-C(44)-C(43)	126(6)		
C(17)-C(18)-C(19)	117.5(10)	C(44)-C(45)-C(46)	126(6)		

Crystallographic tables for dye 2a

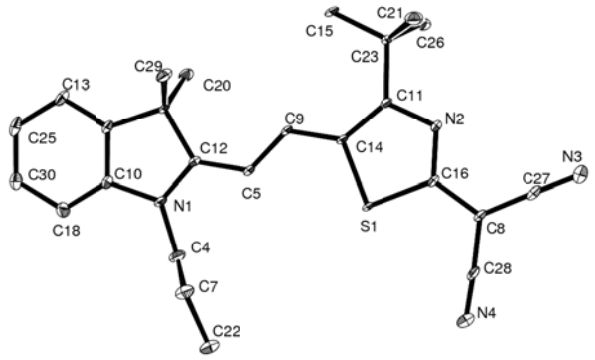

Figure A7. ORTEP drawing of **2a** with atom labelling and 50% probability ellipsoids.

Table A15. Atomic coordinates ($\times 10^4$) and equivalent isotropic displacement parameters ($Å^2 \times 10^3$) for **2a**

Atom	x	y	z	U(eq)
S(1)	5473(1)	7395(1)	2443(1)	9(1)
N(1)	8451(1)	7264(2)	3944(1)	12(1)
N(2)	3404(1)	7433(2)	2526(1)	10(1)
C(4)	9021(1)	6844(3)	3449(1)	16(1)
C(5)	6705(1)	7335(2)	3525(1)	10(1)
N(4)	5601(1)	7447(2)	991(1)	19(1)
C(7)	9177(1)	8613(3)	3094(1)	17(1)
C(8)	3992(1)	7427(2)	1612(1)	10(1)
C(9)	5601(1)	7410(2)	3537(1)	9(1)
C(10)	8960(1)	7389(2)	4455(1)	11(1)
C(11)	3795(1)	7438(2)	3032(1)	9(1)
C(12)	7380(1)	7378(2)	3977(1)	9(1)
C(13)	8456(1)	7633(2)	5375(1)	15(1)
C(14)	4925(1)	7416(2)	3085(1)	9(1)
C(15)	3345(1)	7488(3)	4038(1)	16(1)
C(16)	4186(1)	7419(2)	2168(1)	8(1)
C(17)	7077(1)	7504(2)	4565(1)	9(1)
C(18)	10043(1)	7384(2)	4584(1)	14(1)

N(3)	2065(1)	7499(2)	1231(1)	18(1)
C(20)	6453(1)	5696(2)	4732(1)	13(1)
C(21)	2236(1)	9223(3)	3360(1)	16(1)
C(22)	9639(2)	7980(3)	2560(1)	20(1)
C(23)	2936(1)	7440(2)	3459(1)	10(1)
C(24)	8169(1)	7527(2)	4837(1)	10(1)
C(25)	9545(2)	7626(2)	5513(1)	18(1)
C(26)	2273(1)	5598(3)	3373(1)	16(1)
C(27)	2928(1)	7468(2)	1406(1)	11(1)
C(28)	4863(1)	7443(2)	1260(1)	12(1)
C(29)	6457(1)	9342(2)	4700(1)	13(1)
C(30)	10325(1)	7502(2)	5127(1)	16(1)

Table A16. Bond lengths [Å] and angles [°] for **2a**

S(1)-C(16)	1.7366(16)	C(8)-C(16)	1.4072(19)	C(17)-C(24)	1.513(2)
S(1)-C(14)	1.7595(15)	C(8)-C(28)	1.414(2)	C(17)-C(29)	1.538(2)
N(1)-C(12)	1.3438(19)	C(8)-C(27)	1.417(2)	C(17)-C(20)	1.543(2)
N(1)-C(10)	1.4204(19)	C(9)-C(14)	1.398(2)	C(18)-C(30)	1.399(2)
N(1)-C(4)	1.471(2)	C(10)-C(18)	1.383(2)	N(3)-C(27)	1.155(2)
N(2)-C(16)	1.3389(19)	C(10)-C(24)	1.393(2)	C(21)-C(23)	1.537(2)
N(2)-C(11)	1.3497(18)	C(11)-C(14)	1.415(2)	C(23)-C(26)	1.540(2)
C(4)-C(7)	1.534(2)	C(11)-C(23)	1.528(2)	C(25)-C(30)	1.390(3)
C(5)-C(9)	1.382(2)	C(12)-C(17)	1.530(2)		
C(5)-C(12)	1.399(2)	C(13)-C(24)	1.388(2)		
N(4)-C(28)	1.153(2)	C(13)-C(25)	1.397(2)		
C(7)-C(22)	1.532(2)	C(15)-C(23)	1.529(2)		
C(16)-S(1)-C(14)	89.36(7)	N(1)-C(12)-C(17)	109.22(13)	C(11)-C(23)-C(26)	106.58(12)
C(12)-N(1)-C(10)	111.67(13)	C(5)-C(12)-C(17)	128.62(13)	C(15)-C(23)-C(26)	108.53(13)
C(12)-N(1)-C(4)	124.31(13)	C(24)-C(13)-C(25)	118.12(15)	C(21)-C(23)-C(26)	110.42(13)
C(10)-N(1)-C(4)	123.68(13)	C(9)-C(14)-C(11)	131.32(13)	C(13)-C(24)-C(10)	119.83(14)
C(16)-N(2)-C(11)	111.99(13)	C(9)-C(14)-S(1)	120.00(11)	C(13)-C(24)-C(17)	130.55(14)
N(1)-C(4)-C(7)	113.41(15)	C(11)-C(14)-S(1)	108.68(11)	C(10)-C(24)-C(17)	109.61(13)
C(9)-C(5)-C(12)	124.45(14)	N(2)-C(16)-C(8)	123.25(14)	C(30)-C(25)-C(13)	121.37(15)
C(22)-C(7)-C(4)	109.20(15)	N(2)-C(16)-S(1)	114.56(11)	N(3)-C(27)-C(8)	179.22(17)
C(16)-C(8)-C(28)	119.77(14)	C(8)-C(16)-S(1)	122.19(12)	N(4)-C(28)-C(8)	177.21(17)
C(16)-C(8)-C(27)	120.21(14)	C(24)-C(17)-C(12)	101.27(12)	C(25)-C(30)-C(18)	120.85(15)
C(28)-C(8)-C(27)	120.00(13)	C(24)-C(17)-C(29)	110.22(12)		
C(5)-C(9)-C(14)	124.62(14)	C(12)-C(17)-C(29)	113.22(12)		
C(18)-C(10)-C(24)	122.84(14)	C(24)-C(17)-C(20)	110.01(12)		
C(18)-C(10)-N(1)	128.99(15)	C(12)-C(17)-C(20)	110.47(12)		
C(24)-C(10)-N(1)	108.17(13)	C(29)-C(17)-C(20)	111.22(13)		
N(2)-C(11)-C(14)	115.41(13)	C(10)-C(18)-C(30)	116.98(16)		
N(2)-C(11)-C(23)	114.23(13)	C(11)-C(23)-C(15)	115.93(13)		
C(14)-C(11)-C(23)	130.35(13)	C(11)-C(23)-C(21)	107.10(12)		
N(1)-C(12)-C(5)	122.14(13)	C(15)-C(23)-C(21)	108.25(13)		

Crystallographic tables for dye 2b

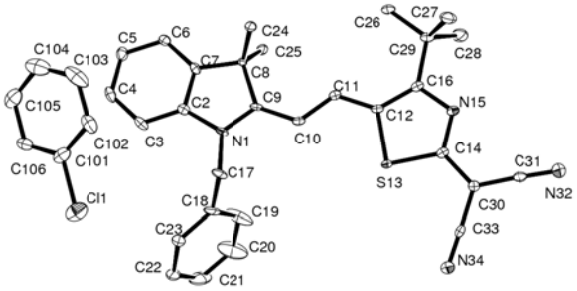

Figure A8. ORTEP drawing of **2b** with atom labelling and 50% probability ellipsoids.

Table A17. Atomic coordinates ($\times 10^4$) and equivalent isotropic displacement parameters ($Å^2 \times 10^3$) for **2b**

Atom	x	y	z	U(eq)
N(1)	6948(1)	4364(2)	1182(1)	11(1)
C(2)	5901(1)	4410(3)	1000(1)	11(1)
C(3)	5553(2)	4076(3)	577(1)	16(1)
C(4)	4469(2)	4191(3)	488(1)	17(1)
C(5)	3780(2)	4612(3)	807(1)	16(1)
C(6)	4144(2)	4927(3)	1234(1)	14(1)
C(7)	5220(2)	4813(3)	1324(1)	10(1)
C(8)	5837(1)	4973(2)	1749(1)	9(1)
C(9)	6972(1)	4733(2)	1608(1)	10(1)
C(10)	7901(1)	4823(3)	1866(1)	12(1)
C(11)	7944(1)	5010(2)	2312(1)	11(1)
C(12)	8875(1)	5046(2)	2572(1)	11(1)
S(13)	10093(1)	5015(1)	2325(1)	10(1)
C(14)	10730(1)	5006(2)	2833(1)	10(1)
N(15)	10084(1)	5022(2)	3163(1)	11(1)
C(16)	9064(1)	5051(2)	3026(1)	11(1)
C(17)	7829(2)	3707(3)	929(1)	16(1)
C(18)	8241(2)	5196(3)	624(1)	19(1)
C(19)	8584(2)	6969(4)	776(1)	44(1)
C(20)	8985(3)	8290(4)	496(1)	54(1)
C(21)	9069(2)	7841(4)	63(1)	41(1)
C(22)	8762(2)	6083(5)	-86(1)	42(1)
C(23)	8340(2)	4747(4)	194(1)	30(1)
C(24)	5538(1)	3276(3)	2038(1)	14(1)
C(25)	5620(1)	6880(3)	1969(1)	14(1)
C(26)	7119(2)	5171(3)	3248(1)	18(1)
C(27)	8464(2)	3183(3)	3645(1)	21(1)
C(28)	8555(2)	6762(3)	3684(1)	23(1)
C(29)	8286(2)	5048(3)	3390(1)	14(1)
C(30)	11835(2)	4990(2)	2885(1)	10(1)
C(31)	12348(2)	4955(3)	3300(1)	13(1)
N(32)	12796(1)	4921(2)	3632(1)	20(1)
C(33)	12453(1)	5063(3)	2518(1)	12(1)
N(34)	12938(1)	5131(2)	2213(1)	19(1)
Cl(1)	6773(1)	615(2)	-334(1)	34(1)
C(101)	5534(3)	293(6)	-131(2)	22(1)
C(102)	5493(14)	-480(20)	281(4)	25(3)

C(103)	4463(6)	-717(7)	439(2)	39(1)
C(104)	3578(6)	-192(8)	174(2)	38(2)
C(105)	3659(4)	540(7)	-220(2)	29(1)
C(106)	4674(12)	785(18)	-384(4)	18(2)

Table A18. Bond lengths [Å] and angles [°] for **2b**

N(1)-C(9)	1.344(2)	C(12)-C(16)	1.417(3)	C(28)-C(29)	1.539(3)
N(1)-C(2)	1.420(2)	C(12)-S(13)	1.7571(19)	C(30)-C(33)	1.413(3)
N(1)-C(17)	1.470(2)	S(13)-C(14)	1.735(2)	C(30)-C(31)	1.416(3)
C(2)-C(3)	1.383(3)	C(14)-N(15)	1.341(2)	C(31)-N(32)	1.152(3)
C(2)-C(7)	1.385(3)	C(14)-C(30)	1.404(3)	C(33)-N(34)	1.154(3)
C(3)-C(4)	1.393(3)	N(15)-C(16)	1.344(2)	Cl(1)-C(101)	1.737(5)
C(4)-C(5)	1.381(3)	C(16)-C(29)	1.533(3)	C(101)-C(106)	1.358(17)
C(5)-C(6)	1.399(3)	C(17)-C(18)	1.519(3)	C(101)-C(102)	1.390(11)
C(6)-C(7)	1.383(3)	C(18)-C(23)	1.382(3)	C(102)-C(103)	1.427(14)
C(7)-C(8)	1.506(2)	C(18)-C(19)	1.393(4)	C(103)-C(104)	1.409(10)
C(8)-C(25)	1.533(2)	C(19)-C(20)	1.384(4)	C(104)-C(105)	1.333(9)
C(8)-C(9)	1.535(2)	C(20)-C(21)	1.388(4)	C(105)-C(106)	1.418(12)
C(8)-C(24)	1.547(2)	C(21)-C(22)	1.368(4)		
C(9)-C(10)	1.394(3)	C(22)-C(23)	1.401(3)		
C(10)-C(11)	1.386(3)	C(26)-C(29)	1.528(3)		
C(11)-C(12)	1.399(3)	C(27)-C(29)	1.541(3)		
C(9)-N(1)-C(2)	111.35(15)	C(10)-C(9)-C(8)	127.62(16)	C(21)-C(22)-C(23)	120.4(2)
C(9)-N(1)-C(17)	126.99(16)	C(11)-C(10)-C(9)	124.63(17)	C(18)-C(23)-C(22)	120.0(2)
C(2)-N(1)-C(17)	121.07(16)	C(10)-C(11)-C(12)	124.62(17)	C(26)-C(29)-C(16)	115.91(16)
C(3)-C(2)-C(7)	122.69(17)	C(11)-C(12)-C(16)	132.16(17)	C(26)-C(29)-C(28)	108.15(16)
C(3)-C(2)-N(1)	128.61(17)	C(11)-C(12)-S(13)	119.02(15)	C(16)-C(29)-C(28)	107.62(15)
C(7)-C(2)-N(1)	108.68(16)	C(16)-C(12)-S(13)	108.79(14)	C(26)-C(29)-C(27)	108.18(16)
C(2)-C(3)-C(4)	116.44(18)	C(14)-S(13)-C(12)	89.21(9)	C(16)-C(29)-C(27)	107.20(15)
C(5)-C(4)-C(3)	121.57(18)	N(15)-C(14)-C(30)	123.69(18)	C(28)-C(29)-C(27)	109.69(18)
C(4)-C(5)-C(6)	121.25(18)	N(15)-C(14)-S(13)	114.69(14)	C(14)-C(30)-C(33)	119.77(17)
C(7)-C(6)-C(5)	117.46(18)	C(30)-C(14)-S(13)	121.62(15)	C(14)-C(30)-C(31)	121.30(17)
C(6)-C(7)-C(2)	120.58(17)	C(14)-N(15)-C(16)	111.90(16)	C(33)-C(30)-C(31)	118.91(17)
C(6)-C(7)-C(8)	129.81(17)	N(15)-C(16)-C(12)	115.41(17)	N(32)-C(31)-C(30)	177.9(2)
C(2)-C(7)-C(8)	109.54(16)	N(15)-C(16)-C(29)	114.31(16)	N(34)-C(33)-C(30)	178.4(2)
C(7)-C(8)-C(25)	110.97(15)	C(12)-C(16)-C(29)	130.27(17)	C(106)-C(101)-C(102)	124.4(10)
C(7)-C(8)-C(9)	101.40(14)	N(1)-C(17)-C(18)	114.15(16)	C(106)-C(101)-Cl(1)	118.3(5)
C(25)-C(8)-C(9)	114.38(15)	C(23)-C(18)-C(19)	119.3(2)	C(102)-C(101)-Cl(1)	117.3(8)
C(7)-C(8)-C(24)	108.52(15)	C(23)-C(18)-C(17)	119.6(2)	C(101)-C(102)-C(103)	115.9(13)
C(25)-C(8)-C(24)	111.20(15)	C(19)-C(18)-C(17)	121.02(19)	C(104)-C(103)-C(102)	119.1(9)
C(9)-C(8)-C(24)	109.85(14)	C(20)-C(19)-C(18)	120.3(3)	C(105)-C(104)-C(103)	122.8(7)
N(1)-C(9)-C(10)	123.50(16)	C(19)-C(20)-C(21)	120.2(3)	C(104)-C(105)-C(106)	119.1(7)
N(1)-C(9)-C(8)	108.87(15)	C(22)-C(21)-C(20)	119.8(2)	C(101)-C(106)-C(105)	118.7(8)

Crystallographic tables for dye 2c

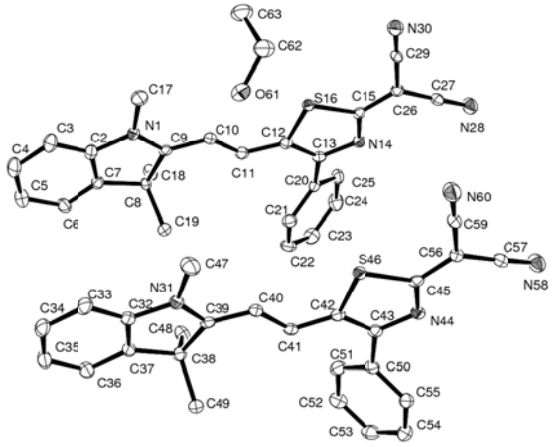

Figure A9. ORTEP drawing of **2c** with atom labelling and 50% probability ellipsoids.

Table A19. Atomic coordinates ($\times 10^4$) and equivalent isotropic displacement parameters ($Å^2 \times 10^3$) for **2c**

Atom	x	y	z	U(eq)
S16	0.48500(7)	0.62394(5)	0.04802(6)	0.0143(2)
N1	0.0448(2)	0.6276(2)	0.3304(2)	0.0167(8)
N14	0.5656(2)	0.63310(19)	-0.1589(2)	0.0156(8)
N28	0.8742(3)	0.6218(2)	-0.2903(2)	0.0271(10)
N30	0.7653(3)	0.6218(2)	0.0575(2)	0.0226(9)
C2	-0.0764(3)	0.6254(2)	0.3734(3)	0.0182(9)
C3	-0.1561(3)	0.6219(3)	0.4787(3)	0.0236(10)
C4	-0.2702(3)	0.6192(3)	0.4980(3)	0.0284(11)
C5	-0.3011(3)	0.6203(3)	0.4145(3)	0.0262(11)
C6	-0.2189(3)	0.6237(2)	0.3091(3)	0.0208(10)
C7	-0.1054(3)	0.6264(2)	0.2890(3)	0.0167(9)
C8	0.0024(3)	0.6297(2)	0.1843(2)	0.0145(9)
C9	0.0940(3)	0.6304(2)	0.2242(2)	0.0142(9)
C10	0.2134(3)	0.6292(2)	0.1640(2)	0.0152(9)
C11	0.2692(3)	0.6363(2)	0.0546(3)	0.0171(9)
C12	0.3884(3)	0.6318(2)	-0.0072(3)	0.0159(9)
C13	0.4503(3)	0.6365(2)	-0.1189(3)	0.0155(9)
C15	0.5969(3)	0.6273(2)	-0.0798(2)	0.0141(9)
C17	0.1046(3)	0.6277(3)	0.3970(3)	0.0247(11)
C18	0.0027(3)	0.7205(3)	0.1205(3)	0.0212(11)
C19	0.0108(3)	0.5386(3)	0.1198(3)	0.0235(11)
C20	0.4041(3)	0.6476(2)	-0.1976(3)	0.0160(9)
C21	0.3068(3)	0.5995(2)	-0.1885(3)	0.0205(10)
C22	0.2700(3)	0.6111(3)	-0.2672(3)	0.0229(11)
C23	0.3299(3)	0.6687(3)	-0.3552(3)	0.0269(11)
C24	0.4267(4)	0.7170(3)	-0.3650(3)	0.0281(11)
C25	0.4633(3)	0.7072(3)	-0.2866(3)	0.0218(10)
C26	0.7125(3)	0.6232(2)	-0.0987(3)	0.0150(9)
C27	0.8007(3)	0.6222(2)	-0.2045(3)	0.0168(10)
C29	0.7423(3)	0.6218(2)	-0.0131(3)	0.0156(9)
S46	0.49414(7)	0.12844(5)	0.05368(6)	0.0153(2)
N31	0.0754(2)	0.1244(2)	0.3365(2)	0.0167(8)

N44	0.5830(2)	0.11462(19)	-0.1536(2)	0.0167(8)
N58	0.8921(3)	0.1272(2)	-0.2720(2)	0.0262(10)
N60	0.7662(3)	0.1278(2)	0.0782(2)	0.0279(10)
C32	-0.0456(3)	0.1234(2)	0.3899(3)	0.0178(9)
C33	-0.1143(3)	0.1217(2)	0.4993(3)	0.0231(10)
C34	-0.2314(3)	0.1206(2)	0.5316(3)	0.0233(10)
C35	-0.2751(3)	0.1214(3)	0.4572(3)	0.0257(10)
C36	-0.2036(3)	0.1223(2)	0.3476(3)	0.0208(10)
C37	-0.0871(3)	0.1230(2)	0.3149(3)	0.0166(9)
C38	0.0115(3)	0.1253(2)	0.2040(2)	0.0159(9)
C39	0.1135(3)	0.1235(2)	0.2295(3)	0.0151(9)
C40	0.2306(3)	0.1256(2)	0.1629(3)	0.0162(9)
C41	0.2838(3)	0.1203(2)	0.0523(3)	0.0157(9)
C42	0.4021(3)	0.1227(2)	-0.0066(3)	0.0154(9)
C43	0.4690(3)	0.1156(2)	-0.1184(3)	0.0159(9)
C45	0.6105(3)	0.1216(2)	-0.0716(2)	0.0153(9)
C47	0.1476(3)	0.1278(3)	0.3913(3)	0.0284(11)
C48	0.0102(3)	0.2194(3)	0.1452(3)	0.0211(10)
C49	0.0068(3)	0.0378(3)	0.1386(3)	0.0214(10)
C50	0.4241(3)	0.1032(2)	-0.1974(3)	0.0175(9)
C51	0.3331(3)	0.1567(2)	-0.1961(3)	0.0224(10)
C52	0.2964(3)	0.1435(3)	-0.2742(3)	0.0256(11)
C53	0.3486(4)	0.0764(3)	-0.3531(3)	0.0275(11)
C54	0.4382(3)	0.0217(3)	-0.3536(3)	0.0254(11)
C55	0.4761(3)	0.0350(2)	-0.2769(3)	0.0205(10)
C56	0.7230(3)	0.1236(2)	-0.0845(3)	0.0158(9)
C57	0.8157(3)	0.1251(2)	-0.1887(3)	0.0182(10)
C59	0.7475(3)	0.1260(2)	0.0045(3)	0.0180(9)
O61	0.3591(2)	0.53588(19)	0.2937(2)	0.0307(9)
C62	0.4504(4)	0.5739(3)	0.3107(3)	0.0321(12)
C63	0.4234(4)	0.6783(3)	0.3400(3)	0.0348(14)

Table A20. Bond lengths [Å] and angles [°] for **2c**

N1-C9	1.331(4)	C8-C9	1.528(6)	C38-C39	1.525(6)
N1-C17	1.456(5)	C8-C18	1.536(5)	C38-C48	1.541(5)
N1-C2	1.424(5)	C10-C11	1.374(5)	C39-C40	1.396(6)
N14-C15	1.339(4)	C11-C12	1.410(6)	C40-C41	1.388(5)
N14-C13	1.357(5)	C12-C13	1.405(5)	S16-C12	1.749(4)
N28-C27	1.158(5)	C13-C20	1.477(6)	S16-C15	1.737(3)
N30-C29	1.151(5)	C15-C26	1.415(6)	S46-C45	1.741(3)
N31-C39	1.351(5)	C20-C21	1.394(6)	S46-C42	1.750(4)
N31-C32	1.419(5)	C20-C25	1.401(5)	O61-C62	1.421(6)
N31-C47	1.456(5)	C21-C22	1.389(6)	C41-C42	1.394(6)
N44-C45	1.348(4)	C22-C23	1.377(6)	C42-C43	1.417(5)
N44-C43	1.347(5)	C23-C24	1.386(7)	C43-C50	1.473(6)
N58-C57	1.150(5)	C24-C25	1.381(6)	C45-C56	1.400(6)
N60-C59	1.159(5)	C26-C29	1.412(6)	C50-C55	1.395(5)
C9-C10	1.408(5)	C26-C27	1.416(5)	C50-C51	1.394(6)
C2-C7	1.389(6)	C32-C37	1.377(6)	C51-C52	1.387(6)
C2-C3	1.376(5)	C32-C33	1.388(5)	C52-C53	1.380(6)
C3-C4	1.394(6)	C33-C34	1.391(6)	C53-C54	1.391(7)
C4-C5	1.393(6)	C34-C35	1.390(6)	C54-C55	1.379(6)
C5-C6	1.387(5)	C35-C36	1.397(5)	C56-C59	1.415(6)
C6-C7	1.383(6)	C36-C37	1.383(6)	C56-C57	1.424(5)

C7-C8	1.517(5)	C37-C38	1.515(5)	C62-C63	1.510(6)
C8-C19	1.538(5)	C38-C49	1.547(5)		
N1-C9-C10	121.8(3)	C43-C50-C51	122.9(3)	N31-C39-C40	119.7(4)
N1-C9-C8	109.7(3)	C51-C50-C55	119.2(4)	C53-C54-C55	120.6(4)
C9-C10-C11	124.5(4)	C43-C50-C55	117.9(3)	C50-C55-C54	120.1(4)
C10-C11-C12	125.3(4)	C50-C51-C52	120.3(3)	C51-C52-C53	120.3(4)
S16-C12-C13	108.6(3)	N31-C32-C33	127.3(4)	C52-C53-C54	119.5(4)
C11-C12-C13	128.0(4)	C32-C33-C34	116.1(4)	C43-N44-C45	110.9(3)
S16-C12-C11	123.4(3)	C33-C34-C35	121.0(4)	C3-C2-C7	123.1(4)
C12-C13-C20	127.3(4)	C34-C35-C36	121.5(4)	N1-C2-C7	108.2(3)
N14-C13-C12	116.4(4)	C35-C36-C37	117.8(4)	N1-C2-C3	128.8(4)
N14-C13-C20	116.3(3)	C32-C37-C38	109.6(4)	C2-C3-C4	116.5(4)
S16-C15-C26	122.3(3)	C36-C37-C38	130.7(4)	C3-C4-C5	121.3(4)
S16-C15-N14	115.1(3)	C32-C37-C36	119.7(4)	C4-C5-C6	120.9(4)
C13-C20-C25	118.0(4)	C37-C38-C39	101.4(3)	C5-C6-C7	118.3(4)
C21-C20-C25	119.1(4)	C37-C38-C49	110.8(3)	C6-C7-C8	130.7(4)
C13-C20-C21	122.9(3)	C39-C38-C48	110.5(3)	C2-C7-C6	119.9(4)
C20-C21-C22	119.9(3)	C15-C26-C29	120.9(3)	C2-C7-C8	109.4(4)
C21-C22-C23	120.5(4)	C27-C26-C29	118.8(4)	C7-C8-C18	109.9(3)
C22-C23-C24	120.1(4)	C15-C26-C27	120.3(3)	C7-C8-C9	101.1(2)
C23-C24-C25	120.0(4)	N28-C27-C26	178.8(5)	C7-C8-C19	109.9(3)
N31-C32-C37	108.8(3)	N30-C29-C26	178.9(4)	C18-C8-C19	110.8(3)
C33-C32-C37	123.8(4)	C12-S16-C15	89.39(19)	C9-C8-C18	113.5(3)
C38-C39-C40	131.2(3)	C42-S46-C45	89.64(19)	C9-C8-C19	111.1(3)
C39-C40-C41	127.0(4)	C2-N1-C17	122.8(3)	C8-C9-C10	128.5(2)
C40-C41-C42	122.3(4)	C2-N1-C9	111.7(3)	C45-C56-C59	121.4(3)
S46-C42-C43	108.3(3)	C9-N1-C17	125.5(3)	C57-C56-C59	118.5(4)
C41-C42-C43	129.1(4)	C13 -N14 -C15	110.6(3)	C45-C56-C57	120.1(3)
S46-C42-C41	122.4(3)	C39 -N31-C47	125.1(3)	N58-C57-C56	178.5(4)
N44-C43-C50	117.9(3)	C32-N31-C39	111.2(3)	N60-C59-C56	179.2(4)
C42-C43-C50	125.4(4)	C32-N31-C47	123.7(3)	O61-C62-C63	107.2(4)
N44-C43-C42	116.5(4)	C37-C38-C48	110.6(3)	C20-C25-C24	120.4(4)
S46-C45-N44	114.6(3)	C48-C38 -C49	109.9(3)	N14-C15-C26	122.6(3)
N44-C45-C56	123.5(3)	C39-C38-C49	113.4(3)		
S46-C45-C56	121.9(3)	N31-C39-C38	109.0(3)		

Crystallographic tables for dye 2e

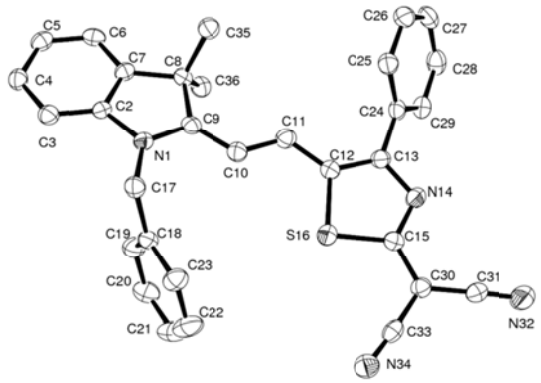

Figure A10. ORTEP drawing of **2e** with atom labelling and 50% probability ellipsoids.

Table A21. Atomic coordinates ($\times 10^4$) and equivalent isotropic displacement parameters ($Å^2 \times 10^3$) for **2e**

Atom	x	y	z	U(eq)
S(16)	-673(1)	929(1)	707(1)	33(1)
N(1)	2392(2)	-1279(2)	2423(1)	25(1)
C(2)	3389(2)	-1443(2)	2914(1)	23(1)
C(8)	3701(2)	183(2)	2174(1)	24(1)
N(14)	-424(2)	2613(2)	-211(1)	28(1)
C(12)	697(2)	1454(2)	630(1)	27(1)
C(17)	1387(2)	-2050(2)	2375(1)	29(1)
N(32)	-3214(2)	3183(2)	-1271(1)	40(1)
C(13)	626(2)	2349(2)	109(1)	26(1)
C(15)	-1215(2)	1916(2)	41(1)	28(1)
C(11)	1649(2)	1015(2)	1056(1)	29(1)
C(25)	2528(2)	2316(2)	-326(1)	30(1)
C(23)	-716(2)	-1637(2)	2214(1)	35(1)
C(6)	5219(2)	-551(2)	3193(1)	28(1)
C(27)	3506(2)	4107(3)	-565(1)	37(1)
C(30)	-2378(2)	1923(2)	-207(1)	28(1)
C(29)	1680(2)	4204(2)	-139(1)	32(1)
C(24)	1627(2)	2968(2)	-119(1)	27(1)
C(18)	343(2)	-1443(2)	2599(1)	27(1)
C(3)	3585(2)	-2257(2)	3462(1)	28(1)
C(7)	4177(2)	-598(2)	2781(1)	23(1)
C(5)	5440(2)	-1351(2)	3749(1)	29(1)
C(19)	433(2)	-688(2)	3175(1)	34(1)
C(31)	-2832(2)	2633(2)	-788(1)	29(1)
C(4)	4633(2)	-2182(2)	3882(1)	29(1)
C(36)	3662(2)	1482(2)	2422(1)	31(1)
C(35)	4401(2)	36(2)	1546(1)	32(1)
N(34)	-3634(2)	404(2)	349(1)	37(1)
C(33)	-3098(2)	1097(2)	85(1)	28(1)
C(10)	1619(2)	65(2)	1510(1)	28(1)
C(9)	2511(2)	-335(2)	1999(1)	24(1)
C(28)	2620(3)	4761(2)	-357(1)	36(1)
C(22)	-1669(2)	-1067(2)	2407(2)	46(1)
C(20)	-524(2)	-122(2)	3368(1)	41(1)
C(21)	-1575(2)	-311(2)	2983(2)	47(1)
C(26)	3462(2)	2880(2)	-553(1)	36(1)

Table A22. Bond lengths [Å] and angles [°] for **2e**

S(16)-C(12)	1.746(2)	C(12)-C(13)	1.409(3)	C(30)-C(31)	1.415(4)
S(16)-C(15)	1.747(2)	C(17)-C(18)	1.516(3)	C(30)-C(33)	1.419(4)
N(1)-C(9)	1.351(3)	N(32)-C(31)	1.153(3)	C(29)-C(28)	1.381(3)
N(1)-C(2)	1.424(3)	C(13)-C(24)	1.482(3)	C(29)-C(24)	1.393(3)
N(1)-C(17)	1.467(3)	C(15)-C(30)	1.399(3)	C(18)-C(19)	1.378(3)
C(2)-C(7)	1.376(3)	C(11)-C(10)	1.377(3)	C(3)-C(4)	1.393(3)
C(2)-C(3)	1.385(3)	C(25)-C(26)	1.387(3)	C(5)-C(4)	1.381(3)
C(8)-C(7)	1.503(3)	C(25)-C(24)	1.390(3)	C(19)-C(20)	1.386(3)
C(8)-C(9)	1.523(3)	C(23)-C(22)	1.383(3)	N(34)-C(33)	1.157(3)
C(8)-C(36)	1.539(3)	C(23)-C(18)	1.389(3)	C(10)-C(9)	1.394(3)
C(8)-C(35)	1.540(3)	C(6)-C(7)	1.380(3)	C(22)-C(21)	1.380(4)
N(14)-C(13)	1.348(3)	C(6)-C(5)	1.388(3)	C(20)-C(21)	1.381(4)
N(14)-C(15)	1.350(3)	C(27)-C(28)	1.378(3)		

C(12)-C(11)	1.395(3)	C(27)-C(26)	1.382(3)		
C(12)-S(16)-C(15)	89.26(12)	C(25)-C(24)-C(29)	118.8(2)	C(4)-C(5)-C(6)	120.5(2)
C(9)-N(1)-C(2)	110.82(18)	C(25)-C(24)-C(13)	120.0(2)	C(18)-C(19)-C(20)	120.4(2)
C(9)-N(1)-C(17)	124.77(19)	C(29)-C(24)-C(13)	121.3(2)	N(32)-C(31)-C(30)	178.0(3)
C(2)-N(1)-C(17)	124.39(19)	C(19)-C(18)-C(23)	119.6(2)	C(5)-C(4)-C(3)	121.5(2)
C(7)-C(2)-N(1)	108.39(19)	C(19)-C(18)-C(17)	120.8(2)	C(21)-C(20)-C(19)	120.1(3)
C(7)-C(8)-C(9)	101.21(18)	C(23)-C(18)-C(17)	119.6(2)	C(22)-C(21)-C(20)	119.7(3)
C(7)-C(8)-C(36)	110.11(18)	C(2)-C(3)-C(4)	116.6(2)	C(27)-C(26)-C(25)	119.8(2)
C(9)-C(8)-C(36)	111.71(19)	C(2)-C(7)-C(6)	120.0(2)	C(15)-C(30)-C(33)	118.5(2)
C(7)-C(8)-C(35)	110.15(19)	C(2)-C(7)-C(8)	110.23(19)	C(31)-C(30)-C(33)	119.1(2)
C(9)-C(8)-C(35)	110.99(18)	N(34)-C(33)-C(30)	176.2(3)	C(28)-C(29)-C(24)	120.2(2)
C(36)-C(8)-C(35)	112.15(19)	C(11)-C(10)-C(9)	126.4(2)	C(26)-C(25)-C(24)	120.8(2)
C(13)-N(14)-C(15)	110.66(19)	N(1)-C(9)-C(10)	121.8(2)	C(22)-C(23)-C(18)	119.9(2)
C(11)-C(12)-C(13)	129.5(2)	N(1)-C(9)-C(8)	109.28(19)	C(6)-C(7)-C(8)	129.7(2)
C(11)-C(12)-S(16)	121.57(18)	C(10)-C(9)-C(8)	128.8(2)	C(15)-C(30)-C(31)	122.1(2)
C(13)-C(12)-S(16)	108.88(17)	C(27)-C(28)-C(29)	120.6(2)	C(10)-C(11)-C(12)	123.9(2)
N(1)-C(17)-C(18)	113.39(19)	C(21)-C(22)-C(23)	120.4(3)		
N(14)-C(13)-C(12)	116.6(2)	C(12)-C(13)-C(24)	124.0(2)		
N(14)-C(13)-C(24)	119.3(2)	N(14)-C(15)-C(30)	124.9(2)		
C(7)-C(6)-C(5)	118.7(2)	N(14)-C(15)-S(16)	114.59(17)		
C(28)-C(27)-C(26)	119.9(2)	C(30)-C(15)-S(16)	120.45(19)		

Crystallographic tables for dye 2f

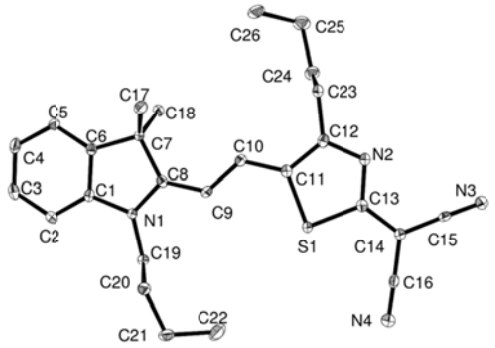

Figure A11. ORTEP drawing of **2f** with atom labelling and 50% probability ellipsoids.

Table A23. Atomic coordinates ($\times 10^4$) and equivalent isotropic displacement parameters ($Å^2 \times 10^3$) for **2f**

Atom	x	y	z	U(eq)
S(1)	2746(1)	3075(1)	2258(1)	50(1)
N(1)	-324(1)	2403(2)	829(1)	38(1)
N(2)	2627(2)	3484(3)	3324(1)	45(1)
C(7)	-1434(2)	2891(3)	1559(1)	38(1)
C(8)	-332(2)	2748(3)	1374(1)	37(1)
C(13)	3293(2)	3230(3)	2914(1)	42(1)
C(14)	4344(2)	3091(3)	3000(1)	41(1)
C(9)	561(2)	2899(3)	1685(1)	44(1)
C(1)	-1318(2)	2342(3)	602(1)	38(1)
C(15)	4773(2)	3116(3)	3541(1)	46(1)
C(6)	-2005(2)	2630(3)	1020(1)	40(1)

C(2)	-1616(2)	2071(3)	58(1)	49(1)
C(5)	-3036(2)	2633(4)	899(1)	52(1)
C(16)	4994(2)	2902(3)	2545(1)	47(1)
C(19)	590(2)	2020(3)	514(1)	44(1)
C(11)	1545(2)	3323(3)	2546(1)	45(1)
C(12)	1667(2)	3551(3)	3122(1)	44(1)
C(10)	637(2)	3227(3)	2244(1)	45(1)
C(23)	802(2)	3802(4)	3506(1)	50(1)
N(3)	5142(2)	3130(3)	3977(1)	65(1)
C(21)	2181(2)	3148(4)	86(1)	64(1)
C(4)	-3351(2)	2344(4)	358(1)	63(1)
C(18)	-1681(2)	4678(4)	1809(1)	58(1)
C(17)	-1690(2)	1406(4)	1964(1)	55(1)
N(4)	5506(2)	2744(4)	2171(1)	72(1)
C(3)	-2650(2)	2073(4)	-53(1)	62(1)
C(20)	1142(2)	3614(3)	309(1)	54(1)
C(24)	358(2)	2099(4)	3703(1)	69(1)
C(25)	-588(3)	2366(5)	4054(2)	88(1)
C(22)	2959(2)	2777(5)	532(2)	96(1)
C(26)	-1474(3)	3075(6)	3729(2)	100(1)

Table A24. Bond lengths [Å] and angles [°] for **2f**

S(1)-C(13)	1.730(2)	C(13)-C(14)	1.397(3)	C(11)-C(10)	1.390(3)
S(1)-C(11)	1.746(2)	C(14)-C(16)	1.409(3)	C(11)-C(12)	1.404(3)
N(1)-C(8)	1.341(3)	C(14)-C(15)	1.411(4)	C(12)-C(23)	1.491(3)
N(1)-C(1)	1.408(3)	C(9)-C(10)	1.371(3)	C(23)-C(24)	1.507(4)
N(1)-C(19)	1.462(3)	C(1)-C(2)	1.378(3)	C(21)-C(22)	1.499(4)
N(2)-C(13)	1.345(3)	C(1)-C(6)	1.383(3)	C(21)-C(20)	1.518(3)
N(2)-C(12)	1.345(3)	C(15)-N(3)	1.150(3)	C(4)-C(3)	1.381(4)
C(7)-C(6)	1.503(3)	C(6)-C(5)	1.381(3)	C(24)-C(25)	1.530(4)
C(7)-C(8)	1.528(3)	C(2)-C(3)	1.380(4)	C(25)-C(26)	1.494(5)
C(7)-C(18)	1.530(3)	C(5)-C(4)	1.378(4)		
C(7)-C(17)	1.538(3)	C(16)-N(4)	1.141(3)		
C(8)-C(9)	1.387(3)	C(19)-C(20)	1.507(3)		
C(13)-S(1)-C(11)	89.57(11)	C(14)-C(13)-S(1)	121.65(18)	C(10)-C(11)-C(12)	127.4(2)
C(8)-N(1)-C(1)	111.37(19)	C(13)-C(14)-C(16)	120.2(2)	C(10)-C(11)-S(1)	123.99(19)
C(8)-N(1)-C(19)	124.6(2)	C(13)-C(14)-C(15)	120.9(2)	C(12)-C(11)-S(1)	108.60(18)
C(1)-N(1)-C(19)	123.92(19)	C(16)-C(14)-C(15)	118.9(2)	N(2)-C(12)-C(11)	116.2(2)
C(13)-N(2)-C(12)	111.06(19)	C(10)-C(9)-C(8)	126.4(2)	N(2)-C(12)-C(23)	120.1(2)
C(6)-C(7)-C(8)	101.51(17)	C(2)-C(1)-C(6)	122.6(2)	C(11)-C(12)-C(23)	123.7(2)
C(6)-C(7)-C(18)	110.7(2)	C(2)-C(1)-N(1)	128.4(2)	C(9)-C(10)-C(11)	124.9(2)
C(8)-C(7)-C(18)	112.8(2)	C(6)-C(1)-N(1)	109.00(19)	C(12)-C(23)-C(24)	112.8(2)
C(6)-C(7)-C(17)	109.85(19)	N(3)-C(15)-C(14)	178.6(3)	C(22)-C(21)-C(20)	113.4(3)
C(8)-C(7)-C(17)	110.58(19)	C(5)-C(6)-C(1)	119.9(2)	C(5)-C(4)-C(3)	120.6(3)
C(18)-C(7)-C(17)	111.0(2)	C(5)-C(6)-C(7)	131.0(2)	C(2)-C(3)-C(4)	122.0(3)
N(1)-C(8)-C(9)	121.7(2)	C(1)-C(6)-C(7)	109.2(2)	C(19)-C(20)-C(21)	111.6(2)
N(1)-C(8)-C(7)	108.89(19)	C(1)-C(2)-C(3)	116.5(3)	C(23)-C(24)-C(25)	112.5(3)
C(9)-C(8)-C(7)	129.4(2)	C(4)-C(5)-C(6)	118.5(3)	C(26)-C(25)-C(24)	113.1(3)
N(2)-C(13)-C(14)	123.8(2)	N(4)-C(16)-C(14)	178.9(3)		
N(2)-C(13)-S(1)	114.50(17)	N(1)-C(19)-C(20)	114.5(2)		

Crystallographic tables for dye 2g

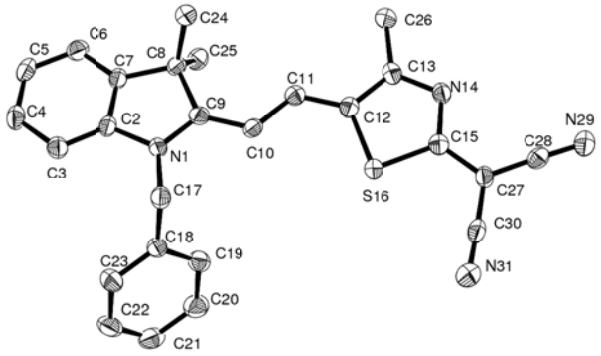

Figure A12. ORTEP drawing of **2g** with atom labelling and 50% probability ellipsoids.

Table A25. Atomic coordinates ($\times 10^4$) and equivalent isotropic displacement parameters ($Å^2 \times 10^3$) for **2g**

Atom	x	y	z	U(eq)
S(16)	2313(1)	597(1)	5076(1)	27(1)
N(14)	2997(3)	-1533(2)	4825(2)	26(1)
N(1)	2590(3)	3608(2)	1950(2)	24(1)
C(2)	2577(4)	4069(2)	912(2)	25(1)
C(5)	2603(4)	4545(2)	-1189(2)	32(1)
C(3)	2482(4)	5153(2)	596(2)	29(1)
N(29)	2915(4)	-2900(2)	7454(2)	35(1)
C(28)	2702(4)	-2027(2)	7079(2)	27(1)
C(8)	2816(4)	2142(2)	802(2)	25(1)
C(7)	2675(4)	3225(2)	216(2)	26(1)
C(10)	2603(4)	1863(2)	2859(2)	25(1)
C(27)	2431(4)	-951(2)	6659(2)	26(1)
C(24)	4871(4)	1460(2)	473(2)	34(1)
C(6)	2686(4)	3462(2)	-853(2)	32(1)
C(15)	2600(4)	-739(2)	5568(2)	25(1)
C(11)	2800(4)	740(2)	2894(2)	26(1)
C(18)	707(4)	4922(2)	3311(2)	27(1)
C(19)	-715(5)	4388(2)	3866(2)	32(1)
C(17)	2680(4)	4284(2)	2858(2)	29(1)
C(23)	291(5)	6051(2)	3208(2)	40(1)
C(12)	2752(4)	80(2)	3799(2)	25(1)
C(4)	2508(4)	5373(2)	-476(2)	31(1)
C(13)	3073(4)	-1072(2)	3853(2)	26(1)
C(9)	2660(4)	2517(2)	1947(2)	24(1)
C(25)	1153(5)	1526(2)	607(2)	34(1)
C(21)	-2873(5)	6106(3)	4204(2)	42(1)
C(20)	-2496(5)	4974(3)	4313(2)	41(1)
C(26)	3520(5)	-1784(2)	2907(2)	34(1)
C(30)	2066(4)	-51(2)	7358(2)	30(1)
N(31)	1767(4)	698(2)	7895(2)	46(1)
C(22)	-1501(6)	6634(2)	3655(2)	44(1)

Table A26. Bond lengths [Å] and angles [°] for **2g**

S(16)-C(15)	1.737(3)	N(29)-C(28)	1.160(3)	C(18)-C(23)	1.383(4)
S(16)-C(12)	1.746(3)	C(28)-C(27)	1.410(4)	C(18)-C(19)	1.386(4)

N(14)-C(13)	1.349(3)	C(8)-C(7)	1.507(4)	C(18)-C(17)	1.514(4)
N(14)-C(15)	1.359(3)	C(8)-C(9)	1.536(4)	C(19)-C(20)	1.386(4)
N(1)-C(9)	1.344(3)	C(8)-C(25)	1.538(4)	C(23)-C(22)	1.390(4)
N(1)-C(2)	1.427(3)	C(8)-C(24)	1.544(4)	C(12)-C(13)	1.405(4)
N(1)-C(17)	1.469(3)	C(7)-C(6)	1.388(4)	C(13)-C(26)	1.490(4)
C(2)-C(3)	1.380(4)	C(10)-C(11)	1.372(4)	C(21)-C(22)	1.355(4)
C(2)-C(7)	1.383(4)	C(10)-C(9)	1.396(4)	C(21)-C(20)	1.386(4)
C(5)-C(4)	1.383(4)	C(27)-C(15)	1.404(4)	C(30)-N(31)	1.146(3)
C(5)-C(6)	1.387(4)	C(27)-C(30)	1.422(4)		
C(3)-C(4)	1.387(4)	C(11)-C(12)	1.393(4)		
C(15)-S(16)-C(12)	89.08(12)	C(2)-C(7)-C(6)	119.3(2)	C(18)-C(23)-C(22)	120.9(3)
C(13)-N(14)-C(15)	109.9(2)	C(2)-C(7)-C(8)	110.2(2)	C(11)-C(12)-C(13)	127.4(3)
C(9)-N(1)-C(2)	111.6(2)	C(6)-C(7)-C(8)	130.5(3)	C(11)-C(12)-S(16)	123.5(2)
C(9)-N(1)-C(17)	126.9(2)	C(11)-C(10)-C(9)	126.0(3)	C(13)-C(12)-S(16)	109.2(2)
C(2)-N(1)-C(17)	121.3(2)	C(15)-C(27)-C(28)	122.1(2)	C(5)-C(4)-C(3)	121.4(3)
C(3)-C(2)-C(7)	123.1(2)	C(15)-C(27)-C(30)	118.8(2)	N(14)-C(13)-C(12)	116.7(2)
C(3)-C(2)-N(1)	128.8(3)	C(28)-C(27)-C(30)	119.1(2)	N(14)-C(13)-C(26)	119.7(2)
C(7)-C(2)-N(1)	108.1(2)	C(5)-C(6)-C(7)	118.6(3)	C(12)-C(13)-C(26)	123.6(2)
C(4)-C(5)-C(6)	120.9(3)	N(14)-C(15)-C(27)	124.0(2)	N(1)-C(9)-C(10)	123.8(2)
C(2)-C(3)-C(4)	116.7(3)	N(14)-C(15)-S(16)	115.16(19)	N(1)-C(9)-C(8)	108.9(2)
N(29)-C(28)-C(27)	178.0(3)	C(27)-C(15)-S(16)	120.9(2)	C(10)-C(9)-C(8)	127.3(2)
C(7)-C(8)-C(9)	101.2(2)	C(10)-C(11)-C(12)	126.4(3)	C(22)-C(21)-C(20)	119.8(3)
C(7)-C(8)-C(25)	111.5(2)	C(23)-C(18)-C(19)	118.2(3)	C(21)-C(20)-C(19)	120.0(3)
C(9)-C(8)-C(25)	113.3(2)	C(23)-C(18)-C(17)	121.2(3)	N(31)-C(30)-C(27)	177.8(3)
C(7)-C(8)-C(24)	108.7(2)	C(19)-C(18)-C(17)	120.6(2)	C(21)-C(22)-C(23)	120.5(3)
C(9)-C(8)-C(24)	109.8(2)	C(20)-C(19)-C(18)	120.7(3)		
C(25)-C(8)-C(24)	111.9(2)	N(1)-C(17)-C(18)	114.0(2)		

Crystallographic tables for dye 4a

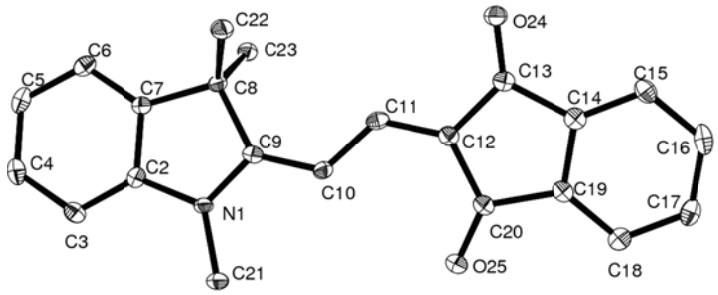

Figure A13. ORTEP drawing of **4a** with atom labelling and 50% probability ellipsoids.

Table A27. Atomic coordinates ($\times 10^4$) and equivalent isotropic displacement parameters ($Å^2 \times 10^3$) for **4a**

Atom	x	y	z	U(eq)
O(24)	3322(1)	2465(1)	5776(1)	18(1)
O(25)	1472(1)	-691(1)	5615(1)	19(1)
N(1)	-1104(1)	73(1)	8533(1)	12(1)
C(12)	2074(2)	961(1)	5983(1)	14(1)
C(8)	-733(2)	1717(1)	8482(1)	12(1)
C(14)	3549(2)	1173(1)	4642(1)	14(1)
C(2)	-1886(2)	459(1)	9286(1)	12(1)
C(18)	3358(2)	-368(1)	3874(1)	17(1)

C(16)	4782(2)	906(1)	3206(1)	20(1)
C(15)	4437(2)	1517(1)	3945(1)	17(1)
C(13)	3009(2)	1649(1)	5519(1)	13(1)
C(21)	-1025(2)	-939(1)	8330(1)	18(1)
C(5)	-3247(2)	1538(1)	10614(1)	19(1)
C(23)	-1701(2)	2329(1)	7732(1)	14(1)
C(10)	458(2)	526(1)	7285(1)	14(1)
C(3)	-2738(2)	-3(1)	9937(1)	16(1)
C(17)	4256(2)	-25(1)	3173(1)	20(1)
C(9)	-382(2)	748(1)	8053(1)	12(1)
C(22)	706(2)	2262(1)	8891(1)	16(1)
C(11)	1301(2)	1169(1)	6778(1)	14(1)
C(6)	-2374(2)	1988(1)	9957(1)	16(1)
C(7)	-1689(2)	1435(1)	9291(1)	12(1)
C(19)	3013(2)	241(1)	4604(1)	13(1)
C(4)	-3411(2)	562(1)	10605(1)	19(1)
C(20)	2084(2)	67(1)	5445(1)	14(1)

Table A28. Bond lengths [Å] and angles [°] for **4a**

O(24)-C(13)	1.2287(19)	C(8)-C(22)	1.538(2)	C(16)-C(17)	1.392(2)
O(25)-C(20)	1.2282(19)	C(8)-C(23)	1.541(2)	C(5)-C(4)	1.385(3)
N(1)-C(9)	1.351(2)	C(14)-C(15)	1.383(2)	C(5)-C(6)	1.394(2)
N(1)-C(2)	1.4089(19)	C(14)-C(19)	1.395(2)	C(10)-C(9)	1.383(2)
N(1)-C(21)	1.458(2)	C(14)-C(13)	1.501(2)	C(10)-C(11)	1.399(2)
C(12)-C(11)	1.377(2)	C(2)-C(3)	1.385(2)	C(3)-C(4)	1.393(2)
C(12)-C(13)	1.458(2)	C(2)-C(7)	1.387(2)	C(6)-C(7)	1.387(2)
C(12)-C(20)	1.465(2)	C(18)-C(19)	1.381(2)	C(19)-C(20)	1.501(2)
C(8)-C(7)	1.512(2)	C(18)-C(17)	1.391(2)		
C(8)-C(9)	1.534(2)	C(16)-C(15)	1.392(2)		
C(9)-N(1)-C(2)	111.93(13)	C(3)-C(2)-N(1)	128.85(15)	C(7)-C(6)-C(5)	118.31(16)
C(9)-N(1)-C(21)	124.21(13)	C(7)-C(2)-N(1)	108.55(13)	C(6)-C(7)-C(2)	120.05(14)
C(2)-N(1)-C(21)	123.79(13)	C(19)-C(18)-C(17)	118.05(16)	C(6)-C(7)-C(8)	130.32(15)
C(11)-C(12)-C(13)	123.30(15)	C(15)-C(16)-C(17)	120.99(15)	C(2)-C(7)-C(8)	109.59(13)
C(11)-C(12)-C(20)	128.01(14)	C(14)-C(15)-C(16)	118.01(16)	C(18)-C(19)-C(14)	121.21(15)
C(13)-C(12)-C(20)	108.66(13)	O(24)-C(13)-C(12)	128.02(14)	C(18)-C(19)-C(20)	129.49(15)
C(7)-C(8)-C(9)	101.34(12)	O(24)-C(13)-C(14)	125.11(14)	C(14)-C(19)-C(20)	109.30(13)
C(7)-C(8)-C(22)	110.61(12)	C(12)-C(13)-C(14)	106.87(13)	C(5)-C(4)-C(3)	121.61(15)
C(9)-C(8)-C(22)	113.61(13)	C(4)-C(5)-C(6)	120.74(15)	O(25)-C(20)-C(12)	128.98(14)
C(7)-C(8)-C(23)	109.72(12)	C(9)-C(10)-C(11)	125.52(15)	O(25)-C(20)-C(19)	124.69(14)
C(9)-C(8)-C(23)	110.86(12)	C(2)-C(3)-C(4)	116.69(16)	C(12)-C(20)-C(19)	106.33(13)
C(22)-C(8)-C(23)	110.35(13)	C(18)-C(17)-C(16)	120.82(15)		
C(15)-C(14)-C(19)	120.92(15)	N(1)-C(9)-C(10)	121.62(14)		
C(15)-C(14)-C(13)	130.30(15)	N(1)-C(9)-C(8)	108.52(12)		
C(19)-C(14)-C(13)	108.78(13)	C(10)-C(9)-C(8)	129.81(14)		
C(3)-C(2)-C(7)	122.59(14)	C(12)-C(11)-C(10)	125.78(15)		

Crystallographic tables for dye 5a

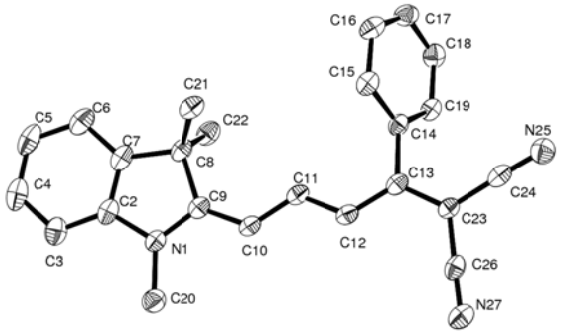

Figure A14. ORTEP drawing of **5a** with atom labelling and 50% probability ellipsoids.

Table A29. Atomic coordinates ($\times 10^4$) and equivalent isotropic displacement parameters ($Å^2 \times 10^3$) for **5a**

Atom	x	y	z	U(eq)
N(1)	1685(1)	1171(2)	3837(1)	28(1)
C(2)	2058(2)	2778(2)	3630(1)	30(1)
C(3)	1747(2)	3412(2)	3120(1)	37(1)
C(4)	2204(2)	5073(2)	3023(1)	46(1)
C(5)	2938(2)	6030(2)	3419(1)	46(1)
C(6)	3252(2)	5355(2)	3929(1)	39(1)
C(7)	2805(2)	3705(2)	4032(1)	30(1)
C(8)	2953(2)	2649(2)	4538(1)	29(1)
C(9)	2111(2)	1031(2)	4364(1)	26(1)
C(10)	1766(2)	-344(2)	4668(1)	27(1)
C(11)	2172(2)	-606(2)	5207(1)	27(1)
C(12)	1706(2)	-1934(2)	5496(1)	27(1)
C(13)	2082(2)	-2240(2)	6040(1)	25(1)
C(14)	3035(2)	-1063(2)	6366(1)	26(1)
C(15)	2745(2)	695(2)	6433(1)	30(1)
C(16)	3602(2)	1738(2)	6762(1)	34(1)
C(17)	4770(2)	1056(2)	7023(1)	34(1)
C(18)	5093(2)	-666(2)	6948(1)	33(1)
C(19)	4227(2)	-1725(2)	6625(1)	28(1)
C(20)	871(2)	-78(2)	3507(1)	35(1)
C(21)	2419(2)	3659(2)	4986(1)	35(1)
C(22)	4425(2)	2149(2)	4696(1)	36(1)
C(23)	1596(2)	-3656(2)	6302(1)	26(1)
C(24)	1857(2)	-3880(2)	6863(1)	27(1)
N(25)	2045(1)	-4113(2)	7316(1)	37(1)
C(26)	763(2)	-4963(2)	6032(1)	27(1)
N(27)	112(2)	-6051(2)	5820(1)	36(1)

Table A30. Bond lengths [Å] and angles [°] for **5a**

N(1)-C(9)	1.359(2)	C(8)-C(21)	1.537(2)	C(14)-C(15)	1.396(2)
N(1)-C(2)	1.412(2)	C(8)-C(9)	1.538(2)	C(15)-C(16)	1.380(2)
N(1)-C(20)	1.455(2)	C(8)-C(22)	1.540(2)	C(16)-C(17)	1.380(2)
C(2)-C(3)	1.384(2)	C(9)-C(10)	1.382(2)	C(17)-C(18)	1.381(2)
C(2)-C(7)	1.387(2)	C(10)-C(11)	1.394(2)	C(18)-C(19)	1.383(2)

C(3)-C(4)	1.389(3)	C(11)-C(12)	1.377(2)	C(23)-C(26)	1.427(2)
C(4)-C(5)	1.381(3)	C(12)-C(13)	1.407(2)	C(23)-C(24)	1.428(3)
C(5)-C(6)	1.395(3)	C(13)-C(23)	1.400(2)	C(24)-N(25)	1.157(2)
C(6)-C(7)	1.381(2)	C(13)-C(14)	1.492(2)	C(26)-N(27)	1.153(2)
C(7)-C(8)	1.513(2)	C(14)-C(19)	1.392(2)		
C(9)-N(1)-C(2)	111.87(13)	C(7)-C(8)-C(9)	101.50(13)	C(19)-C(14)-C(15)	118.56(14)
C(9)-N(1)-C(20)	126.72(13)	C(21)-C(8)-C(9)	112.67(14)	C(19)-C(14)-C(13)	119.96(14)
C(2)-N(1)-C(20)	121.31(13)	C(7)-C(8)-C(22)	109.81(14)	C(15)-C(14)-C(13)	121.45(14)
C(3)-C(2)-C(7)	123.18(16)	C(21)-C(8)-C(22)	110.81(14)	C(16)-C(15)-C(14)	120.59(15)
C(3)-C(2)-N(1)	128.21(16)	C(9)-C(8)-C(22)	110.76(13)	C(15)-C(16)-C(17)	120.15(16)
C(7)-C(2)-N(1)	108.60(14)	N(1)-C(9)-C(10)	122.98(14)	C(16)-C(17)-C(18)	119.94(15)
C(2)-C(3)-C(4)	116.66(17)	N(1)-C(9)-C(8)	108.16(13)	C(17)-C(18)-C(19)	120.12(16)
C(5)-C(4)-C(3)	121.24(18)	C(10)-C(9)-C(8)	128.82(15)	C(18)-C(19)-C(14)	120.58(15)
C(4)-C(5)-C(6)	121.03(17)	C(9)-C(10)-C(11)	126.82(15)	C(13)-C(23)-C(26)	122.55(14)
C(7)-C(6)-C(5)	118.56(17)	C(12)-C(11)-C(10)	123.78(15)	C(13)-C(23)-C(24)	122.77(14)
C(6)-C(7)-C(2)	119.31(16)	C(11)-C(12)-C(13)	125.65(15)	C(26)-C(23)-C(24)	114.64(14)
C(6)-C(7)-C(8)	130.99(16)	C(23)-C(13)-C(12)	122.27(14)	N(25)-C(24)-C(23)	177.72(17)
C(2)-C(7)-C(8)	109.68(14)	C(23)-C(13)-C(14)	116.50(14)	N(27)-C(26)-C(23)	178.28(17)
C(7)-C(8)-C(21)	110.94(13)	C(12)-C(13)-C(14)	121.23(14)		

Crystallographic tables for dye 5b

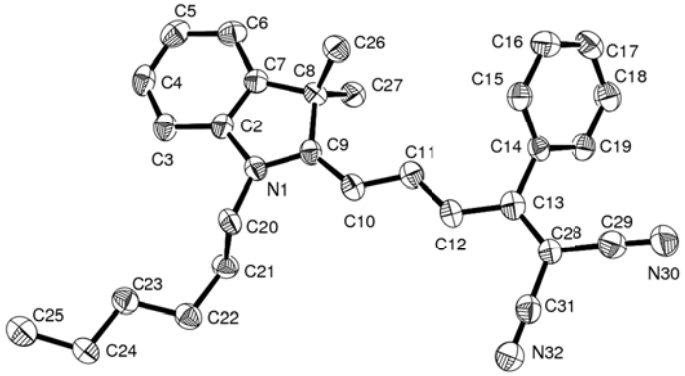

Figure A15. ORTEP drawing of **5b** with atom labelling and 50% probability ellipsoids.

Table A31. Atomic coordinates ($\times 10^4$) and equivalent isotropic displacement parameters ($Å^2 \times 10^3$) for **5b**

Atom	x	y	z	U(eq)
N(1)	6790(2)	1370(2)	833(2)	32(1)
C(2)	6575(2)	1280(2)	-310(3)	32(1)
C(3)	5579(3)	1359(2)	-1183(3)	38(1)
C(4)	5605(3)	1284(2)	-2229(3)	44(1)
C(5)	6565(3)	1144(2)	-2403(3)	45(1)
C(6)	7559(3)	1048(2)	-1507(3)	42(1)
C(7)	7556(2)	1109(2)	-448(3)	32(1)
C(8)	8477(2)	1050(2)	667(2)	30(1)
C(9)	7879(2)	1240(2)	1449(3)	31(1)
C(10)	8294(2)	1288(2)	2580(3)	35(1)
C(11)	9384(3)	1153(2)	3285(3)	35(1)
C(12)	9730(2)	1223(2)	4416(3)	34(1)
C(13)	10806(2)	1093(2)	5197(3)	35(1)
C(14)	11747(2)	951(2)	4847(3)	31(1)

C(15)	11962(2)	1519(2)	4108(3)	36(1)
C(16)	12861(3)	1388(2)	3810(3)	42(1)
C(17)	13563(3)	685(2)	4238(3)	44(1)
C(18)	13350(3)	115(2)	4962(3)	44(1)
C(19)	12464(3)	250(2)	5269(3)	36(1)
C(20)	5939(2)	1644(2)	1239(3)	35(1)
C(21)	5248(2)	885(2)	1404(3)	37(1)
C(22)	4247(2)	1225(2)	1613(3)	39(1)
C(23)	3397(2)	1672(2)	611(3)	40(1)
C(24)	2398(2)	2031(2)	797(3)	39(1)
C(25)	1616(3)	2511(2)	-216(3)	51(1)
C(26)	9363(2)	1749(2)	757(3)	41(1)
C(27)	8975(2)	122(2)	846(3)	40(1)
C(28)	10993(2)	1110(2)	6321(3)	32(1)
C(29)	12064(3)	1099(2)	7154(3)	40(1)
N(30)	12916(2)	1105(2)	7851(2)	54(1)
C(31)	10120(3)	1196(2)	6720(3)	38(1)
N(32)	9400(2)	1266(2)	7023(2)	51(1)

Table A32. Bond lengths [Å] and angles [°] for **5b**

N(1)-C(9)	1.363(4)	C(8)-C(26)	1.543(4)	C(18)-C(19)	1.368(4)
N(1)-C(2)	1.424(4)	C(9)-C(10)	1.378(4)	C(20)-C(21)	1.529(4)
N(1)-C(20)	1.454(3)	C(10)-C(11)	1.395(4)	C(21)-C(22)	1.517(4)
C(2)-C(7)	1.377(4)	C(11)-C(12)	1.383(4)	C(22)-C(23)	1.532(4)
C(2)-C(3)	1.383(4)	C(12)-C(13)	1.413(4)	C(23)-C(24)	1.510(4)
C(3)-C(4)	1.385(4)	C(13)-C(28)	1.399(4)	C(24)-C(25)	1.530(4)
C(4)-C(5)	1.366(4)	C(13)-C(14)	1.472(4)	C(28)-C(29)	1.421(5)
C(5)-C(6)	1.399(4)	C(14)-C(19)	1.395(4)	C(28)-C(31)	1.419(5)
C(6)-C(7)	1.391(4)	C(14)-C(15)	1.400(4)	C(29)-N(30)	1.148(4)
C(7)-C(8)	1.513(4)	C(15)-C(16)	1.376(4)	C(31)-N(32)	1.147(4)
C(8)-C(9)	1.524(4)	C(16)-C(17)	1.388(4)		
C(8)-C(27)	1.540(4)	C(17)-C(18)	1.386(4)		
C(9)-N(1)-C(2)	111.7(2)	C(7)-C(8)-C(26)	109.8(2)	C(15)-C(16)-C(17)	120.0(3)
C(9)-N(1)-C(20)	126.2(3)	C(9)-C(8)-C(26)	111.6(2)	C(18)-C(17)-C(16)	119.6(3)
C(2)-N(1)-C(20)	121.9(2)	C(27)-C(8)-C(26)	111.3(2)	C(19)-C(18)-C(17)	120.4(3)
C(7)-C(2)-C(3)	122.8(3)	N(1)-C(9)-C(10)	122.8(3)	C(18)-C(19)-C(14)	120.8(3)
C(7)-C(2)-N(1)	108.7(3)	N(1)-C(9)-C(8)	107.8(3)	N(1)-C(20)-C(21)	113.5(2)
C(3)-C(2)-N(1)	128.5(3)	C(10)-C(9)-C(8)	129.4(3)	C(22)-C(21)-C(20)	110.7(2)
C(2)-C(3)-C(4)	117.0(3)	C(9)-C(10)-C(11)	127.3(3)	C(21)-C(22)-C(23)	113.4(3)
C(5)-C(4)-C(3)	122.2(3)	C(12)-C(11)-C(10)	123.3(3)	C(24)-C(23)-C(22)	114.7(3)
C(4)-C(5)-C(6)	119.9(3)	C(11)-C(12)-C(13)	127.7(3)	C(23)-C(24)-C(25)	111.9(3)
C(7)-C(6)-C(5)	119.2(3)	C(28)-C(13)-C(12)	120.1(3)	C(13)-C(28)-C(29)	123.3(3)
C(2)-C(7)-C(6)	119.0(3)	C(28)-C(13)-C(14)	119.1(3)	C(13)-C(28)-C(31)	122.2(3)
C(2)-C(7)-C(8)	109.3(3)	C(12)-C(13)-C(14)	120.8(3)	C(29)-C(28)-C(31)	114.3(3)
C(6)-C(7)-C(8)	131.7(3)	C(19)-C(14)-C(15)	118.4(3)	N(30)-C(29)-C(28)	177.6(3)
C(7)-C(8)-C(9)	102.5(2)	C(19)-C(14)-C(13)	120.1(3)	N(32)-C(31)-C(28)	178.8(3)
C(7)-C(8)-C(27)	110.0(2)	C(15)-C(14)-C(13)	121.5(3)		
C(9)-C(8)-C(27)	111.3(2)	C(16)-C(15)-C(14)	120.7(3)		

Crystallographic tables for dye 6

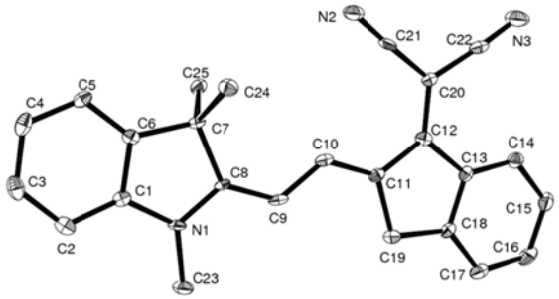

Figure A16. ORTEP drawing of **6** with atom labelling and 50% probability ellipsoids.

Table A33. Atomic coordinates ($\times 10^4$) and equivalent isotropic displacement parameters ($Å^2 \times 10^3$) for **6**

Atom	x	y	z	U(eq)
N(1)	10013(3)	3337(2)	167(2)	12(1)
N(2)	6865(3)	2747(3)	3194(2)	25(1)
N(3)	3180(3)	1277(3)	3177(2)	28(1)
C(3)	13347(3)	4406(3)	702(2)	19(1)
C(2)	12283(3)	4065(3)	174(2)	16(1)
C(1)	11208(3)	3715(3)	543(2)	11(1)
C(8)	9173(3)	3118(3)	739(2)	9(1)
C(9)	7934(3)	2772(3)	522(2)	12(1)
C(10)	7056(3)	2491(3)	1089(2)	13(1)
C(11)	5843(3)	2085(3)	869(2)	12(1)
C(12)	4904(3)	1723(3)	1405(2)	12(1)
C(20)	4968(3)	1826(3)	2268(2)	12(1)
C(21)	6021(3)	2346(3)	2766(2)	15(1)
C(22)	3953(3)	1501(3)	2749(2)	16(1)
C(13)	3810(3)	1221(3)	873(2)	12(1)
C(14)	2676(3)	682(3)	1067(2)	15(1)
C(15)	1803(3)	286(3)	425(2)	19(1)
C(16)	2041(3)	414(3)	-398(2)	20(1)
C(17)	3164(3)	940(3)	-597(2)	18(1)
C(18)	4040(3)	1337(3)	37(2)	13(1)
C(19)	5311(3)	1903(3)	-31(2)	14(1)
C(6)	11184(3)	3705(3)	1404(2)	12(1)
C(7)	9885(3)	3276(3)	1611(2)	11(1)
C(25)	10021(3)	2070(3)	2063(2)	14(1)
C(24)	9265(3)	4201(3)	2146(2)	16(1)
C(5)	12248(3)	4049(3)	1912(2)	15(1)
C(4)	13346(3)	4396(3)	1561(2)	20(1)
C(23)	9719(3)	3178(3)	-726(2)	18(1)

Table A34. Bond lengths [Å] and angles [°] for **6**

N(1)-C(8)	1.365(4)	C(9)-C(10)	1.401(5)	C(15)-C(16)	1.387(5)
N(1)-C(1)	1.405(4)	C(10)-C(11)	1.367(4)	C(16)-C(17)	1.386(5)
N(1)-C(23)	1.455(4)	C(11)-C(12)	1.437(4)	C(17)-C(18)	1.380(5)
N(2)-C(21)	1.159(4)	C(11)-C(19)	1.519(4)	C(18)-C(19)	1.495(4)
N(3)-C(22)	1.147(4)	C(12)-C(20)	1.395(4)	C(6)-C(5)	1.373(4)
C(3)-C(4)	1.389(5)	C(12)-C(13)	1.476(5)	C(6)-C(7)	1.519(4)
C(3)-C(2)	1.390(5)	C(20)-C(21)	1.426(5)	C(7)-C(24)	1.537(4)

C(2)-C(1)	1.388(5)	C(20)-C(22)	1.432(5)	C(7)-C(25)	1.537(4)
C(1)-C(6)	1.395(4)	C(13)-C(14)	1.401(5)	C(5)-C(4)	1.393(5)
C(8)-C(9)	1.371(4)	C(13)-C(18)	1.402(5)		
C(8)-C(7)	1.538(4)	C(14)-C(15)	1.387(5)		
C(8)-N(1)-C(1)	112.0(2)	C(12)-C(11)-C(19)	109.3(3)	C(17)-C(18)-C(19)	128.1(3)
C(8)-N(1)-C(23)	124.3(3)	C(20)-C(12)-C(11)	127.8(3)	C(13)-C(18)-C(19)	110.8(3)
C(1)-N(1)-C(23)	123.8(3)	C(20)-C(12)-C(13)	124.7(3)	C(18)-C(19)-C(11)	103.3(2)
C(4)-C(3)-C(2)	122.0(3)	C(11)-C(12)-C(13)	107.4(3)	C(5)-C(6)-C(1)	119.9(3)
C(1)-C(2)-C(3)	117.0(3)	C(12)-C(20)-C(21)	123.7(3)	C(5)-C(6)-C(7)	130.8(3)
C(2)-C(1)-C(6)	122.0(3)	C(12)-C(20)-C(22)	124.1(3)	C(1)-C(6)-C(7)	109.3(3)
C(2)-C(1)-N(1)	129.2(3)	N(3)-C(22)-C(20)	175.6(4)	C(6)-C(7)-C(25)	109.9(3)
C(6)-C(1)-N(1)	108.8(3)	C(14)-C(13)-C(18)	119.4(3)	C(24)-C(7)-C(25)	110.5(3)
N(1)-C(8)-C(9)	122.8(3)	C(14)-C(13)-C(12)	131.6(3)	C(6)-C(7)-C(8)	101.5(2)
N(1)-C(8)-C(7)	108.2(3)	C(18)-C(13)-C(12)	108.9(3)	C(24)-C(7)-C(8)	113.5(3)
C(9)-C(8)-C(7)	128.9(3)	C(15)-C(14)-C(13)	118.9(3)	C(25)-C(7)-C(8)	110.4(3)
C(8)-C(9)-C(10)	124.7(3)	C(14)-C(15)-C(16)	120.9(3)	C(6)-C(5)-C(4)	119.6(3)
C(11)-C(10)-C(9)	124.4(3)	C(17)-C(16)-C(15)	120.5(3)	C(3)-C(4)-C(5)	119.6(3)
C(10)-C(11)-C(12)	128.2(3)	C(18)-C(17)-C(16)	119.0(3)	C(21)-C(20)-C(22)	112.1(3)
C(10)-C(11)-C(19)	122.4(3)	C(17)-C(18)-C(13)	121.2(3)	C(6)-C(7)-C(24)	110.7(3)

Crystallographic tables for dye 7

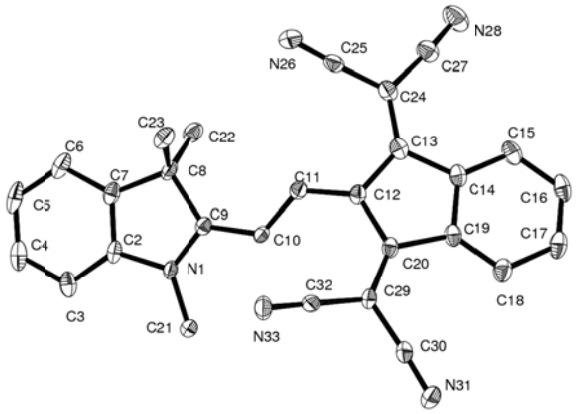

Figure A17. ORTEP drawing of 7 with atom labelling and 50% probability ellipsoids.

Table A35. Atomic coordinates ($\times 10^4$) and equivalent isotropic displacement parameters ($Å^2 \times 10^3$) for **7**

Atom	x	y	z	U(eq)
N(1)	919(1)	1406(1)	6137(1)	17(1)
N(33)	1287(2)	3074(1)	3950(1)	26(1)
C(21)	-228(2)	1991(1)	5954(1)	22(1)
C(30)	1260(2)	5286(1)	4585(1)	21(1)
C(10)	2429(2)	2608(1)	6089(1)	16(1)
C(20)	3208(2)	4576(1)	5574(1)	17(1)
N(28)	8444(2)	4385(1)	7883(1)	38(1)
N(26)	6790(2)	2065(1)	6383(1)	32(1)
C(9)	2144(2)	1692(1)	6208(1)	16(1)
C(12)	4037(2)	3840(1)	5975(1)	18(1)
N(31)	567(2)	5873(1)	4311(1)	30(1)
C(22)	3967(2)	966(1)	7397(1)	25(1)
C(2)	855(2)	455(1)	6242(1)	19(1)

C(32)	1635(2)	3711(1)	4394(1)	19(1)
C(29)	2066(2)	4523(1)	4905(1)	19(1)
C(11)	3665(2)	2935(1)	6123(1)	18(1)
C(18)	3515(2)	6327(1)	5755(1)	23(1)
C(16)	5635(2)	6785(1)	6607(1)	27(1)
C(4)	-24(2)	-1012(1)	6291(1)	29(1)
C(13)	5283(2)	4211(1)	6410(1)	20(1)
C(27)	7534(2)	4135(1)	7362(1)	26(1)
C(6)	2307(2)	-801(1)	6552(1)	29(1)
C(7)	2106(2)	119(1)	6412(1)	21(1)
C(19)	3890(2)	5427(1)	5909(1)	19(1)
C(25)	6599(2)	2812(1)	6555(1)	23(1)
C(14)	5139(2)	5209(1)	6410(1)	19(1)
C(15)	6020(2)	5888(1)	6767(1)	24(1)
C(5)	1229(2)	-1364(1)	6485(1)	33(1)
C(23)	3845(2)	737(1)	5597(1)	25(1)
C(8)	3063(2)	883(1)	6407(1)	20(1)
C(24)	6420(2)	3747(1)	6755(1)	22(1)
C(3)	-241(2)	-89(1)	6172(1)	24(1)
C(17)	4409(2)	6999(1)	6113(1)	28(1)

Table A36. Bond lengths [Å] and angles [°] for **7**

N(1)-C(9)	1.337(2)	C(9)-C(8)	1.529(2)	C(13)-C(24)	1.382(3)
N(1)-C(2)	1.417(2)	C(12)-C(11)	1.420(3)	C(13)-C(14)	1.484(3)
N(1)-C(21)	1.465(2)	C(12)-C(13)	1.443(3)	C(27)-C(24)	1.434(3)
N(33)-C(32)	1.153(2)	C(22)-C(8)	1.542(3)	C(6)-C(7)	1.384(3)
C(30)-N(31)	1.152(2)	C(2)-C(7)	1.381(3)	C(6)-C(5)	1.393(3)
C(30)-C(29)	1.432(3)	C(2)-C(3)	1.391(3)	C(7)-C(8)	1.512(3)
C(10)-C(11)	1.375(3)	C(32)-C(29)	1.430(3)	C(19)-C(14)	1.405(3)
C(10)-C(9)	1.404(2)	C(18)-C(19)	1.394(3)	C(25)-C(24)	1.431(3)
C(20)-C(29)	1.382(3)	C(18)-C(17)	1.394(3)	C(14)-C(15)	1.393(3)
C(20)-C(12)	1.442(2)	C(16)-C(17)	1.379(3)	C(23)-C(8)	1.542(3)
C(20)-C(19)	1.480(2)	C(16)-C(15)	1.393(3)		
N(28)-C(27)	1.152(3)	C(4)-C(3)	1.388(3)		
N(26)-C(25)	1.156(3)	C(4)-C(5)	1.391(3)		
C(9)-N(1)-C(2)	111.67(15)	C(20)-C(29)-C(30)	123.72(16)	C(15)-C(14)-C(13)	131.02(18)
C(9)-N(1)-C(21)	124.80(15)	C(32)-C(29)-C(30)	112.94(16)	C(19)-C(14)-C(13)	108.24(15)
C(2)-N(1)-C(21)	123.51(15)	C(10)-C(11)-C(12)	127.58(17)	C(14)-C(15)-C(16)	118.35(19)
N(31)-C(30)-C(29)	176.9(2)	C(19)-C(18)-C(17)	118.24(19)	C(4)-C(5)-C(6)	120.86(18)
C(11)-C(10)-C(9)	123.78(16)	C(17)-C(16)-C(15)	121.02(18)	C(7)-C(8)-C(9)	100.96(14)
C(29)-C(20)-C(12)	127.32(16)	C(3)-C(4)-C(5)	121.28(19)	C(7)-C(8)-C(22)	110.54(15)
C(29)-C(20)-C(19)	124.91(16)	C(24)-C(13)-C(12)	127.75(17)	C(9)-C(8)-C(22)	111.30(14)
C(12)-C(20)-C(19)	107.30(15)	C(24)-C(13)-C(14)	125.10(17)	C(7)-C(8)-C(23)	110.14(15)
N(1)-C(9)-C(10)	121.26(16)	C(12)-C(13)-C(14)	107.15(15)	C(9)-C(8)-C(23)	112.14(14)
N(1)-C(9)-C(8)	109.23(15)	N(28)-C(27)-C(24)	174.9(2)	C(22)-C(8)-C(23)	111.33(16)
C(10)-C(9)-C(8)	129.50(16)	C(7)-C(6)-C(5)	118.5(2)	C(13)-C(24)-C(25)	123.13(17)
C(11)-C(12)-C(20)	127.44(17)	C(2)-C(7)-C(6)	119.57(18)	C(13)-C(24)-C(27)	124.34(18)
C(11)-C(12)-C(13)	123.14(16)	C(2)-C(7)-C(8)	109.80(15)	C(25)-C(24)-C(27)	112.52(17)
C(20)-C(12)-C(13)	108.09(15)	C(6)-C(7)-C(8)	130.64(18)	C(4)-C(3)-C(2)	116.5(2)
C(7)-C(2)-C(3)	123.23(17)	C(18)-C(19)-C(14)	120.44(17)	C(16)-C(17)-C(18)	121.29(18)
C(7)-C(2)-N(1)	108.33(16)	C(18)-C(19)-C(20)	131.07(18)		
C(3)-C(2)-N(1)	128.43(18)	C(14)-C(19)-C(20)	108.37(16)		
N(33)-C(32)-C(29)	177.47(19)	N(26)-C(25)-C(24)	177.3(2)		

C(20)-C(29)-C(32)	123.08(16)	C(15)-C(14)-C(19)	120.66(18)

Crystallographic tables for dye 8

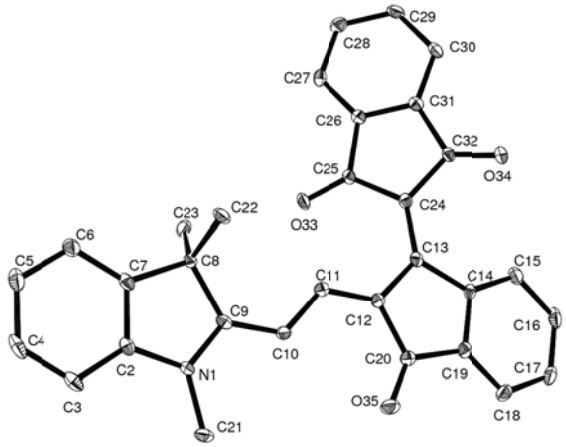

Figure A18. ORTEP drawing of **8** with atom labelling and 50% probability ellipsoids.

Table A37. Atomic coordinates ($\times 10^4$) and equivalent isotropic displacement parameters ($Å^2 \times 10^3$) for **8**

Atom	x	y	z	U(eq)
O(34)	10356(1)	2678(1)	6289(2)	17(1)
O(33)	8099(1)	1240(1)	4056(1)	15(1)
O(35)	11972(1)	329(1)	7404(2)	18(1)
N(1)	8578(1)	-635(1)	8079(2)	11(1)
C(11)	9479(1)	671(1)	6861(2)	11(1)
C(24)	9592(1)	1820(1)	5465(2)	11(1)
C(20)	11646(1)	757(1)	6848(2)	12(1)
C(31)	8439(1)	2573(1)	4767(2)	11(1)
C(25)	8450(1)	1668(1)	4577(2)	10(1)
C(27)	6635(1)	2201(1)	3449(2)	13(1)
C(2)	7490(1)	-841(1)	8368(2)	12(1)
C(9)	8511(1)	-131(1)	7656(2)	10(1)
C(19)	12416(1)	1179(1)	6381(2)	12(1)
C(30)	8005(1)	3069(1)	4540(2)	14(1)
C(10)	9486(1)	154(1)	7333(2)	11(1)
C(28)	6190(1)	2694(1)	3245(2)	15(1)
C(7)	6673(1)	-451(1)	8096(2)	13(1)
C(8)	7259(1)	46(1)	7650(2)	11(1)
C(13)	10509(1)	1487(1)	5981(2)	10(1)
C(12)	10459(1)	957(1)	6525(2)	10(1)
C(22)	7155(1)	442(1)	9187(2)	15(1)
C(6)	5528(1)	-558(1)	8252(2)	16(1)
C(3)	7220(1)	-1340(1)	8846(2)	16(1)
C(17)	14118(1)	1590(1)	5615(2)	18(1)
C(26)	7767(1)	2149(1)	4217(2)	11(1)
C(15)	12287(1)	2048(1)	5229(2)	16(1)
C(21)	9641(1)	-940(1)	8305(2)	14(1)
C(29)	6869(1)	3124(1)	3765(2)	16(1)
C(32)	9604(1)	2390(1)	5573(2)	11(1)
C(18)	13592(1)	1158(1)	6265(2)	16(1)
C(5)	5226(1)	-1059(1)	8699(2)	19(1)

C(14)	11753(1)	1617(1)	5900(2)	11(1)
C(16)	13468(1)	2026(1)	5108(2)	19(1)
C(4)	6060(1)	-1439(1)	9001(2)	19(1)
C(23)	6733(1)	261(1)	5791(2)	16(1)

Table A38. Bond lengths [Å] and angles [°] for **7**

O(33)-C(25)	1.2293(17)	C(31)-C(32)	1.499(2)	C(8)-C(23)	1.541(2)
O(35)-C(20)	1.2291(18)	C(25)-C(26)	1.4876(19)	C(8)-C(22)	1.541(2)
N(1)-C(9)	1.3441(18)	C(27)-C(28)	1.382(2)	C(13)-C(12)	1.435(2)
N(1)-C(2)	1.4130(19)	C(27)-C(26)	1.385(2)	C(13)-C(14)	1.4970(19)
N(1)-C(21)	1.4640(18)	C(2)-C(3)	1.386(2)	C(6)-C(5)	1.395(2)
C(11)-C(10)	1.384(2)	C(2)-C(7)	1.389(2)	C(3)-C(4)	1.394(2)
C(11)-C(12)	1.406(2)	C(9)-C(10)	1.399(2)	C(17)-C(18)	1.387(2)
C(24)-C(13)	1.395(2)	C(9)-C(8)	1.5295(19)	C(17)-C(16)	1.390(2)
C(24)-C(25)	1.473(2)	C(19)-C(18)	1.384(2)	C(15)-C(16)	1.391(2)
C(24)-C(32)	1.479(2)	C(19)-C(14)	1.398(2)	C(15)-C(14)	1.394(2)
C(20)-C(12)	1.4730(19)	C(30)-C(29)	1.392(2)	C(5)-C(4)	1.386(2)
C(20)-C(19)	1.480(2)	C(28)-C(29)	1.397(2)		
C(31)-C(26)	1.385(2)	C(7)-C(6)	1.381(2)		
C(31)-C(30)	1.387(2)	C(7)-C(8)	1.5128(19)		
C(9)-N(1)-C(2)	111.83(11)	C(10)-C(9)-C(8)	129.34(12)	C(7)-C(6)-C(5)	118.45(14)
C(9)-N(1)-C(21)	125.36(12)	C(18)-C(19)-C(14)	122.78(14)	C(2)-C(3)-C(4)	116.25(14)
C(2)-N(1)-C(21)	122.75(12)	C(18)-C(19)-C(20)	127.94(14)	C(18)-C(17)-C(16)	120.09(14)
C(10)-C(11)-C(12)	124.87(13)	C(14)-C(19)-C(20)	109.08(12)	C(31)-C(26)-C(27)	121.77(13)
C(13)-C(24)-C(25)	125.76(13)	C(31)-C(30)-C(29)	117.51(13)	C(31)-C(26)-C(25)	109.77(12)
C(13)-C(24)-C(32)	127.00(13)	C(11)-C(10)-C(9)	124.85(13)	C(27)-C(26)-C(25)	128.46(13)
C(25)-C(24)-C(32)	107.10(12)	C(27)-C(28)-C(29)	120.97(13)	C(16)-C(15)-C(14)	118.24(14)
O(35)-C(20)-C(12)	128.50(13)	C(6)-C(7)-C(2)	119.83(13)	C(30)-C(29)-C(28)	121.14(13)
O(35)-C(20)-C(19)	124.89(13)	C(6)-C(7)-C(8)	130.68(13)	O(34)-C(32)-C(24)	129.26(13)
C(12)-C(20)-C(19)	106.60(12)	C(2)-C(7)-C(8)	109.49(12)	O(34)-C(32)-C(31)	123.57(13)
C(26)-C(31)-C(30)	120.99(13)	C(7)-C(8)-C(9)	101.29(11)	C(24)-C(32)-C(31)	106.96(11)
C(26)-C(31)-C(32)	108.94(12)	C(7)-C(8)-C(23)	110.80(12)	C(19)-C(18)-C(17)	117.82(14)
C(30)-C(31)-C(32)	130.08(13)	C(9)-C(8)-C(23)	113.56(12)	C(4)-C(5)-C(6)	120.70(14)
O(33)-C(25)-C(24)	129.40(13)	C(7)-C(8)-C(22)	109.71(12)	C(15)-C(14)-C(19)	119.00(13)
O(33)-C(25)-C(26)	123.17(13)	C(9)-C(8)-C(22)	110.42(12)	C(15)-C(14)-C(13)	131.75(13)
C(24)-C(25)-C(26)	107.18(12)	C(23)-C(8)-C(22)	110.69(12)	C(19)-C(14)-C(13)	108.59(12)
C(28)-C(27)-C(26)	117.62(13)	C(24)-C(13)-C(12)	128.07(13)	C(17)-C(16)-C(15)	122.05(14)
C(3)-C(2)-C(7)	123.02(14)	C(24)-C(13)-C(14)	124.54(13)	C(5)-C(4)-C(3)	121.72(14)
C(3)-C(2)-N(1)	128.57(13)	C(12)-C(13)-C(14)	107.20(12)		
C(7)-C(2)-N(1)	108.41(12)	C(11)-C(12)-C(13)	127.79(13)		
N(1)-C(9)-C(10)	121.69(13)	C(11)-C(12)-C(20)	123.59(13)		
N(1)-C(9)-C(8)	108.95(12)	C(13)-C(12)-C(20)	108.43(12)		

Crystallographic tables for dye 17a

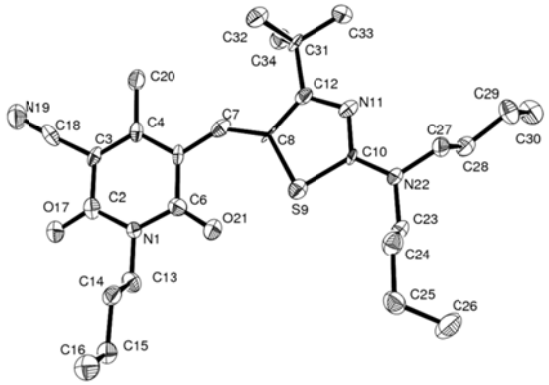

Figure A19. ORTEP drawing of **17a** with atom labelling and 50% probability ellipsoids.

Table A39. Atomic coordinates ($\times 10^4$) and equivalent isotropic displacement parameters ($Å^2 \times 10^3$) for **17a**

Atom	x	y	z	U(eq)
N(1)	9955(4)	1170(2)	8253(4)	24(1)
C(2)	10809(5)	1210(3)	7662(5)	28(2)
C(3)	11015(5)	1803(3)	7225(5)	25(1)
C(4)	10445(5)	2291(2)	7448(5)	23(1)
C(5)	9592(5)	2229(2)	8077(4)	23(1)
C(6)	9299(5)	1642(2)	8464(5)	26(2)
C(7)	8988(5)	2741(2)	8263(4)	27(1)
C(8)	8106(5)	2888(2)	8756(4)	22(1)
S(9)	7319(1)	2409(1)	9460(1)	29(1)
C(10)	6539(5)	3017(2)	9684(5)	21(1)
N(11)	6822(4)	3543(2)	9253(4)	27(1)
C(12)	7668(5)	3482(2)	8736(4)	23(1)
C(13)	9688(4)	572(2)	8634(4)	29(1)
C(14)	8767(4)	257(2)	7406(4)	28(1)
C(15)	8501(4)	-369(2)	7750(4)	30(1)
C(16)	7561(4)	-667(2)	6505(4)	40(2)
O(17)	11341(3)	767(2)	7520(3)	35(1)
C(18)	11833(6)	1828(2)	6521(6)	33(2)
N(19)	12463(5)	1856(2)	5920(5)	44(2)
C(20)	10753(4)	2892(2)	7026(4)	32(2)
O(21)	8539(3)	1555(1)	8961(3)	35(1)
N(22)	5706(4)	2990(2)	10219(4)	24(1)
C(23)	5363(4)	2419(2)	10663(4)	29(1)
C(24)	4386(4)	2108(2)	9495(4)	34(2)
C(25)	4064(5)	1497(2)	9924(5)	38(2)
C(26)	3425(5)	1537(2)	10932(5)	53(2)
C(27)	5077(4)	3524(2)	10379(4)	31(2)
C(28)	5663(4)	3817(2)	11783(4)	31(2)
C(29)	5097(4)	4403(2)	11907(5)	38(2)
C(30)	5725(4)	4693(2)	13328(4)	43(2)
C(31)	8054(4)	4042(2)	8194(4)	22(1)
C(32)	7859(4)	3992(2)	6631(4)	35(2)
C(33)	7326(4)	4569(2)	8346(4)	36(2)
C(34)	9355(4)	4185(2)	9026(4)	35(2)

Table A40. Bond lengths [Å] and angles [°] for **17a**

N(1)-C(2)	1.389(6)	C(8)-C(12)	1.441(6)	C(23)-C(24)	1.530(6)
N(1)-C(6)	1.397(6)	C(8)-S(9)	1.769(5)	C(24)-C(25)	1.544(6)
N(1)-C(13)	1.475(5)	S(9)-C(10)	1.734(5)	C(25)-C(26)	1.514(6)
C(2)-O(17)	1.229(5)	C(10)-N(22)	1.324(6)	C(27)-C(28)	1.522(6)
C(2)-C(3)	1.464(7)	C(10)-N(11)	1.355(5)	C(28)-C(29)	1.518(6)
C(3)-C(4)	1.368(6)	N(11)-C(12)	1.330(6)	C(29)-C(30)	1.540(5)
C(3)-C(18)	1.434(7)	C(12)-C(31)	1.526(6)	C(31)-C(33)	1.525(6)
C(4)-C(5)	1.420(6)	C(13)-C(14)	1.536(5)	C(31)-C(34)	1.544(6)
C(4)-C(20)	1.513(6)	C(14)-C(15)	1.519(5)	C(31)-C(32)	1.555(6)
C(5)-C(7)	1.420(6)	C(15)-C(16)	1.540(5)		
C(5)-C(6)	1.467(6)	C(18)-N(19)	1.152(7)		
C(6)-O(21)	1.228(6)	N(22)-C(27)	1.470(5)		
C(7)-C(8)	1.388(6)	N(22)-C(23)	1.479(5)		
C(2)-N(1)-C(6)	125.7(5)	N(1)-C(6)-C(5)	115.9(6)	C(10)-N(22)-C(27)	121.3(4)
C(2)-N(1)-C(13)	116.8(4)	C(8)-C(7)-C(5)	139.0(5)	C(10)-N(22)-C(23)	121.1(4)
C(6)-N(1)-C(13)	117.4(5)	C(7)-C(8)-C(12)	123.4(5)	C(27)-N(22)-C(23)	117.6(4)
O(17)-C(2)-N(1)	120.8(5)	C(7)-C(8)-S(9)	127.8(4)	N(22)-C(23)-C(24)	112.4(3)
O(17)-C(2)-C(3)	123.3(6)	C(12)-C(8)-S(9)	108.7(4)	C(23)-C(24)-C(25)	112.9(4)
N(1)-C(2)-C(3)	115.8(5)	C(10)-S(9)-C(8)	88.6(3)	C(26)-C(25)-C(24)	113.1(4)
C(4)-C(3)-C(18)	122.9(5)	N(22)-C(10)-N(11)	120.3(5)	N(22)-C(27)-C(28)	112.3(4)
C(4)-C(3)-C(2)	122.0(6)	N(22)-C(10)-S(9)	124.1(4)	C(29)-C(28)-C(27)	112.8(4)
C(18)-C(3)-C(2)	115.0(5)	N(11)-C(10)-S(9)	115.6(4)	C(28)-C(29)-C(30)	111.5(4)
C(3)-C(4)-C(5)	120.0(5)	C(12)-N(11)-C(10)	111.7(4)	C(33)-C(31)-C(12)	109.8(4)
C(3)-C(4)-C(20)	118.6(5)	N(11)-C(12)-C(8)	115.3(4)	C(33)-C(31)-C(34)	107.5(4)
C(5)-C(4)-C(20)	121.3(5)	N(11)-C(12)-C(31)	116.8(5)	C(12)-C(31)-C(34)	111.1(4)
C(7)-C(5)-C(4)	119.0(5)	C(8)-C(12)-C(31)	127.9(5)	C(33)-C(31)-C(32)	106.8(4)
C(7)-C(5)-C(6)	120.6(6)	N(1)-C(13)-C(14)	111.6(4)	C(12)-C(31)-C(32)	111.8(4)
C(4)-C(5)-C(6)	120.4(5)	C(15)-C(14)-C(13)	113.0(3)	C(34)-C(31)-C(32)	109.7(4)
O(21)-C(6)-N(1)	120.4(5)	C(14)-C(15)-C(16)	111.6(4)		
O(21)-C(6)-C(5)	123.6(6)	N(19)-C(18)-C(3)	177.9(6)		

List of Publications and Patents

Publications

"Field dependent exciton dissociation in organic heterojunction solar cells." A. Petersen, A. Ojala, T. Kirchartz, T. A. Wagner, F. Würthner, U. Rau, *submitted for publication.*

"Planar, bulk and hybrid merocyanine/C_{60} heterojunction devices: A case study on thin film morphology and photovoltaic performance." A. Ojala, H. Bürckstümmer, J. Hwang, K. Graf, B. von Vacano, P. Erk, K. Meerholz, F. Würthner, *J. Mater. Chem.* **2011**, DOI:10.1039/C2JM14927C.

"Parallel bulk-heterojunction solar cell by electrostatically driven phase separation." A. Ojala, H. Bürckstümmer, M. Stolte, R. Sens, H. Reichelt, P. Erk, J. Hwang, D. Hertel, K. Meerholz, F. Würthner, *Adv. Mater*. **2011**, DOI: 10.1002/adma.201103167.

"Merocyanine/C_{60} planar heterojunction solar cells: effect of dye orientation on exciton dissociation and solar cell performance." A. Ojala, A. Petersen, A. Fuchs, R. Lovrincic, C. Pölking, J. Trollmann, J. Hwang, C. Lennartz, H. Reichelt, W. Höffken, A. Pucci, P. Erk, T. Kirchartz, F. Würthner, *Adv. Funct. Mater.* **2011**, DOI: 10.1002/ adfm.201101697.

"Comparison of the polymorphs and solvates of two analogous fungicides – a case study of the applicability of a supramolecular synthon approach in crystal engineering." E. Nauha, A. Ojala, M. Nissinen, H. Saxell, *CrystEngComm* **2011**, *13*, 4956.

"Theoretical and experimental investigation on the influence of the molecular polarizability of novel zinc phthalocyanine derivatives on the open circuit voltage of organic heterojunction solar cells." I. Bruder, A. Ojala, C. Lennarz, S. Sudarraj, J. Schöneboom, R. Sens, J. Whang, P. Erk, J. Weis, *Solar Energy Mater. Solar Cells* **2010**, *94*, 310.

”What determines the performance of metal phthalocyanines (MPc, M = Zn, Cu, Ni, Fe) in organic heterojunction solar cells? A combined experimental and theoretical investigation.” I. Bruder, J. Schöneboom, R. Dinnebier, A. Ojala, S. Schäfer, R. Sens, P. Erk, J. Weis, *Org. Electron*. **2010**, *11*, 377.

Patents

“Merocyanines for producing photoactive layers for organic solar cells and organic photodetectors.” Helmut Reichelt, Jaehyung Hwang, Rüdiger Sens, Jan, Schöneboom, Peter Erk, Ingmar Bruder, Antti Ojala, Frank Würthner, Klaus meerholz, (BASF SE, Germany), *PCT Int. Appl.* 2009, WO2010049512, EP2009064331.

“Use of phthalocyanine compounds with aryl or hetaryl substituents in organic solar cells.“ Antti Ojala, Augustine Leow Yoon Wui, Peter Erk, Rüdiger Sens, Thomas Gessner, Sudhakar Sundarraj, Ingmar Bruder, Jae Hyung Hwang, Jan Schöneboom, Martin Könemann, Sheeja Bahulayan, (BASF SE, Germany), *PCT Int. Appl.* 2010, WO2010136420, EP2010057099.

Acknowledgements

I am grateful to BASF SE for funding my PhD work and for the opportunity to work in the exciting organic photovoltaics project at BASF in Ludwigshafen and in collaboration with the group of Prof. Würthner in University of Würzburg.

First of all I want to thank my supervisors Prof. Frank Würthner (University of Würzburg) and Dr. Peter Erk (BASF Ludwigshafen) for their great support.

Many thanks belong to devices engineers Dr. Jaehyung Hwang and Dr. Ingmar Bruder (both at BASF Ludwigshafen) for helpful discussions and wise advices.

Many thanks to Ms. Hannah Bürckstümmer (University of Würzburg) as well as to Dr. Helmut Reichelt (BASF Ludwigshafen) and his lab technicians for synthesizing the merocyanines used in this work. I acknowledge also Ms. Ana-Maria Krause (University of Würzburg) for the cyclic voltammetric measurements and in particular Mr. Marcel Gsänger (University of Würzburg) for solving a considerable number of the crystal structures discussed in Chapter 4.

I am thankful to Dr. Rüdiger Sens and Mr. Johannes Manz (both at BASF Ludwigshafen) for their help with the photoluminescence measurements.

Many thanks to Dr. Wolfgang Höffken and Mr. Wolfgang Houy (both at BASF Ludwigshafen) for the single crystal measurements.

Many thanks to Mr. Andreas Fuchs and Christian Lennartz (both at BASF Ludwigshafen) for the exciton dissociation energy calculations presented in Chapter 6.

I am thankful to Mr. Andreas Petersen (BOSCH Stuttgart) for numerous helpful discussion and the *J-V* simulations presented in Chapter 6.

A big thank to Dr. Robert Lovrincic, Mr. Jens Trollmann, Mr. Carl Pölking, and Prof. Annemarie Pucci (all at University of Heidelberg) for conducting the infrared spectroscopic ellipsometry (IRSE) measurements discussed in Chapter 6.

I owe many thanks to Ms. Katja Graff and Dr. Alberto Sugiharto (both at BASF Ludwigshafen) for the AFM measurements and for the help with the data interpretation.

Many thanks to Dr. Matthias Stolte (University of Würzburg) for the EOA spectroscopy measurements presented in Chapter 4 and Chapter 5. I am also grateful to Matthias for his invaluable help with the preparation of the journal articles.

Many thanks to Dr. Christian Schildknecht (BASF Ludwigshafen) for his help with the mobility measurements.

I am thankful to Dr. Heidi Saxell (BASF Ludwigshafen) and GVC/C for the possibility to operate the X-ray powder diffraction instrument.

Many thanks to Mr. Christian Dörr (BASF Ludwigshafen) for his help with the device fabrication.

I want to give a big thank to the whole Innovation Lab team at Ludwigshafen for the great support.